Universität Rostock
Institut für Physik

Dissertation
zur Erlangung des akademischen Grades
doctor rerum naturalium
der Mathematisch-Naturwissenschaftlichen Fakultät
der Universität Rostock

Structure Formation in Strongly Correlated Few-Particle Systems in Traps

vorgelegt von

Patrick Ludwig

geb. am 27.07.1978 in Rostock

aus Kiel

Rostock, August 2008

Referent: _____

Erster Korreferent: _____

Zweiter Korreferent: _____

Tag der mündlichen Prüfung: _____

Zum Druck genehmigt: _____

Der Dekan

The fundamental laws necessary for the mathematical treatment of large parts of physics and the whole of chemistry are thus completely known, and the difficulty lies only in the fact that application of these laws leads to equations that are too complex to be solved.

—————————————————

(Paul A. M. Dirac, 1929)

Contents

Abstract

The objective of the present work is the theoretical investigation physical structure formation by means of computational simulation methods. Of particular interest are charged few-particle systems in external trapping potentials, which allow one to realize and control strong correlation and quantum effects. Such "artificial atoms" have unique features absent in real atoms: by controlling the confinement strength they can be transformed from a weakly coupled state to a strongly coupled, crystal-like phase.

The first central topic is devoted to the structural properties of 3D Coulomb crystals, which have been observed in trapped ion systems as well as in (multi-component) complex plasmas. The ground state properties, such as the shell structure, are studied by first-principle molecular dynamics simulations. The detailed comparison of the theoretical results with experiments provides the basis for a theory of these strongly correlated classical systems.

The second major topic concerns electron-hole quantum plasmas in dimensionality reduced semiconductor heterostructures. At first, the realization of a quantum Stark confinement for spatially indirect excitons in a single quantum well is investigated in view of an experimental implementation. Furthermore, the effects of field-strength, temperature, density, exciton dipole moment, and electron-hole mass asymmetry are extensively studied by means of quantum Monte Carlo simulations. As a universal melting criterion for classical and quantum few-particle systems a modified version of the Lindemann parameter for the pair distance fluctuations is introduced.

Abstract

8

Kurzfassung

Die Zielsetzung der vorliegenden Arbeit ist die theoretische Untersuchung von physikalischer Strukturbildung mit Hilfe von Computersimulationen. Von besonderem Interesse sind Systeme aus nur wenigen geladene Teilchen in externen Fallenpotentialen, welche die Realisierung und Kontrolle von starken Korrelations- und Quanteneffekten ermöglichen. Derartige "künstliche Atome" besitzen im Gegensatz zu echten Atomen besondere Eigenschaften: durch Steuerung des Einschlusspotentials können sie von einem schwach gekoppelten Zustand in eine stark gekoppelte, kristalline Phase überführt werden.

Die erste zentrale Fragestellung ist den strukturellen Eigenschaften dreidimensionaler Coulombkristalle gewidmet, die als Ionensysteme in Fallen sowie als komplexe (Vielkomponenten-) Plasmen beobachtet werden. Die Grundzustandseigenschaften, wie die Schalenstruktur, werden mittels Molekulardynamik-Simulationen näherungsfrei studiert. Ein detaillierter Vergleich der theoretischen Resultate mit Experimenten dient als Basis für eine Theorie dieser stark korrelierten klassischen Systeme.

Der zweite Themenkomplex befasst sich mit Elektron-Loch-Plasmen in dimensionalitätsreduzierten Halbleiterheterostrukturen. Zunächst wird die Realisierung einer geeigneten Potentialgeometrie für räumlich indirekte Exzitonen in einem einzelnen Quantenfilm durch Anwendung des Quanten-Stark-Effekts im Hinblick auf eine experimentelle Umsetzung untersucht. Desweiteren wird der Einfluss von Feldstärke, Temperatur, Dichte, Dipolmoment der Exzitonen sowie Massenasymmetrie von Elektronen und Löchern mit sehr umfangreichen Quanten-Monte-Carlo-Simulationen studiert. Als ein universelles Schmelzkriterium für klassische und Quantensysteme aus nur wenigen Teilchen wird eine modifizierte Form des auf den Paarabstandfluktuationen basierenden Lindemann-Parameters eingeführt.

1 Introduction: Plasma Crystals and Artificial Atoms

1.1 Outline of the Thesis

Self-organized structure formation is one of the most fundamental processes in nature and among the most exciting cooperative phenomena in the field of charged many-particle systems. Many questions of many-body physics are not related to specific materials, but rather of fundamental nature. Thus, the understanding of the details of physical structure formation is of very general interest. In particular few-particle systems in external trapping potentials are of interest in many fields of science, since they allow to realize and control strong correlation and quantum effects.

Aim of this thesis is the investigation of structure formation of small particle ensembles in confined geometries by means of computational simulation methods. Thereby, this thesis focuses on two central topics related to mesoscopic classical and quantum Coulomb systems: (1) spherically confined (multi-component) complex plasmas, and (2) electron-hole quantum plasmas in dimensionality reduced semiconductor heterostructures.

The main results of this cumulative dissertation have been published in peer-reviewed journal publications. Each chapter opens with a short introduction and overview, and gives the reader additional information which is not included in the publications. The publications are listed and appended at the end of the respective chapter to allow for an easy access by the reader. The outline of this thesis is as follows:

Chapter 1 – Introductory Part. The first chapter provides a brief introduction into the topic of strongly correlated few-particle systems in traps. Besides an overview of the current status of research, this part introduces the theoretical model system, physical key parameters and the problems of interest.

Chapter 2 – Computational Approaches to the Many-Body-Problem. This second introductory chapter briefly discusses the main concepts and ideas of the numerical methods, which are centrally used in the frame of this work. In particular, the specific advantages and limitations of the different many-particle simulation approaches are critically reviewed. Additionally, the imaginary time path integral representation of the density matrix is derived and its numerical solution with efficient Monte Carlo methods is discussed.

Chapter 3 – First Principle Simulations of Finite Classical Systems in Traps. The third chapter contains the first central topic of the present thesis and is devoted to the structural properties of 3D Coulomb crystals, which have been observed in trapped ion systems as well as in dusty plasmas. We study the ground state properties, such as the shell structure, by first-principle molecular dynamics simulations. The detailed comparison of the theoretical results with the experiments provides the basis for a theory of these strongly correlated classical systems.

Chapter 4 – Statistical Properties of Confined Systems. Chapter 4 aims at a deeper insight into the statistical properties of confined plasmas and thereby naturally connects the investigations on complex plasmas (chapter 3) and those of electron-hole plasmas (chapter 5). The theoretical objective concerns (i) the dependence of the ground state particle distribution of a confined plasma on the range of the interaction potential, and (ii) the role of pair distance fluctuations as a universal melting criterion for classical and quantum few-particle systems.

Chapter 5 – Spatially Indirect Electron-Hole Systems in Mesoscopic Traps. The fifth chapter contains the results of the second major topic of this thesis. First of all, we investigate the realization of a quantum Stark confinement for spatially indirect excitons in a single quantum well in view of an experimental realization. Further, we extensively study the effects of field-strength, temperature, density, exciton dipole moment, and electron-hole mass asymmetry. The quantitative results of this chapter were primarily obtained with the finite temperature quantum Monte Carlo method as introduced in chapter 2. Recent progress in the field of strongly correlated classical and quantum plasmas is described in the review article contained at the end of this chapter.

Chapter 6 – Summary and Discussion. The last chapter summarizes the main results obtained in the thesis at hand.

1.2 Mesoscopic Strongly Coupled Coulomb Systems

The question concerning a finite number of interacting particles and how they arrange themselves energetically most favourably is of fundamental interest not only in many fields of physics, but also in chemistry, biology and beyond. Examples of strongly correlated, two- and three-dimensional confined classical and quantum systems are:

- Localized charge densities of electrons in quantum dots and wells [1, 2] or electron dimples on the surface of a helium droplet [3, 4] (as shown in figure 1.1).

- Crystallization of holes in mass asymmetric electron-hole-plasma in semiconductors [5], see section 5.3.

- Laser-cooled ion plasma crystals, which are confined by electromagnetic fields in Paul or Penning traps [6]-[9] (see for instance figure 1.2). The classical ground states which apply to recently observed spherical ion Coulomb crystals, see figure 1.3, are systematically analyzed in section 3.2.

- Two- and three-dimensional complex plasma crystals of highly charged dust microspheres which are immersed in a discharge plasma of electrons, positive ions and neutral atoms [10]-[15] (see figure 1.5 and 1.4). Dusty plasma crystals are the main subject of chapter 3.

- Spatial, correlation-driven structures of inter-well exciton photoluminescence as shown in figure 1.7 [16, 17, 18]. Strongly correlated states of spatially indirect excitons are the central topic of chapter 5.

- Polymers [19], atomic and molecular clusters [20, 21, 22].

- Folded small protein structures in biochemical systems, e.g. [23].

The different nature of the mentioned examples shows that the occurrence of structure formation is not a question of high or low temperatures; however, it is closely related with the ratio of the mean interaction energy E_{int} to the average kinetic energy E_{kin}. This defines the plasma coupling parameter

$$\Gamma = \frac{|E_{int}|}{E_{kin}} \quad .$$

(1.1)

A system becomes strongly coupled whenever the interaction energy dominates over the kinetic energy. Furthermore, if the dimensionless parameter Γ exceeds a critical value that is typically around $\Gamma_{cr} \gtrsim 100$; the system of charged particles self-organizes in an
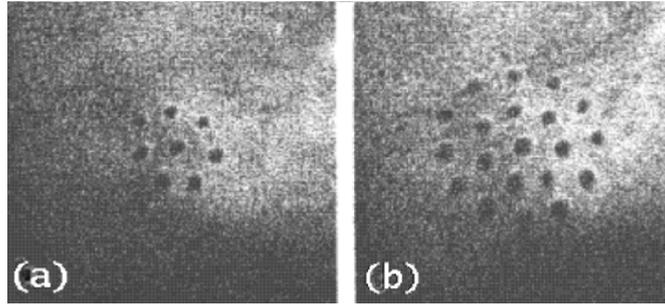
Figure 1.1: *Electrons in macroscopic dimples on the surface of liquid helium ^4He. Configurations of (a) 8 and (b) 20 dimples (appearing as dark spots) in an external potential of cylindrical symmetry. From Ref. [4].*

ordered, crystal-like state, and the detailed spatial arrangement as well as the structural properties of the particle ensemble become important, e.g. [24].

In physical situations where the sizes of the particle wave functions are of the same order of magnitude as the mean interparticle distance, quantum-mechanics becomes essential. A second key quantity, which describes the particle correlations in quantum systems is the Brueckner parameter r_s defined by

$$r_s = \frac{a}{a_B} \; .$$
(1.2)

This means that the quantum coupling parameter is given as the ratio between mean interparticle particle distance a and the effective Bohr radius is $a_B = 4\pi\varepsilon\hbar^2/(mq^2)$. In few-particle systems a is typically taken as the first peak of the pair distribution function[1]. In the case of electrons (holes), q and m are the elementary charge $e = 1.602{\cdot}10^{-19}$ C and the effective electron (hole) band mass $m_{e(h)}$, respectively. Hence, the Brueckner parameter r_s expresses the transition from a weakly coupled, ideal quantum system ($r_s \ll 1$) to a pure classical one ($r_s \rightarrow \infty$). While both limits of $\Gamma \ll 1$ and $r_s \ll 1$ are fully structureless, crystal-like states of matter are known to exist only under the condition that $\Gamma \geq \Gamma_{cr} \gtrsim 100$ and $r_s \geq r_{s,cr} \gtrsim 100$. Consequently, the regime of strong coupling can be achieved at moderate densities and low kinetic energies in the case of elementary charged particles, but also at room temperature if the individual particles are highly charged (such as complex plasmas with typically $q = 1000e \ldots 10000e$, depending on the particle size).

---

[1]In macroscopic homogeneous systems the interparticle distance a is often referred to as the Wigner-Seitz radius $a^{2D} = (\pi n)^{-1/2}$ for 2D systems and $a^{3D} = (4/3\pi n)^{-1/3}$ for 3D systems with n being the average density.
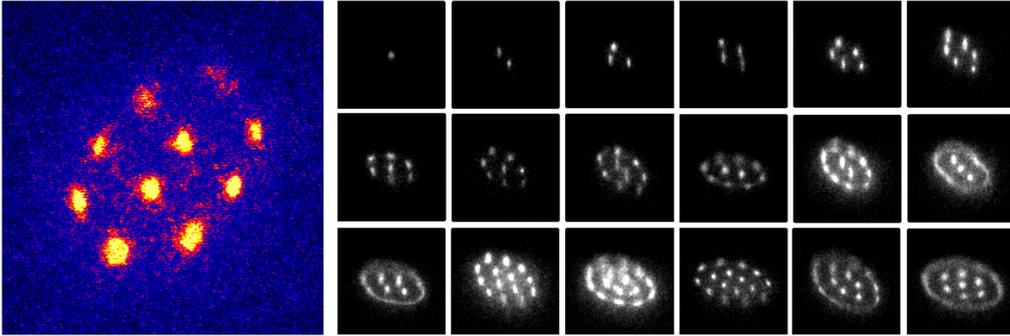
Figure 1.2: *Crystalline structures formed by laser cooled Ca^+ ions in a Paul trap [8]: <u>Left:</u> Fluorescence pattern of $N = 10$ ions in the quasi-two-dimensional confinement showing a $\overline{(2,8)}$ configuration. <u>Right:</u> Periodic system of 2D crystals for 1 to 18 ions. The side length of each image is $123\mu m$. The configurations are essentially in agreement with molecular dynamics calculations in static 2D parabolic potentials [25, 26].*
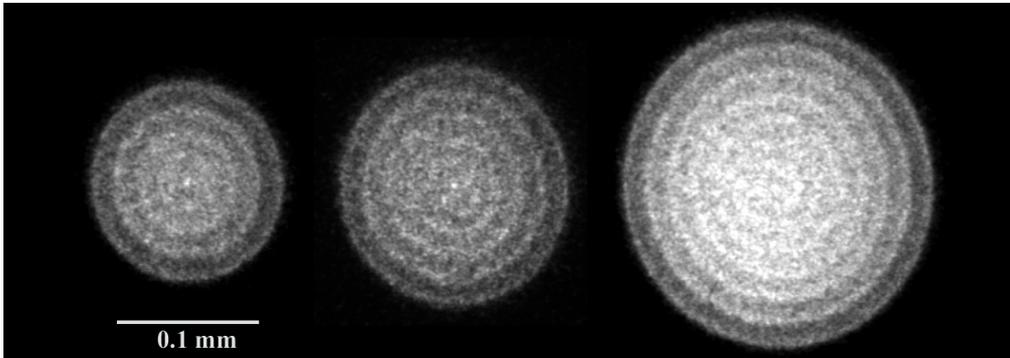
Figure 1.3: *Recent observation of three-dimensional spherical Ca^+ ion Coulomb crystals showing shell structures. The Coulomb crystals are confined in a Paul trap and contain about 300, 700 and 1400 ions, from left to right. Typically, the temperature is $T \approx 5$ mK, and the coupling parameter is $\Gamma \approx 400$. From Ref. [9, 27].*
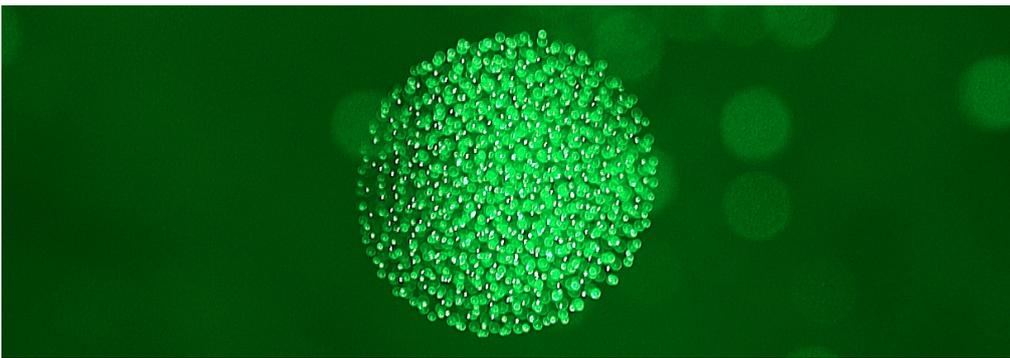
Figure 1.4: *Picture of a Yukawa ball consisting of several hundred dust particles (white dots). The ball has a diameter of about 7 mm and the dust grains are 3.5 μm sized. One clearly recognizes the spherical shape and the nested shell structure of the cluster. The dust-dust coupling parameter is on the order of $\Gamma \approx 1000$. The electron and ion temperatures are $T_e \approx 40,000$ K and $T_i \leq 1000$ K, respectively. From Ref [28].*

1.3 Theoretical Modeling

The theoretical description of the classical and quantum Coulomb systems under consideration begins with the many-particle Hamiltonian. This reads in coordinate representation as

$$\hat{H}(\mathbf{r}_i) = \sum_{i=1}^{N} -\frac{\hbar^2}{2m_i}\nabla_i^2 + \sum_{i=1}^{N-1}\sum_{j=i+1}^{N} V^{\text{int}}(|\mathbf{r}_i - \mathbf{r}_j|) + \sum_{i=1}^{N} V^{\text{ext}}(\mathbf{r}_i) \ , \qquad (1.3)$$

where $\mathbf{r}_i$ denotes the coordinate of the i-th particle. The first term describes the dynamics of the particles and gives rise to structural disorder as well as an increase of entropy. In contrast, the combination of a repulsive pair potential V^{int} and a stabilizing external confinement V^{ext} allows for arbitrarily strong coupling of particles leading to collective behaviour.

The fundamental, infinitely-long-ranged Coulomb pair potential causes the structure of atoms, solid state matter, and all classical plasma correlation effects:

$$V^{\text{int}}(\mathbf{r}_i - \mathbf{r}_j) = \frac{q^2}{4\pi\varepsilon|\mathbf{r}_i - \mathbf{r}_j|} \ . \qquad (1.4)$$

In section 3.2 and 4.3 the Coulomb potential is applied in its pure form to describe the ground state and the melting process of spherical Coulomb clusters. It is also used within all sections of chapter 5 for the first principle treatment of electron-hole bilayer systems. Based on this fundamental potential, two (effective) short-ranged potentials emerge which are implemented:

- in section 3.3 and 4.1, the Yukawa pair potential as an electrostatically screened Coulomb potential,

- in section 5.2, the repulsive dipole-dipole interaction potential.

Within the present work we focus on external trapping potentials of harmonic form

$$V^{\text{ext}}(\mathbf{r}_i) = \frac{m}{2}\omega_0^2 \mathbf{r}_i^{\,2} \ , \qquad (1.5)$$

which provides a useful approximation for arbitrary types of (especially isotropic) potentials in the vicinity of the stable equilibrium point. Within a suitable range, the parabolic approximation also applies to the lateral electrostatic exciton confinement, which is analyzed in section 5.2. Considering the case of a pure Coulomb interaction, due to the quadratic increase of confinement strength in the radial direction, one finds

the density to be constant over the entire cluster (see section 4.2). This implies that melting effects on the cluster surface are strongly reduced (see section 4.3).

In total, the considered model (1.3-1.5) has been very successful in describing charged few-particle systems in various traps. This model has the advantage of analyzing order-disorder transition phenomena in both classical and quantum systems on equal footing. Due to *universal scaling laws* [29], similar physical correlation phenomena, such as plasma crystallization, are present in completely different physical regimes. By use of dimensionless energy and length scales, the theoretical results become universally valid; nevertheless, they are still easily applicable to a particular experimental measurement. Within the thesis at hand all quantities are reduced to a dimensionless form by choosing characteristic units.

Classical systems: The most suitable base units of length and energy for classical systems are

$$r_0 = (q^2/2\pi\varepsilon m\omega_0^2)^{1/3} \quad , \quad E_0 = q^2/(4\pi\varepsilon r_0) = (m\omega_0^2 q^4/32\pi^2\varepsilon^2)^{1/3} \ . \qquad (1.6)$$

Here, the base length r_0 is the equilibrium distance of two identical classical particles in a harmonic confinement that interact via a Coulomb potential. Energies are expressed in terms of the pair interaction energy E_0 for this distance. A dimensionless system of units is obtained by applying the transformation rules $\{r \to r/r_0,\ E \to E/E_0\}$. The strength of the external confinement potential is controllable by the harmonic trap frequency ω_0, which defines in the classical case the characteristic scales r_0 and E_0, but does not affect the obtained dimensionless results. This fact clearly underlines the universal scaling behaviour of classical many-body effects. Note that quantum effects naturally limit the universal scaling which is found for classical systems.

Quantum systems: In contrast to the classical limit, in a pure quantum system the kinetic energy does not vanish even for temperature $T \to 0$, resulting in a finite spatial particle extension. For harmonically trapped quantum particles it is therefore useful to introduce the oscillator length and energy as base units

$$l_0 = \sqrt{\hbar/(m_{e(h)}\omega_0)} \ , \quad E_0^* = \hbar\omega_0 \ . \qquad (1.7)$$

The strength of the harmonic confinement (and density) of a mesoscopic trapped

system is characterized by the dimensionless coupling parameter

$$\lambda(\omega_0) = \frac{E_C}{E_0^*} = \frac{q^2}{4\pi\epsilon l_0 \hbar\omega_0} = \frac{l_0}{a_B} \; . \tag{1.8}$$

This relates the characteristic Coulomb energy $E_C = q^2/(4\pi\epsilon l_0)$ to the characteristic confinement energy E_0^*. Starting with a non-interacting quantum system at $\lambda = 0$, we find that the system gradually becomes strongly coupled, as λ is increased. Furthermore, in the limit $\lambda \to \infty$, the system transforms into a classical one consisting of localized particles (see section 5.4).

Conversion: In order to form a comprehensive picture, it is often instructive to compare the classical and quantum calculations, which can easily be done with the following relations

$$\frac{r_0}{l_0} = (2\lambda)^{1/3} \; , \quad \frac{E_0}{E_0^*} = (\lambda^2/2)^{1/3} \; . \tag{1.9}$$

If one sets the interparticle distance $a = r_0$, according to equation (1.2), one obtains the two-particle approximation $r_s = r_0/a_B = (2\lambda^4)^{1/3}$.

Hence, by specifying the corresponding system properties, the length and energy scale are uniquely determined.

1.4 Finite-Size and Surface Effects

Finite-size, surface effects, as well as charge quantization are exceptional features inherent to quantum and (quasi-)classical strongly coupled few-particle systems (figure 1.1-1.7). From numerous experiments, e.g. [1, 11, 13, 30, 31, 32], and simulations, e.g. [2, 25, 33, 34, 35, 36, 37, 38], finite Coulomb systems in a parabolic confinement potential are known to arrange themselves in nested concentric rings (in 2D) or shells (in 3D systems). The arrangements have characteristic occupation numbers $(N_1, N_2, \ldots)$, where N_i denotes the number of particles on the i-th ring or shell (starting from the center).

A striking feature common to all mentioned few-particle systems is that their structure and properties are very sensitive to the exact particle number. Different exceptional physical situations were identified, in particular those involving so called "magic" configurations [2, 34, 39, 40]. Interestingly enough, even without change of density or
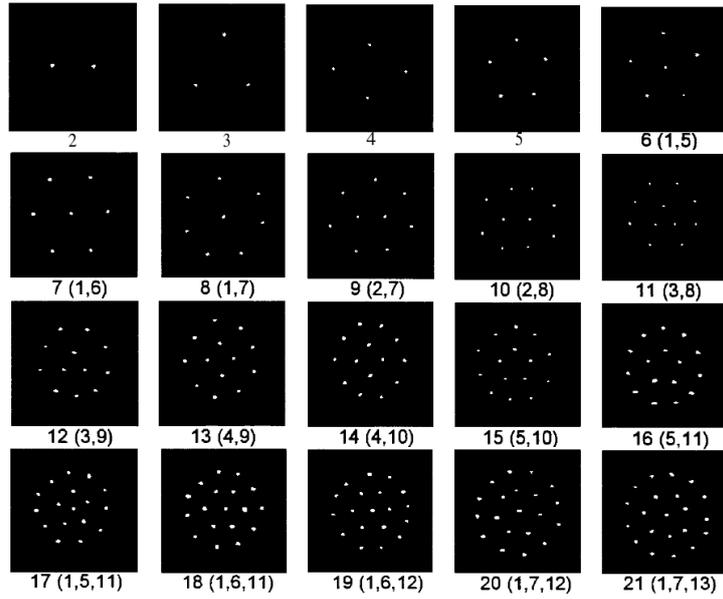
Figure 1.5: *Microimages of experimentally determined ground state configurations of dust crystals in a 2D circular symmetric rf plasma trap with $N = 2$ to $N = 21$. The snap shots (exposure time $1/30s$) are taken from experiments by the group of Lin I (Taiwan) [11]. Note that the comparison of the experimentally observed structures and packing rules, see figure 1.6, with theoretical results allows one to clearly identify the combination of the underlying interparticle interaction and trapping potential as well; cf. e.g. the different shell population numbers of screened 2D dust clusters with that obtained for 2D ion Coulomb crystals in figure 1.2.*

Figure 1.6: *Classical 2D periodic table of the packing sequence for small N corresponding to figure 1.5. For $N = 3$ to 5, the particles occupy a single shell only. For $N = 6$, a pentagon with a single particle at the center is formed. In contrast to real atoms, where new electrons add to outer orbitals if N is increased, the generic behavior is that the clusters grow alternately one-by-one first in the center and then successively fill up the outer shell. For $N = 17$, the third shell appears with the (1,5,11) configuration. Increasing N the particles periodically fill the third shell. From Ref. [11].*

Figure 1.7: *Experiments on the spatial resolution of interwell exciton photoluminescence observed within a circular electrostatic trap created by a 5 μm window in a opaque metallic mask on top of GaAs/AlGaAs double quantum wells of 12 nm width. Luminescence patterns measured for excitation power $P_{HeNe} = 50\mu W$ and temperatures of (a) 1.74, (b) 3.90, (c) 4.25 and (d) 4.33 K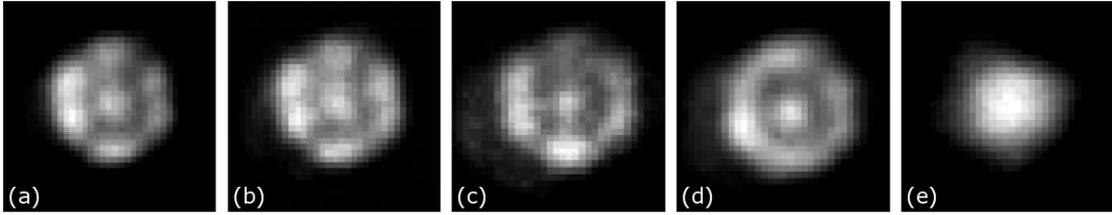. At $T < 4\,K$ discrete patterns consisting of six equidistant spots were observed which start to wash off with temperature increase. (e) the spatial structure of intrawell exciton luminescence, here at 1.7 K, is not found to show such correlated states. From Ref [16].*

temperature, qualitative transformations of the physical properties can be achieved just by adding or removing a single charged particle [2]. This behavior of few-particle systems reflects the basis of chemistry: even the change of the particle number by a single particle can result in drastically different collective properties (structural, electronic, magnetic, transport or optical).

In addition, compared to real atoms, an even wider range of interesting physical arrangements becomes accessible by controlling the confinement parameters via external electric or magnetic fields [41] or even by tuning the effective particle interaction strength [22, 38] (for details see chapter 5). An additional degree of freedom arises from the various confinement geometries. Examples include:

- Self-assembled quantum dots, which have a typical size between 10 and 50 nm. Quantum dots are often considered as quasi-zero-dimensional because their strong confinement in all three spatial directions allows for a full quantization of the electron's motion. This implies that the structure of their energy spectrum can be engineered by tuning the shape and size of the potential well.

- Thin two-dimensional single or multilayer traps, such as single or bilayer semi-conductor quantum wells. These consist of one or two *nm*-thin epitaxial layers that are sandwiched between layers of another semiconductor material with higher conduction-band energy.

- Real three-dimensional geometries, have been recently generated for ion plasmas [27] as well as dusty plasmas [15]. 3D traps allow for spherical but also strongly anisotropic (e.g. ellipsoidal) cluster shapes, see e.g. [42].

Aside from the number of confined dimensions, the particular shape and strength of the trapping potential, there are variable particle properties such as the dipole moment (e.g. that of spatially indirect of excitons in semiconductors), the effective band mass of electrons and holes (of different semiconductor materials), or the particle charge in dusty plasmas. Hence, controlling all mentioned trap and particle parameters as well as the exact number of trapped particles, their polarity etc. offers researchers an excellent opportunity to study finite-size phenomena and phase transitions under a vast variety of different conditions.

With respect to the outlined high degree of variability, strongly coupled few-particle systems in traps are often considered as manufacture-designed "artificial atoms" or "superatoms" [30]. In allusion to the periodic table of the chemical elements, periodic Mendeleev-type tables have been extensively studied, in particular for parabolically confined classical systems, where the number of particles N is the only free parameter (in dimensionless units). Many of these investigations focused primarily on two-dimensional single layer systems, see e.g. figure 1.5 and figure 1.6 [2, 13, 14, 26, 34, 36, 39, 43, 44, 45, 46, 47]. Within the frame of this work, the ground state configurations of parabolically confined mesoscopic 3D Coulomb crystals (see section 3.2) and that of dipolar electron-hole bilayer systems (see section 5.4) have been systematically analyzed, extended and partially corrected. The obtained results are of utmost significance, as the structural symmetries have a deep impact on most static and dynamical properties of strongly coupled few-particle systems. Moreover, special interest arises from the fact that the shell configurations are very sensitive to the fundamental interactions (as exposed in section 3.3 and 5.4). Hence, the question about the structure of few-particle clusters in strongly confined geometries emerges as a key issue for a variety of phenomena occurring physical systems at different energy and length scales, and has immediate importance for the understanding of collective behaviour.

2 Computational Approaches to the Many-Body-Problem

Structure formation of matter was (and still is) one of the main open problems in science for long times. The problem is closely related to the exact treatment of many-body correlations. To rigorously take into account the mutual interplay between a large number of individual particles requires either solving multi-dimensional integrals or systems of high-order differential equations, which are coupled by interaction terms. In the case of strong correlations, the mathematical problem cannot be reduced without oversimplifications, because analytical approaches often involve more or less uncontrollable approximations to reduce the problem's inherent strongly non-linear feedback effects.

However, the tremendously fast development of digital computers in the last decades, and in particular the growing availability of cheap computer equipment such as desktop PCs and Linux clusters, enables researches nowadays to solve many of the fundamental equations of physics without mathematical simplifications — from first principles.

Today, modern numerical methods are central part of all directions in (natural) sciences as well as industrial engineering, research and development for several reasons:

- computer-simulated experiments do not require extensive laboratory facilities,

- the model "experiments" can be arbitrarily often repeated and easily modified,

- comprehensive and concurrently detailed scans of large parameter sets and ranges can help to define the conditions of exceptional physical phenomena or optimal settings for real physical experiments,

- computer simulations can provide maximum information at the microscopic level and therefore help to give a deeper understanding of laboratory measurements.

In the work at hand, we will concentrate in particular on trapped few-particle systems.

These small systems serve as very suitable (classical and quantum) laboratories for the investigation of fundamental many-body interaction phenomena because they do not require undesirable simplifications of the fundamental equations with regard to limited computational capabilities. Moreover, in trapped systems there are no periodic boundary conditions to consider that may introduce correlational artifacts.

Two essentially different particle-based bottom-up approaches have been used for our theoretical investigations.

Deterministic simulation models: The strict deterministic integration of the classical equations of motion for many-particle systems are commonly named molecular dynamics. Once the positions and velocities of all individual particles are known, their dynamical propagation through the *position-momentum phase-space* can be directly computed. Molecular dynamics has been utilized to calculate the energetically most favourable states of Coulomb and Yukawa balls (see chapter 3).

Stochastic simulation models: Random number based Metropolis Monte Carlo methods (MC) are applied to efficiently sample the high-dimensional *configuration space*. Both, classical thermodynamic and quantum MC techniques are applied to study finite-temperature equilibrium problems (see sections 4.3, 5.2 and 5.3).

The aforementioned computational tools are standard and widely used to investigate structures, dynamics and thermodynamics in physics, chemistry, biology, economics, material science, astrophysics etc. Hence, we will limit our explanations to a brief overview of the conceptual ideas behind the pursued methods.

2.1 Molecular Dynamics Simulation

The molecular dynamics method (MD) was originally introduced by B. J. Alder and T. E. Wainwright in the late 1950's with the aim to calculate many-body correlations of classical hard sphere systems exactly by means of "electronic computors" [48, 49, 50] (see figure 2.1). Valuable insights concerning the collective behavior of interacting many-body systems emerged from their studies with the first super computers. A prominent example is the evidence of crystal-like stable structures in 2D systems at finite temperature. Down to the present day, molecular dynamics has evolved into the probably most frequently used method to study time-dependent processes in many-particle physics.

In molecular dynamics the time propagation of the N-particle Hamiltonian (1.3) is
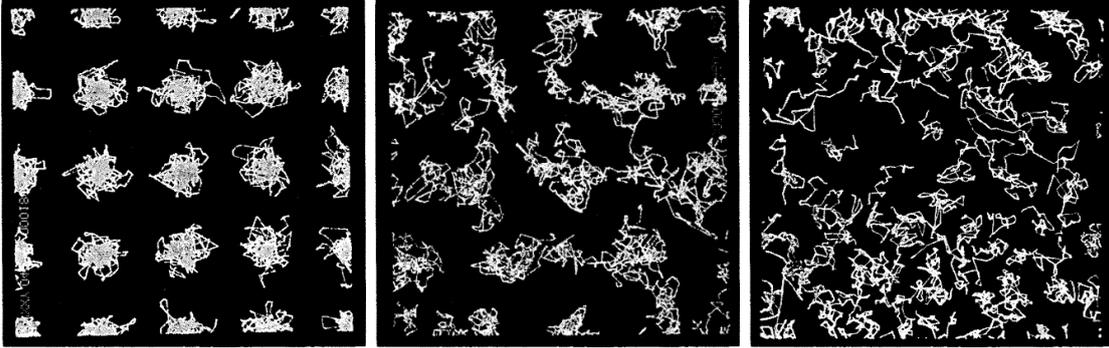
Figure 2.1: *Molecular dynamic motion simulated by means of the first mainframe computers by Alder and Wainwright [49, 50]. Shown are the trajectories of several ten hard sphere particles with periodic boundary conditions in the quasi-long-range ordered solid phase (left), after it has transformed to the short-range ordered fluid phase (middle), and in the liquid-vapor region (right). Each picture follows the system for 3000 collisions.*

achieved by high-precision numerical integration of the N coupled Newtonian differential equations $\mathbf{F}_i = m_i \frac{d^2}{dt^2} \mathbf{r}_i$. These equations can be split into a coupled system of first-order ordinary differential equations (ODEs)

$$\frac{d}{dt}\mathbf{r}_i = \mathbf{v}_i \,, \tag{2.1}$$

$$\frac{d}{dt}\mathbf{v}_i = \frac{\mathbf{F}_i}{m_i} \,, \tag{2.2}$$

for the motion of the particles $i = 1 \ldots N$ of mass m_i, position $\mathbf{r}_i$, velocity $\mathbf{v}_i$ and the total force

$$\mathbf{F}_i = -\nabla_{\mathbf{r}_i} \left(V^{\text{ext}}(\mathbf{r}_i) + \frac{1}{2} \sum_{j \neq i}^{N} V^{\text{int}}(\mathbf{r}_i - \mathbf{r}_j) \right) \,. \tag{2.3}$$

The considered conservative force is due to the external confinement and the mutual particle-particle interaction energies.

The numerical time integration is performed by means of an adaptive stepsize controlled

algorithm based on the *fifth-order* Runge-Kutta formula

$$
\begin{aligned}
k_1 &= hf(x_n, y_n) \,, & (2.4)\\
k_2 &= hf(x_n + a_2 h, y_n + b_{21} k_1) \,, & (2.5)\\
&\cdots \\
k_6 &= hf(x_n + a_6 h, y_n + b_{61} k_1 + \cdots + b_{65} k_5) \,, & (2.6)\\
y_{n+1} &= y_n + c_1 k_1 + c_2 k_2 + c_3 k_3 + c_4 k_4 + c_5 k_5 + c_6 k_6 + \mathcal{O}(h^6) \,, & (2.7)
\end{aligned}
$$

which requires six (force) function evaluations to advance the solution through the interval h from x_n to $x_{n+1} \equiv x_n + h$. Another combination of the six functions yields an embedded *fourth-order* Runge-Kutta formula

$$
y_{n+1}^* = y_n + c_1^* k_1 + c_2^* k_2 + c_3^* k_3 + c_4^* k_4 + c_5^* k_5 + c_6^* k_6 + \mathcal{O}(h^5) \,, \qquad (2.8)
$$

where a_i, b_{ij}, c_i and c_i^* are the Cash-Karp coefficients [51]. The difference between the fourth- and fifth-order accurate estimates of $y(x + h)$ gives an appropriate estimate of the local numerical truncation error

$$
\Delta(h) \equiv y_{n+1} - y_{n+1}^* = \sum_{i=1}^{6} (c_i - c_i^*) k_i \,, \qquad (2.9)
$$

which is employed to adapt the stepsize h in a way that the desired degree of pre-determined accuracy in the trajectories is achieved with minimum computational effort. Especially for small particle numbers, where the minimum two-particle distance (and hence the force field amplitude) strongly alternates during the simulation run, the adaptive algorithm provides drastic performance gains by a factor of ten to hundred compared with the standard fixed step size Runge-Kutta method of fourth-order. For implementation details see Ref. [52, 53].

2.2 Metropolis Monte Carlo Method

The classical Monte Carlo approach has been applied to study the liquid-to-solid transition as a function of the heat-bath temperature (see section 4.3 and 5.2). Unlike molecular dynamics, the Monte Carlo method is stochastic rather than dynamical and thus, following the general concept, only statistical averages of equilibrium properties can be computed.

The original idea of this stochastic simulation method was coined by E. Fermi, J. von Neumann, S. Ulam, and N. Metropolis, who proposed in 1953 a stochastic algorithm to generate microstates according to the Boltzmann distribution, so that thermal averages can be computed easily [54]. This famous Metropolis sampling scheme has been recently rated as being among the top ten algorithms having the "greatest influence on the development and practice of science and engineering in the 20th century" [55].

To describe the considered model system (1.3) by means of MC methods the dynamical physical process has to be transformed into a stochastic one. A key element in the Metropolis Monte Carlo procedure is thus the concept of the Markov chain. It means that the immediate sequencing state depends on the present state only, regardless of the preceding development of the system. The Markov process generates a path in the configuration space and all quantities of interest are averaged along this trajectory which is the probabilistic analogue to that generated by the equations of motion in molecular dynamics [56, 57] (see figure 2.1).

In mathematical terms the Markov chain is defined as a sequence of sample points i in the configuration space Ω

$$\mathbf{r}_0^N \quad \xrightarrow{W} \quad \ldots \quad \xrightarrow{W} \quad \mathbf{r}_i^N \quad \xrightarrow{W} \quad \mathbf{r}_{i+1}^N \quad \xrightarrow{W} \quad \mathbf{r}_{i+2}^N \quad \xrightarrow{W} \quad \ldots \quad , \tag{2.10}$$

where the vector $\mathbf{r}_i^N = (\mathbf{r}_1, \mathbf{r}_2, \ldots, \mathbf{r}_N)_i \in \Omega$ of dimension $3N$ comprises the coordinates of all N particles. The transition operator $W(\mathbf{r}_i^N \to \mathbf{r}_j^N)$ has to obey the *detailed balance* condition [58]

$$P(\mathbf{r}_i^N)W(\mathbf{r}_i^N \to \mathbf{r}_j^N) = P(\mathbf{r}_j^N)W(\mathbf{r}_j^N \to \mathbf{r}_i^N) \, , \tag{2.11}$$

for each MC step from one to any other state. In thermal equilibrium at fixed external heat bath temperature T the probability $P(\mathbf{r}_i^N)$ of obtaining configuration $\mathbf{r}_i^N$ is weighted according to the Boltzmann probability distribution

$$P(\mathbf{r}_i^N) = e^{-\beta E(\mathbf{r}_i^N)}/Z \, , \tag{2.12}$$

where $\beta = E_0/k_B T$ is the dimensionless inverse temperature, k_B is Boltzmann's constant, E the (dimensionless) total system energy according to Hamiltonian (1.3) and $Z = \sum_\Omega e^{-\beta E(\mathbf{r}_i^N)}$ the partition function of the canonical ensemble. Hence, the relative transition probability for the step $\mathbf{r}_i^N \to \mathbf{r}_j^N$ is a function of the total energy change

$\Delta E = E(\mathbf{r}_j^N) - E(\mathbf{r}_i^N)$ only

$$\frac{W(\mathbf{r}_i^N \to \mathbf{r}_j^N)}{W(\mathbf{r}_j^N \to \mathbf{r}_i^N)} = e^{-\beta \Delta E} \ . \tag{2.13}$$

This equation is satisfied by the Metropolis function [54]

$$W(\mathbf{r}_i^N \to \mathbf{r}_j^N) = \begin{cases} \exp(-\beta \Delta E) & \Delta E > 0 \\ 1 & \Delta E \leq 0 \ . \end{cases} \tag{2.14}$$

This means, if a trial move $\mathbf{r}_i^N \to \mathbf{r}_j^N$ lowers the energy, then the step is always accepted. However, if the energy is increased, the trial step is accomplished with a probability $W < 1$ only and otherwise rejected.

Starting from an arbitrary configuration $\mathbf{r}_0^N \in \Omega$, after an initial thermalization time of the simulation, the expectation value of the ensemble average of a generic physical quantity $A(\mathbf{r}^N)$ can be estimated as an arithmetic mean over the Markov chain of K consecutive MC steps

$$\langle A \rangle = \sum_{i \in \Omega} P(\mathbf{r}_i^N) A(\mathbf{r}_i^N) \approx \frac{1}{K} \sum_{k=1}^{K} A(\mathbf{r}_k^N) \ . \tag{2.15}$$

A central point in this context is the ergodicity of the Markov process which refers to the condition that any state in the configuration space has to be accessible from any other state in a finite number of MC steps. An inherent problem with respect to the ergodicity in strongly correlated systems is, naturally, the (exponentially) growing autocorrelation time with the system size which may easily exceed the simulation time. Especially at low temperatures it has to be taken care of that the statistics are not biased, since the expectation values of the observed quantities may seem to have converged although the system is trapped in local minima and has barely moved in the configuration space Ω. However, one should be aware of that long simulation times do not automatically guarantee more accurate results generally as accounted for in section 4.3.

Recommendable reviews on the subject of classical Monte Carlo simulations are to be found, for example, in Ref. [56, 57, 59, 60].

2.3 Path Integral Monte Carlo

The path integral Monte Carlo simulation (PIMC) technique is founded on R.P. Feynman's path integral formulation of quantum mechanics which, contrary to E. Schrödinger's and W. Heisenberg's differential equation formalism, naturally generalizes the ideas and concepts of classical mechanics, especially Hamilton's principle of least action. In spite of its intuitivity and theoretical smartness, the evaluation of the path integrals is by far not trivial since one has to integrate over all possible states of the system for each moment in time [61].

In analogy to classical statistical mechanics, where thermal equilibrium expectation values are defined as a canonical average of all microstates weighted by the Boltzmann factor (see equation 2.15), the equilibrium state of a quantum system at a given inverse temperature β is fully characterized by the *many-body density operator*,

$$\hat{\rho}(\beta) = e^{-\beta \hat{H}} = \sum_n |\psi_n\rangle \, e^{-\beta E_n} \, \langle \psi_n| \; . \tag{2.16}$$

This statistical operator $\hat{\rho}$ is defined as the superposition of the pure N-particle eigenfunctions $|\psi_n\rangle$, which are exponentially weighted with their eigenvalues E_n according to the stationary Schrödinger equation $\hat{H} |\psi_n\rangle = E_n |\psi_n\rangle$. Thus, the concept of the density operator generalizes that of the wave function to finite temperatures, i.e., mixed ensembles. The thermal average of an observable $\hat{A}$, which is diagonal in basis $|\psi_n\rangle$, is in the thermodynamic equilibrium, defined as

$$\langle \hat{A} \rangle(\beta) = \frac{\sum_n e^{-\beta E_n} \langle \psi_n|\hat{A}|\psi_n\rangle}{\sum_n e^{-\beta E_n} \langle \psi_n|\psi_n\rangle} = \frac{Sp[\hat{\rho}\hat{A}]}{Sp[\hat{\rho}]} = \frac{Sp[\hat{\rho}\hat{A}]}{Z} \; , \tag{2.17}$$

where the trace of $\hat{\rho}$ provides the quantum partition function

$$Z = Sp[\hat{\rho}] \equiv \sum_n e^{-\beta E_n} \; . \tag{2.18}$$

The partition function determines all thermodynamic quantities of the system in question. However, equation (2.16) requires to find the complete energy spectrum by solving the N-particle Schrödinger equation, which in most cases is impossible for interacting systems. As we will see, we can get around this problem by using a (path) integral representation of the N-particle density matrix, which can be evaluated efficiently with the help of numerical Monte Carlo methods.

To do so, we first change into the *basis of position vectors* $\mathbf{r}^N = (\mathbf{r}_1, \mathbf{r}_2, \ldots, \mathbf{r}_N)$, where

the off-diagonal density matrix becomes a function of $6N$ particle coordinates, i.e.,

$$\hat{\rho} \to \rho(\mathbf{r}^N, \mathbf{r}^{N'}; \beta) \equiv \langle \mathbf{r}^N | e^{-\beta \hat{H}} | \mathbf{r}^{N'} \rangle = \sum_n \psi_n^*(\mathbf{r}^N) e^{-\beta E_n} \psi_n(\mathbf{r}^{N'}) . \qquad (2.19)$$

Note that in the position basis all particles are labeled. Moreover, the function values of the density matrix are positive[1] for all of its arguments and have the meaning of a probability for the transition from the initial $\mathbf{r}^N$ to the final state $\mathbf{r}^{N'}$. The non-negativity of the density matrix elements is an essential prerequisite for the subsequent application of Monte Carlo methods. In coordinate representation the thermal average of operator $\hat{A}$ becomes

$$\langle \hat{A} \rangle (\beta) = \frac{\int \mathrm{d}\mathbf{r}^N \, \langle \mathbf{r}^N | \rho \hat{A} | \mathbf{r}^N \rangle}{Z} = \frac{\int \mathrm{d}\mathbf{r}^N \int \mathrm{d}\mathbf{r}^{N'} \rho(\mathbf{r}^N, \mathbf{r}^{N'}; \beta) \, \langle \mathbf{r}^N | \hat{A} | \mathbf{r}^{N'} \rangle}{Z} , \qquad (2.20)$$

and the partition function

$$Z(\beta) = \int \mathrm{d}\mathbf{r}^N \rho(\mathbf{r}^N, \mathbf{r}^N; \beta) . \qquad (2.21)$$

In general, these functional integrals cannot be carried out since an explicit analytical form of $\rho(\mathbf{r}^N, \mathbf{r}^{N'}; \beta)$ is most commonly unknown for non-ideal quantum systems. To overcome this problem, we will reduce the density matrix to the one known for free particles in the *high-temperature limit*. To this end we utilize the *product property of the density matrix*

$$\hat{\rho}(\beta) = e^{-\beta \hat{H}} = \underbrace{e^{-\frac{\beta}{M} \hat{H}} \cdot \ldots \cdot e^{-\frac{\beta}{M} \hat{H}}}_{\text{M times}} = \prod_{s=1}^{M} \hat{\rho} \left(\frac{\beta}{M} \right) , \qquad (2.22)$$

which allows us to expand a low-temperature density matrix into a series of density matrices at M times higher temperature, where the particle interactions are strongly reduced (by a factor $1/M$). Insertion of $M - 1$ high-temperature factors gives us the

---

[1]Here we do not yet consider the problematic issue of Fermi statistics.

density matrix in the position basis

$$
\begin{aligned}
\rho(\mathbf{r}^N, \mathbf{r}^{N'}; \beta) &= \langle \mathbf{r}^N | e^{-\beta \hat{H}} | \mathbf{r}^{N'} \rangle \\
&= \langle \mathbf{r}^N | \prod_{s=1}^{M} e^{-\frac{\beta}{M} \hat{H}} | \mathbf{r}^{N'} \rangle && (2.23) \\
&= \int \ldots \int d\mathbf{r}_1^N \, d\mathbf{r}_2^N \ldots d\mathbf{r}_{M-1}^N \prod_{s=0}^{M-1} \langle \mathbf{r}_s^N | e^{-\frac{\beta}{M} \hat{H}} | \mathbf{r}_{s+1}^N \rangle && (2.24) \\
&= \int \ldots \int d\mathbf{r}_1^N \, d\mathbf{r}_2^N \ldots d\mathbf{r}_{M-1}^N \prod_{s=0}^{M-1} \rho\left(\mathbf{r}_s^N, \mathbf{r}_{s+1}^N; \frac{\beta}{M} \right), && (2.25)
\end{aligned}
$$

where the ordered set $(\mathbf{r}_0^N, \mathbf{r}_1^N, \ldots, \mathbf{r}_M^N)$ represents a path in the configuration space. Expression (2.25) is exact and comprises in the limit $M \to \infty$ an integration over all possible paths through configurational space linking the fixed initial and final points $\mathbf{r}_0^N = \mathbf{r}^N$ and $\mathbf{r}_M^N = \mathbf{r}^{N'}$. Interestingly, the partition function, equation (2.21), now becomes an integral that runs over closed paths

$$
Z(\beta) = \int \ldots \int d\mathbf{r}_1^N \, d\mathbf{r}_2^N \ldots d\mathbf{r}_{M-1}^N \prod_{s=0}^{M-1} \rho\left(\mathbf{r}_s^N, \mathbf{r}_{s+1}^N; \frac{\beta}{M} \right), \quad \mathbf{r}_0^N = \mathbf{r}_M^N, \quad (2.26)
$$

and is thus determined by the off-diagonal (high-temperature) density matrix elements.

Considering the system in question (see section 1.3), the Hamiltonian consists in its general form,

$$
\hat{H} = \hat{K} + \hat{V}, \qquad (2.27)
$$

essentially of two non-commuting N-particle operators, the kinetic $\hat{K}$ and the potential $\hat{V}$ operator with $[\hat{K}, \hat{V}] \neq 0$. Expansion yields a cumbersome expression for the exponential operator

$$
\begin{aligned}
e^{-\frac{\beta}{M}(\hat{K}+\hat{V})} &\approx e^{-\frac{\beta}{M}\hat{K}} e^{-\frac{\beta}{M}\hat{V}} e^{-(\frac{\beta}{M})^2 [\hat{K},\hat{V}]/2} e^{-(\frac{\beta}{M})^3 [[\hat{V},\hat{K}],\hat{K}+2\hat{V}]/6} + \mathcal{O}((\beta/M)^4) && (2.28) \\
&\approx e^{-\frac{\beta}{M}\hat{K}} e^{-\frac{\beta}{M}\hat{V}} e^{-(\frac{\beta}{M})^2 [\hat{K},\hat{V}]/2} + \mathcal{O}((\beta/M)^3) && (2.29) \\
&\approx e^{-\frac{\beta}{M}\hat{K}} e^{-\frac{\beta}{M}\hat{V}} + \mathcal{O}((\beta/M)^2). && (2.30)
\end{aligned}
$$

However, *Trotter's product formula* states for the self-adjoint operators $\hat{K}$ and $\hat{V}$, which are bounded from below in a Hilbert space, that in the limit of a large number of high-temperature factors, $M \to \infty$, the total density matrix (2.22) can be approximated as a simple product of potential and kinetic density matrices by neglecting the commutators

from the exact operator identity (2.28)-(2.30), i.e.,

$$\hat{\rho}(\beta) \;=\; e^{-\beta(\hat{K}+\hat{V})} = \left[e^{-\frac{\beta}{M}(\hat{K}+\hat{V})}\right]^{M} \tag{2.31}$$

$$\overset{!}{=}\; \lim_{M\to\infty}\left[e^{-\frac{\beta}{M}\hat{K}}e^{-\frac{\beta}{M}\hat{V}}\right]^{M} \tag{2.32}$$

$$\approx\; \left[e^{-\frac{\beta}{M}\hat{K}}e^{-\frac{\beta}{M}\hat{V}}\right]^{M} + \mathcal{O}\left(\frac{1}{M}\right) . \tag{2.33}$$

Note that the validity of the approximation made for finite M in the last step (2.33) is not at all obvious due to the propagation of the error terms with respect to the ratio β/M [62, 63]. The error of the high-temperature representation is therefore strongly affected by the number of high-temperature factors M. Hence, the convergence with M has to be checked carefully for each particular system under study.

The high-temperature matrix element $\rho(\mathbf{r}_s^N, \mathbf{r}_{s+1}^N; \beta/M)$ in the equations (2.25) and (2.26) can be approximated as

$$\rho(\mathbf{r}_s^N, \mathbf{r}_{s+1}^N; \beta/M) \;\equiv\; \langle\mathbf{r}_s^N|e^{-\frac{\beta}{M}(\hat{K}+\hat{V})}|\mathbf{r}_{s+1}^N\rangle \tag{2.34}$$

$$\approx\; \langle\mathbf{r}_s^N|e^{-\frac{\beta}{M}\hat{K}}e^{-\frac{\beta}{M}\hat{V}}|\mathbf{r}_{s+1}^N\rangle \tag{2.35}$$

$$=\; e^{-\frac{\beta}{M}V(\mathbf{r}_s^N)}\,\langle\mathbf{r}_s^N|e^{-\frac{\beta}{M}\hat{K}}|\mathbf{r}_{s+1}^N\rangle , \tag{2.36}$$

where $\hat{V}$ is diagonal in the spatial coordinate representation. The kinetic energy density matrix elements of free particles are obtained by a momentum eigenstate expansion

$$\langle\mathbf{r}_s^N|e^{-\frac{\beta}{M}\hat{K}}|\mathbf{r}_{s+1}^N\rangle \;=\; \int d\mathbf{p}^N\,\langle\mathbf{r}_s^N|\mathbf{p}^N\rangle\, e^{-\frac{\beta}{M}\sum_{i=1}^{N}\frac{\hat{\mathbf{p}}_i^2}{2m_i}}\,\langle\mathbf{p}^N|\mathbf{r}_{s+1}^N\rangle \tag{2.37}$$

$$=\; \lambda_M^{-3N}e^{-\frac{\pi}{\lambda_M^2}(\mathbf{r}_s^N-\mathbf{r}_{s+1}^N)^2} . \tag{2.38}$$

Here we take advantage of the diagonality of the kinetic operator $\hat{K} = \sum_{i=1}^{N}\frac{\hat{\mathbf{p}}_i^2}{2m_i}$ in momentum space, and that the Gaussian type integral can be evaluated analytically after the explicit expressions for the plane waves $\langle\mathbf{r}_s^N|\mathbf{p}^N\rangle$ and $\langle\mathbf{p}^N|\mathbf{r}_{s+1}^N\rangle$ have been substituted. The term $\lambda_M = \sqrt{2\pi\hbar^2\beta/mM}$ denotes hereby the thermal De Broglie wave length. Insertion of the high-temperature matrices (2.36) and (2.38) into equation (2.25) provides us the *discrete time path integral representation of the N-particle density matrix*

$$\rho(\mathbf{r}^N, \mathbf{r}^{N\prime}; \beta) \approx \int\cdots\int d\mathbf{r}_1^N\,d\mathbf{r}_2^N\ldots d\mathbf{r}_{M-1}^N e^{-\frac{\pi}{\lambda_M^2}\sum_{s=0}^{M-1}(\mathbf{r}_s^N-\mathbf{r}_{s+1}^N)^2}e^{-\frac{\beta}{M}\sum_{s=0}^{M-1}V(\mathbf{r}_s^N)}, \tag{2.39}$$

which is valid for arbitrary quantum systems with the Hamiltonian (2.27).

Following the analogy between Feynman's original idea of a time-evolution operator $\hat{U}(t, t') = e^{-i\hat{H}t/\hbar}$ and the definition in equation (2.16), the inverse temperature β is often considered as imaginary time, where $t \leftrightarrow \beta\hbar/i$ and the imaginary time step $\delta\beta = \beta/M$. Thus, the integer numbers $s = 1 \ldots M-1$ are commonly named "imaginary time slices" since only particle images within the same slice $\mathbf{r}_s^N$ interact via the weakened (iso-time) potential $v(\mathbf{r}_s^N) = V(\mathbf{r}_s^N)/M$ with each other. The classical-like particle images in successive slices $\{\mathbf{r}_s^N, \mathbf{r}_{s+1}^N\}$ are linked by a spring-like energy term, which is due to the quantum mechanical kinetic energy of the free particle and ensures a finite particle extension. Hence, in the imaginary-time path integral formulation a quantum system becomes mapped onto a classical one such that each physical (quantum) particle is represented by a path through M positions (here called particle images) in the configuration space at different values in imaginary time. This path forms a classical (!) ring polymer of M links. Depending on the inverse temperature β and particle mass m the spring coupling becomes more or less rigid and, consequently, the quantum particles become more or less delocalized.

Most of the thermodynamic quantities, such as energies, are determined by the trace of the density matrix (2.39), i.e., closed imaginary time trajectories form $\mathbf{r}^N$ to $\mathbf{r}^{N'} = \mathbf{r}^N$. For instance the probability $p(\mathbf{r}^*)$ to observe an arbitrary particle at the position $\mathbf{r}^*$ is given as arithmetic average over the imaginary time paths of all N particles

$$p(\mathbf{r}^*) = \frac{1}{NM} \sum_{i=1}^{N} \sum_{s=0}^{M-1} \langle \delta(\mathbf{r}^* - \mathbf{r}_s^i) \rangle_{\rho_N} \, , \tag{2.40}$$

where $\langle \ldots \rangle_{\rho_N}$ defines the thermodynamic average according to equation (2.20).

So far, only quantum systems composed of distinguishable spinless particles (Boltzmannons) have been considered. However, even in the considered case that the Hamiltonian does not explicitly depend on the particle spin, inclusion of quantum statistics requires sampling of the particle permutations in addition to the integrations in coordinate space. More specifically, the obtained many-body density matrix (2.39) has to be properly *symmetrized* with respect to an arbitrary exchange of two indistinguishable *Bosons* (e.g. bosonic atoms, molecules or excitons), i.e.,

$$\rho^S(\mathbf{r}^N, \mathbf{r}^{N'}; \beta) = \frac{1}{N!} \sum_P (+1)^P \rho(\mathbf{r}^N, \hat{P}\mathbf{r}^{N'}; \beta) \, , \tag{2.41}$$

or, respectively, *antisymmetrized* under arbitrary exchange of two indistinguishable

Fermions (such as electrons or holes with the same spin projection), i.e.,

$$\rho^A(\mathbf{r}^N, \mathbf{r}^{N'}; \beta) = \frac{1}{N!} \sum_P (-1)^P \rho(\mathbf{r}^N, \hat{P}\mathbf{r}^{N'}; \beta) \,, \tag{2.42}$$

where $\hat{P}$ is the permutation operator on the particle indices and P is the parity of the permutation. In the picture of path integral theory, the permutations can be decomposed into a sequence of two-particle exchanges along the imaginary timeline. The pair exchanges are carried out by transposition of particle positions in particular time slices by what the paths of several particles can become merged into a single one. Such multi-particle paths correspond to the off-diagonal elements of the density matrix.

The superposition of all $N!$ permutations of N identical particles leads to the inherent (numerical) *Fermion sign problem* since the alternating sign of the prefactor in the case of Fermions, equation (2.42), causes an essential cancellation of positive and negative contributions corresponding to even and odd permutations, respectively. Thus, an accurate calculation of this vanishing differences is strongly aggravated with the increase of quantum degeneracy arising at low temperatures and high densities, where all permutations appear with equal probability.

The high-dimensional convolution integrals of the density matrix, equation (2.39), (2.41), and (2.42), over $3N(M-1)$ degrees of freedom[2] can be numerically evaluated by a slightly modified version of the Metropolis sampling algorithm outlined for the classical systems. However, to reduce the computational efforts and to increase the efficiency of the Monte Carlo sampling various sophisticated move strategies (e.g. the multi-level bisection sampling method or the worm algorithm [64]), approximations for the pair density matrix (e.g. using matrix-squaring technique [65, 66]), fast converging estimators with less statistical variance and many further improvements have been developed over the last decades. For further (technical) details on this subject, we refer the interested reader to the following recommended in-depth references [58, 59, 67, 68, 69].

2.4 Aspects of Many-Particle Simulations

Today, modern experimental techniques allow for a selective manipulation of small micro- and nanoscale systems of only ten or hundred particles. Although the fundamental physical laws which can describe these measurements are well-known, exact an-

---

[2]We typically use numbers of high-temperature factors M in the range $100 \leq M \leq 300$.

alytical solutions are available only for a very limited number of many-particle systems such as ideal solids (i.e. highly periodic structures without any lattice defects or distortions) or non-interacting classical (i.e. $\Gamma \ll 1$) or quantum gases ($r_s \ll 1$). However, interaction makes things much more interesting but also more complex and theoretically challenging. In most practical cases the fundamental many-body Hamiltonian (1.3) cannot be directly diagonalized and more efficient numerical methods are needed. As a matter of fact, even simple models used to describe interacting quantum systems in the regime of strong particle correlations are computationally very demanding (see chapter 5).

For the investigation of ground states and phase transitions we utilize different classical and quantum *bottom-up approaches*. This means, the theoretical description starts at the microscopic level of individual particles and, thereby, takes fully into account all microscopic many-particle interactions. The only simulation input data involved are the fundamental pair interaction potentials as well as the boundary (confinement) conditions. Hence, the theoretical framework of computational bottom-up methods on hand allows for a highly flexible modeling with regard to the specific experimental setup (trap geometry, external fields, number of particles etc.) and yields direct results that are free from any fit parameters.

In the following we give a short comparison of the advantages and shortcomings of the different computational approaches we used to solve the many-body-problem (see table 2.1).

Particle Picture

The most obvious difference between the considered computational simulation methods lies in the underlying description of the particle nature. Molecular dynamics and thermodynamic Monte Carlo are purely classical techniques, i.e., the individual particles are reduced to their center of mass coordinates. The classical approach is doubtlessly well-suited in the limits of high temperatures and low densities and allows for an efficient treatment of large particle numbers.

The basic idea of PIMC lies in the isomorphism between quantum particles and classical ring polymers, which allows to model quantum systems accurately with high-performant classical Monte Carlo methods, under inclusion of quantum effects such as finite spatial particle extensions, quantum zero-point energy, tunneling and quantum statistics. However, in contrast to wave-function based methods like Hartree-Fock, PIMC provides

Feature	MD	NMA	MC	PIMC	SCHF
Particle descrip.	point mass	point mass	point mass	polymer[†]	wave fctn.
Dynamical prop.	+++	+	−	−	+
Correlations	+++	++	+++	+++	−
Quantum statistics	−	−	−	++[‡]	+++
No. of particles	≤ 10000	≤ 1000	≤ 10000	≤ 250	≤ 25
Ensemble[§]	NVE	−	NVT	NVT	μVT

Table 2.1: *Rating of different computational approaches to the many-body problem of classical and quantum systems used in this work: molecular dynamics (MD), linear dynamics by normal mode analysis (NMA), Metropolis Monte Carlo (MC), path integral Monte Carlo (PIMC), and self-consistent (ground state) Hartree-Fock (SCHF). The shortcomings and strengths of the different techniques are rated from − (not accessable) to +++ (excellent), respectively. As a benchmark of the numerical efficiency of the methods we specify the number of individual particles, which can be simulated in a typical run on a desktop PC (in the year 2008). The statistical ensemble can be characterized by (fixed) particle number N, chemical potential μ, total energy E, temperature T or volume V. [†] Polymers of classical-like particles representing the N-particle density, [‡] more specifically: Bosons: +++, Fermions: +, [§] ensembles used in the present work. Details are to be found in the text.*

information on the density level only. This means that the computed quantities of interest (see below) are formally exact, but the density picture may lead to qualitative misinterpretations in the understanding of the system (see section 5.4) as it yields only amplitude, but no phase information of the N-particle wave function.

Many-Particle Correlation Effects

In the present thesis we are interested in strongly interacting plasmas, where the mutual particle interaction is essential and cannot be treated as a small perturbation. With the described computational methods it is possible to include interparticle interactions, such as Coulomb repulsion (1.4), and thus cooperative phenomena from first principles. Molecular dynamics include all dynamical many-body correlations, but neglect quantum dynamical effects. Also the classical and quantum Monte Carlo method take into account correlation effects without any simplifications. Beside these particle-based methods, the idea of Hartree-Fock (as the simplest approximation of many-body theory) is the reduction of the many-body problem to an effective one-particle problem by neglecting all correlation effects[3]. The self-consistent Hartree Fock scheme is appropriate for the exploration of many-particle ground states (that is $T = 0$) and yields essentially better results than perturbation theories for $r_s > 1$ (see section 5.4).

---

[3]More specifically, the pair interactions are replaced by a mean-field (Hartree) potential plus an additional exchange (Fock) term, which assures quantum statistics.

Thermodynamic Ensemble

Another important distinction between the different considered simulation techniques concerns the statistical ensemble and, in particular, the conservation of total energy and fixation of temperature. The Metropolis algorithm generates samples in the *canonical ensemble*, which allows for constant (non-zero) temperature simulations yielding direct thermodynamic averages. Because of this, Monte Carlo methods are particularly well suited for the investigation of phase transitions in classical and quantum systems. Apart from that, MD can be utilized to generate *microcanonical* states in the phase space that conserve the total energy (kinetic plus potential energy) of the system.[4]

Quantum Effects

While many systems can be described in a classical approximation, there is a large class of systems for which a classical or semi-classical approximation is not valid. However, in particular these complex many-body quantum systems are of high scientific interest in this work (see chapter 5). One of the main differences between quantum and classical systems is the finite particle extension and prevailing *quantum fluctuations* even at a temperature of absolute zero, at which all *thermal fluctuations* are frozen out. In the PIMC method the *quantum fluctuations* are ensured by fluctuations on the imaginary timeline, while in classical Monte Carlo simulations no kinetic energy is included at all.

As a matter of fact, the PIMC method is one of the most powerful available numerical tools for the treatment of strongly correlated quantum systems. Despite the complexity of a physical system the PIMC algorithm achieves excellent performance, as long as the particles obey Boltzmann[5] or Bose statistics. While the path integral method is able to treat significantly more than 100 Bosons (or Boltzmannons), it is limited to system sizes of only very few, typically $5 - 10$, Fermions at temperatures in the range of the Fermi temperature. The Fermion sign problem (see section 2.3 for details) manifests itself as one of the most challenging problems in computational physics and restricts our investigations to $3 - 5$ *composite excitons* only (see section 5.2). Although different approaches provide remarkable improvements, either by appropriate approximations at the

---

[4]It is worth to note here that the implementation of (canonical) constant-temperature MD, especially in the context of small few-particle clusters, has always a somewhat manipulative character with respect to the dependence on the choice of the thermostat and the fluctuation contributions [70]. This means that thermodynamic Monte Carlo simulations are often preferred for the computation of equilibrium properties.

[5]PIMC runs most efficiently if quantum statistics is neglected and the particles are assumed to obey Boltzmann statistics. See section 2.3 for details.

analytical level (restricted PIMC [67, 71]), direct simulations (direct PIMC [72, 73]) or algorithmic strategies (such as multilevel blocking [74, 75]), the problem of a sufficiently accurate and efficient computation of the alternating sign of probability contributions to the fermionic expectation values still remains crucial for practical purposes. A general solution to the sign problem would allow to greatly extend the range of applicability of PIMC and mark a big step in the ab initio modeling of strongly correlated electronic systems.

Quantum Dynamics

Based on an equilibrium theory, PIMC simulations are able to yield first-principle results of thermodynamic (equilibrium) properties only. The "exact" treatment of the time evolution of quantum systems requires the solution of the von Neumann equation, i.e., the equation of motion of the N-particle density operator

$$i\hbar\frac{\partial}{\partial t}\hat{\rho}(t) = [\hat{H}, \hat{\rho}(t)] \; , \tag{2.43}$$

where the brackets denote the commutator. However, up to now no numerical efficient and robust method such as PIMC has been established for time-dependent problems. In the case of purely classical, point-like particles (such as ions at low densities or dust grains), equation (2.43) reduces to the classical law of motion and can be directly numerically integrated (see section 2.1). As the name implies, the MD method generates true many-particle dynamics and allows for direct computation of both equilibrium and non-equilibrium properties of classical systems (see figure 2.2). In an important theoretical advance, the classical molecular dynamics framework has been extended to include quantum dynamical effects of many-body systems. In the most straightforward approach, dominant quantum effects are included into "precalculated" pair potentials, which saves the time-consuming effort of the solution of the electronic structure problem at each molecular dynamics step. Using effective interaction potentials, which capture basic quantum diffraction but also spin effects [76], the range of applicability of the classical simulation scheme can be significantly extended, particularly, to the region of weakly and moderatly coupled quantum systems [70]. Alternative trajectory-based concepts that describe dynamical correlations of quantum systems are "wave packet molecular dynamics" [77], "quantum dynamics with Bohmian trajectories" [78], "Wigner function molecular dynamics" [79] or "centroid molecular dynamics" [80], which incorporates discrete path integral formalism into molecular dynamics. However, all these methods (which are currently under active development) have their own strengths but also short-

comings, which are, among others, related to the accurate description of wave packet dispersion, bound-state formation, strong correlation effects, quantum statistics, numerical stability and so on.[6] Moreover, all particle-based schemes do not yield reliable information about the population of quantum energy levels and excitation processes as do powerful time-dependent Hartree-Fock and quantum kinetic approaches [81, 82]. However, the latter are limited by the inefficient treatment of correlation effects [83]. Due to these reasons, we will limit our investigations to the equilibrium properties of electron-hole plasmas in semiconductor nanostructures (see chapter 5).

As mentioned in section 2.2, the correlated subsequent states of a Markov chain can be associated with a "time series". According to that the Metropolis Monte Carlo process can be interpreted as a (pseudo) dynamical process obeying a master equation, see e.g. [56, 57]. As a matter of fact, the stochastically generated trajectories through configurational space allow one to analyze the dynamic evolution of one-particle and many-particle system observables and, in particular, the statistical evaluation of fluctuations (e.g. in energy or the pair distances). Of special interest are the energy autocorrelation times as well as the pair distance fluctuations because they are found to be very sensitive to liquid-solid phase transitions (see section 4.3). It is, however, important to note that the Markov process does not correspond to the strict time evolution such as generated by the Newtonian equation of motion, as it is lacking a "real-time" scale. This means that in contrast to molecular dynamics, Monte Carlo simulations are not able to adequately model relaxation processes or non-Hamiltonian system behavior (e.g. introduced by friction effects) [84].

Classical Excitation Spectrum

The fundamental dynamical features of classical correlated systems, including the spectrum of all classical collective excitations can be identified by a *normal mode analysis* (NMA) within a harmonic approximation (see figure 2.2). Normal modes are defined by the structure of the system, i.e., more precisely, the topology of the potential energy surface. The classical N-particle normal mode vectors $\mathbf{e}_i^k$ and frequencies ω_k are obtained by diagonalization of the dynamical matrix

$$\mathcal{H}_{ij} = \frac{\partial^2 H}{\partial r_i \partial r_j}\bigg|_{\mathbf{R}} \, , \tag{2.44}$$

---

[6]A balanced review of the different approaches is by far out of the scope of the thesis at hand. We refer an interested reader to reference [59] for more details.
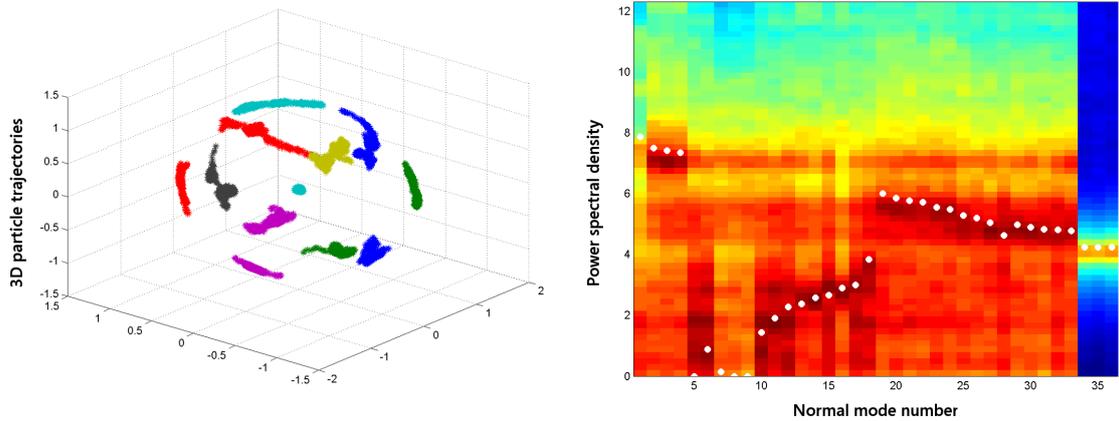
Figure 2.2: *The combination of NMA and MD allows to gain insight into the fundamental dynamical properties of strongly correlated systems. Shown is a 3D Coulomb system consisting of $N = 12$ classical particles in a harmonic trap at $\Gamma = 5000$ (see section 3.2). Left: Molecular dynamics simulation of the thermal particle fluctuations about the local potential energy minimum of the (1,11) configuration. Right: Corresponding power density spectra S_k, equation (2.45) , for the $3N$ normal modes (mode amplitude increases from blue to red). The white circles denote the mode eigenfrequencies ω_k as derived from the dynamical matrix, equation (2.44). The threefold degenerate center-of-mass oscillations of the cluster (mode numbers $34-36$), show distinct peaks due to the harmonic external confinement potential. All values in arbitrary units. [85]*

where H denotes the classical N-particle Hamiltonian, $r_{i(j)} = \{x_1, y_1, z_1, x_2, y_2 \ldots\}$ are the spatial coordinates of the particles, and $\mathbf{R}$ the equilibrium positions of the particles in a stable configuration. Stable means that the lowest eigenvalue of the dynamical matrix is non-negative. Normal modes describe collective classical particle behaviour, such as shell rotations, vortices or breathing-like modes [86, 87] (see section 5.4). The normal mode spectrum of each mode $k = 1 \ldots 3N$ is obtained in form of the spectral power density

$$S_k(\omega) = \frac{1}{T} \left| \int_0^T f_k(t) e^{i\omega t} dt \right|^2 , \tag{2.45}$$

where the quantity

$$f_k(t) = \sum_{i=1}^{N} \mathbf{e}_i^k \cdot \mathbf{v}_i(t) , \tag{2.46}$$

denotes the projection of the MD simulated trajectories $\mathbf{v}_i(t)$ of the particles $i = 1 \ldots N$ onto the normal mode eigenvectors $\mathbf{e}_i^k$, which describe the amplitude and direction of the (collective) particle oscillations.

Quantities of Interest

Thermodynamic and quantum Monte Carlo provide detailed information on the statistical properties of classical and quantum systems such as

- energy, pressure (equation of state), specific heat,

- fluctuations (for instance of the pair distances, see section 4.3),

- distribution functions such as the pair distribution or the density profile,

- the condensate or superfluid fraction, etc.

at any given finite temperature. Quantum Monte Carlo simulations do allow us to follow the evolution of cluster size effects with particle number, temperature, density or other external control parameters with rigorous accuracy. Despite its obvious advantages, there are some practical limitations of PIMC. The calculation of the free energy and entropy is a troublesome task and requires special techniques [88]. Also, in contrast to variational and diffusion Monte Carlo techniques or Hartree-Fock, the PIMC approach does not yield explicit information about single particle orbitals ϕ_i and the quantum energy levels ϵ_i as it directly averages over many pure quantum states by sampling of the density matrix. Consequently, the calculation of optical properties is a serious problem for PIMC. However, the computation of complete energy spectra is a (numerically) challenging task also for the most other present many-body methods such as density functional theory or non-equilibrium Green's functions, e.g. [59].

In contrast, if the particles can be treated as point charges, classical molecular dynamics is the method of choice, in particular, if one is interested in real dynamics at the microscopic level. The classical dynamical method propagates the particle trajectories in the $6N$-dimensional position-momentum phase-space and allows thereby for the exact computation of all classical equilibrium quantities and, in addition, time-dependent features. Molecular dynamics can help to answer questions that are related to

- transport processes such as diffusion or conductivity,

- spatial and time correlations,

- the connection between structure and dynamics,

- (selective) collective excitations, e.g., of normal modes, and so on.

Moreover, in chapter 3 we apply molecular dynamics to determine the classical N-particle ground and meta-stable states by simulated annealing.

Computational Issues

The computational effort of particle-based methods manifests itself primarily in the number of particles that can be simulated in feasible computational time. In the considered classical simulation schemes the *exact* computation of all pair interactions scales quadratic with system size. This limits the cluster size to typically $N = 10000$ classical particles. In contrast to this relatively modest growth of the computational effort with increasing system size, exact diagonalization and many body techniques are often limited to a few particles only because of poor size scaling.

Despite the high accuracy of PIMC simulations, which are only limited by computational time, there is a crucial point related to the *serial correlation of states* and the finiteness of the Markov chain. If we consider a series of n *independent* (canonically distributed) configurations, the statistical error decreases as $1/\sqrt{n}$, where n is generally proportional to the simulation time. However, the sample mean holds this rate of convergence only if the subsequent states are independent of each other. The Monte Carlo algorithm samples serially correlated configurations by locally displacing particles.[7] This local update procedure reduces the practical achievement from a full exploration of the relevant configuration space, because it captures the system for long periods of time in single metastable configurations (corresponding to a small region in the phase space), causing long correlation times. This behavior can easily lead to noisy, or even worse, biased results, when simulating large quantum systems with many degrees of freedom. The running variance of some estimators may be comparatively small in the case of large systems, and it may seem that the thermodynamical observables converge quickly. However, the contrary is true for sufficient exploration of the configuration space. Typically we require much longer simulation runs than in small systems and may easily exceed available computing capabilities. Therefore, it is necessary to carefully check that the asymptotic regime of the central-limit theorem has been achieved in each special case. To do so it is suggestive to inspect the system size scaling of the autocorrelation times by starting with very small systems. By a gradual increase of the system size it can be ensured that the autocorrelation times do not exceed the simulation [60].

Strongly correlated many-particle systems are found to be very sensitive to even small

---

[7]Due to the correlation of subsequent configurations a straightforward calculation of the statistical error using the standard deviation will lead to an significant underestimation of the error.

modifications in the (effective) pair potential. These can be caused for instance by screening or quantum effects. Consequently, only checks against measurements can clarify the validity of the obtained theoretical results or their underlying model system. Thus, simulated experiments on model systems can not replace experiments on physical systems (but rather complement them). It is also important to note that the validity of numerical computations is strictly limited to the specific case solved. Wherever possible, numerical results should be used to develop general analytical solutions (such as was done for the plasma density profile, see section 4.2).

3 First Principle Simulations of Finite Classical Systems in Traps

This chapter is primarily devoted to the structure formation in dusty plasmas. We begin with a brief introduction to the topic in section 3.1. Thereafter, in section 3.2, we study the shell structure, the cluster stability, and symmetry of ground and metastable states of spherical Coulomb clusters by means of first-principle molecular dynamics simulations. The model of a *pure Coulomb interaction* is very general and, among others, of direct practical importance for (laser-cooled) ion crystals in traps [27, 89]. Afterwards in section 3.3, we include the effect of Debye screening of the ambient plasma on the dust-dust interaction by using a *screened Coulomb potential*. The simulation results are found to be in excellent agreement with dust clusters from experiments [32, 89, 90] including the details of the shell radii and the particle distribution over the shells. A major part of the work in section 3.3 is focused on the detailed comparison of the simulations with experimental data, which serves as a basis for a theory of these strongly correlated classical systems.

3.1 Introduction and Overview

The field of macroscopic and mesoscopic complex plasmas has become an important part of plasma physics in recent years. The research interest was initiated in 1994 by the experimental discovery of a new state of (soft) matter — the *plasma (Wigner) crystal* [91]-[94]. In a sheath of a noble gas radio frequency discharge highly charged dust grains of micrometer size were investigated for the first time under laboratory conditions. Due to their charge of several thousand elementary charges, these microspheres are strongly coupled and enable the researchers to observe liquid behavior with short-range order and even macroscopic *Coulomb crystals* of *hcp*, *fcc* and *bcc* lattice structure.

The occurrence of dusty plasma effects exceeds by far basic research interests and has practical importance in micro and nano technology [95]. In the industrial plasma processing the presence of charged dust particulates can completely change characteristic plasma parameters, such as electron and ion densities, temperature, and plasma potential. This makes it difficult to run the processes at optimum settings [96]. Additionally, self-assembling of dust particles plays a crucial role in the fabrication of microchips and solar cells, where growing dust particulates can have both devastating as well as advantageous effects. On the one hand, by the manufacture of highly-integrated electronic circuits, the so called *chip-killing particles* can destroy the damageable plasma-etched nano-structures [97], while on the other hand dust grains included in polymorphous solar cells reduce the degradation of these cells [98]. Besides these technological situations dusty plasmas are, e.g., of great interest in various astrophysical phenomena. For instance, the formation and stability mechanisms of dusty plasma systems are of central interest for the understanding of protoplanetary, protostellar, and accretion disk formation or planetary ring systems [99, 100].

In contrast to the mainly *weakly coupled macroscopic plasmas* in space and technology, in this chapter we will focus on the numerical simulation and analysis of *strongly coupled plasmas*, namely spherical Coulomb and Yukawa balls in traps. These finite systems are subject of exceptional current interest since their recent experimental generation, e.g., in dusty plasmas [15].

Mesoscopic Plasma Crystals in Experiments

Finite plasma crystals consist of tens to hundreds of monodisperse dust (Melamine) grains of $3 \ldots 4 \, \mu m$ size. These spherical microparticles are embedded in a hot plasma background ($T_e = 2 \ldots 3 \, \text{eV}$, $T_i \leq 1000 \, \text{K}$, $T_n \approx 300 \, \text{K}$) of electrons, ions, and neutral (e.g. argon) atoms. The dusty plasma is typically generated by a capacitively coupled 13.56-MHz radio-frequency discharge at moderate damping due to friction with the neutral gas background. Due to the greatly different mobility of electrons and much heavier ions, the dust grains acquire high negative charges (on the order of $10,000$ elementary charges) by collecting more electrons than ions. By collisions with the ambient neutral gas, the dust particles are thermalized to approximately room temperature.

To create a spherical confinement for the dust cloud under earth-laboratory conditions, first of all the gravitational force $\mathbf{F}_g$ has to be balanced. The dust levitation is achieved by compensating gravitational force $\mathbf{F}_g$ and the ion-drag force $\mathbf{F}_{ion}$ with an upward force
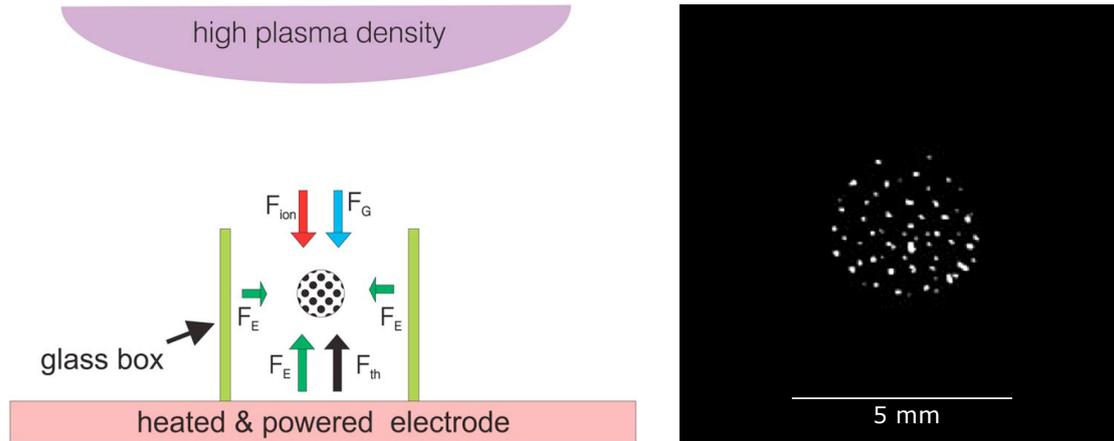
Figure 3.1: *<u>Left:</u> The superposition of gravity $\mathbf{F}_g$, electric field force $\mathbf{F}_E$, upward thermophoretic force $\mathbf{F}_{th}$, and downward ion-drag force $\mathbf{F}_{ion}$, yields a stable spherical confinement inside the glass box. <u>Right:</u> Vertical section through the center of a trapped dust cloud (only a $200\mu m$ thin slice is illuminated by the laser sheet). Note the shell structure of the cluster. From Ref. [90]*

generated by strong electric fields $\mathbf{F}_E$, which are strongest in the plasma sheath region above the lower electrode (see figure 3.1). The downward ion-drag force $\mathbf{F}_{ion}$ is caused by the steady flow of electrons and ions from the bulk plasma onto the lower electrode. Stable three-dimensional dust clouds are created with additional aid of dielectric walls, i.e., a small glass box of 30 mm size, and an upward thermophoretic force $\mathbf{F}_{th}$ caused by temperature gradients in the neutral gas due to a heated lower electrode. Due to surface charges on the dielectric glass wall, the dust particles are repelled from the glass walls. A disperser above the glass box is used to inject the dust grains into the plasma.

Due to the high dust charge, the repulsive electrostatic dust-dust interaction exceeds by far the thermal energy which leads to structure formation. In fact, experiments show that the dust particles arrange themselves in spherically symmetric nested shells with characteristic numbers of particles in each shell (see figure 1.4). Similar to atoms, the structure and properties of these systems strongly depend on the particle number. But unlike atomic systems, the crystal is visible to the unaided eye and can be relatively easily manipulated. Furthermore, the low charge-to-mass ratio of dust particles allows for high resolution measurements of the structural and dynamical behaviour not only in space, but also in real-time. This is due to the fact that dynamical processes occur on a frequency scale of several Hertz, which means that the motion of individual particles is sufficiently slow to be tracked with conventional CCD cameras. Therefore, complex plasmas are very suitable objects to study fundamental interactions and correlation effects leading to collective behavior. Thereby, the investigations affect fundamental

issues of both plasma physics on the one hand and condensed matter physics on the other hand.

The results of this chapter may also be valuable for other kinds of strongly correlated many particle systems, such as crystallized ions. Experiments on laser-cooled ions in traps have shown that the regime of strong coupling can be reached [6]. Moreover, in the case of small ion clouds the particles are found to form spherical onion-like shell structures which are similar to those observed in dusty plasmas [27, 89, 101] (see figure 1.3). Small ensembles of crystallized ions have potential for future technological applications and are presently subject of intense research activities. Cold ions in traps have been proposed, e.g., as one possible way to realize a quantum register [27, 102]. It should be remarked that due to the high ion mass, the ground state structures can be treated classically[1]. For convenience, we will refer also in the case of pure Coulomb interaction (section 3.2) to the dust particles, keeping in mind that they can also be trapped ions or any other (approximately classical) particle species.

Simulation Model and Method

Theoretically, the plasma crystal was predicted by H. Ikezi in 1986 [103]. By means of molecular dynamics simulations he identified the plasma parameters at which a dusty plasma undergoes a phase transition to an ordered crystalline state. Nevertheless, the theoretical description of complex plasmas turns out to be extremely difficult due to their strongly heterogeneous composition, which leads to drastic differences in the underlying space and time scales of the plasma constituents (electrons, ions and dust particles) [104, 105]. An accurate treatment of the multi-scale problem requires to include the effect of streaming ions and collisions on the dynamical charging and screening of the dust particles self-consistently. This challenging task necessitates very large computational capabilities and remains a future task.

Instead of explicitly taking into account all interactions among the constituent particles, we draw on a simple model for dust-plasma interaction which, despite its simplicity, allows to reproduce the experimental measurements without the need of free parameters. The high mass ratio of ions and dust particles allows us to treat the particles classically. The *dynamically*-screened (anisotropic) pair potential, which includes the impact of the

---

[1]Even for quantum Coulomb crystals of electrons [2] the ground state configurations are, in most cases, the same as the classical ones. A detailed analysis of the correspondence between the ground states of classical and quantum bilayer systems is to be found in section 5.4.

plasma environment on the dust-dust interaction, is given by

$$\Phi(\mathbf{r}_{ij}) = \frac{1}{(2\pi)^3} \int d^3\mathbf{k}\, e^{i\mathbf{k}\cdot\mathbf{r}_{ij}} \frac{\Phi_C(k)}{D(\mathbf{k}, \mathbf{k}\cdot\mathbf{u} + i\nu_i)} \ , \tag{3.1}$$

with $\Phi_C(k) = 4\pi q^2/k^2$ being the Fourier transform of the Coulomb potential. The velocity $\mathbf{u}$ describes the constant ion flow, which is directed towards the lower electrode (see figure 3.1). The plasma response is embedded in the dielectric function

$$D(\mathbf{k}, \omega) = 1 + \frac{1}{k^2\lambda_{D_e}^2} - \frac{\omega_i^2}{k^2} \frac{\int d^3\mathbf{v}\frac{\mathbf{k}\cdot\nabla_\mathbf{v} f_{i0}(\mathbf{v})}{\mathbf{k}\cdot\mathbf{v}-\omega}}{1 - i\nu_i \int d^3\mathbf{v}\frac{f_{i0}(\mathbf{v})}{\mathbf{k}\cdot\mathbf{v}-\omega}} \ , \tag{3.2}$$

which includes Landau damping and collisional damping (ν_i is the ion-neutral collision frequency, and $f_{i0}(\mathbf{v})$ the ion distribution function). The electron Debye length is given by $\lambda_{D_e} = \sqrt{\varepsilon_0 k_B T_e / q_e^2 \bar{n}_e}$, where $\bar{n}_{e(i)}$ and $T_{e(i)}$ refer to the mean electron (ion) density and temperature. In the limit of $|\mathbf{u}| \to 0$ we recover the *static* case, where the surrounding plasma of free electrons and ions is taken into account by means of an isotropically screened Coulomb potential — the Debye-Hückel or Yukawa potential

$$\Phi_{ij} = \frac{q^2}{4\pi\varepsilon_0} \frac{e^{-\kappa|\mathbf{r}_i-\mathbf{r}_j|}}{|\mathbf{r}_i - \mathbf{r}_j|} \ . \tag{3.3}$$

Here q denotes the charge of the dust component and ε_o the vacuum permeability. The range of the dust pair potential Φ_{ij} is characterized by the dimensionless[2] screening parameter $\kappa = r_0/\lambda_D$, defined as the inverse Debye screening length,

$$\lambda_D = \left(\frac{q_e^2\bar{n}_e}{\varepsilon_0 k_B T_e} + \frac{q_i^2\bar{n}_i}{\varepsilon_0 k_B T_i} \right)^{-1/2} \ , \tag{3.4}$$

which incorporates the combined effect of static electrons and static ions. Note that the Yukawa potential includes the pure Coulomb interaction as the special case $\kappa = 0$.

In order to accurately model the experimental conditions we employ a spherical parabolic confinement, which is independent of the screening parameter κ [3]

$$U_c(r) = \frac{m}{2}\omega_0^2 r^2 \ , \tag{3.5}$$

where $r = |\mathbf{r}|$ denotes the radial particle position (distance from the trap center). The

---

[2]Dimensionless lengths and energies are obtained by introducing the units $r_0 = (q^2/2\pi\varepsilon m\omega_0^2)^{1/3}$ and $E_0 = (m\omega_0^2 q^4/32\pi^2\varepsilon^2)^{1/3}$ (see section 1.3).

[3]The correctness of the assumed κ-independent external confinement potential is verified in section 3.3.

physical properties of the reduced model of N identical dust grains of equal charge q and mass m are defined by the N-particle Hamiltonian

$$H_N(\mathbf{p}_i, \mathbf{r}_i) = \sum_{i=1}^{N} \frac{\mathbf{p}_i^2}{2m} + \sum_{i=1}^{N-1} \sum_{j>i}^{N} \Phi_{ij}(|\mathbf{r}_i - \mathbf{r}_j|) + \sum_{i=1}^{N} U_c(\mathbf{r}_i) \,. \qquad (3.6)$$

It is interesting to note that this classical system is fully described by only two parameters: coupling strength Γ (equation 1.1) and screening parameter κ [106]. Using molecular dynamics we solve the N-particle problem of dust grains from first principles.

Since we are interested in the ground state structure of Yukawa balls, we apply molecular dynamics to find the lowest energy states. The classical ground state configurations are explored by simulated annealing, i.e., from minimizing the kinetic and potential energy in equation (3.6). Note that in contrast to the quantum case, in classical systems the kinetic energy vanishes at zero temperature. That means that all particle velocities become zero, which leads to infinitely strong coupling according to the definition of Γ (equation 1.1).

Finding the global minimum on a multi-dimensional potential energy surface is conceptually simply, but in practice a challenging problem. To assure that the correct N-particle ground state was detected, the runs were repeated up to several thousand times, where each run starts with different random initial velocities and positions of all particles. The quadratic growth of the number of force computations and the exponential complexity of the problem (due to the growing number of metastable states with only marginally higher energy) with respect to N makes the computation demanding and requires aggressive code optimizations. To speedup the computations we tuned the numerical truncation error $\Delta(h)$, equation (2.9), during the simulated annealings, in dependence of the particular kinetic energy per particle, continuously from 10^{-3} to 10^{-8} (for $E_{kin}/N > 10^{-3}$ we used a fixed minimum accuracy $\Delta(h) = 10^{-3}$ to avoid numerical instabilities). However, in particular for clusters with $N \geq 100$, reliable data can be only obtained within a feasible time (i.e. within a few weeks) by using several, typically 10 to 20, CPUs. Instead of a code (force) parallelization we were running an ensemble of independent simulations on distributed processors. This strategy offers best scalability and makes the most efficient use of the available compute power. The complete table of ground states containing the shell configurations and energies for *spherical 3D Coulomb crystals* in the range of particle numbers $N \leq 160$ are presented in section 3.2. From our simulation data we correct and extend previous results of Hasse and Avilov [33]. Very
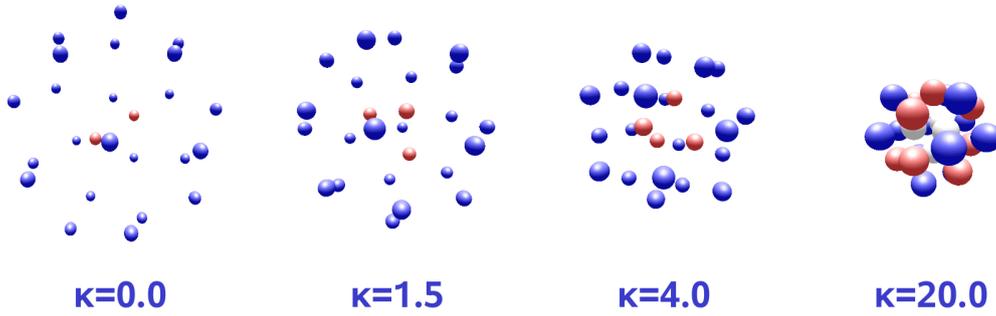
Figure 3.2: *Ground state configuration of a Yukawa ball composed of $N = 25$ dust grains in a parabolic trap. Upon increase of the screening length κ, the cluster size decreases and the shell configuration changes from (2,23) in the Coulomb regime, to (3,22) in the range $0.3 < \kappa < 2.2$ and finally, in the limit of large κ values, to (4,21). Different colors denote particles on different (sub-)shells. Note that not the plotted cluster size, but the point size is correctly scaled with κ.*

recent work confirms that our simulations are exact, and all N-particle ground states have been correctly identified [42, 107, 108, 109].

Structural Properties of Spherical Yukawa Crystals

In the following we will address the question of whether and how the Debye shielding affects the structure formation in dusty plasmas. This question is directly connected to the (structural) relation between trapped laser-cooled ion systems on the one hand and Yukawa balls on the other hand. A detailed numerical analysis of the ground states of pure and screened Coulomb clusters reveals the following generic trends upon increase of the screening parameter κ (see figure 3.2 for one representative example):

1. Screening weakens the repulsive interaction between the dust grains which consequently leads to a compression of the cluster. Including this effect,

2. the shell radii (normalized to mean interparticle distance) are found to be independent of screening.

3. By increase of κ the shell widths broaden and shell splitting as well as the emergence of sub-shells is observed (see figure 3.2 at $\kappa = 20$).

4. The number of shells is generally independent of Debye shielding.

5. In contrast, the shell occupation numbers are found to be highly sensitive to a change of screening.

$\kappa \rightarrow$	0.0	0.2	0.3	0.4	0.5	0.6	0.8	1.0	**Experiment**
s_1	1	1	2	2	2	*2*	3	4	**2**
s_2	18	18	20	20	21	*21*	22	24	**21**
s_3	56	57	57	58	58	*60*	60	60	**60**
s_4	115	114	111	110	109	*107*	105	102	**107**

Table 3.1: *Theoretical shell configurations obtained from MD simulations for the Coulomb ball $N = 190$ as a function of screening parameter κ in comparison with experimental data [15] (last column). Beginning in the cluster center, s_1, ..., s_4 denote the particle numbers on the i-th shell. If the screening parameter κ is increased, the number of shells remains equal to four, but the inner (outer) shell become higher (lower) populated. Further details are given in the text.*

6. At large values of κ the screened Coulomb interaction becomes "hard-sphere"-like. This induces a structural change from a nested shell configuration to a bulk-like close-packed symmetry.

Sure enough, the most remarkable finding is the effect of screening on the detailed shell population and structure of the individual shells. In general it can be stated that the occupation numbers on the inner (outer) shells gradually increase (decrease) with κ.[4] This implies that a Yukawa system contains a smaller (or equal) number of particles on the outer and a higher (or equal) number of particles on the inner shell than a comparable unscreened Coulomb system. A representative example for this general trend is shown in table 3.1. The comprehensive systematic comparison of molecular dynamics simulations with experimental measurements reveals that the change in the shell population numbers can only be attributed to screening (the details of this comparison are presented in section 3.3). Therefore, our simulations allowed us to determine the Coulomb screening parameter $\kappa_{exp} \approx 0.62$ from experimentally measured shell configurations. The value agrees well with independent estimations based on experimental parameters [111].

Further Monte Carlo and molecular dynamics simulations show that a finite temperature and the inclusion of charge fluctuations (in view of a variations of the dust grain sizes) are negligible compared to the effect of screening and do not lead to significant deviations from the ground state shell configurations [112]. Therefore, the shell occupation numbers are found to be very suitable quantities which allow for a non-invasive determination of the experimental Debye screening parameter in dusty plasma experiments.

We note that an alternative theoretical model by H. Totsuji et al. [113] predicts approximately screening-independent shell populations, which differ from the measurements [15, 32].

---

[4]This statement holds with the exception of a very few special cases at very large κ that were recently detected [110].

3.2 Ground State Structure of 3D Coulomb Crystals

*An analysis of the structural properties of three-dimensional Coulomb clusters confined in a spherical parabolic trap is presented. Based on extensive high-accuracy molecular dynamics simulations, a complete table of ground state configurations and energies for particle numbers in the range $N \leq 160$ is compiled, which corrects previous results of Hasse and Avilov [Phys. Rev. A **44**, 4506 (1991)]. Further, the intrashell symmetry of the ground states and lowest metastable states is investigated.*

The results were published as refereed journal publications:

3.2.1 ***Structure of Spherical Three-Dimensional Coulomb Crystals,***
  P. Ludwig, S. Kosse, and M. Bonitz, Physical Review E **71**, 046403 (2005)

3.2.2 ***3D Coulomb Balls: Experiment and Simulation,***
  O. Arp, D. Block, M. Bonitz, H. Fehske, V. Golubnychiy, S. Kosse, P. Ludwig,
  A. Melzer, and A. Piel, Journal of Physics: Conference Series **11**, 234 (2005)

Structure of spherical three-dimensional Coulomb crystals

P. Ludwig,[1,2] S. Kosse,[1,3] and M. Bonitz[1]

[1]*Institut für Theoretische Physik und Astrophysik, Christian-Albrechts-Universität zu Kiel, Leibnizstrasse 15, 24098 Kiel, Germany*
[2]*Fachbereich Physik, Universität Rostock, l8051 Rostock, Germany*
[3]*Sektion Physik, Ernst-Moritz-Arndt Universität Greifswald, Domstrasse 10a, l7487 Greifswald, Germany*
(Received 14 September 2004; revised manuscript received 8 November 2004; published 15 April 2005)

An analysis of the structural properties of three-dimensional Coulomb clusters confined in a spherical parabolic trap is presented. Based on extensive high-accuracy computer simulations the shell configurations and energies for particle numbers in the range $60 \leq N \leq 160$ are reported. Further, the intrashell symmetry and the lowest metastable configurations are analyzed for small clusters and a different type of excited state that does not involve a change of shell configuration is identified.

Spatially confined charged particle systems have a number of unique properties not observed in conventional *quasineutral macroscopic* plasmas of electrons and ions in discharges or solids, electrons and holes in highly excited semiconductors, and so on. With the help of confinement potentials it has now become routine to trap, for long periods of time, *plasmas of a single charge* (nonneutral plasmas), e.g., electrons and ions and even positrons in Paul and Penning traps [1–3] (for an overview see [4]), or colloidal (dusty) plasmas in discharge chambers (e.g., [5]). By varying the confinement strength researchers have achieved liquid behavior and even Coulomb crystallization of ions [3,6] and dust particles [7,8]. These strong correlation phenomena are of exceptional current interest in a large variety of fields ranging from astrophysics (interior of giant planets) and high-power laser compressed laboratory plasmas, to condensed matter and quantum dots [9], etc. Coulomb (Wigner) crystals are expected to exist in many white dwarf stars.

A particular property of trapped small ($N \lesssim 1000$) clusters in spherical traps is the occurrence of concentric shells with characteristic occupation numbers, shell closures, and unusual stable "magic" configurations. Due to their close similarity to nuclei, metal clusters, or atoms, these systems are sometimes called "artificial atoms." A significant number of papers has been devoted to the exploration of the energetically lowest shell configuration (ground state) and metastable ("excited") states of two-dimensional (2D) artificial atoms (e.g., [10–12] and references therein).

On the other hand, *three-dimensional spherical Coulomb crystals* (3D SCCs) have been observed in laboratory experiments with ultracold ion plasmas [3,6], and the interest in them is now rapidly growing [13] after their prediction in expanding laser-cooled neutral plasmas [14] and their experimental creation in dusty plasmas as well [15]. This raises a question about theoretical results for the configurations of spherical 3D Coulomb crystals, which is the subject of this paper. These results are expected to be an important reference for the above experiments but also for other possible candidates for 3D crystals, including semiconductor nanostructures. It is natural to start with an analysis of the ground state and lowest metastable states, deferring finite temperature and melting properties [e.g., [16]] and also deviations

from an isotropic Coulomb interaction to a subsequent study.

The theoretical analysis of 3D SCCs is much more involved than in 2D and has so far mostly been restricted to small cluster sizes with often conflicting results (e.g., [17–19] and references therein). Rafac *et al.* [18], correcting earlier results, identified the first shell closure at $N=12$ (the 13th particle is the first to occupy a second shell) and presented detailed data, including ground state energies for $N \leq 27$, but they missed the onset of the third shell, as did Hasse and Avilov [17]. Tsuruta and Ichimaru extended the table to $N=59$ [19]. The most extensive data, for up to a few thousand particles, have been presented by Hasse and Avilov [17] and has been a valuable reference for theoretical and experimental groups. However, as our calculations show, their tables contain excited states rather than the true ground states for $N=28-31$, 44, 54 and practically for all $N>63$ (except for $N=66$). Therefore, it is an important task to obtain the correct ground state shell configurations and cluster properties for particle numbers beyond $N=60$.

The reason for the computational difficulties is the existence of a large number of excited (metastable) states which are energetically close to the ground state; with increasing N this number grows exponentially whereas the energy difference rapidly vanishes. Calculations with a too low accuracy will then frequently miss the correct ground state. Therefore, we use an improved computational strategy which drastically reduces the probability of such misses (see below).

Model: we consider N classical particles with equal charge q and mass m interacting via the Coulomb force and being confined in a 3D isotropic harmonic trap with frequency ω with the Hamiltonian

$$H_N = \sum_{i=1}^{N} \frac{m}{2}\dot{r}_i^2 + \sum_{i=1}^{N} \frac{m}{2}\omega^2 r_i^2 + \sum_{i>j}^{N} \frac{q^2}{4\pi\varepsilon|\mathbf{r}_i - \mathbf{r}_j|}. \quad (1)$$

Despite its simplicity, the model (1) captures the basic properties of a multitude of classical systems and serves as an important reference point also for more complex 3D systems. Below we will use dimensionless lengths and energies by introducing the units $r_0 = (q^2/2\pi\varepsilon m\omega^2)^{1/3}$ and $E_0 = (m\omega^2 q^4/32\pi^2\varepsilon^2)^{1/3}$, respectively.

TABLE I. Shell configurations, energy per particle for the lowest-lying states (for the excited states the energy difference with respect to the ground state is given in italics), mean radius of the outer shell r_1, symmetry parameter G_M, Eq. (2), and number of Voronoi M-polygons $N(M)$ in brackets. For $N=4$, $N(3)=4$, and for $N=5$, $N(3)=2$, $N(4)=3$.

N	Configuration	E/N	r_1	G_4 [$N(4)$]	G_5 [$N(5)$]	G_6 [$N(6)$]
2	(2)	0.750000	0.5000	–	–	–
3	(3)	1.310371	0.6609	–	–	–
4	(4)	1.785826	0.7715	–	–	–
5	(5)	2.245187	0.8651	1.000 [3]	–	–
6	(6)	2.654039	0.9406	1.000 [6]	–	–
7	(7)	3.064186	1.0106	1.000 [5]	1.000 [2]	–
8	(8)	3.443409	1.0714	0.641 [4]	0.821 [4]	–
9	(9)	3.809782	1.1269	0.965 [3]	0.957 [6]	–
10	(10)	4.164990	1.1783	1.000 [2]	0.861 [8]	–
	(9,1)	*0.021989*	1.2453	0.965 [3]	0.957 [6]	
11	(11)	4.513275	1.2265	0.940 [2]	0.894 [8]	1.000 [1]
	(10,1)	*0.009876*	1.2878	1.000 [2]	0.861 [8]	–
12	(12)	4.838966	1.2700	–	1.000 [12]	–
	(11,1)	*0.015345*	1.3286	0.938 [2]	0.895 [8]	1.000 [1]
13	(12,1)	5.166798	1.3659	–	1.000 [12]	–
	(13)	*0.005061*	1.3130	1.000 [1]	0.894 [10]	0.932 [2]
14	(13,1)	5.485915	1.4033	–	0.893 [10]	0.933 [2]
	(14)	*0.003501*	1.3527	1.000 [1]	0.938 [12]	1.000 [2]
15	(14,1)	5.792094	1.4383	–	0.938 [12]	1.000 [2]
	(15)	*0.009031*	1.3906	–	0.885 [12]	0.963 [3]
16	(15,1)	6.093421	1.4719	–	0.882 [12]	0.962 [3]
	(16)	*0.012200*	1.4266	–	0.897 [12]	0.993 [4]
	(16)	*0.012635*	1.4267	–	0.747 [12]	0.884 [4]
17	(16,1)	6.388610	1.5042	–	0.891 [12]	0.993 [4]
	(16,1)	*0.000365*	1.5042	–	0.746 [12]	0.884 [4]
	(17)	*0.015766*	1.4611	–	0.738 [12]	0.810 [5]
18	(17,1)	6.678830	1.5353	–	0.738 [12]	0.810 [5]
	(18)	*0.018611*	1.4941	1.000 [2]	0.829 [8]	0.920 [8]
19	(18,1)	6.964146	1.5654	1.000 [2]	0.827 [8]	0.920 [8]
20	(19,1)	7.247181	1.5946	–	0.838 [12]	0.918 [7]
	(18,2)	*0.004264*	1.6285	0.991 [2]	0.824 [8]	0.913 [8]
21	(20,1)	7.522378	1.6226	–	0.792 [12]	0.917 [8]
	(19,2)	*0.004668*	1.6557	–	0.847 [12]	0.927 [7]
22	(21,1)	7.795469	1.6499	1.000 [1]	0.877 [10]	0.880 [10]
	(21,1)	$2.5 \cdot 10^{-7}$	1.6499	1.000 [1]	0.859 [10]	0.866 [10]
	(20,2)	*0.000976*	1.6821	–	0.801 [12]	0.935 [8]
	(20,2)	*0.001053*	1.6820	–	0.763 [12]	0.909 [8]

To find the ground and metastable states, we used classical molecular dynamics (MD) together with an optimized version of the standard simulated annealing method. Starting with a random initial configuration of N particles, the system is cooled continuously until all momenta are zero and the particles settle in minima of the potential energy surface. Depending on the particle number, the cooling down process was repeated between several hundred and several thousand times until every one of the computed low-energy states was found more than a given number of times (typically 10–100) assuring a high probability that the ground state has been found. Crucial for a high search efficiency is the use of an

optimized MD time step (it has to be chosen not too small to avoid trapping in local potential minima). The results are shown in Tables I and II.

Consider first the ground state shell configurations beyond the previously reported results [18,19] (see Table II). Closure of the second shell is observed twice: for $N=57$ [19] and 60. Further, we have found the closure of the third shell to occur at $N=154$; all larger clusters have at least four shells (in the ground state). The "noble-gas-like" closed shell clusters are particularly stable, but a few others also have a comparatively high binding energy (addition energy change) $\Delta_2(N) = E(N+1) + E(N-1) - 2E(N)$. Tsuruta and Ichimaru [19]

TABLE II. Ground state shell configurations, energy per particle for the lowest-lying states, and mean shell radii $r_{1,2,3}$ [20].

N	Configuration	E/N	r_1	r_2	r_3
28	(25,3)	9.348368	1.8525	0.6889	–
29	(25,4)	9.595435	1.8992	0.7987	–
30	(26,4)	9.838965	1.9198	0.7961	–
31	(27,4)	10.079511	1.9399	0.7926	–
44	(36,8)	13.020078	2.2454	1.0845	–
54	(44,10)	15.085703	2.4186	1.1872	–
55	(43,12)	15.284703	2.4618	1.2772	–
56	(44,12)	15.482144	2.4743	1.2770	–
57	(45,12)	15.679350	2.4869	1.2763	–
58	(45,12,1)	15.875406	2.5126	1.3765	–
59	(46,12,1)	16.070103	2.5247	1.3764	–
60	(48,12)	16.263707	2.5236	1.2754	–
64	(49,14,1)	17.027289	2.6101	1.4478	–
65	(50,14,1)	17.215361	2.6212	1.4477	–
80	(60,19,1)	19.936690	2.8369	1.6002	–
84	(61,21,2)	20.632759	2.9064	1.7140	0.5426
94	(67,24,3)	22.325841	3.0347	1.8356	0.7001
95	(67,24,4)	22.491878	3.0522	1.8848	0.8089
96	(68,24,4)	22.657271	3.0606	1.8846	0.8083
97	(69,24,4)	22.822032	3.0687	1.8849	0.8095
98	(69,25,4)	22.986199	3.0864	1.9055	0.8081
99	(70,25,4)	23.149758	3.0945	1.9056	0.8071
100	(70,26,4)	23.312759	3.1117	1.9259	0.8055
101	(70,27,4)	23.475164	3.1291	1.9450	0.8028
103	(72,27,4)	23.798274	3.1451	1.9443	0.8017
105	(73,28,4)	24.120223	3.1696	1.9641	0.8020
107	(75,28,4)	24.439666	3.1850	1.9640	0.8011
109	(77,28,4)	24.757151	3.2005	1.9638	0.8006
111	(77,29,5)	25.072584	3.2322	2.0249	0.8968
113	(77,30,6)	25.385842	3.2637	2.0831	0.9640
115	(77,32,6)	25.697308	3.2949	2.1162	0.9630
117	(79,32,6)	26.007089	3.3094	2.1158	0.9622
119	(81,32,6)	26.315442	3.3237	2.1156	0.9624
121	(83,32,6)	26.622118	3.3379	2.1154	0.9614
123	(83,34,6)	26.927195	3.3672	2.1493	0.9625
125	(84,34,7)	27.230458	3.3884	2.1850	1.0340
128	(85,35,8)	27.682123	3.4235	2.2358	1.0922
130	(86,36,8)	27.981234	3.4445	2.2501	1.0917
133	(88,37,8)	28.427062	3.4718	2.2642	1.0912
135	(88,38,9)	28.722421	3.4992	2.3110	1.1436
137	(90,38,9)	29.016328	3.5119	2.3110	1.1440
139	(91,39,9)	29.308774	3.5316	2.3251	1.1430
141	(92,40,9)	29.599900	3.5514	2.3387	1.1417
143	(93,40,10)	29.889733	3.5707	2.3689	1.1932
145	(94,41,10)	30.178106	3.5898	2.3825	1.1920
147	(95,42,10)	30.465219	3.6087	2.3957	1.1923
149	(96,43,10)	30.750998	3.6273	2.4090	1.1926
151	(96,43,12)	31.035390	3.6524	2.4659	1.2814

TABLE II. (*Continued.*)

N	Configuration	E/N	r_1	r_2	r_3
153	(97,44,12)	31.318528	3.6708	2.4781	1.2811
154	(98,44,12)	31.459632	3.6768	2.4777	1.2810
155	(98,44,12,1)	31.600488	3.6887	2.5042	1.3846
156	(98,45,12,1)	31.741100	3.7006	2.5169	1.3839
158	(100,45,12,1)	32.021294	3.7122	2.5166	1.3834
160	(102,45,12,1)	32.300405	3.7238	2.5161	1.3833

found the stable clusters $N = 4, 6, 10, 12, 19, 32, 38, 56$. For larger clusters the binding energy decreases, and the relative differences rapidly decrease. We found the next particularly stable ones to be $N = 81, 94, 103, 116$. The results are shown in Fig. 1. The relative stability of these clusters is linked to a particularly symmetric particle arrangement within the shells which will be analyzed below.

The existence of the shell structure is a marked difference from macroscopic Coulomb systems ($N \rightarrow \infty$) and is, of course, caused by the spherical confinement potential. With increasing N the structure of a macroscopic system emerges gradually (see also Ref. [16]). This can be seen from the relative widths $\bar{\sigma}_m \equiv \sigma_m / r_m$ of the mth shell (σ_m denotes the variance of the shell radius r_m). For example, for $N = 149$ (starting from the outermost shell) $\bar{\sigma}_1 = 0.0089$, $\bar{\sigma}_2 = 0.035$, and $\bar{\sigma}_3 = 0.032$, whereas for $N = 160$ we obtain $\bar{\sigma}_1 = 0.0091$, $\bar{\sigma}_2 = 0.033$, and $\bar{\sigma}_3 = 0.0038$. In both cases the outermost shell is significantly narrower than the second one and this trend becomes more pronounced as N increases. This is easy to understand because the effect of the confinement is strongest at the cluster boundary, i.e., in the outer shell, whereas the inner shells are partially shielded from the trap potential by the surrounding particle shells. In contrast, the behavior of the inner shells is not that systematic: in one case ($N = 149$) the third shell is of similar (relative) width as the second; in the other case ($N = 160$) the inner shell is much narrower. The reason is symmetry effects which particularly strongly influence the width of the innermost shell (the cluster $N = 160$ has a closed inner shell with 12 particles which is very narrow).

In Table I we also provide the first excited states, which correspond to metastable shell configurations that are different from the ground state. While the overall trend is a rapid decrease of the excitation energy (energy gap to the ground state) with increasing N, some additional systematics is observed. Clusters that open a new shell typically possess a close metastable state. For example, for $N = 13$ the relative stability of the configurations $\{N,0\}$ and $\{N-1,1\}$ changes, the latter becomes the ground state and the former the first excited state (see Table I). A similar trend is observed not only when a new shell is opened but also when an additional particle moves onto the inner shell between the states $\{N_1 - 1, N_2\}$ and $\{N_1, N_2 - 1\}$. Away from these transition points the energy difference increases and eventually another configuration becomes the first excited state.

An interesting observation is that frequently simulations yielding the same shell configuration resulted in different total energies; see, e.g., $N = 16, 17, 22$ in Table I. The differ-
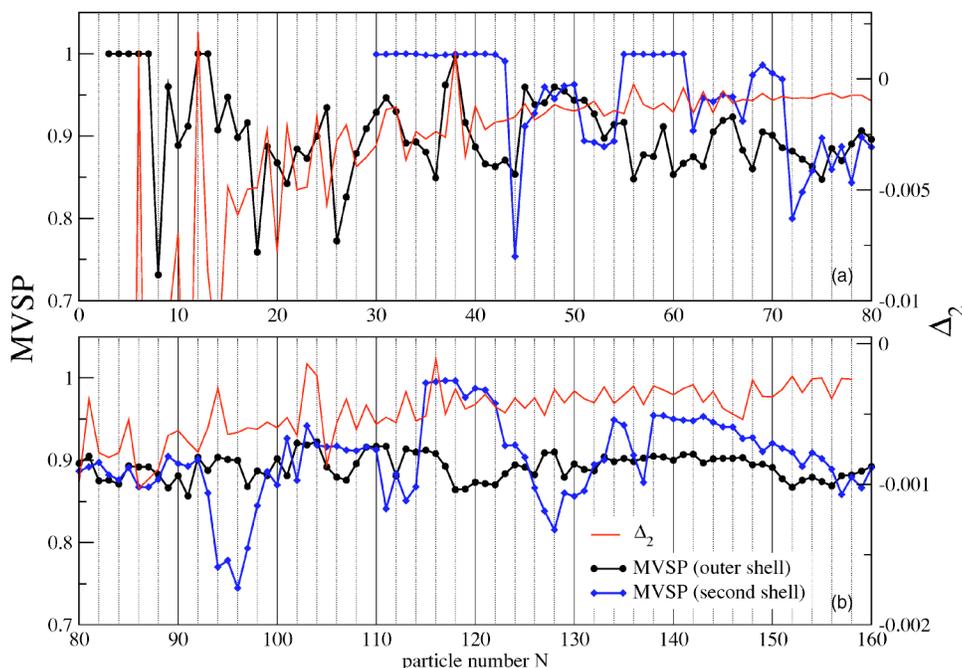
FIG. 1. (Color online) Binding energy Δ_2 (right axis) and mean Voronoi symmetry parameter (MVSP, left axis) for the two outermost cluster shells. (a) $N \leq 80$; (b) $80 \leq N \leq 160$.

ences are much larger than the simulation error; moreover, the energies are reproducible. The obvious explanation is that the state of a cluster is not completely determined by its shell configuration (as is the case in 2D). In addition, there exist further excited states, i.e., a "fine structure," which are due to a *different particle arrangement and symmetry within one shell*. To understand the differences in the structure of these states with the same shell configuration we analyzed the intrashell symmetry by performing a Voronoi analysis, i.e., by constructing polygons around a given particle formed by the lines equally bisecting nearest-neighbor pairs on the shell (see the example of $N = 17$ shown in Fig. 2). Interestingly, the two states do not differ with respect to the number of polygons of each kind on the outer shell: there are $N(5) = 12$ pentagons and $N(6) = 4$ hexagons. However, what is different is the *arrangement of the polygons*: in one case, the four hexagons form a perfect tetrahedron $ABCD$ and are separated from each other by pentagons [see Fig. 2(a)]; in the other two pairs of hexagons touch [see Fig. 2(b)], and the
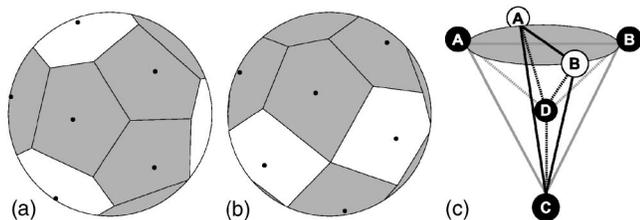
tetrahedron is distorted, as shown in Fig. 2(c). Two edges remain practically constant ($\overline{AB} \approx \overline{CD} \approx 1.63$), but the edge AB rotates with respect to the first case by an angle of $34°$ resulting in a reduction of edges $\overline{BC}$ and $\overline{AD}$ to about 1.24 while $\overline{AC}$ and $\overline{BD}$ increase to 1.94. From this we conclude that of two states the one with the more symmetric arrangement of the Voronoi polygons, i.e., Fig. 2(a), has the lower energy. To quantify this topological criterion, we introduce the *Voronoi symmetry parameter*

$$G_M = \frac{1}{N_M} \sum_{j=1}^{N_M} \frac{1}{M} \left| \sum_{k=1}^{M} e^{iM\theta_{jk}} \right|, \qquad (2)$$

where N_M denotes the number of all particles j in the shell, each of which is surrounded by a Voronoi polygon of order M (M nearest neighbors), and θ_{jk} is the angle between the jth particle and its kth nearest neighbor. A value $G_5 = 1$ ($G_6 = 1$) means that all pentagons (hexagons) are perfect; the magnitude of the reduction of G_M below 1 measures their distortion. Inspection of the values of G_M for the two $\{16,1\}$ configurations for $N = 17$ (Table I) reveals that the state with lower energy has higher values for both G_5 and G_6 than the second, confirming our observation above. This result is verified for all other N (of course it applies only to states with the same shell configuration).

Having obtained with G_M a suitable symmetry measure that is sensitive to the relative stability of ground and metastable states, we now return to the issue of the overall cluster stability. To this end we compute the *mean Voronoi symmetry parameter* by averaging over all G_M of a given shell weighted with the respective particle numbers $N(M)$. The results for the two outer shells for $N \leq 160$ are included in Fig. 1. We clearly see that *magic clusters* have not only a high binding energy but also a prominent symmetry [19]; see in particular $N = 12$, 38, 103, and 116.

In summary, in this paper we have presented extensive

FIG. 2. Voronoi construction for the cluster $N = 17$ for the two energetically lowest states with shell configuration $N = \{1, 16\}$. White (gray) areas are hexagons (pentagons), indicating the number of nearest neighbors of the corresponding particle (black dot). (a) ground state; (b) first excited ("fine structure") state; (c) arrangement of the four particles surrounded by hexagons; the two states differ by rotation of the edge AB, black (white) circles correspond to case (a) [(b)].

simulation results for spherical Coulomb clusters with $N \leq 160$. The observed cluster ground state configurations for $N \geq 60$ differ, in most cases, from the ones previously reported [17] which have a significantly higher energy and thus correspond to excited states of the clusters. The presented tables (for the complete tables, see [20]) should be a valuable reference for experiments with classical 3D Coulomb crystals in dusty plasmas [15], ultracold ions [6], or laser-cooled expanding neutral plasmas [14]. Of course, real experiments with ions or dust grains are likely to exhibit deviations from the simple model (1)—the interaction may deviate from the Coulomb law (e.g., due to screening) and may be direction dependent, the confinement potential is often not perfectly isotropic or parabolic, etc. Therefore, differences in the experimentally observed cluster configurations compared to the above theoretical results may be valuable additional information on imperfections of the experimental setup (possible anisotropic confinement) or on the plasma properties (screening length).

Moreover, the obtained ground state results (shell configurations) are expected to be important also for quantum 3D Coulomb clusters which may exist, e.g., in semiconductor quantum dots in the strong coupling limit. It was found before for 2D systems that, in most cases, the ground state shell configurations in quantum crystals are exactly the same as in the corresponding (essentially simpler) classical crystals [9,12,21]. This remains an interesting question for future analysis.

Further, we have presented an analysis of the lowest excited states of small clusters. Besides metastable states with a shell structure different from the ground state we identified "fine structure" states which are characterized by different particle arrangement within the shells, an important property not existing in 2D crystals. These states have a lower symmetry which is linked to higher values of the total energy.

Finally, knowledge of the lowest metastable states is very important for understanding all dynamic properties of 3D crystals. The metastable states are expected to be of relevance for the collective excitations of the clusters (normal modes that are excited in the system if kinetic energy is supplied) as well as for the melting behavior of the 3D crystals.

[1] F. Diedrich, E. Peik, J. M. Chen, W. Quinnt, and H. Walter, Phys. Rev. Lett. **59**, 2931 (1987).

[2] D. J. Wineland, J. C. Bergquist, W. M. Itano, J. J. Bollinger, and C. H. Manney, Phys. Rev. Lett. **59**, 2935 (1987).

[3] S. L. Gilbert, J. J. Bollinger, and D. J. Wineland, Phys. Rev. Lett. **60**, 2022 (1988).

[4] D. H. E. Dubin and T. M. O'Neill, Rev. Mod. Phys. **71**, 87 (1999).

[5] *Focus on Complex (Dusty) Plasmas*, edited by G. E. Morfill and H. Kersten, special issue of New J. Phys. **5** (2003).

[6] W. M. Itano, J. J. Bollinger, J. N. Tan, B. Jelenkovic, and D. J. Wineland, Science **297**, 686 (1998).

[7] H. Thomas, G. E. Morfill, V. Demmel, J. Goree, B. Feuerbacher, and D. Möhlmann, Phys. Rev. Lett. **73**, 652 (1994).

[8] Y. Hayashi and K. Tachibana, Jpn. J. Appl. Phys., Part 2 **33**, L804 (1994).

[9] A. V. Filinov, M. Bonitz, and Yu. E. Lozovik, Phys. Rev. Lett. **86**, 3851 (2001).

[10] V. M. Bedanov and F. M. Peeters, Phys. Rev. B **49**, 2667 (1994).

[11] M. Kong, B. Partoens, and F. M. Peeters, New J. Phys. **5**, 23.1 (2003).

[12] P. Ludwig, A. V. Filinov, M. Bonitz, and Yu. E. Lozovik, Contrib. Plasma Phys. **43**, 285 (2003).

[13] T. C. Killian, Nature (London) **429**, 815 (2004).

[14] T. Pohl, T. Pattard, and J. M. Rost, Phys. Rev. Lett. **92**, 155003 (2004).

[15] O. Arp, D. Block, A. Piel, and A. Melzer, Phys. Rev. Lett. **93**, 165004 (2004).

[16] J. P. Schiffer, Phys. Rev. Lett. **88**, 205003 (2002).

[17] R. W. Hasse and V. V. Avilov, Phys. Rev. A **44**, 4506 (1991).

[18] R. Rafac, J. P. Schiffer, J. S. Hangst, D. H. E. Dubin, and D. J. Wales, Proc. Natl. Acad. Sci. U.S.A. **88**, 483 (1991).

[19] K. Tsuruta and S. Ichimaru, Phys. Rev. A **48**, 1339 (1993).

[20] A complete table of ground state configurations for $1 \leq N \leq 160$ is available as accompanying material: P. Ludwig, S. Kosse, V. Golubnychiy, M. Bonitz, and H. Fehske, e-print physics/0409100.

[21] A. Filinov, M. Bonitz and Yu. E. Lozovik, J. Phys. A **36**, 5899 (2003).

3D Coulomb Balls: Experiment and Simulation

O Arp[1], D Block[1], M Bonitz[2], H Fehske[3], V Golubnychiy[2], S Kosse[3], P Ludwig[2,4], A Melzer[3], and A Piel[1]

[1] Christian-Albrechts-Universität Kiel, Institut für Experimentelle und Angewandte Physik, 24098 Kiel, Germany
[2] Christian-Albrechts-Universität Kiel, Institut für Theoretische Physik und Astrophysik, 24098 Kiel, Germany
[3] Universität Greifswald, Institut für Physik, l7487 Greifswald, Germany
[4] Universität Rostock, Fachbereich Physik, l8051 Rostock, Germany

Abstract. Spherically symmetric three-dimensional charged particle clusters are analyzed experimentally and theoretically. Based on accurate molecular dynamics simulations ground state configurations and energies with clusters for $N \leq 160$ are presented which correct previous results of Hasse and Avilov [Phys. Rev. A **44**, 4506 (1991)]. A complete table is given in the appendix. Further, the lowest metastable states are analyzed.

1. Introduction

Over the last years the investigation of complex (dusty) macroscopic and mesoscopic plasmas occurring e.g. in astrophysical, laboratory and technical situations has become an important research field. The theoretical description of complex plasmas is extremely difficult due to their heterogeneous composition and the drastic differences in the relevant space and times scales, e.g. [1, 2]. With the help of confinement potentials it has become possible to trap, for long periods of time, plasmas of a single charge (non-neutral plasmas). By varying the confinement strength researchers have achieved liquid behavior and even Coulomb crystallization of ions [3] and dust particles [4, 5]. Such strong correlation phenomena are of exceptional current interest in many fields.

In general, the formation of extended, three dimensional dust clouds in rf-discharges is hampered by the dominance of the gravitational force on the dust particles. Only in a narrow sheath region above the electrode the electric field forces can compensate gravity. Hence, typical dust clouds are two dimensional (2D) structures trapped in the non-equilibrium conditions of the boundary sheath which cause the formation of vertical particle chains [6].

Besides electric field forces thermophoresis is capable to compensate gravitation. This has recently been demonstrated by Rothermel et al. [7], but instead of homogeneous 3D dust clouds the formation of dust free regions in the center of the discharge was observed. Similar observations of these so-called voids are made under microgravity conditions [8]. Although in both situations the electric field force on the particle is directed towards the plasma center, the outward directed ion flow is assumed to produce a friction force which exceeds the electric field forces in the center of the discharge and hence creates the void.

This contribution deals with the simulation and analysis of spherically 3D clusters which were recently first experimentally observed in dusty plasmas [9]. We compare simulation results
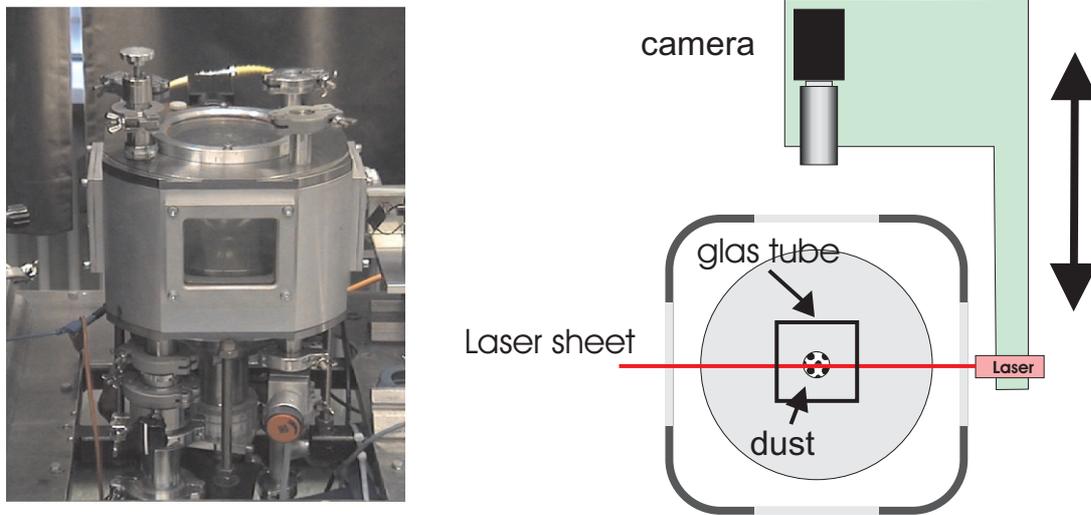
Figure 1. (Color online) Picture of the discharge chamber and a schematic drawing of the experimental setup (top view). The laser produces a vertical laser fan which illuminates vertical cross sections of the particle cloud. The camera looks at the illuminated plane under right angle. Laser and camera are mounted on a common positioning system to allow observation of arbitrary cross sections of the dust cloud.

to real dust clusters from experiments. In the simulations the dust-dust interaction potential is modelled by a Coulomb potential [10].

2. Experiments on Coulomb balls

2.1. Experimental Setup

The experiments presented in this paper are performed in a capacitively coupled rf-discharge in argon. The basic setup is well known from several investigations on 2D plasma crystals [6,11–13]. It consists of two plane parallel electrodes. The rf-power is applied to the lower electrode with 17 cm diameter. The upper electrode is a mesh grid of similar size and is connected to ground. The distance between the electrodes is 6 cm. Compared to previous investigations two changes are applied to the setup. First, the temperature of the lower electrode can be controlled in a range between $20 - 80°$C. With the upper electrode being at room temperature, vertical temperature gradients of up to $10°$C/cm can be established. Second, a glass tube with square cross section is placed in the lower half of the discharge on top of the lower electrode.

Typical parameters for the discharge are vertical temperature gradients of $5 \, \mathrm{Kcm}^{-1}$, rf-power below 30 W and neutral gas pressures of 50-150 Pa. For the experiments we use particles with a diameter of $3.4 \, \mu$m which are injected into the plasma from the top by gently shaking a fine sieve. The dust particles are illuminated by a vertical laser sheet of less than 500μm width. The scattered light of the particles is observed with a CCD-camera under right angle (Fig. 1). The CCD camera is focused to the illuminated plane. Both, camera and laser fan are mounted on a common frame which can be moved in horizontal direction. Hence images of arbitrary cross section of the dust cloud can be recorded. In particular, all three coordinates of the particles can be determined from a systematic scan of the dust cloud.
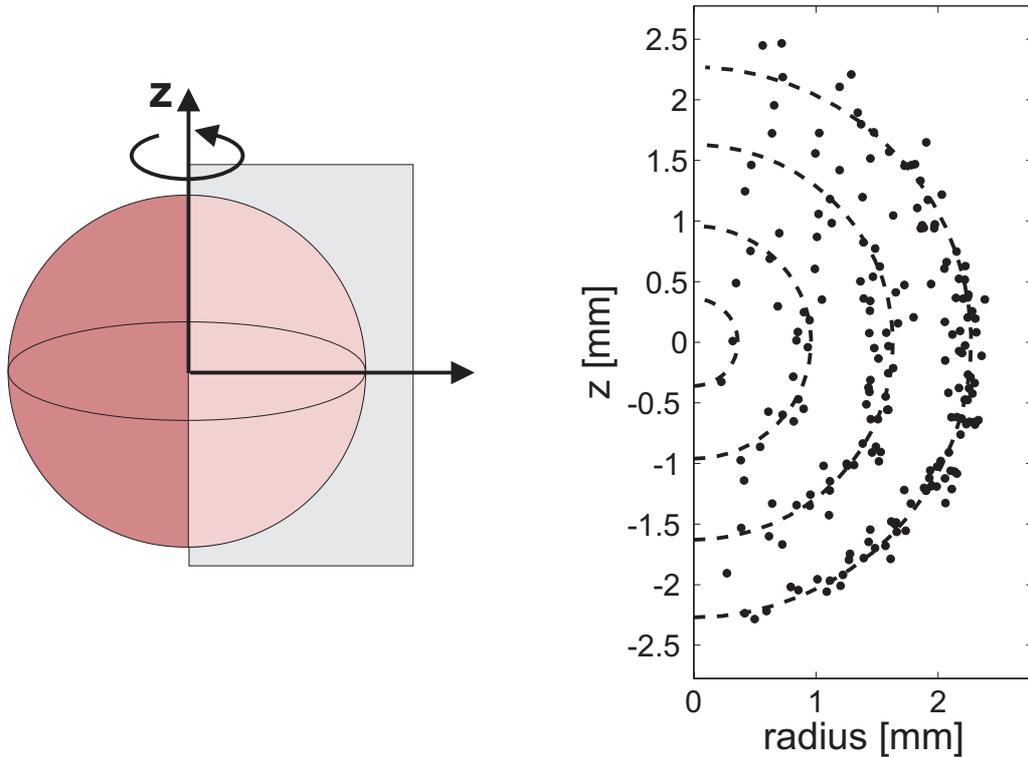
Figure 2. (Color online) The schematic drawing (left) shows a spherical particle cloud and a plane which rotates around an axis through the center of the cloud. The measured positions of all particles hitting this plane are marked with a dot for a particle cluster with 190 particles (right). The dashed lines indicate concentric circles around the cloud center.

2.2. Experimental Results

After injection of the particles the formation of a spherical dust cloud is observed. The cloud is located inside the glass tube close to the geometric center of the discharge arrangement. The example shown in Fig. 2 is a dust cloud consisting of 190 particles which has a diameter about 5 mm. In contrast to previous investigations [6–8] an important finding is that the dust cloud is void-free and that the particles show no chain formation. To investigate the spatial structure in more detail, Fig. 2 shows the particle distribution as a function of the cylindrical coordinates ρ and z, i.e. the azimuthal dependence is omitted in this plot. Besides the overall spherical shape of the dust cloud the occurrence of consentric shells is observed (dashed lines). This becomes evident when the particle position is plotted as a function of radius (spherical coordinates) only. Fig. 3 shows that the radial particle distribution function is strongly modulated. The prominent peaks indicate the formation of concentric spherical shells. A more detailed analysis [9] of the particle arrangement on individual shells shows that the particles arrange in a close hexagonal packing which includes few pentagonal defects to form a convex surface. The shell occupation for the 190 particle cluster is 2, 21, 60 and 107 starting with the innermost shell. This is close to the occupation number [10] found by numerical simulations of Coulomb clusters [20].

The appearance of a highly ordered particle system is further supported by calculations of the pair correlation function which yields a typical interparticle distance of 0.715 mm. Compared with the intershell distance of about 0.63 mm a good agreement with hexagonal closed packed systems is found [18].
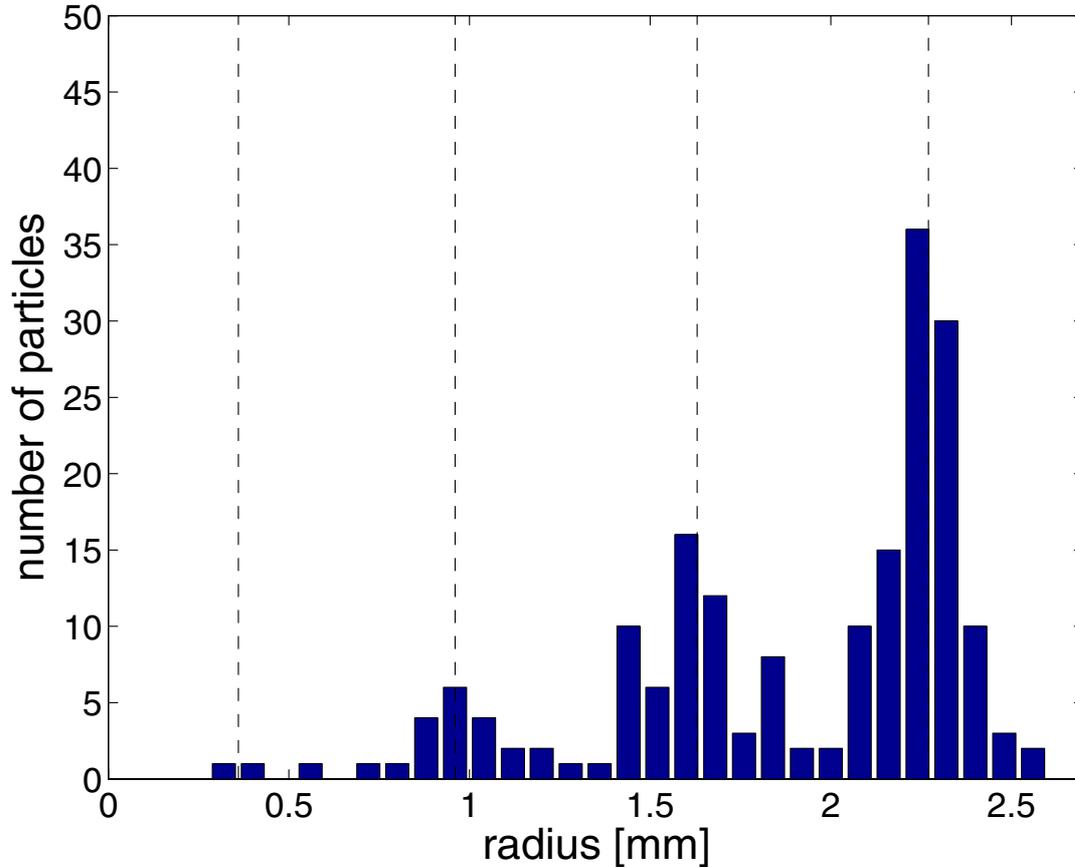
Figure 3. (Color online) Experimental radial particle distribution of a particle cluster with 190 particles.

3. Theory

3.1. Model

To model 3D Coulomb clusters confined in a 3D isotropic harmonic trap we consider N classical particles with equal charge q and mass m interacting via the Coulomb potential. The corresponding Hamilton function is

$$H_N = \sum_{i=1}^{N} \frac{m}{2}\dot{r}_i^{\,2} + \sum_{i=1}^{N} \frac{m}{2}\omega^2 r_i^2 + \sum_{i>j}^{N} \frac{q^2}{4\pi\varepsilon|\mathbf{r}_i - \mathbf{r}_j|}, \tag{1}$$

where ω is the strength of the confinement potential. In what follows below we will use dimensionless lengths and energies by introducing $r_0 = (q^2/2\pi\varepsilon m\omega^2)^{1/3}$ and $E_0 = (m\omega^2 q^4/32\pi^2\varepsilon^2)^{1/3}$. The length r_0 is the stable distance of two particles confined in the considered potential, E_0 denotes their ground state energy.

3.2. MD-Simulation

Three-dimensional classical Coulomb clusters in a spherical parabolic trap have been investigated earlier by different authors with different numerical methods. Rafac et al. [15] simulated the clusters with $N \leq 27$ using MC techniques. An extended table with $N \leq 59$ was given by Tsuruta et al. [16]. The work of Hasse et al. [18] the number of charged particles was increased up to a few
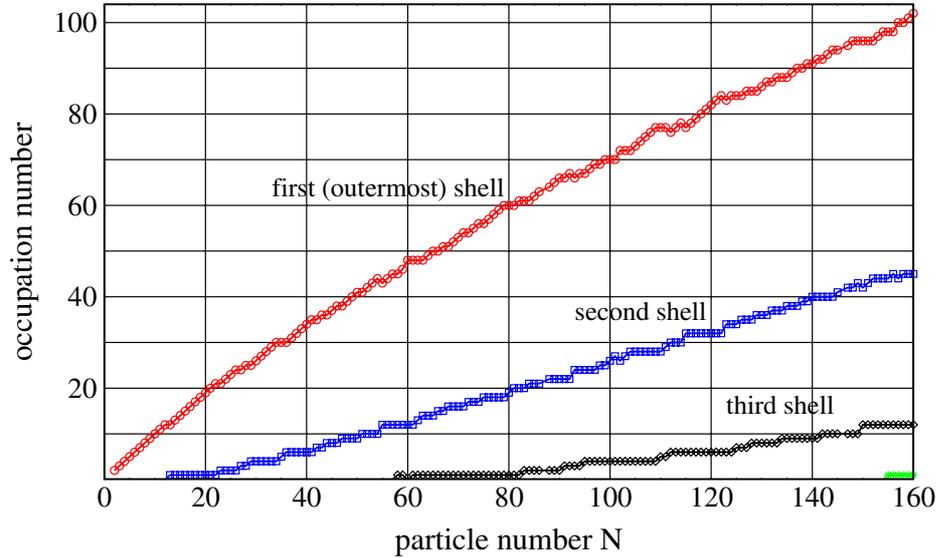
Figure 4. (Color online) Number of particles N_s on shell s vs. N. The 2nd shell is opened at $N = 13$, the 3rd shell at $N = 58$ (and $N = 61$), the 4th shell at $N = 155$. Note the reoccurrence of two shells at $N = 60$.

thousand. But they did not found the true ground state configurations for $N = 28 - 31, 44, 45$ and for clusters with more than 63 particles, due to accuracy limited calculation. To find the ground and metastable states, we used classical molecular dynamics (MD) together with a suitable *simulated annealing* method [10]. Starting with a random initial configuration of N particles, the system is cooled continuously until all momenta are zero and the particles settle in the minima of the potential energy surface. Depending on the particle number, the cooling down process was repeated up to several thousand times until every of the computed low energy states was found more than a given number of times (typically $10 \dots 100$) assuring a high probability that also the ground state has been found. Crucial for a high search efficiency is the use of an optimized MD time step (it has to be chosen not too small to avoid trapping in local potential minima). The complete results for $N = 2 \cdots 160$ are given in Table 1 in the Appendix.

3.3. Cluster characterization

At zero temperature (zero particle velocities $\dot{r}_i$,) concentric shells are found with characteristic closures as well as *magic* clusters. The stability of clusters is characterized by the *binding energy* [16]:

$$\Delta_2(N) = E(N + 1) + E(N - 1) - 2E(N). \tag{2}$$

The symmetry within the shells can be analyzed by performing a Voronoi analysis [10], i.e. by constructing polygons around each particle formed by the lines equally bisecting nearest-neighbor pairs on the shell. To quantify this topological criterion, we introduce the *Voronoi symmetry parameter* defined as
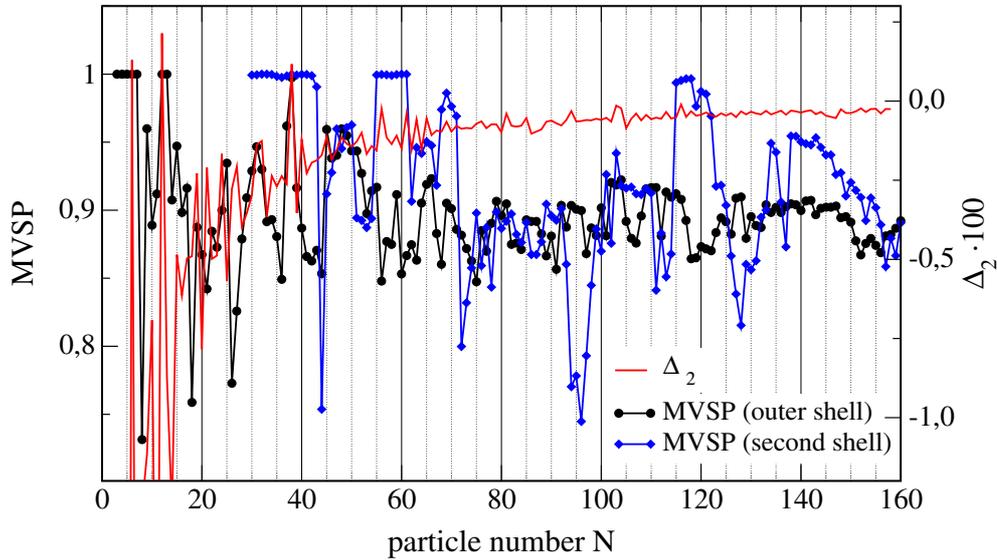
Figure 5. (Color online) Binding energy Δ_2 (Eq. 2) and mean Voronoi symmetry parameter MVSP (Eq. 4) of the two outermost shells vs. particle number N. Magic clusters are $N = 4, 6, 10, 12, 19, 32, 38, 56$ [16] and $N = 81, 94, 103, 116$ [10].

$$G_M = \frac{1}{N_M} \sum_{j=1}^{N_M} \frac{1}{M} \left| \sum_{k=1}^{M} e^{iM\theta_{jk}} \right|. \tag{3}$$

Here N_M denotes the number of particles on the shell, each of which is surrounded by a Voronoi polygon of order M (M nearest neighbors), and θ_{jk} is the angle between the j-th particle and its k-th nearest neighbor. A value $G_5 = 1$ ($G_6 = 1$) means that all pentagons (hexagons) are perfect, the reduction of G_M below 1 is a measure of their distortion. The Voronoi symmetry parameter G_M gives a measure for the symmetry of the Voronoi polygons of order M. To quantify the symmetry of the whole shell we introduce the *mean Voronoi symmetry parameter* (MVSP). We define the *mean Voronoi symmetry parameter* $\langle G^{(s)} \rangle$ of the s-th shell of the cluster as

$$\langle G^{(s)} \rangle = \frac{1}{N_s} \sum_M N_M G_M^{(s)}, \tag{4}$$

where N_s denotes the number of all particles on shell s. The MVSP allows to compare clusters with the same shell configuration because this parameter is very sensitive to the position of the particles within the cluster.
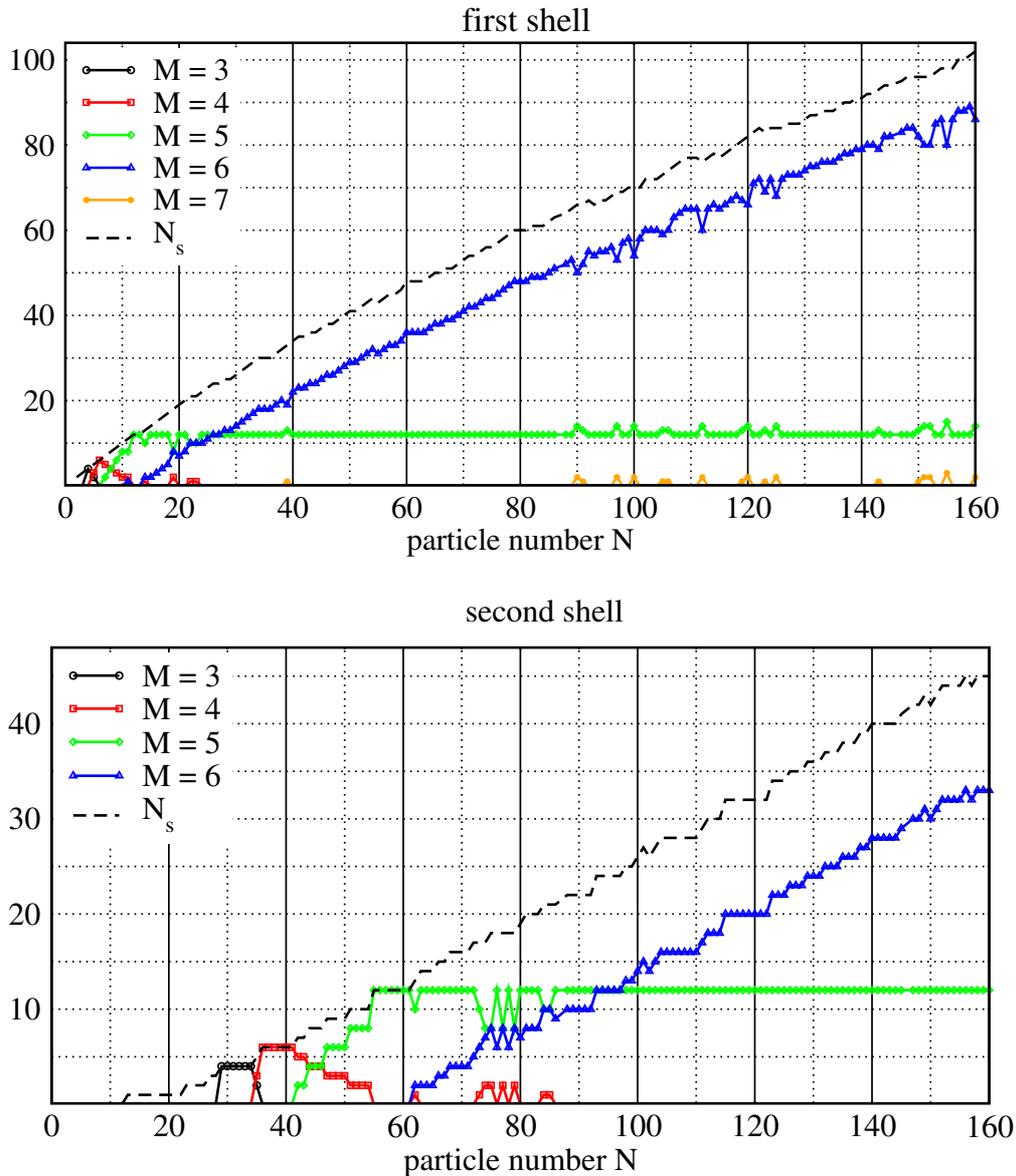
Figure 6. (Color online) Number N_M of Voronoi polygons with M edges in the two outermost shells vs. total particle number N. The top figure shows the first (outermost) shell and the bottom figure the second shell.

3.4. Analysis of 3D Coulomb Clusters

Figure 4 shows the number of particles on different shells of the Coulomb clusters as a function of the total particle number. The figure is easy to understand. For $N \leq 12$ all particles occupy one shell. With $N = 12$, the shell is filled completely (closed shell). The 13th particle opens a new shell, i.e. one particle from the outer shell goes inside. Analogously, the 2nd shell is closed when it contains 12 particles (for $N = 57$), and the 3rd shell is closed for $N = 154$, see table 1.

The existence of the shell structure is a marked peculiarity of mesoscopic Coulomb systems, and is, of course, caused by the spherical confinement potential. With increasing N the structure of a macroscopic system emerges gradually, see also Ref. [19]. The effect of the confinement is

strongest at the cluster boundary, i.e. in the outer shell, whereas the inner shells are partially shielded from the trap potential by the surrounding particle shells. Therefore, bulk properties start to emerge in the center. This trend is, in fact, clearly seen already for $N \leq 200$ by comparing the widths of the shells [10], see table 1.

For the clusters ($N = 2 \ldots 160$) Fig. 5 shows the binding energy Δ_2 (Eq. 2) of the clusters and the MVSP (Eq. 4) of the two outermost shells vs. the particle number. With the help of these two quantities one can identify the so-called *magic clusters*, which are particularly stable. The combination of these quantities (a peak in Δ_2 and a higher MVSP in the shells) allows us to identify magic clusters: $N = 4, 6, 10, 12, 19, 32, 38, 56$ [16] and $N = 81, 94, 103, 116$ [10].

Now we analyze the symmetry of the clusters in more detail. Figure 6 shows the number of Voronoi polygons with M edges on the two outermost shells vs. total particle number. The dashed line in the figures gives the number of particles on the shell. With increasing size the particle number in the shell is increasing too. For smaller particle numbers in the shell we observe polygons with $M = 3, 4$. With increasing particle numbers one can see an increase of the number of polygons with $M = 6$, the number of polygons with $M = 5$ grows up to 12 and is then nearly constant. In each case Euler's theorem $\sum_{M(M \geq 3)} (6 - M) N_M = 12$ is fulfilled.

3.5. Cluster Fine Structure

An interesting observation is that the simulations frequently yield for the same shell configuration different values of the total energy, see e.g. [10]. The differences are much larger than the simulation error, moreover, the energies are reproducible. Obviously the state of a cluster is not completely determined by its shell configuration (contrary to the 2D case). There exist further (excited) states, which have the same shell configuration as the ground state, but a *different particle arrangement and symmetry within one shell*. This can be called *fine structure*. To understand the differences in the structure of these states with same shell configuration we analyze the intrashell symmetry by a Voronoi analysis, i.e. by constructing polygons around a given particle formed by the planes equally bisecting nearest-neighbor pairs on the shell (cf. the example of $N = 17$ shown in Fig. 7). Interestingly, both states do not differ with respect to the number of polygons of each kind in the outer shell: there are $N_5 = 12$ pentagons and $N_6 = 4$ hexagons. Rather the *arrangement of the polygons* is different. In one case, the four hexagons form a perfect tetrahedron ABCD and are separated from each other by pentagons, cf. Fig. 7 (left), in the other case two pairs of hexagons touch, see Fig. 7 (right) and the tetrahedron is distorted (Fig. 8). Two edges remain practically constant ($\overline{AB} \approx \overline{CD} \approx 1.63$), but the edge $\overline{AB}$ rotates with respect to the first case by an angle of 34 degrees resulting in a reduction of edges $\overline{BC}$ and $\overline{AD}$ to about 1.24 while $\overline{AC}$ and $\overline{BD}$ increase to 1.94. Comparing the energies of the two configurations we conclude that the state with the more symmetric arrangement of the Voronoi polygons, i.e. (Fig. 7, left), has the lower energy.

4. Summary and Outlook

In this contribution we have presented numerical simulation results for spherical Coulomb clusters with $N \leq 160$. The observed lowest energy states for $N \geq 60$ are, in most cases, lower than those previously reported and should be reliable baring points for experiments with classical Coulomb balls in dusty plasmas or ultracold ions. Moreover, the shell configurations detected are expected to be important also for quantum Coulomb clusters (e.g. in quantum dots) in the strong coupling limit, as for 2D systems it was found that in most cases they have the same shell configuration as their classical counterpart [14, 17]. In addition we performed an analysis of the lowest excited states of small clusters. Besides metastable states with a shell structure different from the ground state we identified *fine structure* states which are characterized by different particle arrangement within the shells. These states have a lower symmetry which is

Ground state (16,1)

$$E/N = 6.388610$$
$$r_1 = 1.5042$$
$$G_5 = 0.891 \quad [12]$$
$$G_6 = 0.993 \quad [4]$$
$$\langle G^{(1)}\rangle = 0.916$$

First meta-stable state (16,1)

$$E/N = 6.388975$$
$$r_1 = 1.5042$$
$$G_5 = 0.746 \quad [12]$$
$$G_6 = 0.884 \quad [4]$$
$$\langle G^{(1)}\rangle = 0.781$$
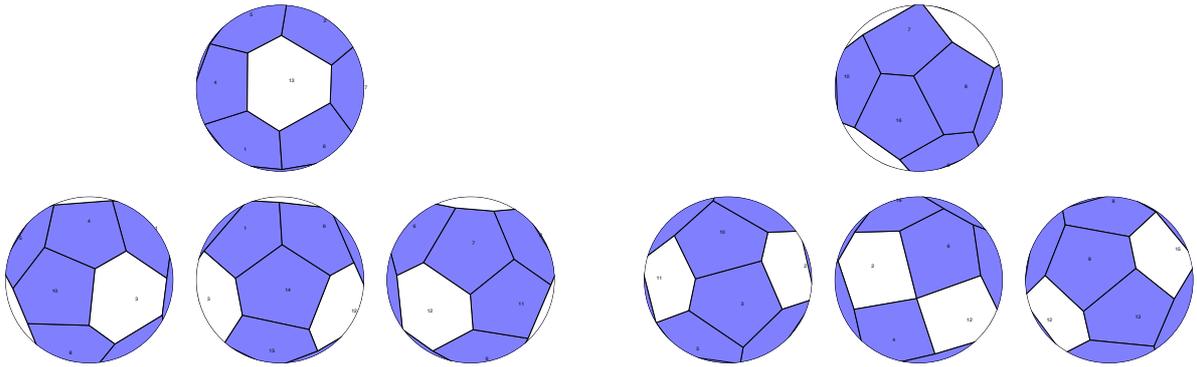
Figure 7. (Color online) Voronoi construction for the cluster $N = 17$. The two energetically lowest states with shell configuration $N = \{1, 16\}$ are shown. White (dark) areas are hexagons (pentagons) – indicating the number of nearest neighbors of the corresponding particle. Left: ground state, right: first excited (*fine structure*) state. Above the figures the energies, radius of the shell r_1 and the symmetry parameters are given.
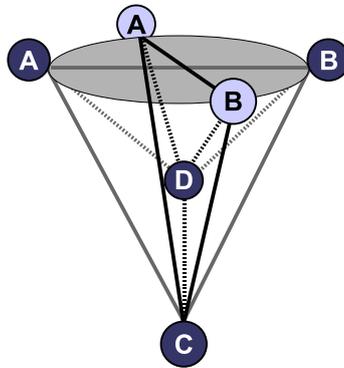
Figure 8. (Color online) Arrangement of the four particles surrounded by hexagons – the two states differ by rotation of the edge AB. Dark (bright) circles corresponds to the configuration shown in Fig. 7, left (right).

linked to higher values of the total energy. Despite the decreasing values of the excitation energy with increasing N, knowledge of the lowest metastable states is important for understanding the dynamic properties of mesoscopic clusters.

From the experemental point of view creation of spherical particle clouds consisting of a relatively large number of charged particles (of order 100 and higher) is rather easily achieved. Creation of small clusters with a predefined number of particles is still under implementation in the experiment. On the other hand, computer simulations become very time consuming for $N > 200$. First preliminary comparisons of experiments and theory show good qualitative agreement of the shell structure of the cluster $N = 190$. The agreement is further improved if a statically screened Coulomb potential (i.e. Yukawa potential) is used instead of the bare Coulomb interaction [20]. However, extensive further comparisons for various N are necessary.

References

[1] Morfill G.E. and Kersten H 2003 *New J. Phys.* **5**
[2] Dubin D H E and O'Neill T M 1999 *Rev. Mod. Phys.* **71** 87
[3] Itano W M, Bollinger J J, Tan J N, Jelenkovic B and Wineland D J 1998 *Science* **297** 686
[4] Thomas H, Morfill G E, Demmel V, Goree J, Feuerbacher B and Möhlmann D 1994 *Phys. Rev. Lett.* **73** 652
[5] Hayashi Y and Tachibana K 1994 *Jpn. J. Appl. Phys.* **33** L804
[6] Melzer A, Schweigert V and Piel A 2000 *Phys. Scripta* **61** 494
[7] Rothermel H, Hagl T, Morfill G E, Thoma M H and Thomas H M 2002 *Phys. Rev. Lett.* **89** 175001
[8] Morfill G E, Thomas H M, Konopka U, Rothermel H, Zuzic M, Ivlev A and Goree J 1999 *Phys. Rev. Lett.* **83** 1598
[9] Arp O, Block D, Melzer A and Piel A 2004 *Phys. Rev. Lett.* **93** 165004
[10] Ludwig P, Kosse S and Bonitz M 2005 *Phys. Rev.* E accepted (*Preprint* arXiv:physics/0409095)
[11] Trottenberg T, Melzer A and Piel A 1995 *Plasma Sources Sci. Technol.* **4** 450
[12] Homann A, Melzer A, Madani R and Piel A 1998 *Phys. Lett.* A **242** 173
[13] Klindworth M, Melzer A, Piel A and Schweigert V 1999 *Phys. Rev.* B. **61** 3194
[14] Ludwig P, Filinov A V, Bonitz M and Lozovik Yu E 2003 *Contrib. Plasma Phys.* **43** 285
[15] Rafac R, Schiffer J P, Hangst J S, Dubin D H E and Wales D J 1991 *Proc. Natl. Acad.Sci. USA* **88** 483
[16] Tsuruta K and Ichimaru S 1993 *Phys. Rev.* A **48** 1339
[17] Filinov A V, Bonitz M and Lozovik Yu E 2001 *Phys. Rev. Lett.* **86** 3851
[18] Hasse R W, Avilov V V 1991 *Phys. Rev.* A **44** 4506
[19] Schiffer J P 2002 *Phys. Rev. Lett.* **88** 205003
[20] Ludwig P, Golubnichiy V and Bonitz M, unpublished

Appendix

Table 1. Ground state shell configurations, energy per particle, mean shell radii $r_{1,2,3,4}$ and widths $\sigma_{1,2,3,4}$

N	Config.	E/N	r_1	r_2	σ_1	σ_2
2	(2)	0.5	0.500(0)	-	0.000(0)	-
3	(3)	1.310370(7)	0.660(9)	-	0.000(0)	-
4	(4)	1.785826(2)	0.771(5)	-	0.000(0)	-
5	(5)	2.245187(2)	0.865(1)	-	0.010(0)	-
6	(6)	2.654039(0)	0.940(6)	-	0.000(0)	-
7	(7)	3.064186(0)	1.010(6)	-	0.013(5)	-
8	(8)	3.443409(4)	1.071(4)	-	0.000(0)	-
9	(9)	3.809782(0)	1.126(9)	-	0.006(3)	-
10	(10)	4.164990(0)	1.178(3)	-	0.005(5)	-
11	(11)	4.513275(4)	1.226(5)	-	0.010(1)	-
12	(12)	4.838966(4)	1.270(0)	-	0.000(0)	-
13	(12, 1)	5.166798(3)	1.365(9)	-	0.000(0)	-
14	(13, 1)	5.485915(4)	1.403(3)	0.007(1)	0.005(8)	-
15	(14, 1)	5.792094(2)	1.438(3)	0.000(0)	0.005(6)	-
16	(15, 1)	6.093421(3)	1.471(9)	0.000(0)	0.005(2)	-
17	(16, 1)	6.388609(9)	1.504(2)	0.000(0)	0.006(2)	-
18	(17, 1)	6.678830(3)	1.535(3)	0.000(0)	0.000(6)	-
19	(18, 1)	6.964146(0)	1.565(4)	0.000(0)	0.004(0)	-
20	(19, 1)	7.247181(0)	1.594(6)	0.000(2)	0.006(9)	-
21	(20, 1)	7.522377(7)	1.622(6)	0.000(0)	0.003(4)	-
22	(21, 1)	7.795468(9)	1.649(9)	0.000(7)	0.006(3)	-
23	(21, 2)	8.063575(4)	1.707(7)	0.530(2)	0.030(2)	-
24	(22, 2)	8.326802(8)	1.732(6)	0.526(0)	0.029(4)	0.009(2)
25	(23, 2)	8.588360(7)	1.757(0)	0.526(2)	0.026(3)	0.000(0)
26	(24, 2)	8.844236(2)	1.780(5)	0.524(1)	0.026(3)	0.000(8)
27	(24, 3)	9.097334(6)	1.830(5)	0.689(8)	0.036(9)	0.009(6)
28	(25, 3)	9.348367(8)	1.852(5)	0.688(9)	0.036(4)	0.001(6)
29	(25, 4)	9.595435(1)	1.899(2)	0.798(7)	0.037(4)	0.011(9)
30	(26, 4)	9.838964(7)	1.919(7)	0.796(1)	0.034(7)	0.018(0)
31	(27, 4)	10.079511(0)	1.939(9)	0.792(6)	0.038(3)	0.007(1)
32	(28, 4)	10.318678(8)	1.959(6)	0.793(5)	0.033(8)	0.000(0)
33	(29, 4)	10.556587(1)	1.979(1)	0.791(4)	0.034(6)	0.010(7)
34	(30, 4)	10.790841(9)	1.998(0)	0.790(1)	0.035(8)	0.000(0)
35	(30, 5)	11.022731(0)	2.038(1)	0.885(9)	0.041(0)	0.038(0)
36	(30, 6)	11.251922(6)	2.077(5)	0.958(2)	0.035(3)	0.000(0)
37	(31, 6)	11.478747(2)	2.094(7)	0.958(5)	0.035(8)	0.017(8)
38	(32, 6)	11.702951(6)	2.111(9)	0.954(9)	0.039(4)	0.000(0)
39	(33, 6)	11.928322(8)	2.128(9)	0.954(9)	0.035(2)	0.012(0)
40	(34, 6)	12.150162(9)	2.145(3)	0.954(7)	0.038(0)	0.011(8)
41	(35, 6)	12.370791(5)	2.161(8)	0.953(8)	0.035(4)	0.006(4)
42	(35, 7)	12.589139(3)	2.196(1)	1.026(0)	0.040(6)	0.050(7)
43	(36, 7)	12.805545(2)	2.211(9)	1.025(2)	0.037(4)	0.045(6)
44	(36, 8)	13.020077(9)	2.245(4)	1.084(5)	0.038(0)	0.013(2)
45	(37, 8)	13.232901(2)	2.260(3)	1.084(5)	0.038(0)	0.034(0)

Continuation of Table 1

N	Config.	E/N	r_1	r_2	r_3	σ_1	σ_2	σ_3
46	(38, 8)	13.444601(5)	2.275(1)	1.084(2)	-	0.036(4)	0.037(3)	-
47	(38, 9)	13.654458(5)	2.306(6)	1.139(1)	-	0.034(0)	0.048(8)	-
48	(39, 9)	13.862762(0)	2.321(0)	1.137(9)	-	0.033(0)	0.036(2)	-
49	(40, 9)	14.069919(9)	2.335(1)	1.137(1)	-	0.034(1)	0.035(4)	-
50	(41, 9)	14.275728(5)	2.349(0)	1.137(2)	-	0.036(8)	0.026(7)	-
51	(41, 10)	14.480101(0)	2.378(8)	1.187(7)	-	0.035(2)	0.029(8)	-
52	(42, 10)	14.683192(6)	2.392(2)	1.187(5)	-	0.034(0)	0.029(4)	-
53	(43, 10)	14.885283(9)	2.405(5)	1.187(2)	-	0.037(5)	0.029(5)	-
54	(44, 10)	15.085702(8)	2.418(6)	1.187(2)	-	0.035(2)	0.024(5)	-
55	(43, 12)	15.284702(6)	2.461(8)	1.277(3)	-	0.031(8)	0.010(1)	-
56	(44, 12)	15.482144(4)	2.474(3)	1.278(0)	-	0.036(9)	0.010(1)	-
57	(45, 12)	15.679350(2)	2.486(9)	1.276(3)	-	0.036(3)	0.007(2)	-
58	(45, 12, 1)	15.875406(2)	2.512(6)	1.376(5)	0.005(2)	0.046(3)	0.004(3)	-
59	(46, 12, 1)	16.070103(4)	2.524(7)	1.376(4)	0.000(0)	0.048(0)	0.000(0)	-
60	(48, 12)	16.263707(3)	2.523(6)	1.275(5)	-	0.036(0)	0.003(6)	-
61	(48, 12, 1)	16.455812(8)	2.548(8)	1.375(1)	0.004(2)	0.045(1)	0.002(4)	-
62	(48, 13, 1)	16.647519(7)	2.573(8)	1.413(4)	0.016(3)	0.044(3)	0.023(5)	-
63	(48, 14, 1)	16.837694(0)	2.598(8)	1.447(3)	0.004(6)	0.039(3)	0.024(7)	-
64	(49, 14, 1)	17.027288(9)	2.610(1)	1.447(8)	0.001(9)	0.037(3)	0.023(7)	-
65	(50, 14, 1)	17.215360(8)	2.621(2)	1.447(7)	0.000(0)	0.049(5)	0.018(8)	-
66	(50, 15, 1)	17.402891(3)	2.645(3)	1.480(5)	0.005(9)	0.043(2)	0.026(6)	-
67	(51, 15, 1)	17.589347(4)	2.656(3)	1.480(3)	0.004(6)	0.043(0)	0.024(3)	-
68	(51, 16, 1)	17.774874(4)	2.679(7)	1.512(3)	0.003(4)	0.034(5)	0.031(1)	-
69	(52, 16, 1)	17.959432(2)	2.690(3)	1.512(6)	0.001(0)	0.039(3)	0.034(3)	-
70	(53, 16, 1)	18.143338(3)	2.701(0)	1.511(9)	0.002(3)	0.041(1)	0.031(7)	-
71	(54, 16, 1)	18.326281(9)	2.711(6)	1.511(8)	0.008(3)	0.041(2)	0.028(0)	-
72	(54, 17, 1)	18.508444(3)	2.734(2)	1.542(3)	0.005(9)	0.035(3)	0.020(1)	-
73	(55, 17, 1)	18.689729(4)	2.744(5)	1.542(2)	0.004(7)	0.037(5)	0.020(4)	-
74	(56, 17, 1)	18.870167(9)	2.754(6)	1.542(3)	0.008(8)	0.042(2)	0.017(8)	-
75	(56, 18, 1)	19.049742(1)	2.776(5)	1.571(7)	0.005(5)	0.037(2)	0.031(8)	-
76	(57, 18, 1)	19.228600(2)	2.786(5)	1.571(4)	0.000(0)	0.037(2)	0.025(3)	-
77	(58, 18, 1)	19.406816(5)	2.796(4)	1.571(4)	0.003(3)	0.038(5)	0.031(4)	-
78	(59, 18, 1)	19.584175(2)	2.806(3)	1.571(5)	0.004(6)	0.039(8)	0.027(1)	-
79	(60, 18, 1)	19.760799(9)	2.816(1)	1.570(9)	0.005(0)	0.040(2)	0.027(4)	-
80	(60, 19, 1)	19.936689(9)	2.837(0)	1.600(2)	0.003(0)	0.038(4)	0.038(4)	-
81	(60, 20, 1)	20.111592(4)	2.857(7)	1.627(1)	0.006(4)	0.031(1)	0.040(6)	-
82	(61, 20, 1)	20.286103(1)	2.867(1)	1.627(4)	0.005(0)	0.031(1)	0.040(6)	-
83	(61, 20, 2)	20.459834(2)	2.886(6)	1.688(6)	0.544(7)	0.039(0)	0.061(9)	0.044(5)
84	(61, 21, 2)	20.632758(9)	2.906(4)	1.714(0)	0.542(6)	0.034(1)	0.069(2)	0.003(3)
85	(62, 21, 2)	20.804907(5)	2.915(6)	1.713(5)	0.542(2)	0.038(6)	0.063(9)	0.021(7)
86	(63, 21, 2)	20.976517(8)	2.924(7)	1.713(8)	0.540(3)	0.041(2)	0.061(4)	0.009(6)
88	(64, 22, 2)	21.317682(0)	2.953(2)	1.737(8)	0.538(5)	0.033(9)	0.059(1)	0.005(7)
89	(65, 22, 2)	21.487369(1)	2.962(1)	1.737(8)	0.537(5)	0.034(4)	0.057(0)	-
90	(66, 22, 2)	21.656403(7)	2.970(9)	1.737(6)	0.535(9)	0.037(4)	0.057(5)	-

Continuation of Table 1

N	Config.	E/N	r_1	r_2	r_3	σ_1	σ_2	σ_3
91	(66, 22, 3)	21.824823(2)	2.989(1)	1.791(6)	0.705(0)	0.043(4)	0.066(7)	0.004(0)
92	(67, 22, 3)	21.992541(8)	2.997(9)	1.791(1)	0.705(2)	0.044(4)	0.064(9)	0.015(2)
93	(66, 24, 3)	22.159489(7)	3.026(0)	1.836(1)	0.701(9)	0.035(8)	0.078(1)	0.013(0)
94	(67, 24, 3)	22.325841(4)	3.034(7)	1.835(6)	0.700(1)	0.034(9)	0.068(3)	0.019(6)
95	(67, 24, 4)	22.491878(2)	3.052(2)	1.884(8)	0.808(9)	0.035(3)	0.067(7)	0.021(5)
96	(68, 24, 4)	22.657270(6)	3.060(6)	1.884(6)	0.808(3)	0.040(8)	0.067(5)	0.033(0)
97	(69, 24, 4)	22.822032(2)	3.068(7)	1.884(9)	0.809(5)	0.046(1)	0.067(8)	0.029(9)
98	(69, 25, 4)	22.986199(1)	3.086(4)	1.905(5)	0.808(1)	0.035(7)	0.075(0)	0.028(0)
99	(70, 25, 4)	23.149758(0)	3.094(5)	1.905(6)	0.807(1)	0.043(0)	0.072(2)	0.027(9)
100	(70, 26, 4)	23.312759(3)	3.111(7)	1.925(9)	0.805(5)	0.041(7)	0.074(0)	0.022(6)
101	(70, 27, 4)	23.475164(4)	3.129(1)	1.945(0)	0.802(8)	0.030(1)	0.073(1)	0.005(8)
102	(72, 26, 4)	23.637044(1)	3.128(0)	1.924(8)	0.805(2)	0.043(3)	0.071(0)	0.018(9)
103	(72, 27, 4)	23.798274(3)	3.145(1)	1.944(3)	0.801(7)	0.037(7)	0.071(2)	0.008(2)
104	(72, 28, 4)	23.959361(3)	3.161(7)	1.964(1)	0.802(1)	0.034(5)	0.078(1)	0.001(9)
105	(73, 28, 4)	24.120222(9)	3.169(6)	1.964(1)	0.802(0)	0.036(3)	0.076(8)	0.010(2)
106	(74, 28, 4)	24.280223(2)	3.177(3)	1.964(2)	0.802(3)	0.038(7)	0.077(2)	0.009(2)
107	(75, 28, 4)	24.439665(7)	3.185(0)	1.964(0)	0.801(0)	0.040(4)	0.074(4)	0.006(7)
108	(76, 28, 4)	24.598713(7)	3.192(7)	1.964(0)	0.800(7)	0.041(0)	0.072(3)	0.005(3)
109	(77, 28, 4)	24.757151(3)	3.200(5)	1.963(8)	0.800(6)	0.040(6)	0.070(5)	0.003(4)
110	(77, 28, 5)	24.915153(9)	3.216(3)	2.006(3)	0.896(1)	0.043(5)	0.076(3)	0.041(5)
111	(77, 29, 5)	25.072584(2)	3.232(2)	2.024(9)	0.896(9)	0.040(9)	0.081(7)	0.030(3)
112	(76, 30, 6)	25.229492(1)	3.255(4)	2.085(7)	0.967(0)	0.035(8)	0.095(0)	0.041(7)
113	(77, 30, 6)	25.385842(0)	3.263(7)	2.083(1)	0.964(0)	0.036(8)	0.073(2)	0.016(9)
114	(78, 30, 6)	25.541848(2)	3.271(1)	2.082(9)	0.964(0)	0.036(6)	0.074(5)	0.009(6)
115	(77, 32, 6)	25.697308(2)	3.294(9)	2.116(2)	0.963(0)	0.026(6)	0.077(4)	0.004(4)
116	(78, 32, 6)	25.852252(8)	3.302(2)	2.115(9)	0.963(3)	0.021(8)	0.076(0)	0.004(5)
117	(79, 32, 6)	26.007089(4)	3.309(4)	2.115(8)	0.962(2)	0.032(4)	0.075(3)	0.005(0)
118	(80, 32, 6)	26.161426(8)	3.316(7)	2.115(5)	0.961(3)	0.028(6)	0.068(5)	0.007(1)
119	(81, 32, 6)	26.315442(5)	3.323(7)	2.115(6)	0.962(4)	0.036(8)	0.069(8)	0.003(1)
120	(82, 32, 6)	26.468996(0)	3.330(8)	2.115(7)	0.962(0)	0.037(4)	0.070(2)	0.004(0)
121	(83, 32, 6)	26.622118(4)	3.337(9)	2.115(4)	0.961(4)	0.038(1)	0.067(6)	0.002(8)
122	(84, 32, 6)	26.774879(2)	3.344(9)	2.115(5)	0.962(0)	0.039(8)	0.068(5)	0.003(7)
123	(83, 34, 6)	26.927194(9)	3.367(2)	2.149(3)	0.962(5)	0.036(7)	0.085(6)	0.004(3)
124	(84, 34, 6)	27.079019(5)	3.374(1)	2.149(1)	0.962(7)	0.034(4)	0.086(7)	0.009(6)
125	(84, 34, 7)	27.230457(6)	3.388(4)	2.185(0)	1.034(0)	0.035(9)	0.085(2)	0.062(7)
126	(84, 35, 7)	27.381438(1)	3.402(7)	2.200(9)	1.034(1)	0.036(9)	0.089(2)	0.067(6)
127	(85, 35, 7)	27.532034(0)	3.409(4)	2.201(4)	1.034(0)	0.040(1)	0.091(0)	0.042(8)
128	(85, 35, 8)	27.682123(2)	3.423(5)	2.235(8)	1.092(2)	0.040(7)	0.083(2)	0.036(8)
129	(85, 36, 8)	27.831888(6)	3.437(9)	2.250(2)	1.091(9)	0.032(8)	0.081(5)	0.034(1)
130	(86, 36, 8)	27.981234(3)	3.444(5)	2.250(1)	1.091(7)	0.035(2)	0.083(2)	0.048(8)
131	(87, 36, 8)	28.130244(0)	3.451(3)	2.249(8)	1.090(9)	0.034(2)	0.078(5)	0.030(5)
132	(87, 37, 8)	28.278862(5)	3.465(1)	2.264(9)	1.090(5)	0.034(4)	0.081(8)	0.014(0)
133	(88, 37, 8)	28.427061(5)	3.471(8)	2.264(2)	1.091(2)	0.035(5)	0.085(7)	0.013(4)
134	(88, 37, 9)	28.574953(4)	3.485(5)	2.297(0)	1.144(0)	0.031(2)	0.071(5)	0.054(1)
135	(88, 38, 9)	28.722421(1)	3.499(2)	2.311(0)	1.143(6)	0.030(2)	0.073(9)	0.048(8)

Continuation of Table 1

N	Config.	E/N	r_1	r_2	r_3	σ_1	σ_2	σ_3
136	(89, 38, 9)	28.869526(8)	3.505(4)	2.311(2)	1.144(0)	0.031(5)	0.078(7)	0.043(7)
137	(90, 38, 9)	29.016328(0)	3.511(9)	2.311(0)	1.144(0)	0.033(4)	0.078(9)	0.040(2)
138	(90, 39, 9)	29.162701(3)	3.525(4)	2.325(1)	1.143(3)	0.029(9)	0.080(5)	0.037(0)
139	(91, 39, 9)	29.308773(6)	3.531(6)	2.325(1)	1.143(0)	0.034(2)	0.085(7)	0.034(9)
140	(91, 40, 9)	29.454518(1)	3.544(9)	2.339(1)	1.142(9)	0.029(5)	0.084(2)	0.042(4)
141	(92, 40, 9)	29.599899(6)	3.551(4)	2.338(7)	1.141(7)	0.033(5)	0.075(1)	0.038(4)
142	(92, 40, 10)	29.744962(8)	3.564(4)	2.368(9)	1.193(0)	0.034(1)	0.070(0)	0.045(4)
143	(93, 40, 10)	29.889733(5)	3.570(7)	2.368(9)	1.193(2)	0.031(4)	0.071(4)	0.032(2)
144	(94, 40, 10)	30.034090(4)	3.576(9)	2.368(8)	1.193(1)	0.033(1)	0.070(7)	0.055(2)
145	(94, 41, 10)	30.178106(2)	3.589(8)	2.382(5)	1.192(0)	0.035(8)	0.071(2)	0.034(8)
147	(95, 42, 10)	30.465219(1)	3.608(7)	2.395(7)	1.192(3)	0.029(9)	0.079(4)	0.039(4)
148	(96, 42, 10)	30.608238(9)	3.614(8)	2.395(5)	1.192(3)	0.030(6)	0.078(8)	0.036(7)
149	(96, 43, 10)	30.750998(2)	3.627(3)	2.409(0)	1.192(6)	0.032(3)	0.085(3)	0.037(6)
150	(96, 42, 12)	30.893383(1)	3.639(5)	2.454(1)	1.281(6)	0.034(8)	0.079(5)	0.010(3)
151	(96, 43, 12)	31.035390(0)	3.652(4)	2.465(9)	1.281(4)	0.027(1)	0.068(5)	0.014(6)
152	(96, 44, 12)	31.177075(2)	3.664(9)	2.478(3)	1.281(1)	0.031(1)	0.067(4)	0.016(5)
153	(97, 44, 12)	31.318527(6)	3.670(8)	2.478(1)	1.281(1)	0.028(2)	0.067(3)	0.012(9)
154	(98, 44, 12)	31.459632(1)	3.676(9)	2.477(7)	1.281(0)	0.026(3)	0.062(5)	0.014(4)

Continuation of Table 1

N	Config.	E/N	r_1	r_2	r_3	r_4
155	(98, 44, 12, 1)	31.600488(0)	3.688(7)	2.504(2)	1.384(6)	0.002(2)
156	(98, 45, 12, 1)	31.741100(1)	3.700(6)	2.516(9)	1.383(8)	0.012(7)
157	(100, 44, 12, 1)	31.881320(7)	3.700(4)	2.503(8)	1.383(9)	0.004(3)
158	(100, 45, 12, 1)	32.021293(6)	3.712(2)	2.516(6)	1.383(4)	0.004(3)
159	(101, 45, 12, 1)	32.161014(1)	3.718(0)	2.516(4)	1.383(7)	0.005(3)
160	(102, 45, 12, 1)	32.300404(8)	3.723(8)	2.516(1)	1.383(3)	0.007(3)

N			σ_1	σ_2	σ_3	σ_4
155			0.030(1)	0.079(9)	0.009(0)	-
156			0.033(3)	0.087(1)	0.006(2)	-
157			0.034(0)	0.076(2)	0.006(5)	-
158			0.032(7)	0.085(2)	0.006(3)	-
159			0.031(0)	0.088(1)	0.005(9)	-
160			0.034(1)	0.082(2)	0.005(2)	-

3.3 Structural Properties of Screened Coulomb Balls

Small three-dimensional strongly coupled charged particles in a spherical confinement potential arrange themselves in a nested shell structure. By means of experiments, computer simulations, and theoretical analysis, the sensitivity of their structural properties to the type of interparticle forces is explored. While the normalized shell radii are found to be independent of shielding, the shell occupation numbers are sensitive to screening and are quantitatively explained by an isotropic Yukawa model.

The results were published as refereed journal publication:

3.3.1 ***Structural Properties of Screened Coulomb Balls,***
M. Bonitz, D. Block, O. Arp, V. Golubnychiy, H. Baumgartner, P. Ludwig,
A. Piel, and A. Filinov, Physical Review Letters **96**, 075001 (2006)

PHYSICAL REVIEW LETTERS

Structural Properties of Screened Coulomb Balls

M. Bonitz,[1] D. Block,[2] O. Arp,[2] V. Golubnychiy,[1] H. Baumgartner,[1] P. Ludwig,[1] A. Piel,[2] and A. Filinov[1]

[1]*ITAP, Christian-Albrechts-Universität zu Kiel, D-24098 Kiel, Germany*
[2]*IEAP, Christian-Albrechts-Universität zu Kiel, D-24098 Kiel, Germany*
(Received 23 August 2005; published 21 February 2006)

Small three-dimensional strongly coupled charged particles in a spherical confinement potential arrange themselves in a nested shell structure. By means of experiments, computer simulations, and theoretical analysis, the sensitivity of their structural properties to the type of interparticle forces is explored. While the normalized shell radii are found to be independent of shielding, the shell occupation numbers are sensitive to screening and are quantitatively explained by an isotropic Yukawa model.

The recently discovered Coulomb balls [1] are an interesting new object for studying strongly coupled systems. Coulomb balls consist of hundreds of micrometer sized plastic spheres embedded in a gas plasma. The plastic spheres attain a high electric charge Q of the order of several thousand elementary charges and arrange themselves into a highly ordered set of nested spherical shells with hexagonal order inside the shells. Coulomb balls are a special form of 3D-plasma crystals [2–4]. The formation of ordered clusters with nested shells was also observed in laser-cooled trapped ion systems, e.g., [5,6], and is expected to occur in expanding neutral plasmas [7,8].

The same kind of ordering was found in molecular dynamics (MD) simulations, e.g., [9–11], and references therein. In particular, the transition to the macroscopic limit [12,13], the symmetry properties of the individual shells including a Voronoi analysis [10] and metastable intrashell configurations [11,14] have been analyzed. Very large systems of trapped ions show a transition to the crystal structure of bulk material, which was measured by laser scattering [15].

Although the shell structure of ion crystals is quite well understood in terms of simulation results, these systems do not yet allow for systematic experimental studies of the structure inside the shells and the detailed occupation numbers of individual shells. The advantage of studying Coulomb balls is the immediate access to the full three-dimensional structure of the nested shell system by means of video microscopy. The tracing of each individual particle is ensured by the high optical transparency of the system, which results from particle diameters of typically 5 μm at interparticle spacings of 500 μm. Compared to atomic particles, the very high mass of the microparticles used here slows down all dynamic phenomena to time scales ranging from 10 ms to seconds. Therefore, studies of Coulomb balls complement investigations of ion crystals, where dynamical studies are difficult.

Coulomb balls are in a strongly coupled state, i.e., the Coulomb coupling parameter, $\Gamma = Q^2/ak_BT$, where a is the mean interparticle distance, attains large values ($\Gamma \gg$

100). Contrary to ion crystals, where the particles interact via the pure Coulomb force, the microparticles in a Coulomb ball are expected to interact by a Yukawa type pair potential, $V_{dd} = (Q^2/r)e^{-r/\lambda_D}$, which was verified experimentally in complex plasmas [16]. Therefore, Coulomb balls are characterized by two parameters, the coupling parameter Γ and the Debye shielding length of the plasma λ_D. It is the intention of this paper to study the influence of shielding on the structure of Coulomb balls, in particular, to pin down the differences from systems with pure Coulomb interaction. This will be done by comparing computer simulations with experimental results. At the same time, a study of spherical crystals with Yukawa interaction opens up an interesting new field which in a natural way bridges the gap between the above mentioned theoretical investigations of finite size Coulomb systems and the theory of macroscopic Yukawa plasmas, e.g. [17,18].

Experiment.—The experiment is described in detail in Refs. [1,14,19], so here we only summarize the main results from a systematic investigation of 43 Coulomb balls consisting of 100 to 500 monodisperse and hence uniformly charged particles. All Coulomb balls were trapped under identical experimental conditions. All of them had a spherical shape and their diameter was in the range of 4–5 mm. A typical experimental result for a cluster and its shell structure is shown in the left part of Fig. 1. In all 43 Coulomb balls a similar shell structure was observed and the shell radii R_s and the shell occupation numbers N_s were measured. Further, from the pair correlation function the typical mean interparticle distance was derived, which for all N was close to $a \simeq 0.6$ mm. The mean intershell distance d was found to be $d = (0.86 \pm 0.06)a$, which is in good agreement with local icosahedral ordering [9]. An important experimental result is that the intershell distance is constant over the whole Coulomb ball and implies a constant average density of particles and ions, which is equivalent to a parabolic electric potential well used for the simulations below. A more detailed experimental verification of the parabolic confinement well is described else-
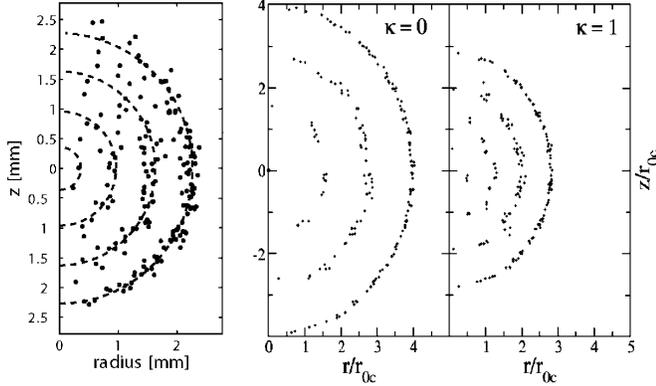
FIG. 1.   Radial particle distribution for $N = 190$ given in cylindrical coordinates. Left: experiment [1], right two figures: MD-simulation results with Coulomb ($\kappa = 0$), and Yukawa ($\kappa = 1$) potential. The shell occupation numbers are compiled in Table I.

where [19]. A different case with ''self-confinement'' of a dust cloud in a strongly anharmonic potential was recently discussed in [20].

Simulations.—For a theoretical explanation of the experimental results we have performed molecular dynamics and thermodynamic Monte Carlo (MC) simulations using the Hamiltonian

$$H = \sum_{i=1}^{N}\left\{\frac{p_i^2}{2m} + U_c(\mathbf{r}_i)\right\} + \frac{1}{2}\sum_{i \neq j} V_{dd}(\mathbf{r}_i - \mathbf{r}_j). \quad (1)$$

We assume that the Coulomb balls consist of particles with the same mass and charge and that a stationary state is reached close to thermodynamic equilibrium. Furthermore, the observed isotropic particle configuration suggests to use an isotropic interaction potential. Screening effects are included in static approximation using Debye(Yukawa)-type pair potentials V_{dd} given above. In the simulations we use dimensionless parameters, with lengths given in units of the ground state distance of two particles, r_{0c}, defined in Eq. (2), hence in this Letter $\kappa = r_{0c}/\lambda_D$. In experimental papers, $\kappa = a/\lambda_D$ is often used. In accordance with the experiment on Coulomb balls [19] and previous experiments and simulations on ion crystals [17], we use a screening-independent confinement potential $U_c(r) = m\omega^2 \cdot r^2/2$. As a result, in our model the configuration of the Coulomb balls is determined by three parameters: particle number N, screening parameter κ, and temperature T. Since experimental plasma densities and temperatures are not precisely known, we have performed a series of calculations for different values of κ and T. Furthermore, a wide range of particle numbers, up to $N = 503$, has been analyzed.

Results.—Consider first the theoretical ground state configurations ($T = 0$) in the case of Coulomb interaction, $\kappa = 0$, which were obtained by classical MD simulations using an optimized simulated annealing technique [11].

Using about 1000 independent runs for each value of N ensured that the ground state is reached. In addition, we have performed MC simulations in the canonic ensemble with a standard Metropolis algorithm, which allows for a rigorous account of finite temperature effects. Both simulations yield identical configurations at low temperature. Figure 1 shows a comparison of MD simulation and experiment for the case of $N = 190$ particles. In both cases four concentric spherical shells are observed, which are the result of a balance between confinement potential U_c and interparticle repulsion V_{dd}.

For a more detailed quantitative comparison between experiment and simulation we analyze the dependence of the shell radii R_s on the cluster size N (Fig. 2). The interparticle distance a serves as a common length scale as it is accessible in experiment and simulation. There is an overall increase $\propto N^{1/3}$ of the experimental R_s for all shells and all 43 analyzed clusters. Exceptions occur around values of N where new shells emerge. The same behavior is obtained from the MD simulations. Without any free parameter a very good agreement of experimental radii and Coulomb MD results (full lines) is observed, in particular, concerning the absolute values, the slope and the equidistance of the shells. Further, these results hold also in case of a Yukawa potential if κ is small (dashed lines in Fig. 2). Interestingly, the general scaling of the shell radii in units of the interparticle distance a of weakly shielded Coulomb balls $\propto N^{1/3}$ is the same as for pure Coulomb systems, such as ion crystals.

However, a marked difference between experiment and simulations of pure Coulomb systems is observed for the shell population numbers $N_1 \ldots N_4$. Table I shows the shell population numbers for various screening parameter κ of a Coulomb ball with $N = 190$ as obtained from MD simulations and experiment. Clearly, for $\kappa = 0$ the MD results yield systematically more particles in the outer part of the cluster than observed in experiment. Further, Table I shows that, with increasing κ, particles move from the outer shell
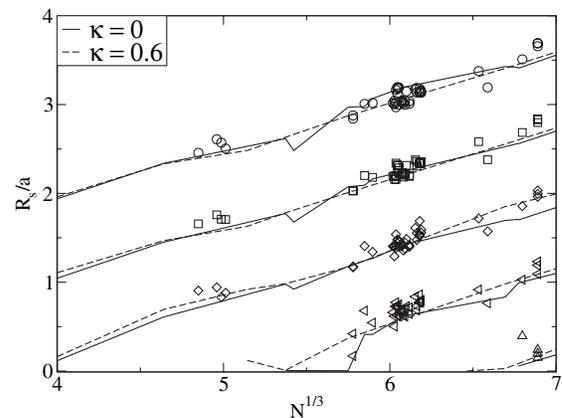

FIG. 2.   Experimental (symbols) and MD-simulation (lines) results for the shell radii of three-dimensional Coulomb balls in units of the mean interparticle distance.

TABLE I. Experimental (last column) and theoretical shell configuration of the Coulomb ball $N = 190$. $N_1 \ldots N_4$ denote the particle numbers on the ith shell beginning in the center.

$\kappa \rightarrow$	0	0.2	0.3	0.4	0.5	0.6	1.0	Experiment
N_1	1	1	2	2	2	2	4	2
N_2	18	18	20	20	21	21	24	21
N_3	56	57	57	58	58	60	60	60
N_4	115	114	111	110	109	107	102	107

inward. Interestingly, for $\kappa = 0.58 \ldots 0.63$, the simulations yield exactly the same shell configuration as the experiment. Therefore, the different population numbers may be attributed to the influence of screening and hence weakening of the interaction potential.

To investigate this in more detail, the comparison was extended to all 43 Coulomb balls. Because of their different size and even different number of shells the systematic differences in shell population of Coulomb and Yukawa systems can be studied comparing the experimental results and MD simulations. The result is shown in Fig. 3. Coulomb and Yukawa simulations as well as the experiment reveal an almost linear behavior of the shell population of all shells as a function of $N^{2/3}$. However, the experimentally obtained population of the outermost shell N_4 is significantly smaller than the one of a Coulomb system (solid line), whereas the inner shells show a systematically higher population. Interestingly, the Yukawa MD simulations (dashed lines) show the same systematic deviation from the Coulomb case. It is clearly found that with increasing κ particles move to inner shells. Hence, the finding discussed for the Coulomb balls with $N = 190$ in Table I holds generally. This tendency reflects the fact that, from an energetic point of view, the higher population of the inner shells becomes less costly, due to the shielding
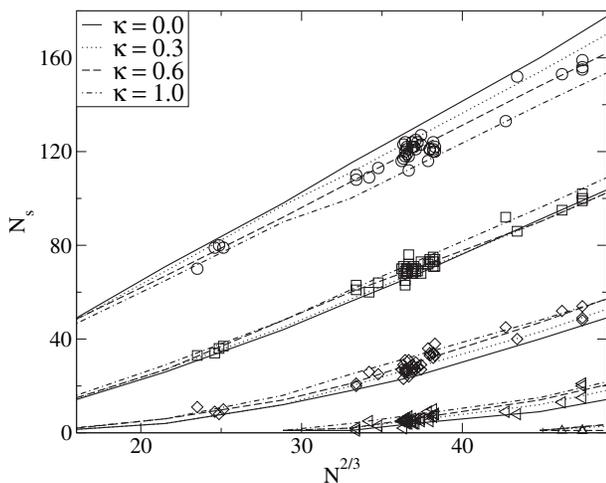

FIG. 3. Experimental (symbols) and simulation (lines) results for the shell population of three-dimensional Coulomb clusters at different values of κ (see inset).

than the occupation of the outermost shell, where the confinement by the trap dominates the potential energy.

In more detail, we find that the outermost shell exhibits the largest absolute change with κ and it is, therefore, best suited for a detailed comparison with the experimental data, see Fig. 3. From a best fit to the experimental data, we find a screening parameter $\kappa^{\mathrm{EXP}} = 0.62 \pm 0.23$. An independent analysis for the other shells confirms this result, e.g., the third shell, yields $\kappa^{\mathrm{EXP}} = 0.58 \pm 0.43$. Determining the mean interparticle distance a from the first peak of the pair distribution function κ^{EXP} translates into an average Debye length $\lambda_D/a = 1.54 \pm 0.7$. Furthermore, as one can see in the right hand part of Fig. 1, an increase of κ leads to compression of the entire cluster, which is due to the reduction of the potential V_{dd}. The fact that more and more particles move from the outer shells inward has the consequence that closed shell configurations are already reached at a smaller number N_c^* of total particles compared to N_c^* in the Coulomb case. While for $\kappa = 0$, the first closed shell is found at $N_1^* = 12$ particles, for $\kappa \gtrsim 4.7$ the ground state of a cluster with 12 (and 11 as well) particles contains one particle in the center and $N_1^* = 10$. For $\kappa = 0.6$ closure of the 2nd to 4th shell is observed for $N_2^* = 54$, $N_3^* = 135$, $N_4^* = 271$, whereas in the Coulomb case $N_{2c}^* = 57$, 60 [10], $N_{3c}^* = 154$ [14] and $N_{4c}^* = 310$ cf. also Fig. 2.

After analyzing the shell populations we now consider the shell width. The larger roughness of the shells in the experiments cf. Fig. 1, is attributed to small anisotropies of the experimental confinement and finite depth resolution of the imaging equipment as well as temperature effects. While the measurements are at room temperature, the MD simulations refer to $T = 0$. Therefore, we have analyzed the influence of temperature on the shell radii and populations with the help of MC simulations. From the results we conclude that the effect of temperature on the shell configurations N_s is negligible for $\kappa = 0.6$. At constant finite T we find that an increase of κ leads to a reduction of shell roughness. Contrary to that, a temperature increase at elsewhere fixed parameters in fact leads to a roughening of the shells proportional to $\sqrt{T}$ for the outer shell and an even stronger effect for the inner shells. This tendency will become evident from the analytical results below.

Analytical results.—The main influence of screening on Coulomb balls is readily understood with the help of analytical results, which can be found for $N = 2$. First, the ground state distance $r_0(\kappa)$ follows from minimizing the potential energy U in Eq. (1):

$$\frac{e^{\kappa r_0} r_0^3}{1 + \kappa r_0} = \frac{Q^2}{m/2\omega^2} \equiv r_{0c}^3. \qquad (2)$$

Equation (2) yields the two-particle distance, r_{0c}, in an unscreened system as a function of r_0 and is easily inverted numerically [21]. The ratio r_0/r_{0c} is always smaller than

unity and monotonically decreasing with κ, thereby confirming the above observation of screening-induced compression of the Coulomb balls. Second, we analyze the cluster stability by expanding the potential U in terms of small fluctuations, $y \equiv r - r_0$, around the ground state, up to second order: $U(r) - U(r_0) = \frac{1}{2} U''(r_0) y^2 \equiv \frac{m}{4} \Omega^2 y^2$. This defines an effective local trap frequency Ω

$$\Omega^2(\kappa) = 3\omega^2 \left(1 + \frac{1}{3} \frac{\kappa^2 r_0^2}{1 + \kappa r_0} \right) = \frac{6}{m} \frac{Q^2}{r_0^3} f_2(\kappa),$$
$$f_2(\kappa) = e^{-\kappa r_0}(1 + \kappa r_0 + \kappa^2 r_0^2/3), \tag{3}$$

which allows us to estimate the width of the Coulomb ball shells. Third, we compute the variance of the particle distance fluctuations, σ_r, for particles in a parabolic potential with frequency Ω at temperature T and obtain $\sigma_r^2 = 2k_B T/(m\Omega^2)$ which is in agreement with our MC simulations. This allows for two interesting conclusions: At constant screening, the shell width grows with temperature as $\sqrt{T}$ while screening reduces the shell width. One might be tempted to conclude that increased screening makes particle transitions between neighboring shells less likely and thus stabilizes the cluster against melting. However, the opposite is true, because screening also reduces the distance between shells which is of the order of r_0. The relative importance of both tendencies can be discussed in terms of the *relative distance fluctuations*, a critical value of which determines the onset of radial melting (Lindemann criterion).

$$u_r^2 \equiv \frac{\sigma_r^2}{r_0^2} = \frac{1}{3} \frac{1}{\Gamma_2^*}, \qquad \Gamma_2^* = \Gamma_2 f_2(\kappa). \tag{4}$$

u_r is related to an effective coupling parameter, Γ_2^* which depends on the interaction strength of two trapped particles—via the Coulomb-type coupling parameter, $\Gamma_2 \equiv Q^2/(k_B T r_0)$, and on the screening strength—via the function $f_2(\kappa)$. f_2 monotonically decreases with κ (u_r increases), thus *screening destabilizes the Coulomb balls*.

Finally, these analytical results are closely related to those for macroscopic homogeneous Yukawa systems, e.g. [17,18]. This limit is recovered by replacing, in (3), r_0 by the mean interparticle distance a at a given density n, $a = (3/4\pi n)^{1/3}$. Then the local trap frequency becomes $\Omega^2 \rightarrow \omega_{pd}^2 f_2(\kappa)$, showing that, in a Coulomb system, Ω approaches the dust plasma frequency ω_{pd} whereas, in the case of screening, the result is modified by a factor $\sqrt{f_2(\kappa)}$ [22]. Also, the effective coupling parameter Γ_2^* is in full analogy to the macroscopic result [18].

In summary, we have presented a combined experimental, numerical, and theoretical analysis of small spherical charged particle clusters. The excellent experimental accessibility of these systems has been demonstrated. The structure of these clusters deviates from models with pure Coulomb interaction and requires the inclusion of static screening. For the particle number range $N = 100 \ldots 500$, comparison with the MD and MC simulations has allowed us to determine the screening parameter averaged over the clusters as $\lambda_D/a \approx 1.5$. These Coulomb balls are representative for finite Yukawa systems, combining shell properties observed in spherical Coulomb clusters with screening effects found in Yukawa plasmas. Since the shell occupation numbers have now been critically analyzed, our results confirm earlier conclusions about the shell structure of ion clusters, where such an analysis was not accessible yet. The results are relevant for other strongly correlated charged particle systems, such as crystal formation of droplets in expanding laser produced plasmas, where shielding becomes important.

[1] O. Arp, D. Block, A. Piel, and A. Melzer, Phys. Rev. Lett. **93**, 165004 (2004).
[2] J. B. Pieper, J. Goree, and R. A. Quinn, Phys. Rev. E **54**, 5636 (1996).
[3] M. Zuzic *et al.*, Phys. Rev. Lett. **85**, 4064 (2000).
[4] Y. Hayashi, Phys. Rev. Lett. **83**, 4764 (1999).
[5] D. J. Wineland *et al.*, Phys. Rev. Lett. **59**, 2935 (1987).
[6] M. Drewsen *et al.*, Phys. Rev. Lett. **81**, 2878 (1998).
[7] T. Pohl, T. Pattard, and J. M. Rost, Phys. Rev. Lett. **92**, 155003 (2004).
[8] T. Killian, Nature (London) **429**, 815 (2004).
[9] R. W. Hasse and V. V. Avilov, Phys. Rev. A **44**, 4506 (1991).
[10] K. Tsuruta and S. Ichimaru, Phys. Rev. A **48**, 1339 (1993).
[11] P. Ludwig, S. Kosse, and M. Bonitz, Phys. Rev. E **71**, 046403 (2005).
[12] H. Totsuji *et al.*, Phys. Rev. Lett. **88**, 125002 (2002).
[13] J. P. Schiffer, Phys. Rev. Lett. **88**, 205003 (2002).
[14] O. Arp *et al.*, J. Phys.: Conf. Ser. **11**, 234 (2005).
[15] W. M. Itano *et al.*, Science **279**, 686 (1998).
[16] U. Konopka, G. E. Morfill, and L. Ratke, Phys. Rev. Lett. **84**, 891 (2000).
[17] D. H. E. Dubin and T. M. O'Neill, Rev. Mod. Phys. **71**, 87 (1999).
[18] V. E. Fortov *et al.*, Phys. Rev. Lett. **90**, 245005 (2003).
[19] O. Arp, D. Block, M. Klindworth, and A. Piel, Phys. Plasmas **12**, 122102 (2005).
[20] H. Totsuji, C. Totsuji, T. Ogawa, and K. Tsuruta, Phys. Rev. E **71**, 045401 (2005).
[21] A useful analytical approximation for r_0 in Eq. (2) as a function of r_{0c} is $x = x_c + (\ln(1 + x_c) - x_c)/(x_c^2 + 3x_c + 3)[x_c(1 + x_c)]$, where $x = \kappa r_0$, which has an error of less than 1%, for $x_c = \kappa r_{0c} < 1.5$.
[22] This result differs slightly from the exact macroscopic result [18] (by the coefficient $1/3$ instead of $1/2$ in the last term in f_2) which is a consequence of performing this replacement in the two-particle expression (2).

4 Statistical Properties of Confined Systems

In this chapter we consider two questions which are of direct importance for the understanding of structure formation in both confined classical complex plasmas (chapter 3) as well as electron-hole quantum plasmas (chapter 5). The first question, considered in section 4.2, is related to the radial density distribution of screened Coulomb plasmas in traps and its dependence on the Debye screening length. The findings pertaining to this question have also implications for the qualitative clarification of configurational transitions in dipolar bilayer systems (see section 5.4). The second question (section 4.3) concerns the reliable identification of order-disorder phase transitions in few-particle systems, which is of fundamental interest for the exploration of finite-size effects and collective behaviour in both classical and quantum systems. A frequently used and well-established melting criterion (often referred to as "Lindemann criterion") was found to yield divergent and ambiguous results for the critical temperatures and densities. We present a very simple quantity which overcomes these problems and allows for a systematic and consistent analysis of crystal phase boundaries in small-scale (classical and quantum) systems.

4.1 Introduction and Overview

Density Profile of Confined Systems with Statically-Screened Coulomb Interaction

It is textbook wisdom that in the case of a harmonically confined unscreened Coulomb system, the (average) radial density profile is constant. However, in chapter 3 we have shown that the experimentally observed shell structure of spherical 3D dust crystals [15] can be successfully explained by a model of *statically-screened Coulomb interaction.*

Furthermore, we found a high sensitivity of the shell occupation numbers of the Yukawa balls in dependence on the range of the interaction potential. This raises the question concerning the ground state particle distribution of a confined Yukawa plasma in the limit of large particle numbers within the *discrete particle model* as well as within a statistical description based upon a *continuous approach.*

Our investigations show that screening has a dramatic effect on the radial charge distribution, see figure 4.1. In the case of a screened Coulomb interaction, i.e. for a screening parameter $\kappa > 0$, the density profile becomes strongly inhomogeneous with a strictly monotonic increase towards the trap center. The combination of MD simulations and the analytical theory for the confined Yukawa plasmas reveals that the configurational rearrangement of Yukawa balls in comparison to unscreened Coulomb balls (see chapter 3) can be explained by the *(strong) inhomogeneous radial density profile*, which is established when the electrostatic dust-dust interaction becomes screened by the ambient plasma and the Debye screening length becomes finite. This essential effect has been disregarded in previous investigations of trapped Yukawa systems [114].

The results for the radial shell-averaged density of *finite systems in the discrete model* consisting of $N = 1000 \ldots 10000$ particles[1] (which exhibit a distinct shell structure) and the analytical model which applies to *macroscopic systems* (where no shell structure exists) are in very good agreement; this accordance was not expected and is not obvious at all. The mean-field (MF) results (see section 4.2.1) are found to give agreement for weak screening, whereas the local density approximation (LDA) with correlations included (see section 4.2.2), yields the proper description in the regime of large screening.

It should be explicitly stated that the formation of distinct shells is a finite-size effect (particle-number dependent), which reflects the geometric constraints due to the spherical confinement potential. Approaching large cluster sizes, the shells break up and regular volume order prevails. Bulk order with *bcc* structure is found for large clusters with typically $10^5 - 10^6$ particles, such as large ion crystals in Paul or Penning traps [7, 115]. These experimental findings are in essential agreement with molecular dynamics simulations, which show that finite-size effects vanish for particle numbers $N > 1000$ in 2D systems and $N > 10^4 \ldots 10^5$ in 3D systems [33, 104, 116].

As a side result of the mean field model for the harmonically confined (continuous) Yukawa system (section 4.2.1) a fit function can be obtained, which allows to approxi-

---

[1]It should be noted here, that the simulations were performed without simplification with regard to $N(N-1)/2$ pairwise interaction terms.
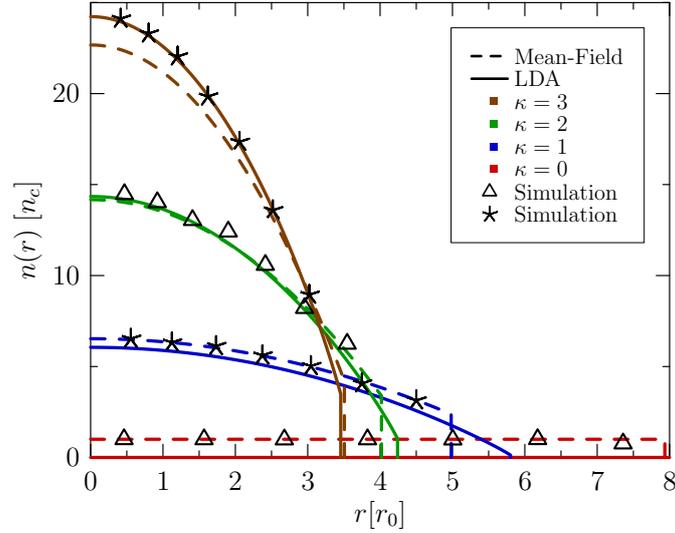
Figure 4.1: *Ground state radial density profiles $n(r)$ of a parabolically confined one-component Yukawa plasma in mean-field (dashed lines) and local density approximation (LDA, solid lines) for different screening parameters. The symbols mark the mean shell densities obtained by MD simulations of $N = 1000$ point charges. The density of the unscreened Coulomb system is constant, whereas shielding introduces a radial density gradient to establish force equilibrium (see section 4.2).*

mate the cluster radius

$$R(N, \kappa) = \exp(-0.278 + 0.308\eta - 0.00439\eta^2 - 0.000154\eta^3 + 0.0000106\eta^4)/\kappa \,, \quad (4.1)$$

in units of r_0 within 1% of relative accuracy in the range $\eta \in [0.001, 6.58 \times 10^6]$, where $\eta = \log(\kappa^3 N)$. This result is very helpful to estimate the cluster size as function of particle number N and screening parameter κ, which is necessary, e.g., to set the random initial particle positions in the MD simulations. A good estimator reduces the initial potential energy of the N-particle system and can thus drastically reduce the computational effort for the simulated annealing process (see section 3.1 for details).

It is also interesting to note that related structural effects are recovered in electron-hole bilayer systems, where a transition from a long-range Coulomb to a short-range dipole interaction is initiated by decreasing layer separation d (see section 5.4 for details).

Fluctuation Based Melting Criterion for Classical and Quantum Few-Particle Systems

Solid and liquid behaviour are collective properties of macroscopic systems and thermodynamics gives clear guidance to identify phase transitions in the limit of very large particle numbers. Nevertheless, qualitatively different collective behaviour already emerges in small-scale systems and is captured by the naming "liquid-like" and "solid-like" phase. While in macroscopic large systems several equivalent definitions for phase transitions exist, the identification of phase behaviour of few-particle (quantum) systems has been a problematic issue, which is due to the lack of an universal parameter to quantify the onset of melting and freezing transitions [117]. To overcome this problem empirical rules are frequently used [118]-[121].

The criterion of choice for studying phase changes in finite disordered systems [19] is the so-called "Lindemann criterion"[2], which is based on an abrupt change of the *relative interparticle distance fluctuations* (IDF) in the order-disorder transition region. The immediate practical importance of this criterion in many fields of (in particular computational) science becomes evident by the more than 14000 publications[3], which utilize this criterion. However, this estimator is found to be dominated by a few (exponentially) rare large fluctuation events.

The averaged fluctuations of all relative interparticle distances (IDF) within a given few-particle system are quantified by

$$u_{rel} = \frac{2}{N(N-1)} \sum_{i=1}^{N-1} \sum_{j=i+1}^{N} \sqrt{\frac{\langle |\mathbf{r}_i - \mathbf{r}_j|^2 \rangle}{\langle |\mathbf{r}_i - \mathbf{r}_j| \rangle^2} - 1} \,, \qquad (4.2)$$

where $\langle \ldots \rangle$ denotes the statistical averaging. The quantity u_{rel} captures two scales of the distance fluctuations: (1) particle vibrations in local minima of the potential energy landscape which are naturally associated with solid-like behaviour as well as (2) particle jumps between different local minima. A jump occurs whenever two particles exchange their local minima positions, which is associated with traversal of a local maximum or saddle point. Above a critical temperature, when particle jumps become probable within the simulation, u_{rel} starts to deviate strongly from the linear low-

---

[2]It should be noted that even though the famous paper [118] to date has been cited more than 1100 times most authors are not aware that it does neither contain a universal ratio u_L nor the concept of the mean square displacement. The latter key idea is due to Gilvarry [119]. Lindemann instead used the concept that melting occurs when two atoms come in contact.

[3]Google Scholar, June 2008.

temperature dependence and exceeds a critical value of typically $u_{cr} \approx 0.10 \ldots 0.15$, which is commonly used as a criterion for the "melting temperature".

Surprisingly, our Monte Carlos simulations (see chapter 5) revealed a fundamental problem of this extensively used melting criterion: The quantity u_{rel} depends on the way it is computed. If the simulation is sufficiently long, even rare jumps will be eventually captured at any finite temperature and u_{rel} will converge towards the value which is associated with liquid behaviour. The finding that longer simulation runs lead to lower values for the critical temperature and densities was already remarked by references [20, 88] but often ignored. To make use of u_{rel} as a melting parameter and to control its convergence problems, it is useful to subdivide the simulation into fixed "time" intervals (in MC simulations given as block size M), which allows for a statistical evaluation of rare fluctuation events (section 5.3). Further investigations suggest the introduction of the *variance of the block averaged relative interparticle distance fluctuations* (VIDF) defined as

$$\sigma_{u_{rel}} = \sqrt{\frac{1}{K}\sum_{s=1}^{K} u_{rel}^2(s) - \bar{u}_{rel}^2} \,, \tag{4.3}$$

where K denotes the number of blocks of equal length $M \approx 1000$ (classical or path integral) Monte Carlo steps and $\bar{u}_{rel} = K^{-}1\sum_{s=1}^{K} u_{rel}(s)$ the *mean of the block averaged IDF*. The information about the "phase" of the system is given by the probability of jumps, which grows with temperature. While in the solid phase jumps are rare events, in the liquid state pair exchanges occur frequently and particles are practically delocalized. The melting is located inbetween these two limits where a maximum of $\sigma_{u_{rel}}$ (connected to strong fluctuations of the block averaged IDF $u_{rel}(s)$) allows one to reliably detect the melting point (see figure 4.2).

The main advantages of the VIDF as a fluctuation based quantity that constitutes a melting criterion, can be summarized by the following points:

Universality: A variety of possible quantities were investigated which are sensitive to the onset of melting, e.g., specific heat, the total energy autocorrelation function, the pair distribution or bond angular symmetry parameters, etc., but only the VIDF was found to be rigorously applicable for quantum systems as well.

Mechanism: The computation (or measurement) is straightforward and transparent as the VIDF is directly related to the physical process, i.e., fluctuations and jumps near the phase transition.
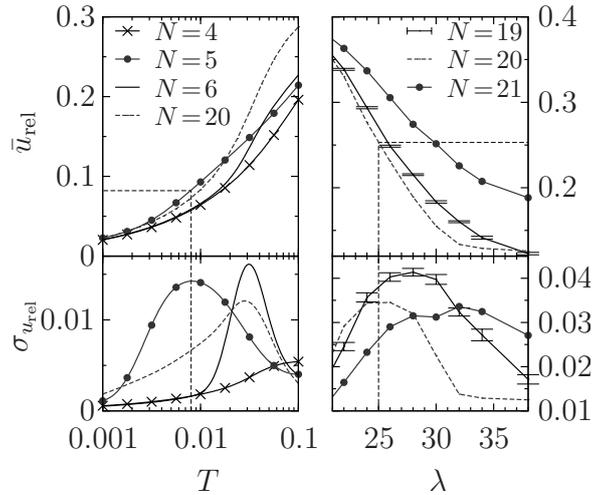
Figure 4.2: *Above: The IDF u_{rel}, commonly called "Lindemann-parameter", is frequently used to identify order-disorder transitions in small systems. Shown is the mean value $\bar{u}_{rel}$ of the block averaged IDF ($M = 1000$) for a classical 3D Coulomb system (left, MC results) and a 2D quantum system (right, PIMC results). The IDF shows a gradual increase in the transition region. Below: The VIDF which is a much more sensitive quantity. The VIDF clearly detects the melting transitions upon temperature increase (left) as well as quantum melting upon density increase (decrease of the Coulomb coupling parameter λ). The dashed lines locate the critical values of T (or λ) and u_{rel}^{crit}. (See section 4.3 for details.)*

Sensitivity: The VIDF does not gradually increase over the transition range, but is rather unambiguously peaked in the center of the finite melting interval.

Locality: As a local quantity, the VIDF can be analyzed locally for a system part only, e.g., in the case of strongly inhomogeneous systems. Such spatially resolved melting analysis is impossible with any thermodynamic quantity or the energy autocorrelation function.

Experimental importance: The individual particle trajectories and the interparticle fluctuations are directly accessible, e.g., in dusty plasma experiments, which allows for a direct comparison with computer simulations and the detection of melting phase transitions (see e.g. [15]).

Generality: The VIDF is a dimensionless (and thus "scale-free") quantity, which makes it easy to compare physical systems on different length scales.

Computational aspects: The VIDF converges fast, it is less time-consuming to compute, robust, and convenient to evaluate.

Continued investigations show that the VIDF can also be used for time-dependent simulations, such as molecular dynamics [122].

4.2 Density Profile of a Confined Yukawa Plasma in the Discrete and Continuum Model

The ground state density profile of an externally confined one-component Yukawa plasma is derived in mean-field approximation (MF) as well as in local density approximation (LDA). By comparison with first-principles simulations for three-dimensional spherical Yukawa crystals, we demonstrate that the two approximations complement each other. While the MF results are more accurate for weak screening, the LDA with correlations included yields the proper description for large screening. Together the analytical results accurately describe the density profile in the full range of screening parameters and agree very well with the shell-averaged density in the discrete model.

The results were published as refereed journal publications:

4.2.1 *Ground State of a Confined Yukawa Plasma,*
C. Henning, H. Baumgartner, A. Piel, P. Ludwig, V. Golubnychiy, M. Bonitz, and D. Block, Physical Review E **74**, 056403 (2006)

4.2.2 *Ground State of a Confined Yukawa Plasma Including Correlation Effects,* C. Henning, P. Ludwig, A. Filinov, A. Piel, and M. Bonitz, Physical Review E **76**, 036404 (2007)

Ground state of a confined Yukawa plasma

C. Henning,[1] H. Baumgartner,[1] A. Piel,[3] P. Ludwig,[1,2] V. Golubnichiy,[1] M. Bonitz,[1,*] and D. Block[3]

[1]*Institut für Theoretische Physik und Astrophysik, Christian-Albrechts-Universität zu Kiel, D-24098 Kiel, Germany*
[2]*Institut für Physik, Universität Rostock, Universitätsplatz 3 D-18051 Rostock, Germany*
[3]*Institut für Experimentelle und Angewandte Physik, Christian-Albrechts-Universität zu Kiel, D-24098 Kiel, Germany*

The ground state of an externally confined one-component Yukawa plasma is derived analytically. In particular, the radial density profile is computed. The results agree very well with computer simulations of three-dimensional spherical Coulomb crystals. We conclude in presenting an exact equation for the density distribution for a confinement potential of arbitrary geometry.

I. INTRODUCTION

Plasmas in external trapping potentials have been attracting increasing interest over the last few years in many fields, including trapped ions (e.g., [1,2]), dusty plasmas (e.g., [3–5]), and electrons and positrons in Penning traps (see, e.g., [6] for an overview). Among the main reasons is that, in these systems, it is relatively easy to realize strong correlation effects in charged particle systems. Probably the most spectacular manifestation of these effects is Coulomb liquid behavior and crystal formation which have been found in various geometries. In particular, the ion crystals and the recently observed spherical dust crystals or "Coulomb balls" [7] have triggered intensive new experimental and theoretical work (e.g., [8–10]). The shell structure of these crystals, including details of the shell radii and the particle distribution over the shells, has been very well explained theoretically by a simple model involving an isotropic Yukawa-type pair repulsion and an harmonic external confinement potential [10].

Still, it remains an open question as to what the average particle distribution inside the trap looks like, if it is the same as in the case of Coulomb interaction. It is well known that in a parabolic potential, particles interacting via the Coulomb potential establish a radially constant-density profile. Here, we extend this analysis to a plasma with Yukawa interaction by solving a variational problem for the ground-state density (Sec. II). Then, in Sec. III we demonstrate that screening has a dramatic effect on the density profile giving rise to a parabolic decrease away from the trap center. There we demonstrate that the result for the density profile can be directly generalized to any anisotropic confinement potential. While our analysis is based on a continuous plasma model on the mean-field level, we find (Sec. IV), by comparison with molecular dynamics simulations, that the results apply also to spherical crystals with a shell structure.

II. GROUND STATE OF A CONFINED PLASMA

We consider a finite one-component plasma (OCP) containing N identical particles with mass m and charge Q in an external potential Φ with pair interaction potential V described by the Hamiltonian

$$H = \sum_{i=1}^{N} \left\{ \frac{p_i^2}{2m} + \Phi(\mathbf{r}_i) \right\} + \frac{1}{2} \sum_{i \neq j}^{N} V(\mathbf{r}_i - \mathbf{r}_j). \quad (1)$$

The classical ground-state energy follows from Eq. (1) for vanishing momenta and can be written as [6,11]

$$E[n] = \int d^3r\, u(\mathbf{r}), \quad (2)$$

with the potential energy density

$$u(\mathbf{r}) = n(\mathbf{r}) \left\{ \Phi(\mathbf{r}) + \frac{N-1}{2N} \int d^3r_2\, n(\mathbf{r}_2) V(|\mathbf{r} - \mathbf{r}_2|) \right\}, \quad (3)$$

being a functional of the density profile $n(\mathbf{r})$, and we neglected correlation contributions. The ground state corresponds to the minimum of the energy (2) with respect to the density profile with the restrictions that the density be nonnegative everywhere and reproduce the total particle number—i.e.,

$$\int d^3r\, n(\mathbf{r}) = N. \quad (4)$$

This gives rise to the variational problem [12]

$$0 \stackrel{!}{=} \frac{\delta \widetilde{E}[n,\mu]}{\delta n(\mathbf{r})}, \quad (5)$$

where

$$\widetilde{E}[n,\mu] = E[n] + \mu \left\{ N - \int d^3r\, n(\mathbf{r}) \right\} \quad (6)$$

and we introduced a Lagrange multiplier μ (the chemical potential) to fulfill condition (4). The variation leads to

$$\Phi(\mathbf{r}) - \mu + \frac{N-1}{N} \int d^3r'\, n(\mathbf{r}') V(|\mathbf{r} - \mathbf{r}'|) = 0, \quad (7)$$

which holds at any point where the density is nonzero. Also, Eq. (7) is equivalent to vanishing of the total force on the particles separately at any space point $\mathbf{r}$ (cf. Sec. III B).

Equation (7) is completely general, applying to any pair interaction V and confinement potentials of arbitrary form and symmetry (see Sec. III C). Of particular interest is the case of an isotropic confinement $\Phi(\mathbf{r}) = \Phi(r)$, which leads to

*Electronic address: bonitz@physik.uni-kiel.de

an isotropic density distribution $n(\mathbf{r}) = n(r) = \tilde{n}(r)\Theta(R-r)$, the outer radius R of which is being fixed by the normalization condition (4) which now becomes $\int_0^R dr r^2 \tilde{n}(r) = N/4\pi$.

III. DENSITY PROFILE OF A YUKAWA OCP

We now consider the case of an isotropic Yukawa pair potential $V(r) = \frac{Q^2}{r} e^{-\kappa r}$, which trivially includes the Coulomb case in the limit $\kappa \to 0$. Carrying out the angle integration in the interaction energy in Eq. (7) we obtain [14]

$$\Phi(r) - \mu = 2\pi \frac{N-1}{N} \frac{Q^2}{\kappa r} \int_0^R dr' r' \tilde{n}(r') [e^{-\kappa(r+r')} - e^{-\kappa|r-r'|}].$$
(8)

This equation is the desired connection between the ground-state density $\tilde{n}(r)$ of the Yukawa plasma and the external confinement $\Phi(r)$. This integral equation can be solved for the density by differentiating 2 times with respect to r [15] with the result (details are given in the Appendix)

$$4\pi \frac{N-1}{N} Q^2 \tilde{n}(r) = \frac{2\Phi'(r)}{r} + \Phi''(r) - \kappa^2\Phi + \kappa^2\mu. \quad (9)$$

The yet unknown Lagrange multiplier can be obtained by inserting this explicit solution into Eq. (8), which is then treated as an equation for μ, with the result

$$\mu = \Phi(R) + \frac{R\Phi'(R)}{1 + \kappa R}. \quad (10)$$

A. Parabolic confinement potential

For the frequently encountered case of a parabolic external potential $\Phi(r) = \frac{\alpha}{2} r^2$, we obtain, for the density from Eq. (9),

$$n(r) = \frac{\alpha N}{4\pi(N-1)Q^2}\left(c - \frac{\kappa^2 r^2}{2}\right)\Theta(R-r), \quad (11)$$

where the constant c is given by

$$c = 3 + \frac{R^2\kappa^2}{2}\frac{3 + \kappa R}{1 + \kappa R}. \quad (12)$$

Finally, the outer radius R limiting the density profile is calculated from the normalization (4) with the result

$$-15\frac{Q^2}{\alpha}(N-1) - 15\frac{Q^2}{\alpha}\kappa(N-1)R + 15R^3 + 15\kappa R^4 + 6\kappa^2 R^5$$
$$+ \kappa^3 R^6 = 0. \quad (13)$$

This equation has four complex and two real solutions, only one of which is non-negative, and thus constitutes the unique proper result entering Eq. (12). In the Coulomb limit, Eq. (11) reduces to the familiar result of a step profile,

$$n_c(r) = \frac{3\alpha}{4\pi Q^2}\frac{N}{N-1}\Theta(R_c - r), \quad (14)$$
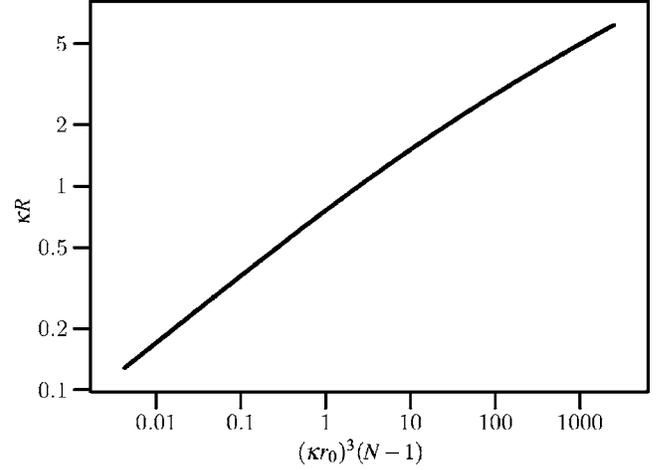
where the outer radius is given by

FIG. 1. Plasma cloud radius R [positive real solution of Eq. (13)] for a parabolic confinement potential $\Phi(r) = \frac{\alpha}{2} r^2$ and Yukawa interaction with screening parameter κ.

$$R_c = \sqrt[3]{\frac{Q^2(N-1)}{\alpha}} = r_0 \sqrt[3]{\frac{N-1}{2}}, \quad (15)$$

which is fixed by the number of particles and the constant density, the latter being controlled by the curvature α of the potential. In the right part of Eq. (15) we introduced the length scale $r_0 = \sqrt[3]{2Q^2/\alpha}$, which is the stable distance of two charged particles in the absence of screening [10] and which will be used below as the proper unit for lengths, screening parameter, and density. Note that Eq. (15) holds also for a weakly screened Yukawa plasma with $\kappa R \ll 1$.

In the other limiting case $\kappa R \gg 1$, the radius has the asymptotics $\kappa R \approx \left[\frac{15}{2}(\kappa r_0)^3(N-1)\right]^{1/5} - 1$. In general Eq. (13) cannot be solved for R explicitly. However, a general analytical result can be found by noting that all parameters entering Eq. (13) combine into only two parameters $x = (\kappa r_0)^3(N-1)$ and $y = \kappa R$. Introducing these parameters into Eq. (13), an explicit solution is found for the inverse function $x(y)$, which can be written as

$$x(y) = \frac{2y^3}{15}\frac{y^3 + 6y^2 + 15y + 15}{y + 1}. \quad (16)$$

Figure 1 shows the result for the dimensionless radius $\kappa R = y$ of the plasma cloud—i.e., the solution of Eq. (13), which for all values of κ and N is given by a single curve.

With the result for R the constant c, which is proportional to central density, can be computed from Eq. (12) and the complete density profile, Eq. (11), is found. The results are shown in Fig. 2 for four particle numbers between $N = 100$ and $N = 2000$. One clearly recognizes the inverted parabola which terminates in a finite-density value—i.e., in a discontinuity—at $r = R$. With increasing N, the density increases continuously at every space point and, at the same time, extends to higher values R. Thereby the density profile retains its shape.

On the other hand, when the plasma screening is increased, at constant N, the density profile changes dramatically (compare the two curves for $N = 2000$). Increase of κ
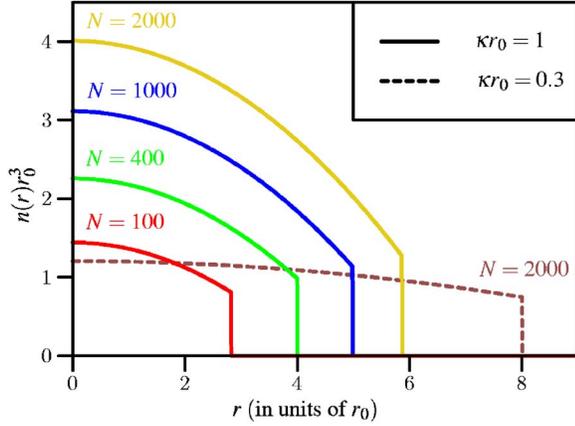
FIG. 2. (Color online) Radial density profile for a parabolic confinement potential $\Phi(r)=\alpha r^2/2$ and a constant screening parameter $\kappa r_0=1$ and four different particle numbers N shown in the figure. For comparison, also the result for $\kappa r_0=0.3$ and $N=2000$ is shown by the dashed line.

leads to compression of the plasma: the radius R decreases, and the absolute value of the density increases, most significantly in the center. This compressional behavior is shown in Fig. 3 (cf. the solid green line showing the ratio of the inner to outer densities of the plasma).

The dependence on κ is analyzed more in detail in Fig. 4 below for a fixed particle number $N=2000$. In the case of a Coulomb interaction $\kappa=0$, we recover the constant density profile (14). On the other hand, in the case of a screened potential, the density decays parabolically with increasing distance from the trap center [cf. Eq. (11)]. Also, the density discontinuity at $r=R$ is softened compared to the Coulomb case and the step height increases.

B. Force equilibrium

Besides minimizing the total energy [cf. Eq. (7)], the ground-state density profile can be obtained from the condition of a local equilibrium of the total force (internal plus
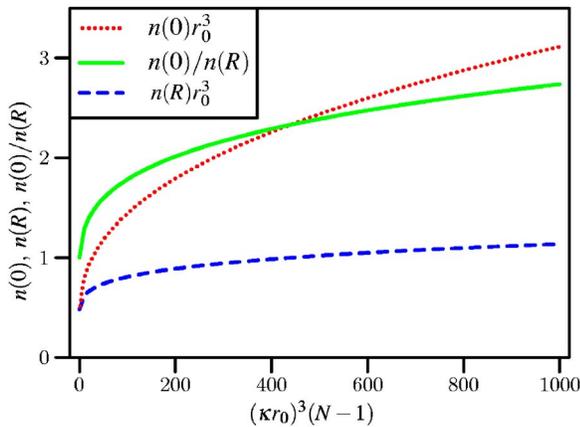

FIG. 3. (Color online) Dependence of the central density $n(0)$ (red dotted line), density at the boundary, $n(R)$ (blue dashed line), and compression $n(0)/n(R)$ of the plasma (green solid line) as a function of particle number and screening parameter.
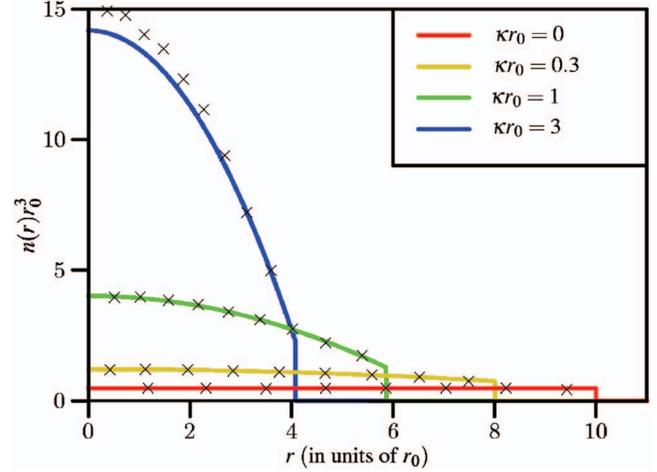

FIG. 4. (Color) Radial density profile, solutions of Eq. (11), of a three-dimensional plasma of $N=2000$ for four values of the screening parameter (lines), from bottom to top: $\kappa=0$ (red), $\kappa r_0=0.3$ (yellow), $\kappa r_0=1$ (green), and $\kappa r_0=3$ (blue). Symbols the denote molecular dynamics results of a plasma crystal for the same parameters where the average density at the positions of the shells is shown (for details see discussion in Sec. IV B).

external ones) at each point where the density is nonzero. On the other hand, the shape of the radial density profile and its change with variation of κ is directly related to a change of the force equilibrium. Here, we demonstrate this for the special case of a spherically symmetric confinement potential $\Phi(r)$. The forces can be directly derived from Eq. (8) by taking the gradient in radial direction,

$$\Phi'(r) = F_<(r) + F_>(r), \tag{17}$$

which means that, for any spherical layer at a distance r from the center, the external force $F_\Phi(r)=-\Phi'(r)$ which acts towards the center is balanced by the internal force due to the Yukawa repulsion between the particles. The internal force contains two parts where $F_<$ arises from the action of all particles inside the given layer, $r' \leqslant r$, and acts outward, whereas $F_>$ results from the action of all particles located outside $r' \geqslant r$, and acts inward,

$$F_<(r) = 4\pi\frac{N-1}{N}Q^2\frac{e^{-\kappa r}}{r}\left(1+\frac{1}{\kappa r}\right)\int_0^r dr' r' \widetilde{n}(r')\sinh(\kappa r'), \tag{18a}$$

$$F_>(r) = 4\pi\frac{N-1}{N}Q^2\frac{1}{r}\left(-\cosh(\kappa r)\right.$$
$$\left.+\frac{\sinh(\kappa r)}{\kappa r}\right)\int_r^R dr' r' \widetilde{n}(r')e^{-\kappa r'} \tag{18b}$$

This force balance can be used to obtain the ground-state density profile. Alternatively, we can use the computed profile to analyze the two internal force contributions and their dependence on κ.

Consider first the limit of weak screening, $\kappa R \ll 1$. Then the forces approach the Coulomb case and, in the case of a constant density profile (14),

$$F_{C,<}(r) = \frac{N-1}{N}\frac{Q^2}{r^2}N_< = \alpha r,$$

$$F_{C,>}(r) = 0,$$

with $N_< = n_c 4\pi r^3/3$ being the particle number in the inner region. This means that the force is repulsive and increases linearly with r and exactly compensates the linear external force $F_\Phi(r) = -\alpha r$ for all values $r < R$.

In the general case of finite screening the outer force $F_>(r)$ does not vanish [cf. Eq. (18b)]. Since its direction is always towards the center, the force $F_<(r)$ has to increase simultaneously in order to compensate the combined effect of $F_\Phi(r)$ and $F_>(r)$. This effect increases continuously with increasing κ which is directly verified by evaluating the expressions in Eq. (18a).

C. Generalization to arbitrary confinement geometry

The result for the density profile in an isotropic confinement, Eq. (9), can be easily extended to arbitrary geometry. For this purpose we use the textbook result that the charge density corresponding to the Yukawa potential is $Q\delta(\mathbf{r}) - Q\kappa^2 e^{-\kappa r}/r$. This allows us to rewrite the Poisson equation as

$$(\Delta - \kappa^2)\frac{e^{-\kappa r}}{r} = -4\pi\delta(\mathbf{r}), \tag{19}$$

showing that the Yukawa potential is the Green's function of the Helmholtz equation. For the case of a confinement potential Φ of arbitrary geometry this fact can be used by applying the operator $(\Delta - \kappa^2)$ to Eq. (7):

$$\frac{N-1}{N}Q^2 \int d^3r'\, n(\mathbf{r}')(\Delta_\mathbf{r} - \kappa^2)\frac{e^{-\kappa|\mathbf{r}-\mathbf{r}'|}}{|\mathbf{r}-\mathbf{r}'|}$$
$$+ (\Delta - \kappa^2)[\Phi(\mathbf{r}) - \mu] = 0. \tag{20}$$

Using Eq. (19) the integral can be computed with help of the δ function with the explicit result for the density profile

$$4\pi\frac{N-1}{N}Q^2 n(\mathbf{r}) = \Delta\Phi(\mathbf{r}) - \kappa^2\Phi(\mathbf{r}) + \kappa^2\mu. \tag{21}$$

IV. DENSITY PROFILE OF CONFINED COULOMB AND YUKAWA CRYSTALS

So far we have considered the model of a continuous density distribution $n(r)$. On the other hand, the ground state of a confined spherically symmetric system of discrete point-like charged particles is known to have a shell structure as was demonstrated for dusty plasmas in Ref. [7]. It is, therefore, of interest to verify if such a shell structure can be derived from our starting equation (2) for the total energy

and to compare our results to the radial density distribution in such Coulomb or Yukawa balls.

A. Derivation of a shell model for a trapped finite Yukawa plasma

The concentric shells observed in spherical trapped Coulomb crystals have led to the proposal of simple analytical models (cf., e.g., [16,17,21,22]). Such a model for a trapped one-component plasma is trivially derived from the total energy expression (2) by inserting for the density the ansatz

$$n_s(\mathbf{r}) = n_s(r) = \sum_{\nu=1}^{L}\frac{N_\nu}{4\pi R_\nu^2}\delta(r - R_\nu), \tag{22}$$

which describes L concentric shells of zero thickness with N_ν particles on shell ν with radius R_ν and $\Sigma_{\nu=1}^L N_\nu + \zeta = N$, where ζ denotes the number of particles in the trap center (0 or 1) [17,22]. As a result, we obtain, for the total ground-state energy of a Yukawa plasma in an isotropic general confinement potential Φ,

$$E_s(N;\kappa) = \sum_{\nu=1}^{L} N_\nu \Biggl\{ \Phi(R_\nu) + Q^2\frac{e^{-\kappa R_\nu}}{R_\nu}\Biggl(\frac{\sinh(\kappa R_\nu)}{\kappa R_\nu}\frac{N_\nu - 1}{2}$$
$$+ \zeta + \sum_{\mu<\nu}\frac{\sinh(\kappa R_\mu)}{\kappa R_\mu}N_\mu\Biggr)\Biggr\}.$$

This is essentially the Yukawa shell model of Totsuji *et al.* [21] where, however, the finite-size correction factor $(N_\nu - 1)/N_\nu$ in the intrashell contribution and the term ζ are missing. In the Coulomb limit $\kappa \to 0$, the result simplifies with $e^{-\kappa R_\nu} \to 1$ and $\frac{\sin \kappa R_\nu}{\kappa R_\nu} \to 1$, and we immediately recover the Coulomb shell model of Hasse and Avilov [16] (plus the additional correction factor).

A further improvement is possible by including intrashell correlations [17]. The simplest model is obtained by replacing $N_\nu - 1 \to N_\nu - \epsilon(N)\sqrt{N_\nu}$, where ϵ is a fit parameter close to 1 which allows one to achieve excellent agreement with the exact ground state [22]. An alternative way to include correlations was proposed by Ref. [21].

B. Comparison with simulation results for finite Yukawa crystals

In order to compare the density profile $n(r)$ of our continuous model with the density of discrete spherical Yukawa crystals, we performed molecular dynamics simulations of the ground state of a large number of Coulomb balls (for details, see Refs. [9,10]). As an example, the numerical results for a Coulomb ball with $N = 2000$ which is large enough to exhibit macroscopic behavior [18,19] are included in Fig. 4. The symbols denote the average particle density around each of the shells. The averaging was accomplished by substituting each particle by a small but finite sphere, so that a smooth radial density profile was obtained.

With increasing κ the crosses move towards the center, confirming the compression of the Coulomb balls observed before [10]. Obviously, the simulation results are very well

reproduced by the analytical density profile (11) of a continuous plasma. But there are also small discrepancies in the central part which grow continuously with κ. These are due to the neglect of the correlation contributions in the energy functional (2), which become important with increasing density.

V. SUMMARY AND DISCUSSION

In summary, we have presented a theoretical analysis of the ground-state density profile of spatially confined one-component plasmas in dependence on the form of the pair interaction. An explicit result for the density profile for an arbitrary confinement potential has been derived. In particular, for an isotropic confinement, we have found that screening of the Coulomb interaction substantially modifies the radial density distribution. In contrast to a bare Coulomb interaction for which the density inside a parabolic external potential is constant, for a screened interaction, a quadratic decay away form the center is found.

Interestingly, while our results were derived for a continuous density distribution (a macroscopic system) and with neglect of binary correlations, our analytical results agree very well also with first-principles simulation results for strongly correlated Coulomb and Yukawa clusters containing several thousands of particles for screening paramters $\kappa r_0 \lesssim 1$. For larger values of the screening parameter correlation contributions are significant [20]. The modification of the density profile by these correlation contributions and by finite-temperature effects, which are of importance, e.g., for dusty plasmas [23], deserve further analysis and will be the subject of forthcoming work.

APPENDIX: DERIVATION OF THE DENSITY PROFILE, Eq. (9)

The explicit expression for the density, Eq. (9), can be derived from the integral equation (8) by first splitting up the integral in the latter equation in two parts. One part contains the integration from 0 to r, the other part the integration from r to R:

$$\Phi(r) - \mu = -4\pi \frac{N-1}{N} Q^2 \left[\frac{e^{-\kappa r}}{\kappa r} \int_0^r dr' r' \tilde{n}(r') \sinh(\kappa r') \right.$$
$$\left. + \frac{\sinh(\kappa r)}{\kappa r} \int_r^R dr' r' \tilde{n}(r') e^{-\kappa r'} \right]. \quad \text{(A1)}$$

Thereby the modulus in the second exponent in Eq. (8) is removed and this expression can directly be differentiated with respect to r. The first and second derivatives are given by

$$\Phi'(r) = 4\pi \frac{N-1}{N} Q^2 \left[\frac{e^{-\kappa r}}{\kappa r} \left(\kappa + \frac{1}{r} \right) \int_0^r dr' r' \tilde{n}(r') \sinh(\kappa r') \right.$$
$$\left. + \left(-\frac{\cosh(\kappa r)}{r} + \frac{\sinh(\kappa r)}{\kappa r^2} \right) \int_r^R dr' r' \tilde{n}(r') e^{-\kappa r'} \right], \quad \text{(A2)}$$

$$\Phi''(r) = 4\pi \frac{N-1}{N} Q^2 \left\{ -\frac{e^{-\kappa r}}{\kappa r} \left[\left(\kappa + \frac{1}{r} \right)^2 + \frac{1}{r^2} \right] \right.$$
$$\times \int_0^r dr' r' \tilde{n}(r') \sinh(\kappa r')$$
$$+ \left(-\frac{\kappa \sinh(\kappa r)}{r} + \frac{2 \cosh(\kappa r)}{r^2} - \frac{2 \sinh(\kappa r)}{\kappa r^3} \right)$$
$$\left. \times \int_r^R dr' r' \tilde{n}(r') e^{-\kappa r'} + \tilde{n}(r) \right\}. \quad \text{(A3)}$$

The explicit expression for the density profile, Eq. (9), can then be obtained by considering the combination $\frac{2\Phi'(r)}{r} + \Phi''(r) - \kappa^2[\Phi(r) - \mu]$. After some algebra and cancellations one directly obtains $4\pi \frac{N-1}{N} Q^2 \tilde{n}(r)$; i.e., we recover the final result, Eq. (9). We mention that this result follows also as a special case of Eq. (21). In fact, in the case of an isotropic potential $\Delta \rightarrow \frac{\partial^2}{\partial r^2} + \frac{2}{r} \frac{\partial}{\partial r}$ and Eq. (21) reduces to Eq. (9).

[1] D. J. Wineland, J. C. Bergquist, W. M. Itano, J. J. Bollinger, and C. H. Manney, Phys. Rev. Lett. **59**, 2935 (1987).

[2] M. Drewsen, C. Brodersen, L. Hornekaer, J. S. Hangst, and J. P. Schiffer, Phys. Rev. Lett. **81**, 2878 (1998).

[3] J. B. Pieper, J. Goree, and R. A. Quinn, Phys. Rev. E **54**, 5636 (1996).

[4] M. Zuzic, A. V. Ivlev, J. Goree, G. E. Morfill, H. M. Thomas, H. Rothermal, U. Konopka, R. Sutterlin, and D. D. Goldbeck, Phys. Rev. Lett. **85**, 4064 (2000).

[5] Y. Hayashi, Phys. Rev. Lett. **83**, 4764 (1999).

[6] D. H. E. Dubin, and T. M. O'Neill, Rev. Mod. Phys. **71**, 87 (1999).

[7] O. Arp, D. Block, A. Piel, and A. Melzer, Phys. Rev. Lett. **93**, 165004 (2004).

[8] H. Totsuji, C. Totsuji, T. Ogawa, and K. Tsuruta, Phys. Rev. E **71**, 045401(R) (2005).

[9] P. Ludwig, S. Kosse, and M. Bonitz, Phys. Rev. E **71**, 046403 (2005).

[10] M. Bonitz, D. Block, O. Arp, V. Golubnychiy, H. Baumgartner, P. Ludwig, A. Piel, and A. Filinov, Phys. Rev. Lett. **96**, 075001 (2006).

[11] W. D. Kraeft and M. Bonitz, J. Phys.: Conf. Ser. **35**, 78 (2006).

[12] This variation procedure is analogous to Thomas-Fermi theory in atomic physics and density functional theory. A similar calculation for a two-dimensional Yukawa plasma has been per-

formed in Ref. [13] based on the local density approximation which is significantly less accurate than the present mean field result.

[13] H. Totsuji, C. Totsuji, and K. Tsuruta, Phys. Rev. E **64**, 066402 (2001).

[14] The procedure is the same as for the Coulomb interaction. See M. Bonitz and J. W. Dufty, Condens. Matter Phys. **7**, 483 (2004).

[15] If Φ is not 2 times differentiable, the problem has to be solved separately in space regions where the second derivative exists.

[16] R. W. Hasse and V. V. Avilov, Phys. Rev. A **44**, 4506 (1991).

[17] K. Tsuruta and S. Ichimaru, Phys. Rev. A **48**, 1339 (1993).

[18] H. Totsuji, T. Kishimoto, C. Totsuji, and K. Tsuruta, Phys. Rev. Lett. **88**, 125002 (2002).

[19] J. P. Schiffer, Phys. Rev. Lett. **88**, 205003 (2002).

[20] O. Arp *et al.*, J. Phys.: Conf. Ser. **11**, 234 (2005).

[21] H. Totsuji, T. Ogawa, C. Totsuji, and K. Tsuruta, Phys. Rev. E **72**, 036406 (2005).

[22] W. D. Kraeft and M. Bonitz, J. Phys.: Conf. Ser. **35**, 94 (2006).

[23] V. Golubnychiy, H. Baumgartner, M. Bonitz, A. Filinov, and H. Fehske, J. Phys. A **39**, 4527 (2006).

Ground state of a confined Yukawa plasma including correlation effects

C. Henning,[1] P. Ludwig,[1,2] A. Filinov,[1] A. Piel,[3] and M. Bonitz[1,*]

[1]*Institut für Theoretische Physik und Astrophysik, Christian-Albrechts-Universität zu Kiel, D-24118 Kiel, Germany*
[2]*Institut für Physik, Universität Rostock, Universitätsplatz 3, D-18051 Rostock, Germany*
[3]*Institut für Experimentelle und Angewandte Physik, Christian-Albrechts-Universität zu Kiel, D-24118 Kiel, Germany*

The ground state of an externally confined one-component Yukawa plasma is derived analytically using the local density approximation (LDA). In particular, the radial density profile is computed. The results are compared with the recently obtained mean-field (MF) density profile [Henning *et al.*, Phys. Rev. E **74**, 056403 (2006)]. While the MF results are more accurate for weak screening, the LDA with correlations included yields the proper description for large screening. By comparison with first-principles simulations for three-dimensional spherical Yukawa crystals, we demonstrate that the two approximations complement each other. Together they accurately describe the density profile in the full range of screening parameters.

I. INTRODUCTION

Interacting particles in confinement potentials are omnipresent in nature and laboratory systems such as trapped ions, e.g., [1,2], dusty plasmas, e.g., [3–5], or ultracold Bose and Fermi gases [6,7] and quantum confined semiconductor structures [8]. An interesting aspect of particle traps is that it is easy to realize situations of strong correlations. The observed particle arrangements extend from gaslike and liquid-like to solid behavior where the symmetry is influenced by the trap geometry. Of particular recent interest have been spherical traps, in which plasma crystals consisting of spherical shells (Yukawa balls) are formed, e.g., [9–11]. The particle distribution among the shells is by now well understood [11–13].

In a recent study [14], we also analyzed the average particle density in the trap and found that it is very sensitive to the binary interaction: it changes from a flat profile in the case of long-range Coulomb interaction to a profile rapidly decaying away from the trap center in the case of a screened Yukawa potential. Using a nonlocal mean-field (MF) approximation the density profile could be computed analytically and was found to agree very well with first-principles computer simulations for Yukawa crystals. However, when the screening is increased, deviations in the trap center kept growing, which was attributed to correlation effects missing in the mean-field model.

The goal of this paper is to remove these discrepancies. For this we extend the analysis of Ref. [14] by including correlation effects following an idea of Totsuji *et al.* [15] applied to two-dimensional systems. We apply the local density approximation (LDA) using known results [16] for the correlation energy of a homogeneous one-component Yukawa plasma. The results clearly confirm that correlation effects are responsible for the strong density increase in the trap center. We find that the LDA with correlations included agrees very well with simulations of Yukawa crystals in the limit of strong screening. On the other hand, for weak

screening, the previous MF result turns out to be more accurate. Interestingly, for intermediate values of the screening parameter both methods are accurate, so a combination of both allows one to quantitatively describe the density profile in the whole range of screening parameters.

This paper is organized as follows. In Sec. II we introduce the LDA and use it first to compute the density profile in a mean-field approximation, which, of course, gives worse results than a MF calculation, but helps to understand the LDA. Then in Sec. III we improve the LDA model by including correlation effects. In Sec. IV the results for the density profile are compared to molecular dynamics simulations. A discussion is given in Sec. V.

II. GROUND STATE OF A CONFINED PLASMA WITHIN THE LDA

We consider N identical particles with mass m and charge Q confined by an external potential Φ and interacting with the isotropic Yukawa-type pair potential $V(r)=(Q^2/r)\times\exp(-\kappa r)$. To derive the properties of interest we start with the expression of the ground-state energy, which is given by

$$E[n] = \int d^3r\, u(\mathbf{r}), \qquad (1)$$

with the energy density $u(\mathbf{r})=u^{\mathrm{conf}}(\mathbf{r})+u^{\mathrm{MF}}(\mathbf{r})+u^{\mathrm{cor}}(\mathbf{r})$, where the energy densities from confinement and from the mean-field interaction are

$$u^{\mathrm{conf}}(\mathbf{r}) = n(\mathbf{r})\Phi(\mathbf{r}), \qquad (2a)$$

$$u^{\mathrm{MF}}(\mathbf{r}) = n(\mathbf{r})\frac{N-1}{2N}\int d^3r_2\, n(\mathbf{r}_2)V(|\mathbf{r}-\mathbf{r}_2|). \qquad (2b)$$

The correlation contribution u^{cor} will be discussed below (Sec. III) by means of the local density approximation. First, we introduce this approximation and obtain first the LDA results in the mean-field approximation (LDA-MF). These results will not be as accurate as the MF results, due to the applied approximation, but the LDA-MF helps in familiarization with the LDA and its characteristics.

*bonitz@physik.uni-kiel.de

The local density approximation is based upon the idea of replacing the nonlocal terms within the energy density at point **r** by local expressions using the known energy density of the homogeneous system with its density n_0 equal to the local density $n(\mathbf{r})$ of the true inhomogeneous system in question. Therefore, to derive the LDA-MF we need to substitute for the nonlocal term (2b), i.e., for the density of interaction energy, the corresponding expression of the infinite homogeneous system, which is given by (details are given in the Appendix)

$$u_0(\kappa) = n_0 \frac{N-1}{2N} Q^2 \int d^3 r_2 n_0 \frac{e^{-\kappa|\mathbf{r}-\mathbf{r}_2|}}{|\mathbf{r}-\mathbf{r}_2|} = \frac{N-1}{N} Q^2 n_0^2 \frac{2\pi}{\kappa^2}, \tag{3}$$

and, as a second step, replace the homogeneous density n_0 by the local density $n(\mathbf{r})$. Thus we obtain the LDA-MF ground-state energy

$$E_{\text{LDA}}^{\text{MF}}[n] = \int d^3 r \, u(\mathbf{r}) \tag{4}$$

with the energy density

$$u(\mathbf{r}) = n(\mathbf{r}) \left(\Phi(\mathbf{r}) + \frac{N-1}{N} Q^2 n(\mathbf{r}) \frac{2\pi}{\kappa^2} \right). \tag{5}$$

The variation of the energy

$$\tilde{E}_{\text{LDA}}^{\text{MF}}[n,\mu] = E_{\text{LDA}}^{\text{MF}}[n] + \mu \left(N - \int d^3 r \, n(\mathbf{r}) \right) \tag{6}$$

with respect to the density $n(\mathbf{r})$ (for details see Ref. [14]) yields an explicit expression for the density profile in an arbitrary confinement potential,

$$n(\mathbf{r}) = \frac{N\kappa^2}{4\pi(N-1)Q^2} [\mu - \Phi(\mathbf{r})], \tag{7}$$

which holds at any point where the density is positive. Due to (6) this density is normalized by

$$\int d^3 r \, n(\mathbf{r}) = N. \tag{8}$$

The case of isotropic confinement $\Phi(\mathbf{r}) = \Phi(r)$, which is of particular interest, leads to an isotropic density distribution $n(\mathbf{r}) = n(r) = \tilde{n}(r)\Theta(R-r)$, the outer radius R of which is fixed by the normalization condition (8), which now becomes $\int_0^R dr \, r^2 \tilde{n}(r) = N/4\pi$. In this isotropic case the yet unknown Lagrange multiplier μ can be obtained by taking the variation also with respect to R [15], which yields

$$\mu = \Phi(R). \tag{9}$$

Compared to the MF result, which was given in [14],

$$n^{\text{MF}}(\mathbf{r}) = \frac{N}{4\pi(N-1)Q^2} [\Delta\Phi(\mathbf{r}) + \kappa^2 \mu^{\text{MF}} - \kappa^2 \Phi(\mathbf{r})], \tag{10}$$
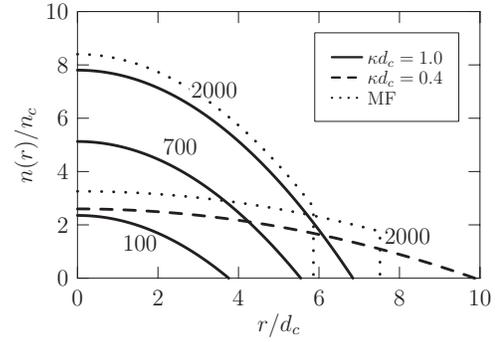

FIG. 1. Radial density profile for a parabolic confinement potential $\Phi(r) = (\alpha/2)r^2$, a constant screening parameter $\kappa d_c = 1$, and three different particle numbers $N = 100, 700, 2000$. The result for $\kappa d_c = 0.4$, $N = 2000$ is also shown by the dashed line. For comparison, the nonlocal MF results for $\kappa d_c = 0.4, 1.0$, $N = 2000$ are given by the dotted lines.

$$\mu^{\text{MF}} = \Phi(R^{\text{MF}}) + \frac{R^{\text{MF}} \Phi'(R^{\text{MF}})}{1 + \kappa R^{\text{MF}}}, \tag{11}$$

the LDA-MF density (7) shows important differences. On the one hand, the Laplacian of the potential $\Delta\Phi(\mathbf{r})$ is missing and, on the other hand, the expression for the chemical potential μ is simpler than μ^{MF}. That is based upon the fact that the missing terms contain derivatives and thus information about contiguous values of the potential, which is suppressed within the LDA-MF and generally within the LDA. Consequently, the finite density jump at $r = R$, which is familiar from electrostatics of charged bodies and appears in the MF approximation, Fig. 1, is not reproduced by the LDA-MF.

A. Parabolic confinement potential

For the case of a parabolic external potential $\Phi(r) = (\alpha/2)r^2$ the density following from Eqs. (7) and (9) is

$$n(r) = \frac{\alpha N}{4\pi(N-1)Q^2} \left(\frac{\kappa^2 R^2}{2} - \frac{\kappa^2 r^2}{2} \right) \Theta(R-r). \tag{12}$$

The dimensionless combination κR, which contains the limiting outer radius, can be obtained from the normalization (8) and is given by

$$\kappa R = \sqrt[5]{\frac{15(N-1)Q^2\kappa^3}{\alpha}} = \sqrt[5]{\frac{15}{2}(\kappa d_c)^3(N-1)}. \tag{13}$$

Here, we introduced the length scale $d_c = (2Q^2/\alpha)^{1/3}$, which is the stable distance between two charged particles in the absence of screening [11] and which will be used below as the proper unit for lengths and screening parameters. As the unit for densities we use the average density of a large Coulomb system, which is given by $n_c = (3\alpha)/(4\pi Q^2)$.

The results of (12) are shown in Fig. 1 for three particle numbers from $N = 100$ to 2000. One clearly sees the parabolic decrease of the density away from the trap center until it terminates in zero. The curvature of the density does not
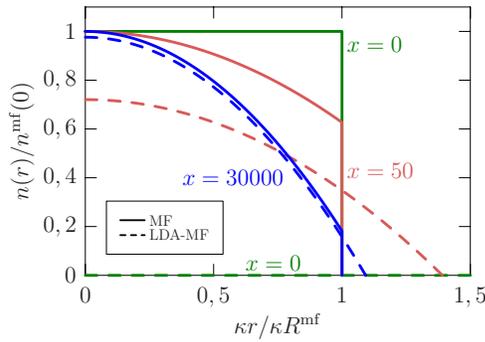
FIG. 2. (Color online) Radial MF density profile (solid lines) compared to the LDA-MF (dashed lines) for three different density parameters $x=(\kappa d_c)^3(N-1)$. The abscissa is normalized with the MF radius R^{MF}, while the ordinate is normalized with the corresponding MF density $n^{\mathrm{MF}}(0)$ at the trap center.

change on increasing the particle number—just the density increases continuously at every space point and, at the same time, extends to higher values of the limiting radius R. However, the curvature of the density profile changes dramatically when the plasma screening is increased at constant N.

Thus, in the case of an isotropic parabolic potential, the LDA density profile bears a qualitative resemblance to the density profile in the nonlocal mean-field approximation, although in the case of other confinement potentials the deviations of the LDA-MF from the MF approximation are stronger [cf. Eqs. (7) and (10)]. However, quantitatively at two points the MF result differs from the LDA-MF for parabolic confinement as well, as can also be seen in Fig. 1.

First, the density in this local density approximation does not show a discontinuity at $r=R$, in contrast to the MF result, Eqs. (10) and (11). This is due to the neglect of edge effects in this derivation of the LDA result. Second, the LDA-MF yields too small values of the density. This error is reduced (see Fig. 2) with increasing values of the density parameter $x=(\kappa d_c)^3(N-1)$ (cf. Ref. [14]), which, regardless of the factor $N/(N-1)$, solely determines the density profile. The reason for this improved behavior with increasing x is that an increase of κ contracts the effective area of integration within (2b) as well as within (3). The contraction finally is in favor of the accuracy of the LDA-MF, because the decreased integration volume contains a more homogeneous density. Also, an increase of the particle number N, which flattens the density profile, will similarly improve the LDA-MF.

Because the validity of the mean-field model depends on the value of the screening parameter κd_c, there are the following two cases. In the first case, for small values of the screening parameter, the MF approximation provides a good description of the density profile, but the LDA-MF underrates this profile and so does not give a good description on its own. (That applies also if finite-size effects are included; see Fig. 3.) In the second case, for large values of the screening parameter, the LDA-MF approaches the MF approximation; however, there, the latter does not describe the density profile correctly due to the neglect of the now relevant correlation contributions [15]. Thus, the local density approximation of the mean-field energy alone does not give a good description of the density profile.
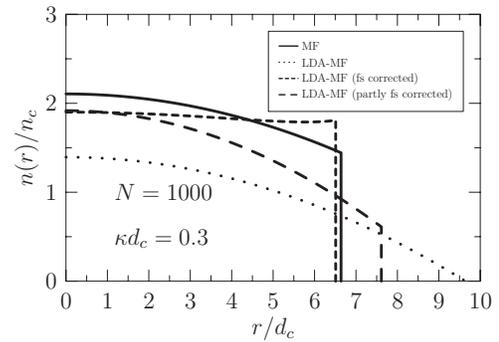

FIG. 3. Radial density profiles of a spherical plasma of $N =1000$ and $\kappa d_c=0.3$ calculated by the LDA-MF with (fs corrected) and without finite-size effects included. For comparison, the exact MF result is also given (solid line). The difference between the finite-size correction and the partial finite-size correction is described in the text.

However, it gives a straightforward way to include the missing correlation contributions in the energy density by usage of the result for the homogeneous system; see Sec. III.

B. Improvement of the LDA by inclusion of finite-size effects

As can be seen from Fig. 2 and from Eq. (7) the density profile obtained by the LDA-MF breaks down in the Coulomb case—the density can no longer be normalized, which is the same as in the two-dimensional case [15]. But the application of a local density approximation cannot be the reason for this, because the method of the LDA is based upon the usage of results from the homogeneous system, and the Coulomb system is homogeneous with $n_0=[N/(N-1)]n_c$.

In fact, the cause of the breakdown is the use of results from the infinite homogeneous system, neglecting finite-size effects. This failure can be avoided by replacing (3) by the corresponding expression for the finite homogeneous system. In the Appendix such an expression is derived for isotropic confinement. As a result, the finite-size effects lead to a corrected density profile

$$n(r) = \frac{N\kappa^2}{4\pi(N-1)Q^2} \frac{\mu - \Phi(r)}{1 - e^{-\kappa R}(1 + \kappa R)\sinh(\kappa r)/(\kappa r)} \times \Theta(R-r), \tag{14}$$

instead of Eq. (7), which indeed yields the constant MF solution in Coulomb case also for the LDA-MF. As another example, in Fig. 3 the density profiles with [LDA-MF (fs corrected)] and without these finite-size contributions are shown for $N=1000$, $\kappa d_c=0.3$. One clearly sees that in the case of finite-size correction the density profile shows a discontinuity at the boundary and, due to that, it yields increased values of the density. However, the density profile including edge effects is not monotonically decreasing away from the trap center but has a density-increasing part in the outer range, which is not correct. This is due to the space dependence of the denominator of Eq. (14).

By contrast a more accurate monotonically decreasing density profile can also be obtained by taking the finite-size effects only partly into account [LDA-MF (partly fs corrected)], as derived in the Appendix. The final result is given by

$$n(r) = \frac{N\kappa^2}{4\pi(N-1)Q^2} \frac{\mu - \Phi(r)}{1 - e^{-\kappa R}(1 + \kappa R)} \Theta(R - r), \quad (15)$$

which now misses the r dependence in the denominator. The corresponding result is also given in Fig. 3.

Consequently, for Yukawa systems like those analyzed here, an improvement of LDA is possible by including edge effects. However, for small values of the screening parameter even the improved local density approximation does not approach the degree of accuracy obtained by the nonlocal mean-field model MF (cf. Fig. 3). On the other hand, for increased screening the finite-size effects do not alter the density profile significantly.

Therefore, below we continue to use Eq. (3) from the infinite homogeneous system.

III. INCLUSION OF CORRELATION CONTRIBUTIONS

The energy expression $E_{\text{LDA}}^{\text{MF}}$ (4), (5) contains only the energy density of the confinement and of the mean-field interaction. To include the contribution of the particle correlations, we can make use of the result for the density of the correlation energy of the homogeneous system which is given by Eq. (3) of Ref. [16]:

$$u^{\text{cor}}(n_0, \kappa) = -1.444 Q^2 n_0^{4/3} \exp[-0.375\kappa n_0^{-1/3} + 7.4 \times 10^{-5}(\kappa n_0^{-1/3})^4], \quad (16)$$

where n_0 is the corresponding density of the homogeneous system. By replacing this density with the local density $n(\mathbf{r})$ of the inhomogeneous system, one obtains the correlation contribution of the energy density within the LDA. Thus we derive the complete ground-state energy in the local density approximation,

$$E_{\text{LDA}}[n] = \int d^3 r \, u(\mathbf{r}), \quad (17)$$

with energy density

$$u(\mathbf{r}) = n(\mathbf{r})\Phi(\mathbf{r}) + \frac{N-1}{N} Q^2 n(\mathbf{r})^2 \frac{2\pi}{\kappa^2} - 1.444 Q^2 n(\mathbf{r})^{4/3}$$
$$\times \exp\{-0.375\kappa n(\mathbf{r})^{-1/3} + 7.4 \times 10^{-5}[\kappa n(\mathbf{r})^{-1/3}]^4\}. \quad (18)$$

As before, variation of the energy (17) at constant particle number [cf. Eq. (6)] yields the ground-state density profile, but now with correlation effects included. In this case the strong nonlinear character of the energy density does not allow for an explicit solution. Just an implicit solution is possible and is given by the following equation for $z^3(\mathbf{r}) = \kappa^{-3} n(\mathbf{r})$, which can be regarded as the local plasma parameter of the system:
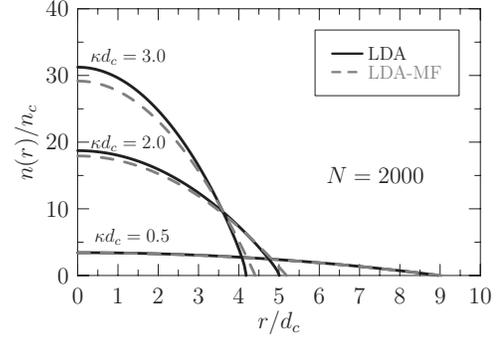

FIG. 4. Radial density profile of a confined spherical plasma of $N=2000$ particles calculated with the LDA including correlation contributions (solid lines) compared to the LDA-MF (dashed lines) for three different screening parameters.

$$0 = \frac{N-1}{N} z^3(\mathbf{r}) + \frac{\Phi(\mathbf{r}) - \mu}{4\pi Q^2 \kappa} - [c_1 z(\mathbf{r}) + c_2 - c_3 z(\mathbf{r})^{-3}]$$
$$\times \exp[-0.375 z(\mathbf{r})^{-1} + 7.4 \times 10^{-5} z(\mathbf{r})^{-4}]. \quad (19)$$

The constants c_i are given by

$$c_1 = 0.153, \quad (20a)$$

$$c_2 = 0.0144, \quad (20b)$$

$$c_3 = 1.134 \times 10^{-5}. \quad (20c)$$

The solution of Eq. (19) can be obtained numerically. For the case of a parabolic external potential $\Phi(r) = (\alpha/2)r^2$ results are given in Fig. 4. There, the density profile of a plasma of $N=2000$ particles within LDA is shown for three different screening parameters: $\kappa d_c = 0.5$, 2.0, and 3.0. For comparison the LDA-MF density profile is shown, too.

It can be seen that for a small screening parameter (see the line $\kappa d_c = 0.5$) both density profiles are nearly identical. But with increasing screening, i.e., for smaller values of the local plasma parameter z^3, the correlation contributions within the LDA alter the curvature of the profile, which rises more steeply toward the center. So the particle correlations tend to increase the central density of the plasma, which can also be seen in Fig. 6 in comparison with the mean-field approximation.

IV. COMPARISON WITH SIMULATION RESULTS FOR FINITE YUKAWA CRYSTALS

We performed molecular dynamics simulations of the ground state of a large number of Coulomb balls for the purpose of comparison of their average density with the analytical results of the present model (for simulation details, see Refs. [10,11]). In order to obtain a smooth average radial density profile, the averaging process was accomplished by substituting for each particle a small but finite sphere. In Fig. 5 these smoothed density profiles are shown for different sphere radii of the particles: $0.3d_c$, $0.4d_c$, and $0.5d_c$. Also the average particle densities in the vicinity of the corresponding shells are shown (crosses). Note that there is only a small
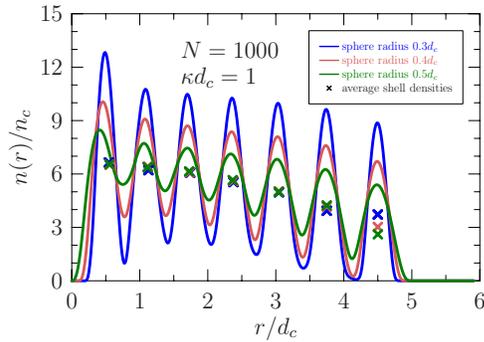
FIG. 5. (Color online) Smoothed density of a simulated spherical Yukawa crystal with $N=1000$ and $\kappa d_c=1$ with application of different sphere sizes for substitution of the particles: $0.3d_c$ (top curve), $0.4d_c$ and $0.5d_c$. The symbols show the averaged densities of the shells placed on the centers of mass of the shells.

range of reasonable sphere radii: for values smaller than $0.3d_c$ the shells break up into subshells, whereas for values larger than $0.5d_c$ the amplitude of the oscillations decreases further without effect on the average density. Only the outer shell density is somewhat sensitive to the sphere radius due to the increase of the size of this shell with increasing sphere radius. Therefore, for the comparisons below, we use the sphere radius corresponding to the average of the possible density values which, in the figure, is close to the value for $0.4d_c$.

Numerical results of the comparison with a Coulomb ball of $N=1000$ particles are included in Fig. 6 for four different screening parameters. The symbols denote the average shell density, while the lines represent the MF (solid) and the LDA density (dashed). For small values of the screening parameter $\kappa d_c<2$ the simulation results are very well reproduced by the analytical density profile of the nonlocal mean-field model (MF), whereas the local density approximation underrates the results [lower lines in Fig. 6(a)]. On the other hand, for larger values of the screening parameter $\kappa d_c>2$ the simulation results are reproduced by the LDA, whereas MF underestimates these results in the center. This underestimation is accompanied by a wrong prediction of the profile curvature [Fig. 6(b)]. For intermediate values of the screening parameter $\kappa d_c \approx 2$, both methods are very close to the averaged simulation results [upper lines in Fig. 6(a)]. We have verified this behavior also for other Coulomb balls. Another representative example is shown in Fig. 7 for a Coulomb ball with $N=10\,000$. There, the same behavior as in Fig. 6 is seen.

V. SUMMARY AND DISCUSSION

A theoretical analysis of the ground-state density profile of a spatially confined one-component plasma within the local density approximation was presented. We derived a closed equation, Eq. (19), for the density profile, including correlation effects for arbitrary confinement potentials with any symmetry. In contrast to the result without particle correlations, the density profile shows an increased central density with increasing screening parameter. The validity of the
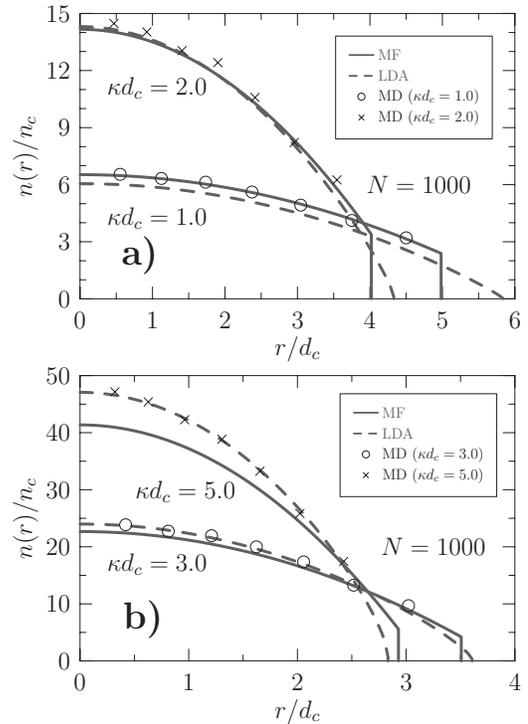

FIG. 6. Radial density profiles of a three-dimensional plasma of $N=1000$ particles calculated with the exact mean-field model (solid lines) and with the LDA including correlation contributions (dashed lines) for four different screening parameters: $\kappa d_c=1$, 2, 3, and 5. Averaged shell densities of molecular dynamics results of a plasma crystal for the same parameters are shown by the symbols. For details, see the discussion in Sec. IV.

LDA is, however, limited to not too small values of the screening parameter, $\kappa d_c \gtrsim 2$.

Comparisons with first-principles simulation results of strongly correlated Coulomb clusters with varying screening parameter showed that the LDA allows one to remove the problem of the MF approximation observed in Ref. [14] which arises with increasing screening parameter. Therefore,
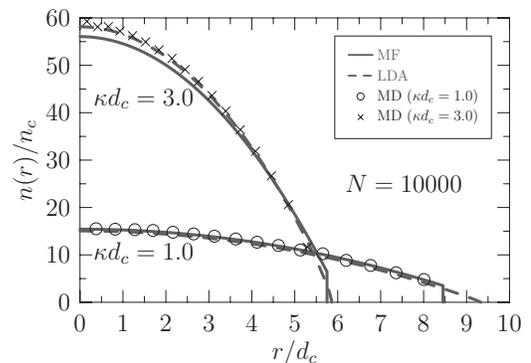

FIG. 7. Radial density profiles of a three-dimensional plasma with $N=10\,000$ and two different screening parameters ($\kappa d_c=1$, $\kappa d_c=3$). The solid (dashed) lines show MF (LDA) calculation results. Symbols denote molecular dynamics results of a plasma crystal for the same parameters where the average density at the positions of the shells is shown.

the mean-field model together with the presented local density approximation complement one another in the description of strongly correlated spatially confined one-component plasmas.

APPENDIX: LOCAL DENSITY APPROXIMATION USING A FINITE REFERENCE SYSTEM

The investigation of an inhomogeneous system within the LDA uses known results from the corresponding homogeneous system. There, the infinite homogeneous system is often used as a reference system, which entails the neglect of finite-size effects. To take these into account, the finite homogeneous system has to be used as reference. In the present derivation such a modification is made for an isotropic confinement and leads to a change of the expression for the density of interaction energy, Eq. (3),

$$
\begin{aligned}
u_0(\kappa) &= n_0 \frac{N-1}{2N} Q^2 \int d^3 r_2 n_0 \frac{e^{-\kappa|\mathbf{r}-\mathbf{r}_2|}}{|\mathbf{r}-\mathbf{r}_2|} \\
&= n_0^2 \frac{N-1}{2N} Q^2 \int dr_2 \, 4\pi r_2^2 \frac{e^{-\kappa r_2}}{r_2} \\
&= \frac{N-1}{N} Q^2 n_0^2 \frac{2\pi}{\kappa^2}.
\end{aligned} \tag{A1}
$$

This formula has no spatial dependence due to the infinite integration volume and it diverges in the limit of Coulomb interaction ($\kappa \to 0$), leading to a breakdown of the approximation.

By contrast, the density of interaction energy of the corresponding finite homogeneous system (a sphere with center $\mathbf{r}_2 = \mathbf{0}$ and radius R) is given by

$$
\begin{aligned}
u_0(\kappa, r) &= n_0 \frac{N-1}{2N} Q^2 \int_{\mathcal{S}(0,R)} d^3 r_2 n_0 \frac{e^{-\kappa|\mathbf{r}-\mathbf{r}_2|}}{|\mathbf{r}-\mathbf{r}_2|} \\
&= n_0^2 \frac{N-1}{2N} Q^2 \frac{2\pi}{\kappa r} \int_0^R dr_2 r_2 (-e^{-\kappa(r+r_2)} + e^{-\kappa|r-r_2|}) \\
&= n_0^2 \frac{N-1}{2N} Q^2 \frac{4\pi}{\kappa r} \left(e^{-\kappa r} \int_0^r dr_2 r_2 \sinh(\kappa r_2) \right. \\
&\quad \left. + \sinh(\kappa r) \int_r^R dr_2 \, r_2 e^{-\kappa r_2} \right) \\
&= \frac{N-1}{N} Q^2 n_0^2 \frac{2\pi}{\kappa^2} \left(1 - e^{-\kappa R}(1 + \kappa R) \frac{\sinh(\kappa r)}{\kappa r} \right),
\end{aligned} \tag{A2}
$$

including a finite-size contribution, which prevents the problem of divergence at $\kappa \to 0$. As already mentioned in Sec.
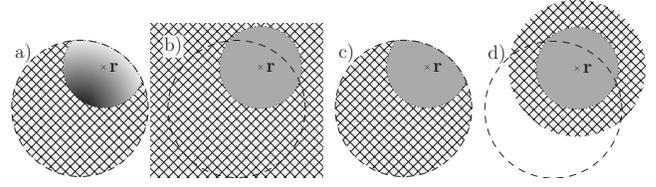

FIG. 8. Comparison of the MF method and the different LDA methods for calculating the energy density of interaction $u^{\mathrm{MF}}(\mathbf{r})$ in the case of finite screening: (a) MF, (b) LDA (infinite reference system), (c) LDA (fs corrected), and (d) LDA (partly fs corrected). Within the graphics the system is represented by the dashed line. The hatched region shows the integration area used within the method, whereas the solid gray region shows the effective integration area due to finite screening. The color gradient within (a) represents the nonconstant density of the system, which is taken into account within the MF method in contrast to the LDA methods, which take the density at point $\mathbf{r}$ for the whole integration area.

II B the resulting density profiles show the incorrect behavior of a nonmonotonic density profile (cf. Fig. 3).

An improved correction, which partly takes edge effects of the system into account too, can be obtained by using the finite homogeneous sphere centered not at $\mathbf{r}_2 = \mathbf{0}$ but at $\mathbf{r}_2 = \mathbf{r}$, i.e., on the point where we are calculating the density of interaction energy,

$$
\begin{aligned}
u_0(\kappa, r) &= n_0 \frac{N-1}{2N} Q^2 \int_{\mathcal{S}(\mathbf{r},R)} d^3 r_2 n_0 \frac{e^{-\kappa|\mathbf{r}-\mathbf{r}_2|}}{|\mathbf{r}-\mathbf{r}_2|} \\
&= n_0^2 \frac{N-1}{N} Q^2 2\pi \int_0^R dr_2 r_2 e^{-\kappa r_2} \\
&= \frac{N-1}{N} Q^2 n_0^2 \frac{2\pi}{\kappa^2} [1 - e^{-\kappa R}(1 + \kappa R)].
\end{aligned} \tag{A3}
$$

This expression also has no divergent limit for $\kappa \to 0$, and, at the same time, yields monotonically decreasing density profiles as can also be seen in Fig. 3.

All these methods described above are compared, together with the MF approximation, in Fig. 8 showing the (effective) integration area of the methods. First consider the Coulomb case, i.e., that where the solid regions fill out the hatched ones and where the density is constant within the MF method too. There, the integration in Fig. 8(a) is equal to that in Fig. 8(c); thus the density obtained by the LDA (fs corrected) is equal to that of the MF method. In contrast to that, the effective integration area within Fig. 8(b) is infinite, leading to the breakdown mentioned above. In the case of finite screening, where effectively the integration area is reduced, Figs. 8(a) and 8(c) still have the same region of integration. But the constant approximation within Fig. 8(c), in contrast to Fig. 8(a), leads to an underestimation of the energy density in the outer region of the system—the high values of density toward the center will be ignored. Eventually this leads to the nonmonotonic density profile of the LDA (fs corrected). By contrast, Fig. 8(d) features an additional effective integration region, which partly prevents the underestimation, leading to the more accurate density profile of the LDA (partly fs corrected).

[1] D. J. Wineland, J. C. Bergquist, W. M. Itano, J. J. Bollinger, and C. H. Manney, Phys. Rev. Lett. **59**, 2935 (1987).

[2] M. Drewsen, C. Brodersen, L. Hornekaer, J. S. Hangst, and J. P. Schiffer, Phys. Rev. Lett. **81**, 2878 (1998).

[3] J. B. Pieper, J. Goree, and R. A. Quinn, Phys. Rev. E **54**, 5636 (1996).

[4] M. Zuzic, A. V. Ivlev, J. Goree, G. E. Morfill, H. M. Thomas, H. Rothermel, U. Konopka, R. Sütterlin, and D. D. Goldbeck, Phys. Rev. Lett. **85**, 4064 (2000).

[5] Y. Hayashi, Phys. Rev. Lett. **83**, 4764 (1999).

[6] Y. Ohashi, Phys. Rev. A **70**, 063613 (2004).

[7] C. J. Pethick and H. Smith, *Bose-Einstein Condensation in Dilute Gases* (Cambridge University Press, New York, 2002).

[8] A. Filinov, M. Bonitz, and Yu. Lozovik, Phys. Rev. Lett. **86**, 3851 (2001).

[9] H. Totsuji, C. Totsuji, T. Ogawa, and K. Tsuruta, Phys. Rev. E **71**, 045401(R) (2005).

[10] P. Ludwig, S. Kosse, and M. Bonitz, Phys. Rev. E **71**, 046403 (2005).

[11] M. Bonitz, D. Block, O. Arp, V. Golubnychiy, H. Baumgartner, P. Ludwig, A. Piel, and A. Filinov, Phys. Rev. Lett. **96**, 075001 (2006).

[12] V. Golubnychiy, H. Baumgartner, M. Bonitz, A. Filinov, and H. Fehske, J. Phys. A **39**, 4527 (2006).

[13] H. Baumgartner, H. Kählert, V. Golubnychiy, C. Henning, S. Käding, A. Melzer, and M. Bonitz, Contrib. Plasma Phys. **47**, 281 (2007).

[14] C. Henning, H. Baumgartner, A. Piel, P. Ludwig, V. Golubnichiy, M. Bonitz, and D. Block, Phys. Rev. E **74**, 056403 (2006).

[15] H. Totsuji, C. Totsuji, and K. Tsuruta, Phys. Rev. E **64**, 066402 (2001).

[16] H. Totsuji, J. Phys. A **39**, 4565 (2006).

4.3 Melting of Trapped Few-Particle Systems

In small confined systems predictions for the melting point strongly depend on the choice of quantity and on the way it is computed, even yielding divergent and ambiguous results. We present a very simple quantity that allows us to control these problems – the variance of the block averaged interparticle distance fluctuations (VIDF). Further, it is shown how many particles are required to reliably detect liquid or solid behaviour and the melting point in a few-particle system.

The results were published as refereed journal publication:

4.3.1 *Melting of Trapped Few-Particle Systems,*
J. Böning, A. Filinov, P. Ludwig, H. Baumgartner, M. Bonitz, and Yu.E. Lozovik, Physical Review Letters **100**, 113401 (2008)

Melting of Trapped Few-Particle Systems

J. Böning,[1] A. Filinov,[1] P. Ludwig,[1] H. Baumgartner,[1] M. Bonitz,[1] and Yu. E. Lozovik[2]

[1]*Institut für Theoretische Physik und Astrophysik, Christian-Albrechts-Universität zu Kiel, D-24098 Kiel, Germany*
[2]*Institute for Optics and Spectroscopy of the RAS, Troitsk, Russia*
(Received 8 November 2007; published 20 March 2008)

In small confined systems predictions for the melting point strongly depend on the choice of quantity and on the way it is computed, even yielding divergent and ambiguous results. We present a very simple quantity that allows us to control these problems—the variance of the block averaged interparticle distance fluctuations.

Crystallization and melting and, more generally, phase transitions are well known to pertain to very large systems only. At the same time, solidlike or liquidlike behavior has been observed in finite systems containing only 100 or even 10 particles and is becoming of increasing interest in many fields of physics, chemistry, and beyond. Current examples include bosonic crystals and supersolids, e.g., [1], electrons or excitons in quantum dots [2], ions in traps [3], dusty plasma crystals [4], atomic clusters [5,6], polymers [7], etc. The notion of liquid and solid "phases" has been used successfully to characterize qualitatively different behaviors that resemble the corresponding properties in macroscopic systems and will be used here as well, following the definition of Ref. [6]. From the existence of phaselike states in very small systems arises the fundamental question of how to characterize phase changes and, further, how many particles it takes at least to observe a phase transition.

In macroscopic systems a solid-liquid transition can be verified by a variety of quantities including free energy differences, order parameters, specific heat, transport properties, structure factors, correlation functions and so on, e.g., [6,8,9], which yield more or less equivalent results for the melting point. A particularly simple and transparent quantity is magnitude of the particle position fluctuations normalized to the interparticle distance (Lindemann ratio u_L); for an overview see [9]. But when applied to two-dimensional (2D) systems, u_L shows a logarithmic divergence with system size [10]. This led to modified definitions, including the relative interparticle distance fluctuations (IDF) [11–13]

$$u_{\text{rel}} = \frac{2}{N(N-1)} \sum_{1 \le i < j}^{N} \sqrt{\frac{\langle r_{ij}^2 \rangle}{\langle r_{ij} \rangle^2} - 1}, \qquad (1)$$

which are also well behaved in macroscopic 2D and 1D systems. Here $r_{ij} = |\mathbf{r}_i - \mathbf{r}_j|$ is the distance between two particles and $\langle \ldots \rangle$ denotes thermal averaging. In macrosopic systems u_{rel} shows a jump at the melting point, which clearly reflects the increased delocalization of particles in the liquid phase compared to a crystal.

However, when applied to small systems, $N < 100$, neither u_L nor u_{rel} exhibit a jump upon classical or quan-

tum melting, but rather a continuous increase over some finite temperature or density interval—a familiar finite size effect [2,5]. Thus, it is problematic to determine a transition point and the critical magnitude of the fluctuations $u_{\text{rel}}^{\text{crit}}$. Even worse, the results for u_{rel} and the melting point depend crucially on the method of calculation and on its duration. Increasing the length of a simulation (and the expected accuracy) may lead to growing systematic errors predicting a too low melting temperature, as was noted by Frantz [5]. This is, of course, critical for reliable computer simulation of phase transitions in finite systems. In this Letter, we analyze the reasons for this behavior and present a solution. We propose a novel quantity, the variance of the block averaged interparticle distance fluctuations, which is sensitive to melting transitions and does not exhibit the convergence problems of u_{rel}. We demonstrate the behavior of this quantity for both classical and quantum melting by performing classical Monte Carlo (MC) and path integral Monte Carlo (PIMC) simulations, respectively.

Model and parameters.—While our approach is generally applicable, we concentrate on strongly correlated classical or quantum particles in a parabolic trap in 2D and 3D described by the Hamiltonian

$$\hat{H} = \sum_{i=1}^{N} \frac{\hat{\mathbf{p}}_i^2}{2m} + \sum_{i=1}^{N} \frac{m}{2} \omega^2 \mathbf{r}_i^2 + \sum_{1 \le i < j}^{N} \frac{e^2}{|\mathbf{r}_i - \mathbf{r}_j|}. \qquad (2)$$

The system is in a heat bath with temperature T and has a fixed particle number N (canonical ensemble). Below we use the dimensionless temperature $k_B T r_0 / e^2 \rightarrow T$ where r_0 denotes the ground state interparticle distance in the $N = 2$ case, $r_0^3 = 2e^2 / m\omega^2$. For quantum systems, the coupling parameter is $\lambda = e^2 / (l_0 \hbar \omega)$ where l_0 is the oscillator length $l_0^2 = \hbar / (m\omega)$. The ground state of this system consists of concentric spherical rings (2D) (cf. Fig. 1) or shells (3D) [3,4]. This model has the advantage that classical melting (by temperature increase) and quantum melting (via compression by increasing ω), including spin effects, can be analyzed on equal footing [2,14].

Liquid and solid phases.—The potential energy landscape of the system (2) has numerous local minima but, in contrast to other finite systems such as atomic clusters [6,7], they are not associated with phases but rather corre-
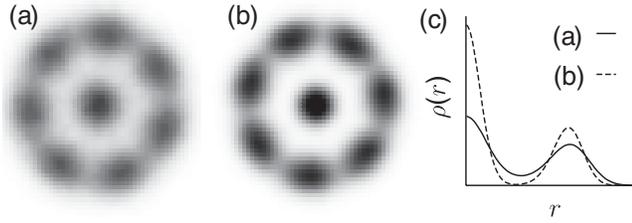
FIG. 1. Configuration of a 2D trapped quantum system [Eq. (2)] of $N = 8$ spin-polarized bosons at a temperature close to the ground state. (a),(b) The liquidlike ($\lambda = 14$) and solidlike ($\lambda = 30$) states, respectively. (c) The corresponding radial density profiles $\rho(r)$.

spond to the ground state and metastable states (e.g., different shell configurations), which often are energetically very close, e.g., [15]. With increasing temperature, an increasing number of these states becomes occupied. Melting proceeds as an isomerization transition with the system switching rapidly between a fast growing number of different configurations above some threshold temperature [16].

However, with reduction of N the number of stationary states decreases until only the ground state remains. This is the case for $N = 4$ in 2D, which, due to its simplicity, allows for a transparent analysis of melting processes in the system (2). The pair distances show a characteristic behavior as a function of simulation time (MC step) k; cf. Fig. 2(a): oscillations around some average value followed by a jump to a different value and again oscillations around a different mean and so on. This is readily understood: in its ground state the particles occupy the corners of a square of length a, so there exist two possible values for the six pair distances, a and the diagonal $b = \sqrt{2}a$, which are the mean values around which the distances fluctuate. A jump occurs whenever two particles, i and j, exchange their positions. Then the distances r_{ik} and r_{jk} to the remaining particles will change. While this leads to the same ground state (permutational isomer) this process costs energy associated with overcoming of a potential energy barrier. With increasing temperature, the frequency ν_j of these jumps grows steadily until around $T = T_2$ a rapid growth of ν_j is observed. Finally, at $T = T_4$, pair exchanges occur constantly [bottom of Fig. 2(a)], and particles are practically delocalized. This behavior of ν_j clearly resembles a "phase transition" with the melting point being located in between the two limits T_1 (solid) and T_4 (liquid).

We verify this hypothesis by computing the IDF, Eq. (1); cf. Fig. 2(b). At low temperatures, u_{rel} is small, slowly increasing with T. Around $T = T_2$ the increase steepens slightly (rightmost curve). Aiming for a higher accuracy, we repeated the calculations by subsequently increasing the simulation length L (MC steps) by factors 10, 100, 1000. With no evident convergence, this effectively shifts u_{rel} towards smaller temperatures and deeper into the solidlike regime where jumps are very rare. Thus, the results for u_{rel} are ambiguous and unreliable. The reason is that even
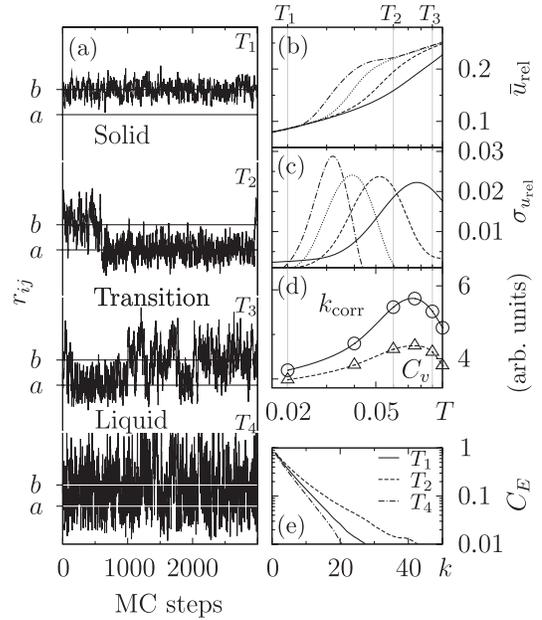

FIG. 2. (a) Distance of an arbitrary pair of $N = 4$ classical particles in 2D as a function of the MC step. From top to bottom: $T_1 = 0.02$ (solidlike), $T_2 = 0.06$ and $T_3 = 0.09$ (transition region), and $T_4 = 0.5$ (liquidlike). a and $b = \sqrt{2}a$ denote the two possible interparticle distances in the ground state. (b) Temperature dependence of the mean block averaged IDF $\bar{u}_{rel}$, for different block lengths $M = 10^3$, 10^4, 10^5, 10^6 (right to left) [equivalent to computing u_{rel}, Eq. (1), from multiple simulations of length $L = M$]. (c) The corresponding second moment $\sigma_{u_{rel}}$, Eq. (3). (d) Specific heat C_v and energy correlation time k_{corr}. (e) Total energy autocorrelation function C_E, Eq. (4), for three temperatures.

rare jumps will be eventually captured if L is sufficiently long. This immediately leads to a significant increase of u_{rel} emulating liquidlike behavior [17]. Similar observations were made for clusters [5].

Solution of the convergence problem of u_{rel}.—We solve this problem by subdividing the time sequence in K blocks of equal length M ($L = KM$) and compute the block averaged IDF $u_{rel}(s)$ according to Eq. (1) for each block [18,19] and its mean $\bar{u}_{rel} = K^{-1} \sum_{s=1}^{K} u_{rel}(s)$. To suppress the influence of jumps to $\bar{u}_{rel}$ in the solid regime, M must be chosen small enough to restrict jump-related contributions to a small number of blocks and, at the same time, large enough to allow for convergence of contributions related to local vibrations. This choice does not influence the convergence of $\bar{u}_{rel}$ in the liquid regime, which is dominated by frequent jumps on a time scale comparable to that of local vibrations and, hence, well below M. We demonstrate the behavior of $u_{rel}(s)$ for a quantum phase transition of $N = 8$ bosons in 2D; cf. Fig. 3. In the solid regime the rare spikes of $u_{rel}(s)$ in the otherwise flat curve indicate blocks containing one jump resulting in a sharply peaked probability distribution $P(u_{rel})$. In the transition region, each block may "catch" from zero to a few jumps, so the
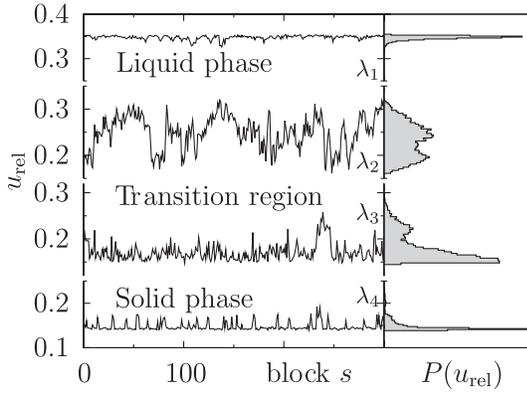
FIG. 3. Left: Typical behavior of the block averaged IDF vs
block number s for $N = 8$ charged bosons in 2D (cf. Fig. 1) for
different coupling strengths: $\lambda_1 = 14$, $\lambda_2 = 22$, $\lambda_3 = 26$, and
$\lambda_4 = 30$. Each point is an average over a block of length $M =
1000$. Right: Histograms show the probability P of different
values $u_{\rm rel}$ averaged over a total of 9,000 blocks. Results are
from PIMC simulations of system (2).

fluctuations of $u_{\rm rel}(s)$ increase and $P(u_{\rm rel})$ broadens.
Finally, in the liquid regime, jumps occur with an almost
constant rate in every block, so the fluctuations of $u_{\rm rel}(s)$
are small, though its mean is shifted to a higher value above
0.3.

Consequently, the width of the distribution $P(u_{\rm rel})$
reaches a maximum in the vicinity of the melting transi-
tion. This behavior is well captured by the second moment
of $u_{\rm rel}(s)$, i.e., the variance of the block averaged interpar-
ticle distance fluctuations (VIDF)

$$\sigma_{u_{\rm rel}} = \frac{1}{K} \sum_{s=1}^{K} \sqrt{\langle u_{\rm rel}^2(s) \rangle - \langle u_{\rm rel}(s) \rangle^2}. \qquad (3)$$

This allows us to obtain a reasonable estimate of the
melting temperature $T_u^{\rm crit}$ from the peak of $\sigma_{u_{\rm rel}}(T)$ [20].
Note that $\bar{u}_{\rm rel}$ is sensitive to the jump frequency ν_j, in
contrast to $u_{\rm rel}$ of Eq. (1). The sensitivity does depend on
the block length M: larger M cause an increase of $\bar{u}_{\rm rel}$ (as
discussed before) and shift the maximum of $\sigma_{u_{\rm rel}}$ to lower
temperatures; cf. Figs. 2(b) and 2(c).

Hence, to properly choose M, an independent quantity is
needed that should not require block averaging and be
invariant with respect to particle exchanges and pair dis-
tance jumps. A quantity fulfilling these requirements is the
total energy E and its autocorrelation function,

$$C_E(k) = \frac{\sum_{i=1}^{L-k}(E_{i+k} - \langle E \rangle)(E_i - \langle E \rangle)}{(L - k)(\langle E^2 \rangle - \langle E \rangle^2)}. \qquad (4)$$

We found that the decay rate of $C_E(k)$ varies nonmonotoni-
cally with temperature where the slowest decay is observed
just in the transition region; cf. the example shown in
Fig. 2(e). This suggests that the correlation time, $k_{\rm corr}(T) =
\sum_k C_E(k, T)$ (cf. Fig. 2(d)), is sensitive to thermal melting,

allowing us to identify the melting temperature $T_E^{\rm crit}$ from
the maximum of $k_{\rm corr}$. Comparing the values $T_E^{\rm crit}$ and
$T_u^{\rm crit}(M)$ provides a straightforward way to identify the
proper block length M. In all cases of thermal melting
we investigated that agreement is found for M in the range
of $1000, \ldots, 10000$, where the common definition of a
Monte Carlo step is used [21].

We mention that in the case of quantum melting the
situation is more complex. Nevertheless, we found that the
same range of M seems appropriate as well; however, the
analysis requires us to use a combination of different
quantities such as the pair distribution or bond angular
symmetry parameters, etc.

Applications.—We have verified the behavior of the
VIDF, $\sigma_{u_{\rm rel}}$, for a large variety of classical and quantum
systems described by Eq. (2) of various sizes and dimen-
sionality. As a first illustration we show in Fig. 4 (left side)
MC results for a classical 3D system of $N = 4, \ldots, 20$
particles, the state of which is completely characterized
by the temperature T. One clearly sees that in all cases $\bar{u}_{\rm rel}$
increases with T, but for small N the reduction is very
gradual, not allowing us to single out a "melting tempera-
ture" from $\bar{u}_{\rm rel}$. At the same time, in all but one case $\sigma_{u_{\rm rel}}$
has a well pronounced peak at a certain T, which is
identified as $T^{\rm crit}$. Also, the critical value of the fluctuations
may be deduced from the peak position of $\sigma_{u_{\rm rel}}$, yielding
$u_{\rm rel}^{\rm crit} \approx 0.08, \ldots, 0.16$, which is in good agreement with
macroscopic classical Coulomb systems. Note the special
case of $N = 5$ showing a low value of $T^{\rm crit}$, which is well
known and explained by the low symmetry of this cluster
[15]. While this behavior is hardly visible in $\bar{u}_{\rm rel}$, it is
clearly detected by $\sigma_{u_{\rm rel}}$.
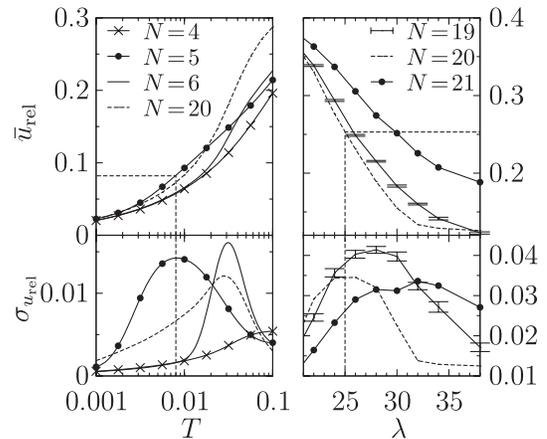
FIG. 4. Mean value $\bar{u}_{\rm rel}$ (top) and second moment $\sigma_{u_{\rm rel}}$ (bot-
tom) of the block averaged IDF for different particle numbers N.
Left: temperature dependence of a classical 3D system (classical
melting, classical MC simulations). Right: 2D quantum system,
dependence on the quantum coupling parameter λ (quantum
melting, PIMC results). In both cases the block length equals
$M = 1000$. Dashed lines locate the critical values of T (or λ) and
$u_{\rm rel}^{\rm crit}$.

As a second example we consider quantum melting upon compression in a 2D system of spin-polarized charged bosons at very low temperature. Calculations for N up to 60 were done using PIMC simulations; for details see, e.g., [22]. The right-hand side of Fig. 4 shows results for three cases, $N = 19$, 20, 21, and more examples are given in Ref. [14]. For large λ, the particles are localized resembling a crystal as seen in Fig. 1. Decrease of λ is associated with increasing wave function overlap and eventually quantum melting by tunneling of particles between lattice sites. Again we observe a gradual reduction of $\bar{u}_{rel}$ when λ is increased. In contrast, $\sigma_{u_{rel}}$ has a pronounced peak that allows us to determine the critical value of λ to $\lambda \approx 25, \ldots, 30$ depending on the particle number. The corresponding critical fluctuations, $u_{rel}^{crit} \approx 0.22, \ldots, 0.25$, are again close to the value known from simulations of macroscopic Bose systems.

These two examples are representative for the classical and quantum melting behavior of the system (2), also for other pair potentials. All our calculations have confirmed the robustness and efficiency of the VIDF for the analysis of melting in small systems. The criterion works also for macroscopic systems as will be shown elsewhere. We can now proceed and analyze the question, what is the minimum system size to observe crystallization or melting? Our simulations have revealed that $\sigma_{u_{rel}}$ has a maximum for particle numbers as small as 4 in 2D and 5 in 3D. In contrast, for 4 particles in 3D, $\sigma_{u_{rel}}$ shows a monotonic increase; see Fig. 4 (top left). This is easily understood. The ground state of 4 (3) particles in 3D (2D) resembles a unilateral tetraeder (triangle) with only a single pair distance. Thus, a jump does not alter the distribution of pair distances, and $\sigma_{u_{rel}}$ has no maximum.

In summary, we have proposed a novel quantity—the variance of the block averaged interparticle distance fluctuations. A maximum of $\sigma_{u_{rel}}$ allows one to reliably detect the existence of structural changes that are analogous to solid-liquid phase transitions in macroscopic systems. It further directly yields a consistent estimate of the melting point [20] and the critical fluctuations u_{rel}^{crit} in classical and quantum systems, thereby curing the sensitivity and convergence problems of the conventional distance fluctuation parameters. While for classical systems the energy autocorrelation function C_E allows for a calibration of the block length, this does not work for quantum melting where further analysis is required. Also, it remains an interesting question to analyze the behavior of $\sigma_{u_{rel}}$ in other finite systems, including atomic clusters or homopolymers, etc., as well as in time-dependent simulations (such as

molecular dynamics). Finally, in the case of large inhomogeneous systems where melting may proceed via a sequence of different processes, the VIDF should allow for a deeper insight and a space-resolved analysis of the fluctuations.

[1] F. Mezzacapo and M. Boninsegni, Phys. Rev. A **75**, 033201 (2007).
[2] A. Filinov, M. Bonitz, and Yu. Lozovik, Phys. Rev. Lett. **86**, 3851 (2001).
[3] D. J. Wineland *et al.*, Phys. Rev. Lett. **59**, 2935 (1987).
[4] M. Bonitz *et al.*, Phys. Rev. Lett. **96**, 075001 (2006).
[5] D. D. Frantz, J. Chem. Phys. **115**, 6136 (2001).
[6] A. Proykova and R. S. Berry, J. Phys. B **39**, R167 (2006).
[7] Y. Zhou *et al.*, J. Chem. Phys. **116**, 2323 (2002).
[8] K. Binder and D. W. Heermann, *Monte Carlo Simulation in Statistical Physics* (Springer, New York, 2002), 4th ed.
[9] H. Löwen, Phys. Rep. **237**, 249 (1994); E. J. Meijer and D. Frenkel, J. Chem. Phys. **94**, 2269 (1991).
[10] N. D. Mermin, Phys. Rev. **176**, 250 (1968).
[11] V. M. Bedanov, G. V. Gadiyak, and Yu. E. Lozovik, Phys. Lett. **109A**, 289 (1985).
[12] R. D. Etters and J. Kaelberer, Phys. Rev. A **11**, 1068 (1975).
[13] R. S. Berry *et al.*, Adv. Chem. Phys. B **70**, 75 (1988).
[14] A. Filinov, J. Böning, M. Bonitz, and Yu. Lozovik, arXiv:0711.1255 (to be published).
[15] P. Ludwig, S. Kosse, and M. Bonitz, Phys. Rev. E **71**, 046403 (2005).
[16] F. Baletto and R. Ferrando, Rev. Mod. Phys. **77**, 371 (2005).
[17] u_{rel} accounts only for the distribution of pair distances and not the jump frequency.
[18] A similar idea has been used by R. E. Kunz and R. S. Berry, Phys. Rev. Lett. **71**, 3987 (1993).
[19] Another solution is the exclusion of jump-related contributions to u_{rel}. However, for the system (2), this would erase the "phase" information and is, therefore, not used.
[20] By "melting point" it is understood that T_u^{crit} is located in the center of the finite melting interval.
[21] A Monte Carlo step is defined as N displacement attempts in a N-particle system. Additional move types like bisectioning or end-point permutation occur in PIMC simulations; cf. [8,22]
[22] *Introduction to Computational Methods for Many-body Systems*, edited by M. Bonitz and D. Semkat (Rinton Press, Princeton, 2006).

5 Spatially Indirect Electron-Hole Systems in Mesoscopic Traps

In this chapter we consider small ensembles of optically excited (spatially) indirect excitons especially in a single semiconductor quantum well. After a brief introduction in section 5.1, we start with the investigation of the quantum Stark effect on excitonic complexes in a homogeneous electric field (section 5.2). Using the path integral Monte Carlo method, we compute from first principles the field dependence of the energies and the spatial separation of electrons and holes (the effective exciton dipole moment) for different quantum well widths. Discussing two different semiconductor quantum well heterostructures (GaAs/AlGaAs and ZnSe/ZnSSe) we propose a possible experimental setup for a harmonic exciton confinement, which is produced by the strong inhomogeneous electric field of a single tip electrode. The lateral confinement of the excitons in the quantum well thereby arises from the quantum-confined Stark effect. On the basis of this specific trap, we discuss the influence of the electric field strength, the tip-to-sample distance, the excitation intensity (related to the exciton population of the trap), the exciton density, and the temperature on the confined N-exciton system. Our theoretical results allow us to predict the parameter range where interesting many-particle phenomena, including exciton Wigner crystallization, are expected to occur.

In section 5.3, we consider electrons and holes in a bilayer system. Performing quantum Monte Carlo simulations, we vary the mass ratio M of holes and electrons between 1 and 100 for a fixed layer separation and analyze structural changes in the system. While, for the chosen density, the electrons remain nearly homogeneously distributed, with increasing M, the holes undergo a transition from a quantum liquid to a crystalline (quasi-classical) state with a spatially ordered structure. This is verified for both, mesoscopic bilayers in a parabolic trap and for a macroscopic system. In section 5.4, we focus on the Coulomb-to-dipole transition, which occurs when the separation d of an electron-hole bilayer system is varied with respect to the in-layer particle density. An

analysis of the classical ground state configurations for clusters with $N \leq 30$ electron-hole pairs reveals that the energetically most favorable state can differ from that of two-dimensional pure dipole or Coulomb systems. Performing a normal mode analysis for the "magic" $N = 19$ cluster it is found that the lowest mode frequencies exhibit drastic changes when d is varied. Furthermore, we investigate the quantum mechanical ground states for $N = 6$, 10 and 12 electrons and holes. The results include the single-particle ground state energies and orbitals for a broad range of layer separations and coupling strengths between the limits of the ideal Fermi gas and the Wigner crystal phase. The results in this section are based upon a combination of extensive molecular dynamics and self-consistent Hartree-Fock calculations. An overview and detailed description of the current status of research is postponed until section 5.5 in order to allow for a discussion in conjunction with the research results presented in this chapter.

5.1 Introduction and Overview

Dynamics and Interaction of Electrons and Holes

In the present work we use the notation of electrons and holes, instead of considering electrons in different states (energy bands) and limit ourselves to a two-band model. In the electron-hole picture, holes are defined as missing electrons in the valence band and their charge is just opposite to that of the electrons, i.e., $q_h = -e$. In a semiconductor at low temperature the upper conduction band (CB) is unoccupied and the lower valence band (VB) is completely filled by electrons. Hence, it is convenient to describe excited states, where electrons have moved from the valence band to the conduction band, by counting the conduction electrons N_e and holes N_h. The excited electrons can freely move in the sparsely populated conduction band and likewise the holes left behind in the valence band are free to move. In the vicinity of the CB minimum (VB maximum), i.e., at the Γ point (k=0) in the first Brillouin zone, the band structure can in many cases be well described by a parabola with an effective mass

$$E_B^{e(h)}(\mathbf{k}) = E_B^{e(h)}(\Gamma) \pm \frac{\hbar^2 k^2}{2m_{e(h)}^*} \, , \tag{5.1}$$

where $E_B(\mathbf{k})$ denotes the electronic band energy and $\mathbf{k} = \mathbf{p}/\hbar$ the wave vector. In the effective mass approximation electrons and holes can be treated as quasi-free particles with an effective mass $m_{e(h)}^*$ and a quasi-momentum $\mathbf{p}$. A low (large) curvature of

the band corresponds to a large (low) effective mass.[1] A negative electron in the CB and a positive hole in the VB attract each other via Coulomb interaction and can minimize their total energy (at low temperature and low density) if they form a bound state, which is known as an exciton [123, 124]. However, the electron-hole binding energy is comparatively weak, and the exciton state is much more fragile than its atomic counterpart — the hydrogen atom. This is due to the dense solid matrix of many other electrons and nuclei that occupy the same space and which effectively screen the attractive Coulomb interaction. The electron-hole interaction potential is approximately given by

$$V_{\text{eh}}^{\text{int}}(\mathbf{r}_e - \mathbf{r}_h) = \frac{-e^2}{\varepsilon|\mathbf{r}_e - \mathbf{r}_h|} \ , \tag{5.2}$$

where ε is the dielectric constant of the semiconductor.

Excitonic Effects

Excitons are currently of exceptionally high scientific interest due to their bosonic character in view of the possible realization of a collective, coherent many-particle state of matter — the Bose-Einstein condensate (BEC) [125]-[128]. As the (quantum) degeneracy temperature scales inversely with mass [129] and in view of the exceptionally low effective mass of excitons (which is even below the electron rest mass) the critical temperature for the BEC is expected to be in the temperature regime of liquid Helium, i.e., at several orders of magnitude higher temperatures than in cold atom gases. Exciting experimental findings are the observed signatures of BECs in semiconductor heterostructures [18, 130, 131, 132, 133, 134] and bulk semiconductors [135, 136, 137] in recent years. Besides this fundamental research issue, there are further practical motivations for the investigation of excitonic matter, because excitons are directly connected to the optical properties of semiconductors. Technological potential of these single photon sources arises particularly with regard to the development of novel optoelectronic micro-devices [138], which may allow for the realization of novel computing methods such as "photon computing" or "quantum computing". Additional interest is given by the possibility to observe new (quantum) states of matter such as exciton Wigner crystallization [43, 86, 139, 140, 141, 142, 143], excitonic superfluidity (allowing for frictionless transport of electronic energy through the crystal) [144, 145] or even the Wigner supersolid of excitons. In this speculative quantum phase the excitons are required to be phase coherent and to form a Wigner crystal at the same time [146, 147].

---

[1]The effect of mass-asymmetry in electron-hole bilayers is subject of investigation in section 5.3.

Spatially Indirect Excitons

Excitons possess a finite lifetime. The electron-hole pairs typically annihilate (recombine) radiatively on the time scale of a nanosecond (or even below) in direct band-gap semiconductors. In order to study correlation effects, the initially photogenerated hot excitons are required at least to thermalize down to lattice (helium bath) temperature and to reach a quasi-equilibrium state in a time that is considerably shorter than their radiative decay. One possibility to lower the spontaneous recombination probability of excitons is to reduce the electron-hole wave function overlap by spatial separation of electrons and holes. Considering a quasi 2D *single quantum well*[2] the spatial separation of electrons and holes can be achieved by a strong electric field, which is applied perpendicular to the quantum well plane (i.e. in z-direction), see figure 5.1. These spatially indirect excitons possess several unique features (all values are given for GaAs/AlGaAs samples):

- The spatial separation of electrons and holes in the z-direction results in a *greatly enhanced exciton lifetime* that may be more than three orders of magnitude longer than that of spatially direct excitons. (In wide single QWs [149] and double QWs [150] lifetimes of tens of microseconds have been recorded).

- The quantum well confinement leads to a relaxation of the momentum conservation in z-direction. Therefore, *thermalization down to the lattice temperature* via emission of bulk longitudinal acoustic phonons is about 10^3 times faster for excitons in dimensionality reduced QWs than in 3D bulk structures [151]. (In agreement to [152], indirect excitons were reported to cool down to $400\,\mathrm{mK}$ in about $5\,\mathrm{ns}$ [153]. This time is much shorter than their lifetime. We note that a recent experiment gives "evidence for equilibration" to $5\,\mathrm{K}$ lattice temperature of the harmonically confined gas of indirect excitons, however, within a considerably larger time of a few microseconds [150, 154].[3])

- The spatial separation of electrons and holes leads to a strong (cross-well) *permanent dipole moment* giving rise to a repulsive exciton-exciton interaction, which results in an effective screening of the in-plane disorder potential (caused by QW interface fluctuations, impurities, etc.).

---

[2]The advantages of a wide single well over a double well are discussed in section 5.2.2. Further arguments, which are related to the creation and investigation of indirect recombination, are to be found in reference [148].

[3]We expect a longer radiative lifetime of indirect excitons in ZnSe based QWs (see section 5.2.2). Therefore, we will consider the exciton system to be thermalized and study its equilibrium properties.
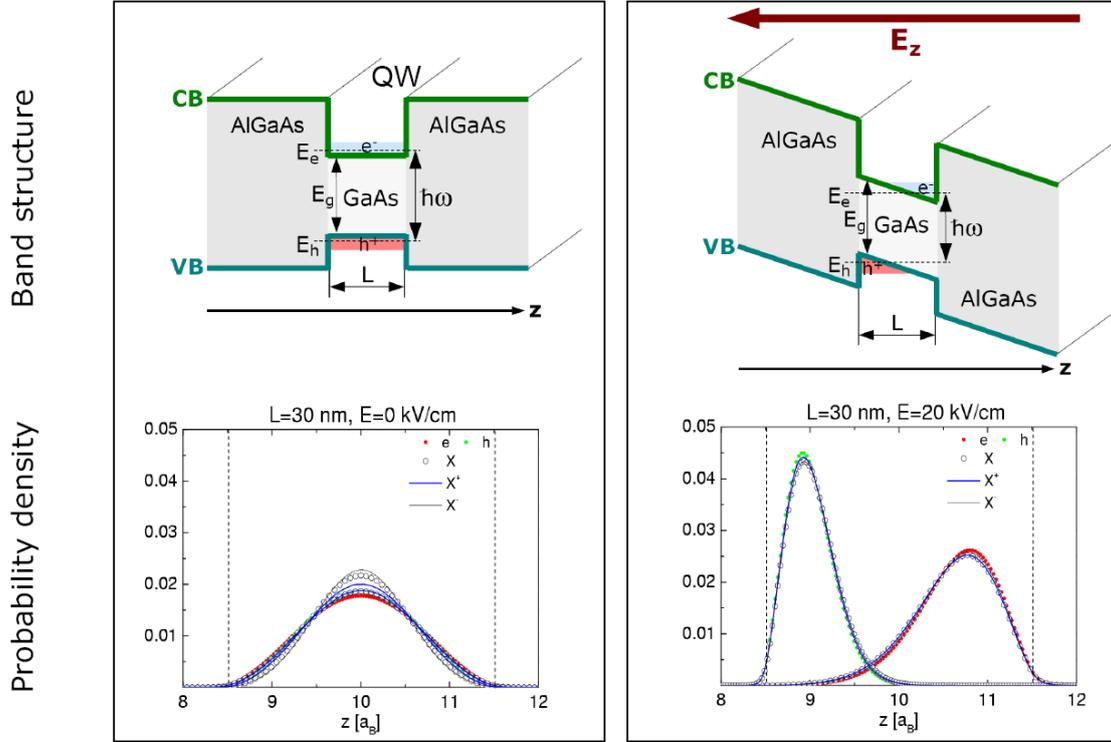
Figure 5.1: *Effect of a strong electric field on the excitonic states in a GaAs/AlGaAs quantum well (QW) of width $L = 30\,nm \approx 3a_B$. Shown are schematic band structure diagrams (top) and the corresponding probability densities in (growth) z-direction (bottom) of free charge carriers (electron e, hole h) and particles in excitonic bound states: the exciton X and excitonic complexes (positive trions X^+, negative trions X^-).*

Left panel: Electrons are promoted into the conduction band (CB) and the defect electrons (positively charged holes) remain in the valence band (VB). The energy scale for the pair production is the material-specific band gap energy $E_g \sim 1\,eV$, which separates the CB with the lower band edge from the VB with the upper band edge. In absence of the electric field all (quasi-) particles are symmetrically distributed in the z-direction of the QW. Due to the attractive electron-hole Coulomb interaction, the (spatially direct) exciton is stronger localized than a free electron or free hole in the same z-confinement.

Right panel: Application of a homogeneous electric field E_z in growth direction of the QW leads to a tilting of the energy bands (Stark shift) and a separation of the charge carriers at different sides of the QW. This leads (at low temperatures) to formation of stable spatially indirect excitons with a finite permanent dipole moment in z-direction. Note that the hole is more strongly localized than the electron due to its higher effective mass. The Stark effect allows for a flexible band-structure design and thus adjustable electrostatic trap geometries giving rise to a broad range of accessible exciton parameters and correlation effects (see section 5.2).

- The repulsive exciton-exciton interaction shifts the peak of the pair correlation function to larger exciton-exciton distances and masks the fermionic character of the exciton constituents (at moderate densities, see section 5.2.3).

- A strong repulsion between the "dipole"-like excitons prevents further binding of excitons into larger complexes, such as biexcitons or electron-hole droplets (see section 5.2.1).

- The mutual repulsive interaction reduces thermal fluctuations and stabilizes the exciton state. (Note that the reduction of the binding energy $E_b(X) = E_e + E_h - E_x$ by the electric field is relatively modest due to the QW confinement, which naturally limits the charge separation; see section 5.2.1 for details.)

- The separation of electrons and holes leads at low temperature to a spontaneous spin polarization of the indirect exciton, i.e., a transition to a ferromagnetic exciton phase [155]. (In our PIMC simulations we will consider spin-polarized exciton systems, where all excitons are identical. This means that the degeneracy is higher than in an unpolarized system.)

In turn, to bring correlation effects into play an external confinement within the quantum well plane is required, which balances the repulsive exciton-exciton interaction. As will be discussed in section 5.2, a suitable lateral (harmonic) trap can be generated by means of an inhomogeneous electrostatic z-field of a fine tip electrode due to the *quantum-confined Stark effect*. The resulting occupied trap region below the tip is on the micron scale. The proposed electrostatic harmonic exciton confinement in the 2D quantum well structure permits for a voltage-controlled transition from the direct to the indirect exciton regime and a high flexibility with regard to the exciton parameters (dipole moment, lifetime etc.). The vertical tip position relative to the sample provides an additional degree of freedom and allows for a flexible control of the lateral confinement strength (exciton density) and a broad accessible range of exciton-exciton correlation effects. Furthermore, the number of excitons can be tuned with the intensity of the (pulsed) laser used to generate the excitons[4]. The mentioned features make indirect excitons a very suitable system for the exploration of collective quantum states and many-body phenomena of cold bosons. Our numerical PIMC studies, section 5.2.3, support theoretical predictions of the possibility of exciton condensation and should give the motivation for ongoing efforts in the preparation of experiments for example those currently set up at Rostock University [156].

---

[4]By collecting the excitons in a trap, a lower flux of excitons allows for a low photoexcitation intensity, which reduces the heat input into the system.

Wigner Crystallization of Indirect Excitons

The idea of Coulomb correlation induced crystallization of the electron gas in metals was first considered by E. P. Wigner in 1934 [157]. Following his ideas, at low densities (considerably lower than the electron density in atoms or metals) and low temperatures the system of electrons spontaneously crystallizes into a regular lattice structure if the mutual electron wave function overlap is strongly reduced and thus the formation of energy bands with delocalized electrons suppressed, e.g. [2, 158, 159].

In the following we will use quantum Monte Carlo simulations to give a first principle thermodynamic description of indirect excitons in the moderate density regime, where the composite quasi-particles show strong bosonic many-particle features. In this connection, we will address the issue of whether the dipole-like exciton-exciton interaction in the "bosonic density regime" is strong enough to suppress the quantum fluctuations, so that a Wigner crystal phase of spatially indirect excitons can be established, and, if at all, for which realistic parameters.

Model system. The results presented below apply particularly to semiconductor single QWs, but can be generalized to coupled QW heterostructures as well. The well-accepted N-particle Hamiltonian based on the equations (5.1) and (5.2) captures many qualitative features of semiconductors and includes all Coulomb correlation contributions without simplification. It reads

$$\hat{H} = \hat{H}_e + \hat{H}_h + \sum_{i=1}^{N} \sum_{j=i+1}^{N} \frac{q_i q_j}{\varepsilon \sqrt{(\mathbf{r}_i - \mathbf{r}_j)^2 + (z_i - z_j)^2}} \ , \tag{5.3}$$

where the $N = N_e + N_h$ single particle contributions are given by

$$\hat{H}_{e(h)} = \sum_{i=1}^{N_{e(h)}} \left(-\frac{\hbar^2}{2m_{e(h)}^*} \nabla_{\mathbf{r}_i}^2 + \frac{m_{e(h)}^*}{2} \omega_0^2 \mathbf{r}_i^2 + V_{e(h)}^{ext}(z_i) \right) \ , \tag{5.4}$$

which consists of the kinetic (band) energy, the lateral electron (hole) harmonic confinement potential and an additional external potential

$$V_{e(h)}^{ext}(z_i) = \begin{cases} q_i E_z z_i, & |z| \leq L/2 \\ V_i^0 + q_i E_z z_i, & |z| > L/2 \ . \end{cases} \tag{5.5}$$

The external potential $V_{e(h)}^{ext}(z_i)$ combines thereby the effect of the QW confinement (presented as a square well, see figure 5.1) and the applied electric field in z-direction.

Within this model q_i is the particle's charge, ε the static permittivity, $m^*_{e(h)}$ the electron (hole) effective mass, ω_0 the in-plane trap frequency, L the QW width, and E_z the electric field applied perpendicular to the quantum well plane. The vectors $\mathbf{r}_i$ describe the in-plane particle positions.

Reduced bosonic model of indirect excitons. At low temperatures (well below the exciton binding energy) and small electron-hole separations the electrons and holes form stable spatially indirect excitons (see section 5.2.1). The results of section 5.2.3, where the Fermi statistics of the exciton constituents is taken fully into account, allow us to treat indirect excitons in the moderate density regime, i.e., for $\lambda > 15$, approximately as composite Bose particles. At higher densities the fermionic nature of the exciton constituents becomes unmasked and the treatment of a two-component fermion system consisting of electrons and holes becomes indispensable.[5]

In the following we consider the representative example of a mesoscopic system consisting of 56 spin-polarized indirect excitons with an effective electron-hole pair separation of $d = 20 nm = 6.6 a_B$. This carrier separation can be produced by an electric field of strength $E_z = 20$ kV/cm in a single ZnSe-based quantum well of $L = 30$ nm width (see section 5.2.2). In the strong coupling regime, $\lambda = 17$, i.e., at a moderate in-plane density of $1.5 \cdot 10^{10}/\text{cm}^2$, the effective electron-hole separation d is much smaller than the exciton-exciton distance within the layer. Consequently, the electron-hole binding energy of an individual exciton is much larger than the repulsive exciton-exciton interaction $U_{eh} \gg U_{xx}$. This allows for a separation of the z-problem by averaging over the QW thickness by solving the single exciton problem (in a homogeneous field) and an introduction of relative and center of mass (COM) coordinates of the composite excitons (see section 5.2.1). The relative problem describes the inner exciton structure (exciton wave function) giving rise to the effective dipole moment $\mu = ed$, which is characterized by the effective e-h separation

$$d = \langle z_e - z_h \rangle_{\rho_e(z_e,\beta)\rho_h(z_h,\beta)} \;. \tag{5.6}$$

Furthermore, the COM coordinate $\mathbf{R}_i$ describes the position of the i-th exciton in the external potential. In the considered model, the N-particle problem reduces to an effective 2D-Hamiltonian of $N_x = N/2$ composite bosonic excitons. These are confined

---

[5]The structural ground state properties of an electron-hole bilayer system in the regime $\lambda < 15$ (where Fermi exchange effects become essential) are considered in section 5.4.

in the QW plane and interact via a repulsive dipole interaction potential

$$\hat{H}_x = \sum_{i=1}^{N_x} \left(-\frac{\hbar^2}{2m_x^*} \nabla_{\mathbf{R}_i}^2 + \frac{m_x^*}{2} \omega_0^2 \mathbf{R}_i^2 + \sum_{i<j}^{N_x} \frac{\mu(\mathbf{R}_i)\mu(\mathbf{R}_j)}{\varepsilon |\mathbf{R}_i - \mathbf{R}_j|^3} \right) , \qquad (5.7)$$

where the trap frequency ω_0 arises from the effective lateral quantum Stark confinement potential (see section 5.2 for details). This effective 2D problem of N_x indirect excitons, which obey Bose statistics, is solved by path integral Monte Carlo (PIMC) simulations. These simulations allow for a first principle treatment of the many-particle Coulomb correlation and bosonic exchange effects (details on the PIMC technique are given in section 2.3).

PIMC simulation results. Quantitative predictions on the excitonic states of the considered exciton cluster for three specific temperatures are shown in figure 5.2. The simulations point out that the particles become highly correlated and can stabilize in spatially periodic structure when the temperature is decreased below a critical value of $T_{cr} \lesssim 1.2$ K. Similar to the mesoscopic electron systems [2], a two-stage Wigner crystallization process is observed:

1. At the temperature $T_1 = 3.35$ K, i.e., slightly above the *finite melting interval* (see section 4.3), the indirect excitons are in a Bose fluid state and delocalized within the trap due to thermal fluctuations as well as quantum fluctuations and bosonic exchange.

2. When the temperature is decreased to $T_2 = 830$ mK the indirect excitons become strongly correlated and enter a partially ordered state. The 56 indirect excitons arrange themselves on four distinct rings (a single particle is located in the trap center). Note that the concentric shell structure reflects the radial symmetry of the external confinement.

3. Further lowering of temperature to $T_3 = 210$ mK leads to a full freeze-out of the thermal fluctuations, whereby the (zero-point) quantum fluctuations prevail. The PIMC simulations show that the repulsive inter-exciton interaction is capable of governing the strong quantum fluctuations and establish an intrashell localization of the quasi-particles. Moreover, a highly ordered quantum state with a regular 2D Wigner lattice is observed in the center region of the trap (where the geometrical constraints of the external confinement are reduced).

The two-stage transition process is a well-known phenomenon in confined few-particle systems, e.g. [2, 159]. This is due to the fact that the confinement induced radial

energy barriers are considerably higher than the intrashell energy barriers separating the repelling particles [70]. Because of the short range of the dipole potential, the mesoscopic quantum crystal of indirect excitons appears at higher densities than the electron (Coulomb) Wigner crystal, i.e. the crystal is stabilized. Previous numerical work predicts a transition from the Fermi liquid state to the electron Wigner crystal phase for around $r_s^e \approx 35$ (see [2, 159] and references therein), whereas in the present simulations the exciton Bose-nano-crystal is already found at $r_s^x \approx 25$.[6]

A deeper insight into the structure of the different exciton phases can be obtained from the diffraction picture. Current experiments allow for the measurement of both the real luminescence pattern with a resolution up to $1\mu m$ and also the distribution of exciton luminescence in the far-zone, i.e., the optical Fourier transform of the real image [18, 160]. This motivates us to consider the diffraction pattern of the observed exciton structures, with the objective that it can give a clear evidence for a phase transition in the mesoscopic system. The classification will be in conformity with the *International Union of Crystallography* (IUC) which decided to redefine the term "crystal" to mean "any solid having an essentially discrete diffraction diagram" in 1991 [161].

The static structure factor is obtained from the spatial 2D Fourier transform of the (time averaged) exciton density distribution $\rho(\mathbf{r})$

$$F(\mathbf{h}) = \int_{-\infty}^{+\infty} \rho(\mathbf{x})e^{i2\pi\mathbf{h}\mathbf{x}}d^2x \ , \tag{5.8}$$

and is parametrized by the in-plane (momentum transfer) vector $\mathbf{h}$ (in analogy to a X-ray scattering process). The structure factor F describes the Fourier components of the density fluctuations and diverges as $|\mathbf{h}| \to 0$ indicating long-wavelength fluctuations. The modulus squared of the structure factor provides the diffraction intensity

$$I(\mathbf{h}) = |F(\mathbf{h})|^2 \ . \tag{5.9}$$

The peaks of the function $I(\mathbf{h})$ are closely associated with the structural features of the crystal. If the diffraction vector $\mathbf{h}$ coincides with a reciprocal lattice vector, the function $F(\mathbf{h})$ becomes non-zero, and the diffraction pattern consisting of sharp and intense "Bragg" reflections of the crystal occur.

---

[6]It should be noted that in a recent study of the zero-temperature phase diagram of a *unconfined* 2D Bose system with dipole-dipole interaction, the critical Lindemann ratio (at the transition density) for the quantum phase transition from the gas to the solid phase has been estimated as $u_{crit} = 0.23$ [43]. This critical value is in full agreement with our simulations of *confined* small exciton clusters (we used the VIDF with blocksize $M = 1000$, see section 4.3 for details).
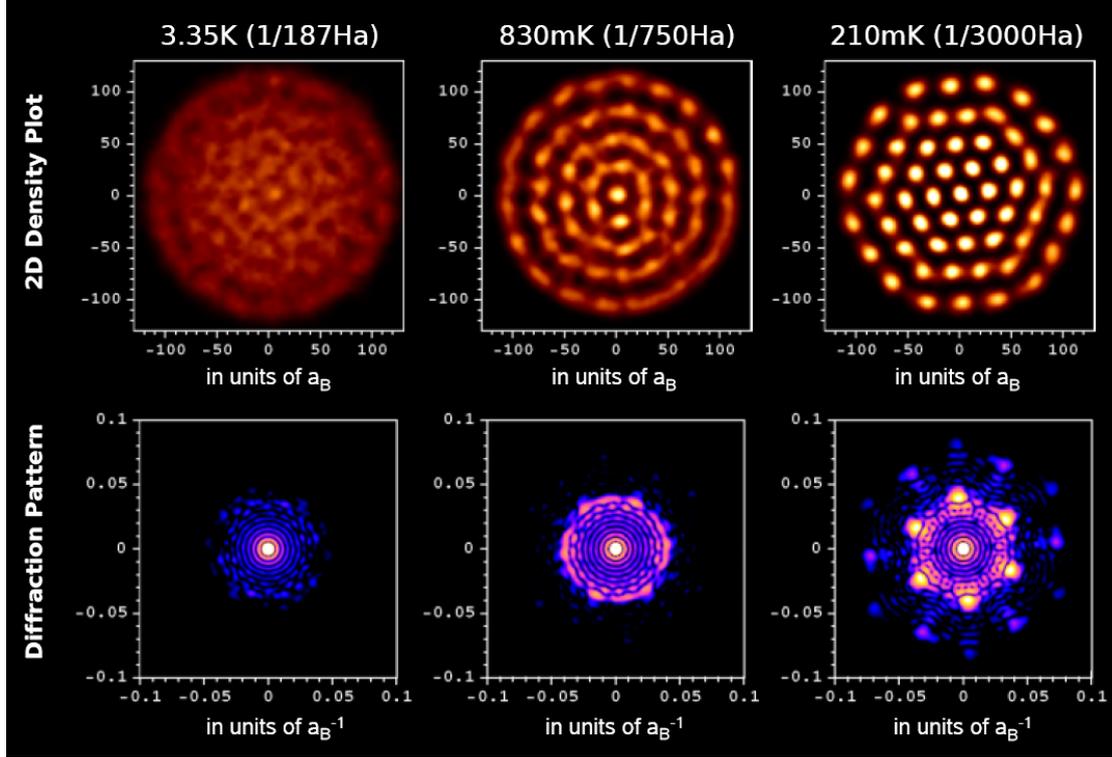
Figure 5.2: *Quantum Monte-Carlo results for a ZnSe-based quantum well with $N = 56$ harmonically trapped indirect excitons obeying Bose statistics. Top row: Density plots of the indirect excitons for the three temperatures: 3.35 K, 830 mK and 210 mK (from left to right). Due to strong inter-exciton correlations highly ordered quantum states are observed; reducing temperature initiates a two-stage crystallization process: (1) radial ordering of the excitons on shells, (2) formation of a bosonic Wigner nano-crystal with a hexagonal lattice structure. Partial exciton delocalization is a result of quantum fluctuations and Bose statistics ("cold" melting). Bottom row: Corresponding Bragg diffraction patterns exhibiting the degree of order in a system by measuring the density-density correlations. The patterns are used as an indicator of a phase transition. (Diffraction intensity is logarithmically scaled.) Simulation parameters: Effective spatial electron-hole z-separation $d = 20$ nm ($6.6a_B$), coupling parameter $\lambda = 17.0$. The probability density plots are averaged over $L = 10000$ Monte Carlo steps (plus $L_{eq} = 10000$ steps for the equilibration), number of high temperature factors $M = 362$ (PIMC, see section 2.3). Effective Hartree energy $1Ha = q^2/\varepsilon a_B = 53.93$ meV (625.8 K) for ZnSe.*

Let us now study the diffraction diagram of an exciton cloud for the three characteristic temperatures displayed in figure 5.2. The leftmost diagram, corresponding to $T_1 = 3.35$ K, reveals (beside the central spot) five weak circular symmetric side maxima. These are a first signature of the growing *inter-exciton correlations*, which give rise to a radial density modulation, i.e., the onset of the formation of shells. Lowering the temperature to $T_2 = 830$ mK leads to pronounced circular main maxima in the diffraction intensity $I(\mathbf{h})$. The value of the wavenumber $h = 0.04/a_B$ corresponds to the almost equidistant

radial density modulation (resp. intershell spacing) of $25\,a_B$. On the contrary the main peaks, which are also found in large clusters, the number of side maxima is affected by the finite size of the cluster. More specifically, the observed Laue oscillations consisting of $n-2=7$ subsidiary maxima and $n-1=8$ subsidiary minima are due to the $n=9$ density peaks in the center cross section of the shell structure.

However, the most interesting and richest diffraction pattern is found at $T_3 = 210\,\text{mK}$. At this temperature, the inner part of the mesoscopic exciton Wigner crystal presents a hexagonal lattice in real space with spacing $a = 25\,a_B$. The hexagonal lattice is actually the two-dimensional lattice with the highest symmetry and the lowest energy (in the unconfined case). This configuration gives rise to six distinct intensity peaks in the diffraction image.[7] Each symmetry axis of the exciton crystal shows up as two symmetry lines in the diffraction pattern. Here the Brillouin zone appears as a hexagon with a nearly circular shape. Moreover, the discrete diffraction picture bears out a strict phase transition of the mesoscopic exciton plasma into a crystalline state (i.e. a 2D crystal without conventional long-range order).

The existence of the exciton Wigner crystal raises the intriguing question about the coherence of this quantum state, which, however, cannot be directly clarified with the present PIMC simulations (see discussion in section 2.4). However, at the considered spatial scale of the 2D micron-scale lateral confinement the phase coherence of the excitons cannot be ruled out. In particular the finite size of the system may allow for a fully coherent state of indirect excitons even in 2D, where the coherence length cannot be infinite. Furthermore, in section 5.4 we show that even in the Wigner crystal phase single density peaks do not one-to-one correspond to single particles, but rather the single-particle orbitals extend over the entire cluster. This means with respect to the Wigner crystal in figure 5.2 that the identification of single excitons (individual exciton wave packets) is not obvious and may lead to misinterpretations due to "matter wave overlap". The question about the quantum properties of the Wigner state (including features such as superfluidity) is a very exciting question and requires for further theoretical and experimental work.

---

[7]Note that increasing the cluster size will just decrease the FWHM and increase the intensity of the Bragg peaks, whereas imperfections in the spatially periodic structure cause broadening of the peaks.

5.2 Strongly Correlated Indirect Excitons in Quantum Wells

We consider a finite number of photogenerated indirect excitons in a single quantum well (QW), where the spatial separation of electrons and holes is due to a strong electric field from a tip electrode. A lateral confinement of the indirect excitons in the QW arises from the quantum-confined Stark effect with a typical trap size being on the order of several micrometers. Using path integral Monte Carlo simulations, electrons and holes are shown to form permanent dipoles with a strong repulsion, which prevents formation of biexcitons and electron-hole droplets. At the same time, the repulsion masks the fermionic character of the indirect exciton constituents, so that the excitons are approximately of bosonic nature. By changing the field strength and geometry, the excitation intensity (exciton number) and temperature, the indirect exciton properties as well as the exciton-exciton correlations can be varied in broad ranges giving rise to interesting many-particle correlation and quantum effects.

The results were published as refereed journal publications:

5.2.1 ***Strongly Correlated Indirect Excitons in Quantum Wells in High Electric Fields,*** A. Filinov, P. Ludwig, Yu.E. Lozovik, M. Bonitz, and H. Stolz, J. Phys: Conf. Series **35**, 197 (2006)

5.2.2 ***Quantum Stark Confined Strongly Correlated Indirect Excitons in Quantum Wells,*** P. Ludwig, A. Filinov, M. Bonitz, and H. Stolz, phys. stat. sol. (b) **243**, No. 10, 2363 (2006)

5.2.3 ***Path Integral Monte Carlo Results for Bose Condensation of Mesoscopic Indirect Excitons,*** A. Filinov, M. Bonitz, P. Ludwig, and Yu.E. Lozovik, phys. stat. sol. (c) **3**, No. 7, 2457 (2006)

Strongly correlated indirect excitons in quantum wells in high electric fields[1]

Alexei Filinov[1,2], Patrick Ludwig[1,3], Yurii E. Lozovik[2], Michael Bonitz[1] and Heinrich Stolz[3]

[1] Christian-Albrechts-Universität zu Kiel, Institut für Theoretische Physik und Astrophysik, Leibnizstrasse 15, 24098 Kiel, Germany,
[2] Institute of Spectroscopy RAS, Moscow region, Troitsk, 142190, Russia,
[3] Universität Rostock, Institut für Physik, Universitätsplatz 3, 18051 Rostock, Germany

E-mail: `filinov@theo-physik.uni-kiel.de`

Abstract.
We study the Stark effect on excitonic complexes confined in a GaAs-based single quantum well. We approach this problem using Path Integral Monte Carlo methods to compute the many-body density matrix. The developed method is applied for investigation of the electric field-dependence of energies, particle distribution and effective exciton dipole moment.

Using these results as an input we apply thermodynamical Monte Carlo methods to investigate systems of several tens to thousands indirect excitons in a 2D quantum well with a lateral confinement arising from the quantum confined Stark effect. Depending on the field strength, exciton density and temperature different phases (gas, liquid and solid) of indirect excitons are predicted.

1. Introduction

In the present work we aim to study equilibrium properties of excitons, charged excitons (trions) and biexcitons under the influence of a quantum well confinement and an external electric field produced by electrostatic contacts.

The field applied along the growth direction separates electrons and holes at different sides of the quantum well (QW) and leads to formation of spatially indirect excitons. This system can be a promising candidate for the observation of Bose condensation [1, 2, 3, 4] or crystallization of excitons in heterostructures. While in many experimental realizations a system of two coupled QWs is considered, here we show that a single QW can also be suitable for this purpose. At high electric fields excitons can be considered as dipoles oriented perpendicular to the QW plane with a repulsive, dipole-dipole like, interaction preventing formation of other bound states, such as biexcitons. If the temperature is low enough the excitons can create bound states with the excess carriers (free electrons or holes) and form positively or negatively charged excitonic complex, i.e. trions, with a binding energy ranging from 2K to 11K (in GaAs-based QWs) depending on the strength of the applied electric field. Hence, the question about the ground state of indirect excitons and dissociation of trions and biexcitons in high electric fields has

---

[1] Based on a talk and a poster presented at the conference "Progress in Nonequilibrium Green's Functions III, Kiel, Germany, 22. – 25. August 2005"

an important implication for possibility to have favorable conditions for Bose condensation or crystallization.

In section II we shortly discuss the basic ideas of our first principle Path integral Monte Carlo (PIMC) technique. In section III we look in detail at the Stark effect and the dependence of the exciton energy on the electric field. Further in Section IV, the obtained results (e.g. the Stark shift and the effective dipole moment of indirect excitons) will be used as an input for thermodynamical Monte Carlo simulations of several thousands of trapped excitons.

2. Path Integral Monte Carlo

The results presented in the next section have been obtained with the Path Integral Monte Carlo technique based on presentation of the many-body density matrix in the terms of Feynman trajectories [5]. The details on theoretical aspects and the practical implementation can be found in the review [6] and Refs. [7, 8]. Below we give a brief overview of the applied technique.

In PIMC calculations we start from the following representation of the N-particle non-diagonal thermal density matrix

$$\rho(\mathbf{R}, \mathbf{R}'; \beta) = \int_V d\mathbf{R}^1 \ldots \int_V d\mathbf{R}^{n-1} \rho(\mathbf{R}, \mathbf{R}^1; \delta\beta) \rho(\mathbf{R}^1, \mathbf{R}^2; \delta\beta) \ldots \rho(\mathbf{R}^{n-1}, \mathbf{R}'; \delta\beta), \quad (1)$$

where $\mathbf{R} = (\mathbf{r}_1, \mathbf{r}_2, \ldots, \mathbf{r}_N)$ are the particle coordinates, and the integrations are performed in the whole coordinate space over additional intermediate varibles on the $n-1$ "imaginary time" slices of a path, which starts at $\mathbf{R}(0) = \mathbf{R}$ and ends at $\mathbf{R}(\beta) = \mathbf{R}'$. Here, the parameter $\beta = 1/k_B T$ denotes the inverse temperature. The main advantage of this representation, as was first recognozed by Feynman, is the fact that a low-temperature density matrix can be expressed through high-temperature density matrices at an n-times higher temperature, i.e. $\delta\beta = \beta/n = 1/nk_B T$. This expression is very useful for practical calculations if we write down the high temperature approximation for each of the non-diagonal N-particle density matrices $\rho_k = \rho(\mathbf{R}^k, \mathbf{R}^{k+1}; \delta\beta)$. Hence, the two main problems treated in PIMC calculations are, first, the construction of the best approximation for ρ_k and, second, development of an efficient Metropolis Monte Carlo integration procedure to sample the density matrix directly from Eq. (1).

For the simulations of particles with Fermi or Bose statistics we should place additional symmetry restrictions on the density matrix in Eq. (1). One of the simple and widely used high-temperature approximations to take into account the antisymmetry property of the fermion density matrix is to express it through the Slater determinants of free-particle propagators for each species of particles with the same spin projection

$$\rho(\mathbf{R}^k, \mathbf{R}^{k+1}; \delta\beta) = \left(\frac{1}{N_\uparrow!}\right) \det A(k, k+1)_{\uparrow\uparrow} \cdot \left(\frac{1}{N_\downarrow!}\right) \det A(k, k+1)_{\downarrow\downarrow} \times \qquad (2)$$
$$\exp\left(-\delta\beta\left[\sum_{i=1}^N V^{ext}(\mathbf{r}_i^k) + \sum_{i\leq j}^N V_{ij}(\mathbf{r}_{ij}^k)\right]\right),$$

where V^{ext} is the external potential, and V_{ij} is the pair potential for particles i and j. The (l, m) element of the $N_{\uparrow(\downarrow)} \times N_{\uparrow(\downarrow)}$ matrix $A(k, k+1)$ is defined as

$$a(k)_{l,m} = \exp\left(-\frac{m}{2\hbar^2\delta\beta}(\mathbf{r}_l^k - \mathbf{r}_m^{k+1})^2\right). \qquad (3)$$

To sample the density matrix from Eq. (1) we use in the Metropolis algorithm the modulus of the short-time propagators $\left|\rho(\mathbf{R}^k, \mathbf{R}^{k+1}; \delta\beta)\right|$ as probability density. For fermions, the non-diagonal short-time density matrix is not positive defined, and hence its sign should be taken

into account by an additional weight function with the values, $W(k, k+1) = \pm 1$, depending on the parity of a permutation. Then the total sign coming from all "imaginary time" slices is defined as $W = \prod\limits_{k=0}^{n-1} W(k, k+1)$. For low temperatures and large systems the sign of each term in the product changes independently, and as a result the total sign strongly oscillates which leads to the so called "fermion sign problem". In the present PIMC calculations, where the maximum number of exchanged particles was two, e.g. in the biexciton - two electrons and two holes, Eq. (3), can be used without modifications. The results presented below are for the singlet state of two electrons or two holes. For zero magnetic field this corresponds to the ground state of the system [9, 10].

For excitonic complexes in the QW in the presence of a homogenous electric field applied normal to the QW plane we consider the hamiltonian of $N = N_e + N_h$ particles

$$\hat{H} = \hat{H}_e + \hat{H}_h + \sum_{i=1}^{N} \sum_{j=i+1}^{N} \frac{e_i e_j}{\varepsilon |\mathbf{r}_i - \mathbf{r}_j|} \tag{4}$$

$$\hat{H}_{e(h)} = \sum_{i=1}^{N_{e(h)}} \left(-\frac{\hbar^2}{2m_{e(h)}} \nabla_{\mathbf{r}_i}^2 + V_{e(h)}^{ext}(z_i) \right) \tag{5}$$

where $V^{ext}(z)$ is the external potential which combines the effect of the QW confinement (presented as a square well) and the applied electric field

$$V_i^{ext}(z) = \begin{cases} e_i E_z \cdot z, & |z| \le L/2 \\ V_i^0 + e_i E_z \cdot z, & |z| > L/2 \end{cases} . \tag{6}$$

Our simulations have shown that use of the classical square well potential (6) leads to a discontinuity of the density distribution at the QW edges. This discontinuity comes from the infinite first derivative of the classical potential and is very slowly converging with the number of time slices n in Eq. (1). This problem, however, can be easily overcome by using an effective temperature-dependent potential (see the detailed discussion in Ref. [11]). We have precomputed for every QW width, L, strength of electric field, E_z, and several inverse temperatures $\delta\beta$ the 1D density matrix of electrons and holes in the z-direction. The effective potential V_{ij}^{eff} can be then obtained from the following definition using the pair density matrix in relative coordinates [6, 12]

$$\rho(\mathbf{r}_{ij}, \mathbf{r}'_{ij}; \delta\beta) = \frac{\mu_{ij}^{3/2}}{(2\pi\hbar\delta\beta)^{3/2}} \exp\left[-\frac{\mu_{ij}}{2\hbar^2\delta\beta}(\mathbf{r}_{ij} - \mathbf{r}'_{ij})^2 \right] \exp[-\delta\beta V_{ij}^{eff}(\mathbf{r}_{ij})], \tag{7}$$

where i and j can be any pair of particles, or a particle and the quantum well potential (represented as an effective particle with the infinite mass; in this case the reduced mass coincides with the particle mass $\mu_{ij} = m_i$).

In the calculations of excitonic states presented below the temperature was varied in the range $T = 1/400 \ldots 1/80$ Ha (for GaAs heterostructure with $1\text{Ha} = 2Ry \approx 133$ K this corresponds to temperatures $0.33 \ldots 1.66$ K) depending on the binding energy, E_B, of the excitonic complex. Usually we choose $T \approx 1/10\,E_B$ and our calculations correspond practically to the ground state. We discretize our density matrix in Eq. (1) into $n = 120 \ldots 1200$ time slices, hence we use the high-temperature density matrices at temperatures $1/\delta\beta = 1.5\text{Ha}$ (199.5 K) or 3Ha (399 K) and for the QW we use the effective potentials $V_{e(h)}^{eff}$ for electrons and holes respectively. All interparticle interactions and the external confinement have been treated in the pair approximation [6] using the off-diagonal pair potentials. More details can be found in Ref. [12].
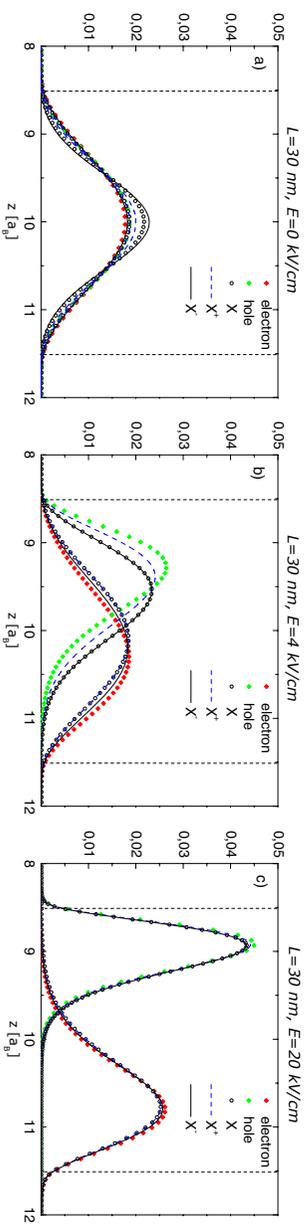
Figure 1. (Color online) Probability density ρ of free particles (electron and hole) and the particles in the bound states (exciton, positive and negative exciton) in a homogeneous electric field of different strength [0, 4, and 20 kV/cm] applied in the growth direction of a QW of the width $L = 30$ nm. In Figs. b) and c), the positive (negative) electrode is at the right (left), therefore, electrons (holes) are shifted to the right (left). Due to the higher mass the hole is stronger localized than the electron ($m_h/m_e = 2.27$).

3. PIMC results for excitonic complexes in a homogeneous electric field

As discussed the electric field modifies the confinement potential and leads to a separation of electrons and holes, which leads at sufficiently low temperatures to formation of spatially indirect excitons, positive/negative trions and biexcitons. Consequently the spontaneous recombination time of the excitonic states can be increased from tens of picoseconds to the 100ns-order and allows for equilibration, i.e. at sufficient low temperatures relaxation to the ground state.

We start our considerations from single excitonic states in GaAs/AlGaAs QWs. With the increase of the homogenous electric field applied perpendicular to the QW plane the probability density for electrons and holes becomes shifted to different edges of the 30 nm wide QW (see Fig. 1). For three different electric field strengths presented in Fig. 1 we calculate the probability density of free carriers (an electron and a hole) as well as the electron and the hole probability density (PD) inside the exciton and the positive and negative trions, $X^{\pm}$. At zero and weak fields, Fig. 1 (a),(b), the probability density in each excitonic state depends on the relative strength of electron-electron repulsion and electron-hole attraction. For the exciton the peaks of electron and hole PD have the smallest separation reflecting the fact that the exciton is the most strongly bound complex.

However, if we now move to high electric fields of about 20 kV/cm and above, the correlation effects in the growth direction of the QW practically vanish. Now only the electric field plus QW confinement plays a dominant role and determines the profile of the PD. In this case, as shows Fig. 1(c), the PD of free particles coincides with that of the exciton and the trions in the same electric field. This result allows us to conclude that in the QWs at high electric fields for both numerical and analytical considerations the usage of the adiabatic approximation in z-direction is resonable and the problem can be effectively reduced to a 2D system similar to the approach used in Ref. [8]. The validity of the adiabatic approximation can be also independently checked by comparing the binding energy of the excitonic complexes vs electric field for the effective 2D and 3D systems [11].

In our calculations we have considered three GaAs/Al$_{0.3}$Ga$_{0.7}$As QWs of the widths, $L = 10$, 20 and 30 nm, which are typical for experimental samples. As we can see, from Fig. 2(a), in the narrow 10 nm QW, excitonic states are practically not influenced by the field and the total energy stays practically constant. In this case the carriers do not become separated, at least for fields up to 20 kV/cm, due to the dominant effect of the QW confinement, therefore $E > 0$ in Fig. 2(a). In contrast, for the wide 30 nm QW the field dependence of the total energy is strong
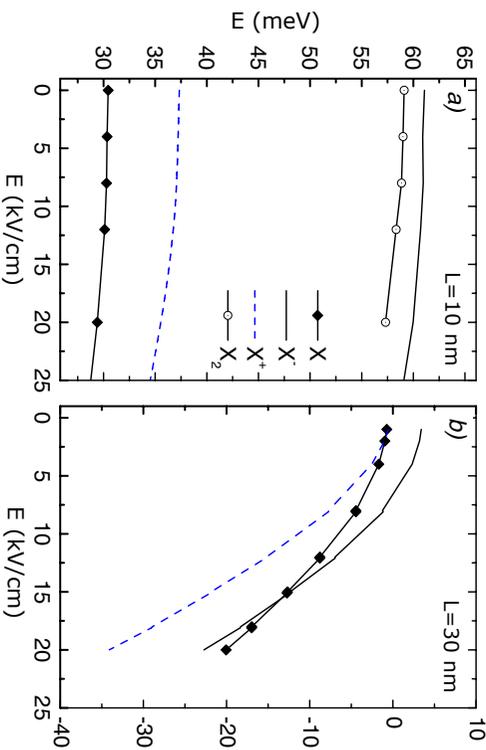
Figure 2. Energy of the exciton, trions and biexciton vs the strength of electric field a) for a 10 nm and b) for a 30 nm wide QW. In weak fields the total energy show a quadratic dependence on the field strength, E_z, (quadratic Stark effect). In the opposite limit of high fields, the dependence becomes similar to the linear Stark effect.

and hence $E < 0$, see Fig. 2(b). First, the energy shows quadratic and then linear dependence on the field strength. The Stark shift, in this case, can be obtained by subtracting the energy at zero-field. Our preliminary investigations of the binding energies of excitonic complexes in a 30 nm QW at field 20 kV/cm shows that the trions can still exist at these fields, while the biexciton becomes unstable already at fields $10 - 12$ kV/cm. Hence, at these conditions both the indirect excitons and trions (for temperatures below $1.1 - 2.2$ K) can exist. In comparison, the biexciton becomes ionized into two excitons at the field $E_z \approx 10$ kV/cm when the induced dipole moment of two coupled excitons becomes sufficiently large, and the repulsive dipole-dipole interaction prevents formation of a bound state.

Now we analyze the field dependence of the induced dipole moment, see Fig. 3. The dipole moment can be obtained directly from the electron and hole density distributions calculated for different field strengths as shown in Fig. 1 (the exciton case). To get the dipole moment, $\mu = e \cdot d$, we use the expression

$$d = \langle z_e \rangle - \langle z_h \rangle = \int z_e \rho_e(z_e) dz_e - \int z_h \rho_h(z_h) dz_h, \qquad (8)$$

which is the difference between the average positions of the electron and the hole inside the QW, see Fig. 3(right panel). The separation d starts from zero at $E_z = 0$ kV/cm when the PD is completely symmetric, and increases monotonically to the value $d = 15.78$ nm at $E_z = 20$ kV/cm. At weak fields, $E_z \leq 10$ kV/cm, the dependence is linear, and it starts to saturate at $E_z \geq 20$ kV/cm.

In the next section we discuss a possible realization of an external lateral confinement for excitons in the QW plane and show how the above results from quantum simulations in the homogenous field can be applied to thermodynamic simulation of many-exciton systems in arbitrary (also inhomogeneous) fields. The excitons get confined in all three spatial dimensions and their density becomes a controllable parameter through the strength of the external field.
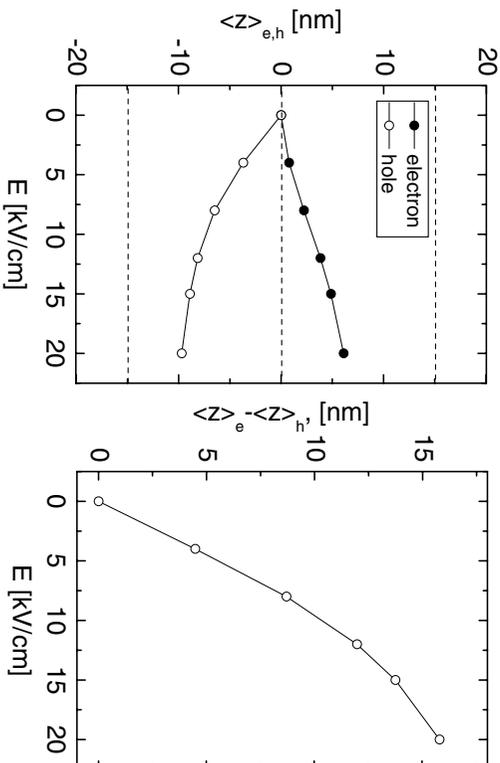
Figure 3. *Left:* Electric field dependence of the average electron (hole) position in a 30 nm wide QW. *Right:* The induced average electron-hole separation giving rise to a dipole moment.

4. Realization of quantum Stark confinement

To realize an electrostatic trap potential for optically created excitons in a single QW we have to put the following constraints on the external potential:

(i) As excitons are quasi particles with a short lifetime we have to assure that they can thermalize to a quasi-equilibrium. By spatial separation of electrons and holes in an electric field perpendicular to the QW plane the exciton radiative lifetime can be extended by more than three orders of magnitude.

(ii) In addition to the spatial separation of electron and holes, a lateral confinement for the excitons arises from the quantum-confined Stark effect, which depends only on the z-component of the electric field. The size of the resulting trap is of the order of several micrometers. A similar trap size has been recently realized by applying deformation stress on the QW surface [13].

(iii) The radial component of the field leads to destabilization of the excitons due to the opposite direction of the external forces acting on the electrons and holes. Hence the radial field has to be minimized by a proper choice of the geometry of the electrostatic contacts.

(iv) Further the applicable field strength is limited as it should not result in ionization of the excitons by tunneling of particles out of the quantum well.

To produce a suitable (inhomogeneous) electrostatic field E_z in the quantum well plane satisfying the above requirements, we consider a single tip electrode placed above the substrate. Thus the in-plane exciton-exciton coupling strength can be adjusted independently by the strength of the external confinement, as well as by the exciton-exciton repulsion strength. While controlling the tip-substrate distance allows to specify the geometry of the quantum Stark confinement and with it the exciton density, changing the tip voltage gives direct access to E_z and the corresponding exciton dipole moment, see Fig. 3 (right panel).

In the following we consider a single QW of the width $L = 30$ nm which provides a sufficient strong Stark shift (see section III). The distance between electrode and sample is $50\mu m$ and the (non-critical) width of the bufferlayer is 300 nm. Due to the symmetry, the radial field E_z below the electrode is zero and increases linearly with the distance from the trap center, see Fig. 4(a).
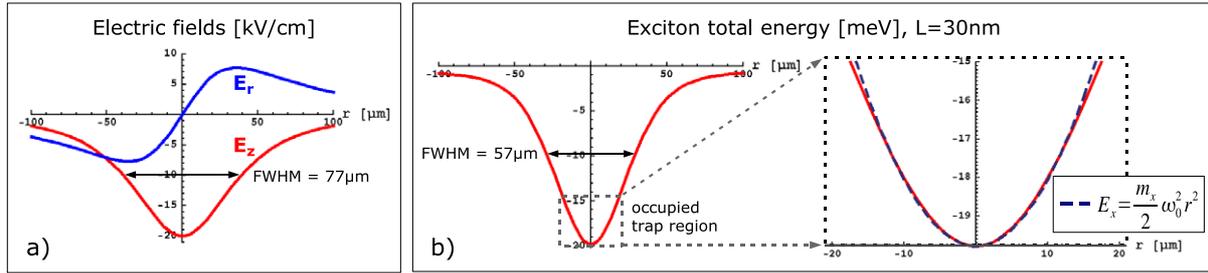
Figure 4. a) Radial, E_r, and vertical, E_z, field component below the electrode. **b)** Exciton energy as a function of the exciton in-plane position (quantum Stark confinement potential), which can be approximated as parabolic in the central region of the trap. Right Figure is an enlargement of the dottet region in part b).

This provides an effective "evaporative" cooling mechanism, because with increased distance from the trap center ionization is enhanced and energetic free electrons and holes leave the trap. In contrast, according to the large tip to sample distance, the radial field in the central region of the trap is negligible.

To avoid formation of other bound states except excitons (biexcitons and trions) the applied field should not be less than $E_z = 20$ kV/cm. On the other hand stronger fields introduce high demands on the experimental realization and lead, as mentioned above, to ionization and tunneling out of the QW. Hence we consider, in the following, an inhomogeneous field induced by a tip electrode, which below the electrode in the QW plane equals 20 kV/cm and causes a Stark shift of 20 meV, see Fig. 2(b). In the relevant central region of the QW, i.e. $R < 15$ μm, the effective lateral confinement of the excitons, as derived in the next section, can be approximated by a harmonic trap, $E_x = \frac{1}{2}m_x\omega_0^2 R^2$ (where $m_x = m_e + m_h = 0.41m_0$ is the total exciton mass in the GaAs QW) with the frequency $\omega_0 = 3.8$ GHz, see Fig 4(b).

By changing the field strength and geometry, the laser intensity (exciton number) and temperature, the exciton-exciton correlations can be varied in broad ranges giving rise to gas-like, liquid-like and solid-like behavior.

5. Model of indirect excitons in the trap

At temperatures much less than the exciton binding energy, i.e. $T \ll E_B(X) \approx 133$ K, and moderate densities, scattering states, i.e. free (unbound) electrons and holes, can be neglected. Further, the strong electric field prevents formation of biexcitons. Due to the strong electron-hole binding indirect excitons are formed. Hence we will now transform the Hamiltonian, Eq. (4), into a Hamiltonian of N_x bound electron hole pairs ($N_e = N_h = N_x$)

$$\hat{H} = \hat{H}_e + \hat{H}_h + \sum_{i=1}^{N_e}\sum_{j=1}^{N_h} V_{eh}(\mathbf{r}_{ei}, z_{ei}, \mathbf{r}_{hj}, z_{hj}) + \sum_{\alpha=e,h}\sum_{i=1}^{N_\alpha}\sum_{j=i+1}^{N_\alpha} V_{\alpha\alpha}(\mathbf{r}_{\alpha i}, z_{\alpha i}, \mathbf{r}_{\alpha j}, z_{\alpha j}) \quad (9)$$

where from now on vectors $\mathbf{r}$ denote 2d vectors in the QW plane. The Hamiltonian of non-interacting electrons (holes) reads

$$\hat{H}_{e(h)} = \sum_{i=1}^{N_{e(h)}} \left[-\frac{\hbar^2}{2m_{e(h)}}\nabla^2_{\mathbf{r}_{e(h)i}} + V_{e(h)}^{QW}(z_i) + V_{e(h)}^F\{E_z(\mathbf{r}_i, z_i)\} \right] \quad (10)$$

where V^{QW} is the QW confinement and V^F is the electrostatic potential due to the electric field. Now we want to distinguish the interaction between the electron i and the hole j bound in the

exciton, $V_{eh}^{i=j}$, and the electron-hole interaction of the particles i, j from two different excitons, $V_{eh}^{i\neq j}$. We call these two types of interactions *intra-* and *inter-*exciton electron-hole correlation terms, respectively. The general expression for all types of interactions is given by

$$V_{\alpha\beta}(\mathbf{r}_{\alpha i}, z_{\alpha i}, \mathbf{r}_{\beta j}, z_{\beta j}) = \frac{e_i e_j}{\varepsilon \sqrt{|\mathbf{r}_{\alpha i} - \mathbf{r}_{\beta j}|^2 + (z_{\alpha i} - z_{\beta j})^2}} \tag{11}$$

where $\alpha = e, h$ and $\beta = e, h$.

5.1. Lateral confinement potential for excitons

Using the results obtained for the single exciton problem from PIMC simulations (Sec. III) allows us to obtain the quantum Stark confinement in the limit $d \ll \bar{r}$, where $\bar{r}$ is the average exciton-exciton separation., i.e. the exciton binding energy is much stronger than all other Coulomb interaction terms. Then the Hamiltonian (9) can be written as

$$\hat{H} = \sum_{i=1}^{N_x} \hat{H}_x^{(i)} + \sum_{i=1}^{N_x} \sum_{j=i+1}^{N_x} U_{xx} \quad, \tag{12}$$

with the single exciton Hamiltonian given by

$$\hat{H}_x^{(i)} = -\frac{\hbar^2}{2m_e}\nabla_{\mathbf{r}_{e_i}}^2 - \frac{\hbar^2}{2m_h}\nabla_{\mathbf{r}_{h_i}}^2 + V_e^{ext}(\mathbf{r}_{e_i}, z_{e_i}) + V_h^{ext}(\mathbf{r}_{h_i}, z_{h_i}) + V_{eh}(\mathbf{r}_{ei}, z_{ei}, \mathbf{r}_{hi}, z_{hi}) \quad, \tag{13}$$

where

$$V_{e(h)}^{ext}(\mathbf{r}_{e(h)_i}, z_{e(h)_i}) = V_{e(h)}^{QW}(z_i) + V_{e(h)}^F\{E_z(\mathbf{r}_i, z_i)\} \tag{14}$$

is the effective external potential due to the external field and the QW. Introducing relative and center of mass coordinates of an electron hole pair

$$\mathbf{R}_i = (m_e \mathbf{r}_{e_i} + m_h \mathbf{r}_{h_i})/m_x, \quad \mathbf{r}_i = \mathbf{r}_{e_i} - \mathbf{r}_{h_i} \quad, \tag{15}$$

$$Z_i = (m_e z_{e_i} + m_h z_{h_i})/m_x, \quad z_i = z_{e_i} - z_{h_i} \quad, \tag{16}$$

$$m_x = m_e + m_h, \quad m_r^{-1} = m_e^{-1} + m_h^{-1} \quad, \tag{17}$$

the relative coordinates $\{\mathbf{r}_i, z_i\}$ describe the internal exciton structure (exciton wave function) whereas the center of mass coordinates $\{\mathbf{R}_i, Z_i\}$ describe the position of the exciton in the external potential.

Using the adiabatic approximation discussed in Sec. III we can separate the z-direction and average the 3D Hamiltonian over the QW thickness using the PD functions of the single electron and hole for the corresponding electric field, see Fig. 1. This reduces the problem to an effective 2D-system of dipoles moving in the QW plane. For our calculations we assume that the field is constant over the (narrow) QW width, i.e. $E_z(\mathbf{r}_i, z_i) = E_z(\mathbf{r}_i)$. Knowing the electron and hole probability distributions ρ_e, ρ_h for a given external field, see Fig. 4(a), we compute the effective electron-hole separation as a function of the exciton center of mass coordinate

$$d(\mathbf{R}_i) = \langle z_{e_i} - z_{h_i} \rangle_{\rho_e(\mathbf{r}_{e_i}, z_{e_i}), \rho_h(\mathbf{r}_{h_i}, z_{h_i})} \quad, \tag{18}$$

as well as the average intra exciton correlation

$$U_{eh}(\mathbf{R}_i) = \langle V_{eh}(\mathbf{r}_{ei}, z_{ei}, \mathbf{r}_{hi}, z_{hi}) \rangle_{\rho_e, \rho_h} + \left\langle -\frac{\hbar^2}{2m_r}\nabla_{\mathbf{r}_i}^2 \right\rangle_{\rho_e, \rho_h} \tag{19}$$

plus the effective confinement potential

$$U_x^{ext}(\mathbf{R}_i) \approx \langle V_e^{ext}(\mathbf{r}_{e_i}, z_{e_i})\rangle_{\rho_e} + \langle V_h^{ext}(\mathbf{r}_{h_i}, z_{h_i})\rangle_{\rho_h} \quad . \tag{20}$$

The total energy of the exciton depending on its position in the trap, see Fig. 4(b), is obtained using the results for Stark shift of the exciton energy (Fig. 2) taken for the z-components of electric field produced by the electrode, see Fig. 4(a). After separation of the relative problem which gives rise to a single exciton Coulomb energy contribution $U_{eh}(\mathbf{R}_i)$, the single exciton Hamiltonian becomes

$$\hat{H}_x^{(i)}(\mathbf{R}_i) = -\frac{\hbar^2}{2m_x}\Delta_{\mathbf{R}_i} + U_x^{ext}(\mathbf{R}_i) + U_{eh}(\mathbf{R}_i) \quad . \tag{21}$$

Due to the quantum confined Stark effect, the exciton total energy has a minimum below the electrode where the E_z-field is the strongest and produces an effective almost parabolic lateral confinement acting in plane of the QW, see Fig. 4(b).

5.2. Effective exciton-exciton interaction

As mentioned above we consider low exciton densities, that means for the considered trap on the micrometer scale the exciton-exciton distances exceed $10\,a_B$ (we use as length unit the effective Bohr radius $a_B = \hbar^2\epsilon/m_e e^2 = 9.98$ nm), i.e. $r_s = \bar{r}/a_B \geq 10$. Furthermore, our PIMC calculations of the effective exciton-exciton interaction $U_{xx}(\mathbf{R}_i, \mathbf{R}_j)$ in the low density limit show that for exciton-exciton distances larger than $3.5\ a_B$ the classical dipole interaction is a good approximation [14]. This means that all pair interactions in the electron hole system (except the electron-hole interaction inside each exciton, i.e. terms V_{eh} with $i = j$) can be reduced to dipole-dipole interactions between (center of masses of) excitons

$$\sum_{i=1}^{N_e}\sum_{j=1,j\neq i}^{N_h} V_{eh} + \sum_{i=1}^{N_e}\sum_{j=i+1}^{N_e} V_{ee} + \sum_{i=1}^{N_h}\sum_{j=i+1}^{N_e} V_{hh} \approx \sum_{i=1}^{N_x}\sum_{j=i+1}^{N_x} U_{xx}(\mathbf{R}_i, \mathbf{R}_j) \tag{22}$$

where $U_{xx}(\mathbf{R}_i, \mathbf{R}_j) = \mu(\mathbf{R}_i)\mu(\mathbf{R}_j)/(\varepsilon|\mathbf{R}_i - \mathbf{R}_j|^3)$. The dipole moment depends on the position of the exciton relative to the trap center $\mu(\mathbf{R}) = e_0 \cdot d(\mathbf{R}) = e_0 \cdot [15.78 - 3.8 \cdot 10^{-9}R^2]$ nm. Here we have neglected all quantum properties of the center of mass motion and the spin statistics of electrons and holes. This is well justified in the low-density regime where the overlap of two electrons (holes) is negligible.

Finally, the problem reduces to a 2D-system of $N_x = N/2$ classical particles in an effective external confinement interacting via dipole-dipole repulsion with the N_x-particle Hamiltonian

$$H = \sum_{i=1}^{N_x} H_x^{(i)}(\mathbf{R}_i) + \sum_{i=1}^{N_x}\sum_{j=i+1}^{N_x} \frac{\mu(\mathbf{R}_i)\mu(\mathbf{R}_j)}{\varepsilon|\mathbf{R}_i - \mathbf{R}_j|^3} \tag{23}$$

which can be efficiently used in classical thermodynamic Monte Carlo simulations discussed in the next section, where we analyze spatial configuration of N_x excitons at different temperatures and densities.

6. Simulation results

In our simulations the control parameters are the temperature $k_B T$ and number of particles, N_x. How many excitons can be created in the trap depends on the laser intensity and recombination rates.
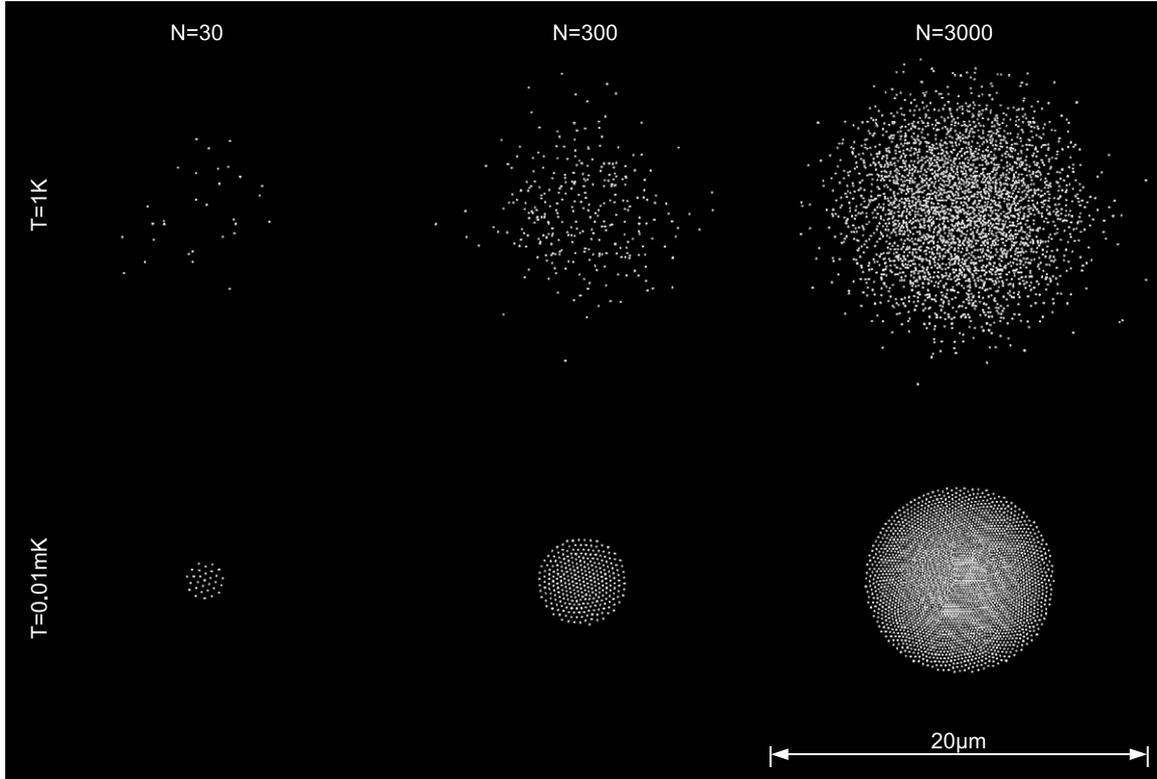
Figure 5. Typical snapshots of thermodynamic Monte Carlo simulations for various numbers of excitons N_x and temperatures T.

Fig. 5 shows typical particle configurations observed in our simulations. First, we find that the size of the exciton cloud and the exciton density in the trap center increase with the number of excitons. Second, with decreasing temperature the cold excitons become localized. The typical size of the exciton cloud, R_{max}, strongly depends on temperature. For $N_x = 3000$ excitons, $R_{max} \approx 10\mu m$ for $T = 4$ K and $R_{max} \approx 3\mu m$ for temperatures around 40 mK.

Fig. 6 shows that, for $T = 4K$, the excitons are in the gas phase. In the fluid state (at $T = 40$ mK) the excitons are localized in the trap center with the diameter $D \approx 3 \ \mu m$. At $T = 0.4$ mK the radial distribution clearly shows a shell structure. This behavior is validated by the temperature dependence of the classical coupling parameter $\Gamma = \langle U_{xx} \rangle / k_B T = \langle e^2 d^2 / \epsilon R_{ij}^3 \rangle / k_B T$, see Fig. 7. When we observe formation of shells, the coupling parameter reaches values $\Gamma \geq 100$. This qualitatively agrees with the well known results for a pure classical 2D Coulomb systems, where the formation of a Wigner lattice has been found for $\Gamma^{cr} \approx 137$.

On the other hand, if we look at the density in the trap center (see inset of Fig. 6), it increases strongly with the exciton number, and a more accurate discription is required. Typical parameters characterizing the "quantum" system are the Brueckner parameter, $r_s = \bar{r}/a_B$, and the dipole parameter, $\gamma = \bar{r}/d$, where $\bar{r}$ is the nearest neighbor distance (first peak of the pair correlation function). Performed estimations of these parameters in the trap center give us the following values (depending on the exciton number N_x): i) for $N_x = 2$ we get $r_s = 35$ and $\gamma = 23$; ii) for $N_x = 3000$ we get $r_s = 11$ and $\gamma = 8$. These estimates show that our classical treatment of the center of mass motion of the excitons is justified. On the other hand, with further increase of N_x, r_s will approach unity, and a full quantum treatment will be necessary. These calculations are under way [14].
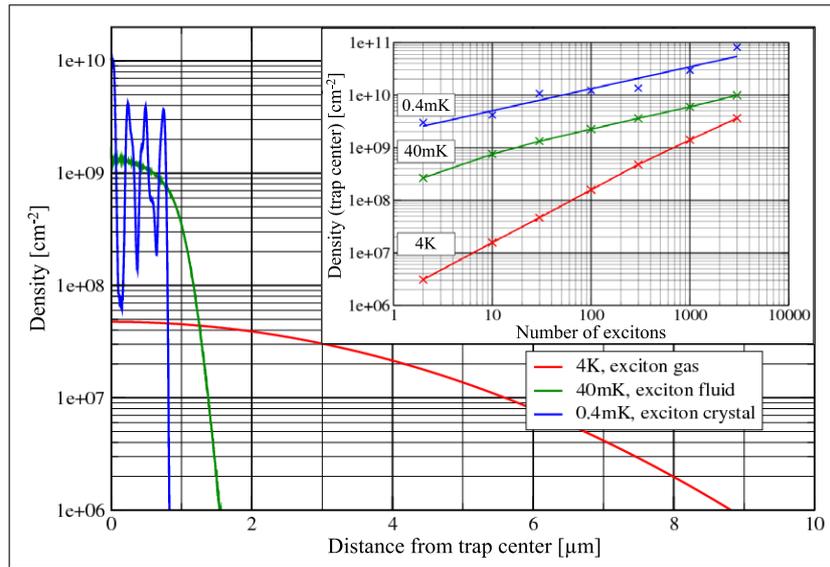
Figure 6. Radial density distribution of $N_x = 30$ excitons for three temperatures. Due to the parabolic trap the highest exciton density is reached in the trap center. *Inset:* trap center density as a function of exciton number.
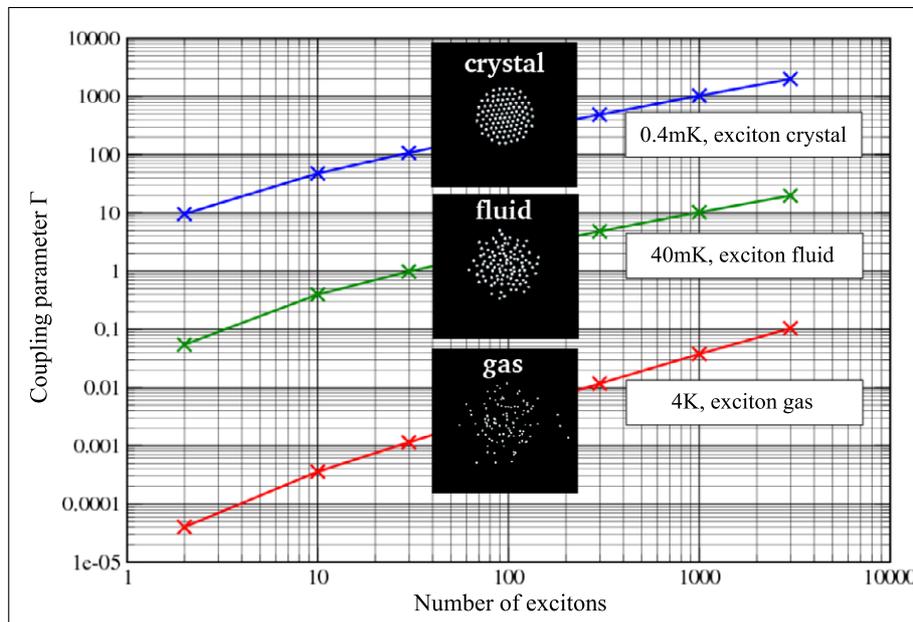
Figure 7. Dipole coupling parameter $\Gamma = \langle U_{xx} \rangle / k_B T$ as a function of exciton number for three different temperatures. *Inset:* Simulation snapshots of $N_x = 100$ excitons. Depending on temperature excitons are in solid, liquid or gas phase.

7. Conclusions

We have considered optically excited indirect excitons in a single QW where the electrostatic field of a tip electrode leads to spatial separation of electrons and holes. The harmonic lateral

confinement of the indirect excitons in the QW plane is due to the quantum confined Stark effect and creates an exciton trap of micrometer size which is much larger than the exciton Bohr radius. In the considered low density regime a strong dipole-dipole repulsion allows for strong localization of the exciton wave functions.

Using Path Integral Monte Carlo we computed the PD and the energy Stark shift for different excitonic complexes influenced by the electric field. We obtained an effective exciton lateral confinement and the dipole moment of indirect excitons depending on the strength of the electric field. We discussed the influence of field strength, QW width, excitation intensity (directly related to the exciton population of the trap) and temperature. Our theoretical results allowed us to predict the parameter range where interesting many-particle states, including exciton crystallization, are expected to exist. With these predictions experimental realization of these effects should be possible.

[1] Lozovik Yu E, Yudson V I 1976 *JETP Lett.* **22** 274; Lozovik Yu E and Berman O L 1997 *JETP* **84** 1027
[2] Bayer M, Timofeev V B, Faller F, Gutbrod V, and Forchel A 1996 *Phys. Rev. B* **54** 008799
[3] Negoita V, Snoke D W, Eberl K, 1999 *Phys. Rev. B* **60** 2661
[4] Butov L V, Ivanov A L, Imamoglu A, Littlewood P B, et al 2001 *Phys. Rev. Lett.* **86** 5608 and references therein.
[5] Feynman R P and Hibbs A R 1965 *Quantum Mechanics and Path Integrals* McGraw Hill, New York
[6] Ceperley D M 1995 *Rev. Mod. Phys.* **65** 279
[7] Filinov A V, and Bonitz M in 2006 *Introduction to Computational Methods in Many Body Physics*, Bonitz M and Semkat D (eds.) Rinton Press, Princeton
[8] Filinov A V, Riva C, Peeters F M, Lozovik Yu E, and Bonitz M 2004 *Phys. Rev. B* **70** 35323
[9] Riva C, Peeters F M, and Varga K 2001 *Phys. Rev. B* **64** 235301
[10] Riva C, Peeters F M, and Varga K 2001 *Phys. Rev. B* **63** 115302
[11] Filinov A V, Ludwig P, Bonitz M, Lozovik Yu E, and Stolz H in preparation
[12] Filinov A V, Golubnychiy V O, Bonitz M, Ebeling W, and Dufty J W 2004 *Phys. Rev. E* **70** 046411
[13] Snoke D W, Liu Y, Voros Z, Pfeiffer L, West K 2004 *arXiv: cond-mat/0410298*
[14] An analysis of improved pair potentials, valid also for high densities, is in progress.
[15] Filinov A, Bonitz M and Lozovik Yu E 2001 *Phys. Rev. Lett.* **86** 3851
[16] Filinov A, Bonitz M, and Lozovik Yu E 2003 *J. Phys. A: Math. Gen.* **36** 5899
[17] Filinov A, Ludwig P, Golubnychyi V, Bonitz M and Lozovik Yu E 2003 *Phys. Stat. Sol. (c)* **0**, No. 5, 1518
[18] Ludwig P, Filinov A, Bonitz M and Lozovik Yu E 2003 *Contrib. Plasma Phys.* **43** 285

Quantum Stark confined strongly correlated indirect excitons in quantum wells

P. Ludwig, A. V. Filinov, M. Bonitz, and H. Stolz

In this contribution we consider small ensembles of spatially correlated indirect condensate in single quantum well. Using Path Integral Monte Carlo we compute from first principles the spatial separation of electrons and holes and the local quantum Stark confinement of the excitons in the quantum well which is produced by an external electric field of a single tip electrode. By changing the field strength, the tip to sample distance, the excitation intensity (exciton number) and temperature, the exciton–exciton correlations can be varied in broad ranges. Discussing two different semiconductor quantum well heterostructures (GaAs/AlGaAs and ZnSe/ZnSSe) we propose a possible setup which should allow to observe in experiment new interesting many-particle phenomena.

1 Introduction

2 Electrostatic trap potential

3 Exciton properties in the confinement field

References

[1] Yu. E. Lozovik and V. I. Yudson, JETP Lett. 22, 274 (1976).
[2] A. Filinov, M. Bonitz, P. Ludwig, and Yu. E. Lozovik, phys. stat. sol. (c) 3, 2457 (2006).
[3] S. Zimmermann, A. O. Govorov, W. Hansen, J. P. Kotthaus, M. Bichler, and W. Wegscheider, Phys. Rev. B 56, 13414 (1997).
[4] T. Baker, A. Stenner, W. Wegscheider, and M. Bichler, phys. stat. sol. (b) 185, 85 (1996).
[5] A. T. Hammack, N. A. Gippius, G. O. Andreev, L. V. Butov, M. Hanson, and A. C. Gossard, arXiv: Cond-mat/0508435 (2005).
[6] R. Rapaport, G. Chen, S. Simon, O. Mitrofanov, L. N. Pfeiffer, and P. M. Platzman, Phys. Rev. B 72, 075428 (2005).
[7] A further reduction of the in-plane field component can be realized with a confining layer close to the QW as discussed in [5, 6].
[8] Due to the smaller dielectric constant, $\varepsilon_{ZnSe} = 8.7 < \varepsilon_{GaAs} = 12.6$, in the case of ZnSe a smaller critical field is sufficient.
[9] A. Filinov, P. Ludwig, Yu. E. Lozovik, M. Bonitz, and H. Stolz, J. Phys. Conf. Ser. 15, 197 (2006).
[10] We use $m_{e,ZnSe} = 0.15 m_0$, $m_{h,ZnSe} = 0.67 m_0$, $m_{e,GaAs} = 0.066 m_0$, $m_{h,GaAs} = 0.17 m_0$, where m_0 is the free electron mass.

Path integral Monte Carlo results for Bose condensation of mesoscopic indirect excitons

A. Filinov*[1,2], M. Bonitz[1], P. Ludwig[1], and Yu. E. Lozovik[2]

[1] Institute of Theoretical Physics and Astrophysics, CAU Kiel, Leibnizstrasse 15, 24098 Kiel, Germany
[2] Institute of Spectroscopy, RAS, Moscow region, Troitsk, 142190, Russia

First principle results for small clusters of strongly correlated indirect excitons in a harmonic confinement potential are presented. At low temperatures Bose condensation is verified. The condensate fraction and the superfluid density are computed. The importance of a correct inclusion of the Bose statistics of excitons and holes is demonstrated.

1 Introduction

2 Model

$$\hat{H} = \hat{H}_e + \hat{H}_h + \sum_{i=1}^{N}\sum_{j>i}^{N}\frac{e^2}{\varepsilon|z_i - z_j|}, \quad \hat{H}_a = \sum_{i=1}^{N}\left(-\frac{\hbar^2}{2m_a}\nabla_i^2 + \frac{m_a\omega^2}{2}r_i^2\right) \quad (1)$$

Fig. 1 Pair distribution (a) and Radial density distribution (b) of a ...

3

4 Fermionic results

5 Discussion

Fig. 2 Evolution of permutation cycles for low temperatures ...

Fig. 3 Comparison of the Bose model and the case fermionic simulation for electron-hole pairs: (a) Radial density distribution of excitons and (b) Superfluid fraction versus coupling parameter ...

References

[1] Yu. E. Lozovik and V. E. Yudson, JETP Lett. 22, 274 (1975)
[2] V. Negoita, D. W. Snoke, and K. Eberl, Phys. Rev. B 60, 2661 (1999)
[3] L. V. Butov, J. Phys.: Condens. Matter 16, R1577 (2004)
[4] A. Filinov, P. Ludwig, Yu. E. Lozovik, M. Bonitz, and E. Sota, accepted for publication in J. Phys.
[5] P. Ludwig, A. Filinov, M. Bonitz, and H. Stolz, phys. status solidi
[6] A. Filinov, M. Bonitz, and Yu. E. Lozovik, Phys. Rev. Lett. 86, 3851 (2001)
[7] A. Filinov, J. Phys. A: Math. Gen. 36, 5896 (2003)
[8] A. Filinov et al., in Introduction to Computational Methods for Many Body Systems, M. Bonitz and D. Semkat (eds.) (Rinton Press, Princeton, 2006)
[9] D. M. Ceperley, Rev. Mod. Phys. 67, 279 (1995)
[10] A. P. Andreev and M. I. Lifshits, Sov. Phys. JETP 29, 1107 (1969)
[11] A. J. Leggett, Phys. Rev. Lett. 25, 1543 (1970)
[12] S. Giorgini, J. Boronat, and J. Casulleras, Phys. Rev. A 60, 5129 (1999)

5.3 Crystallization in Mass-Asymmetric Electron-Hole Bilayers

We consider a mass-asymmetric electron-hole bilayer. Electron and hole Coulomb correlations and electron and hole quantum effects are treated on first principles by path integral Monte Carlo methods. For a fixed layer separation we vary the mass ratio M of holes and electrons between 1 and 100 and analyze the structural changes in the system. While, for the chosen density, the electrons are in a nearly homogeneous state, the hole arrangement changes from homogeneous to localized, with increasing M which is verified for both, mesoscopic bilayers in a parabolic trap and for a macroscopic system.

The results were published as refereed journal publication:

5.3.1 ***Crystallization in Mass-Asymmetric Electron-Hole Bilayers,***
P. Ludwig, A. Filinov, Yu.E. Lozovik, H. Stolz, and M. Bonitz,
Contrib. Plasma Phys. **47**, 335-344 (2007)

Crystallization in mass-asymmetric electron-hole bilayers

P. Ludwig[*1,2], **A. Filinov**[1,3], **Yu.E Lozovik**[3], **H. Stolz**[2], and **M. Bonitz**[1]

[1] Christian-Albrechts-Universität zu Kiel, Institut für Theoretische Physik und Astrophysik, Leibnizstrasse 15, 24098 Kiel, Germany

[2] Universität Rostock, Institut für Physik, Universitätsplatz 3, 18051 Rostock, Germany

[3] Institute of Spectroscopy RAS, Moscow region, Troitsk, 142190, Russia

We consider a *mass-asymmetric* electron and hole bilayer. Electron and hole Coulomb correlations and electron and hole quantum effects are treated on first princles by path integral Monte Carlo methods. For a fixed layer separation we vary the mass ratio M of holes and electrons between 1 and 100 and analyze the structural changes in the system. While, for the chosen density, the electrons are in a nearly homogeneous state, the hole arrangement changes from homogeneous to localized, with increasing M which is verified for both, mesoscopic bilayers in a parabolic trap and for a macroscopic system.

1 Introduction

Strongly correlated Coulomb systems are of growing interest in many fields, including plasmas and condensed matter, see e.g. [1] for an overview. In particular, Wigner crystal formation is one of the most prominent correlation phenomena observed in ultracold ions [2], dusty plasmas [3, 4], quantum dots, e.g. [5, 6] and other confined (non-neutral) systems. Recently crystal formation in two-component (neutral) quantum plasmas was demonstrated by simulations [7] confirming early predictions of hole crystallization in semiconductors by Halperin and Rice [8], Abrikosov [9] and others. Interstingly, this is essentially the same physical phenomenon as crystallization of nuclei in White Dwarf stars [10].

A different type of two-component system, standing in between the neutral and non-neutral Coulomb systems, are bilayer containing spatially separated positive and negative charges which are most easily to realize in semiconductors by means of doping (electron-hole bilayers). These systems are of high interest because the strength of the correlations can be tuned by varying the layer separation d. The interplay of intra-layer and inter-layer correlations in classical bilayers has been studied in detail for macroscopic, e.g. [11] and mesoscopic [12, 13] systems. Quantum bilayers have been treated much less, see e.g. [14, 15, 16, 17] and are much poorer understood. In particular, most investigations have considered symmetric bilayers, where the hole to electron mass ratio $M = m_h/m_e$ equals one. However, the typical mass ratio in semiconductors is on the order of $M = 3 \ldots 10$, and even exotic materials exist where M reaches 40 [18] or even higher values.

For this reason, in this paper we concentrate on the effect of the mass ratio on crystal formation in quantum electron-hole bilayers. Varying M from 1 to 100 at low temperature and high density, we can tune the hole behavior from delocalized (quantum) to localized (quasi-classical) while the electrons remain delocalized all the time. As was recently observed for bulk semiconductors [7], holes undergo a phase transition to a crystalline state if the mass ratio exceeds a critical value of $M_{cr} \approx 80$. Here, we extend this analysis to bilayers where M_{cr} depends on d and the in-layer particle density. To reduce the complexity of the problem, here we will keep d fixed. The complicated overlap of correlation and quantum effects of both, electrons and holes, is fully taken care of by performing first-principle path integral simulations. We present results for two types of e-h bilayers: a mesocsopic system of $N = 36$ particles in a parabolic trap and for a macroscopic system of the same density.

* Corresponding author: e-mail: ludwig@theo-physik.uni-kiel.de, Phone: +49 (0)431 880 4732, Fax: +49 (0)431 880 4094

2   Model and Parameters

The physical realization of the mass asymmetric bilayers considered here can be a system of two coupled quantum wells filled with electrons and holes, respectively. An additional in-plane potential can produce the lateral confinement of the carriers leading to a system of two coupled quantum dots. Recently, we have analyzed in detail a possible realization of a parabolic in-plane potential using the idea of the quantum Stark confinement [19]. An inhomogenous electric field applied perpendicular to the QW plane changes the energy of a particle in the quantum well because the penetration of a particle inside the barrier material depends on the strength of the electric field. For example, in GaAs and ZnSe based QW one can achieve harmonic trap frequencies from 1 GHz to 1 THz for typical electric field strengths of $10 - 20$ kV/cm.

In this paper, we approximate two coupled QWs by a model of two vertically separated 2D layers populated with N_e electrons and N_h holes (we consider the case $N_e = N_h = N/2$). The charges interact via the Coulomb potential. The underlying Hamiltonian is well defined and is of practical importance for semiconductor heterostructures

$$\hat{H} = \hat{H}_e + \hat{H}_h + \sum_{i=1}^{N} \sum_{j=i+1}^{N} \frac{e_i e_j}{\varepsilon \sqrt{(\mathbf{r}_i - \mathbf{r}_j)^2 + (z_i - z_j)^2}}, \quad \hat{H}_a = \sum_{i=1}^{N_a} \left(-\frac{\hbar^2}{2m_a^*} \nabla_{\mathbf{r}_i}^2 + \frac{m_a^*}{2} \omega_a^2 r_i^2 \right), \quad (1)$$

where the electrons (e) are confined to the plane $z = 0$ and the holes (h) to the plane $z = d$; also $\mathbf{r}_i$ and $\mathbf{r}_j$ are the in-plane 2D radius vectors describing the particle coordinates in each layer. In the following all lenghts will be given in units of the effective Bohr radius $a_B = \hbar^2 \epsilon / m_e^* e^2$. For example, for GaAs and ZnSe quantum wells this results in the length units $a_B(GaAs) = 9.98$ nm and $a_B(ZnSe) = 3.07$ nm. Energies and temperatures are measured in Hartree units: $1 Ha(GaAs) = 11.47 meV (133.1\ K)$ and $1 Ha(ZnSe) = 53.93 meV (625.8\ K)$.

For the mesoscopic trapped system the density is controlled by the harmonic trap frequency (we use $m_e^* \omega_e^2 = m_h^* \omega_h^2$) and is characterized by the coupling parameter $\lambda = (e^2/\epsilon l_0)/(\hbar \omega_e) = l_0/a_B$ with $l_0^2 = \hbar/m_e^* \omega_e$. In this case, the coupling parameter for the holes is related to the electron coupling as $\lambda_h = \lambda (m_h^*/m_e^*)^{3/4}$. Also for Coulomb systems in a parabolic trap one can find the following usefull relations. For two classical particles in a parabolic trap their separation distance r_0 in the ground state is given by: $e^2/\epsilon r_0 = m_e \omega_e^2 r_0^2/2$. Now we can define the density parameter $\tilde{r}_s$ (in analogy to the Brueckner parameter $r_s = \langle r \rangle/a_B$ for macroscopic systems) as follows: $\tilde{r}_s = r_0/a_B = (2e^2/\epsilon m_e \omega_e^2)^{1/3}/a_B = 2^{1/3} \lambda^{4/3}$. We will use this formula to obtain approximate relations between the densities in the mesoscopic and macroscopic system by relating $\lambda \leftrightarrow \tilde{r}_s \leftrightarrow r_s$.

2.1   Numerical details

To solve the problem of N interacting particles described by the Hamiltonian (1) we use the path integral Monte Carlo (PIMC) method. The applied PIMC simulation technique was described in detail in Ref. [20]. The effective interaction potentials used in the expressions for the high-temperature pair density matrices were obtained by using the matrix squaring technique [21, 22].

One of the main obstacles that limit applicability of the PIMC method for systems of particles obeing Fermi statistics is the so called *Fermion sign problem*. Without additional approximations the direct fermionic PIMC simulations are only limited to problems where the degeneracy is not very high. This, certainly depends on the physical situation and is related to the particle density, interaction strength and temperature. Full inclusion of the quantum exchange effects for the number of particles considered here, i.e $N_{e(h)} \approx 36 - 64$, will not be possible without neglecting the spin statistics and permutations in the electron and hole subsystems. However, direct comparison of the PIMC simulations without spin [23] with the results of Ref. [25] which include spin effects show, that the errors introduced by neglecting the spin statistics are of the order of few percents and are completely negligible for $\lambda \geq 10$. The considered here electron densities, i.e $r_s \approx 18$, are sufficiently low (for the holes the corresponding parameter $r_s^{(h)}$ is even larger due to their larger mass) and the dominant effect for the interparticle correlations (and in particular for the holes) are driven mainly by the strength of the Coulomb interaction and not by quantum statistics effects. Also, there is no doubt that the spin will have a negligible effect on the localized states of the holes when they form a 2D lattice. Hence, we expect, that the solid-liquid transition investigated in this paper will not be sensitive to the particle spin. Nevertheless, the question about the true ground state of the electron liquid (i.e. spin polarized or unpolarized), just after the solid-liquid transition is currently under active discussion [26] and requires further investigation.

In the simulations presented below we assume that the electrons and holes can reach thermal equilibrium and are cooled down by using, e.g. $^3He/^4He$ dilution refrigeration to a temperature of $k_BT = 1/3000$ Ha. For ZnSe (GaAs) this corresponds to an absolute value of $T = 208.6(44.37)$ mK. At these low temperatures thermal fluctuations are negligible and the system is practically in the ground state.

In the PIMC representation of the density matrix applied in our simulations [20], we have used 256 (in some cases 128) beads (high temperature factors). This was sufficient to reache convergence for the full energy better than 1% and an even better accuracy for the pair distribution functions. The use of such a moderate number of beads was only possible by using pre-computed tables of the pair density matrices for all types of Coulomb interactions, i.e. for the intra-layer and inter-layer interaction terms in the hamiltonian (1), and for the external parabolic confinement for both electrons and holes. To reduce the enormous computational effort for a simulation of fermions, here we used Boltzmann statistics for both electrons and holes, and the spin effects are omitted. For reasons discussed above we expect that this will not influence the results of this paper significantly.

Both layers are treated as pure 2D layers of zero thickness. Considering that the thickness of real physical QWs is of the order of few Bohr radii, this approximation seems to be reasonable for the range of densities considered here, i.e. $r_s = \langle r \rangle / a_B \geq 10$, and an inter-layer distance of $d = 20a_B$. [The case when d and $\langle r \rangle$ become comparable to the well width would require essentially more computationally costly 3D simulations and inclusion additional terms related to the QW potential in the hamiltonian (1)]. For quite narrow QWs with a thickness of about $1a_B$ and less, the addiabatic approximation can be succesfully used with the 2D hamiltonian (1) with slightly changed interaction terms (see Ref. [27]).

For the chosen inter-layer distance, $d = 20a_B$, our system represents essentiall a 3D structure, as the intra-layer and inter-layer correlations are on the same length and energy scales. For small ratios $d/r_s \ll 1$ the system approaches the single layer limit, whereas for $d/r_s \gg 1$, it behaves like two uncoupled layers. Also, for $d = 20a_B$ we can completely neglect the inter-layer tunneling, and the life time of electrons and holes can reach a few microseconds which is much larger than their equilibration time.

The mass ratio of the electrons and holes is varied in the range of $1 \leq m_h^*/m_e^* \leq 100$ which covers practically all semiconductor materials. In our simulations we have found that the initial equilibration time needed to bring the system from an initial randomly chosen configuration to the thermodynamic one, depends on the electron-hole mass ratio and the strength of the external confinement. Usually we skip the first $10\,000 - 100\,000$ MC-steps and only then start to accumulate thermodynamic averages.

2.2 Calculated quantities

2.2.1 Pair and radial distribution functions

The physically relevant quantities to investigate a phase transition are the *radial*, $n(r)$, and *pair* distribution function, $g(r)$. Both functions are a good probe of the short and long-range order in the system and yield information on the importance of correlation effects. In Statistical Mechanics these quantities are given by the expressions

$$g_{ab}(r) = \frac{1}{N_a N_b} \sum_{i=1}^{N_a} \sum_{j=1}^{N_b} \langle \delta(|\mathbf{r}_{ij}| - r) \rangle, \quad n_{a(b)}(r) = \frac{1}{N_{a(b)}} \sum_{i=1}^{N_{a(b)}} \langle \delta(|\mathbf{r}_i| - r_0) \rangle, \tag{2}$$

where a and b are two particle species, r_0 is the reference point for the radial density (e.g the center of the parabolic potential as used here), and $\langle \ldots \rangle$ denotes the thermodynamic average. In the PIMC approach the averaging is performed with the $N-$particle density matrix, i.e

$$\langle \ldots \rangle = \frac{1}{Z} \int \int d\mathbf{r}_1 d\mathbf{r}_2 \ldots d\mathbf{r}_N \, (\ldots) \, \rho(\mathbf{r}_1, \mathbf{r}_2, \ldots, \mathbf{r}_N; \beta). \tag{3}$$

After the high-temperature decomposition this integral includes also additional integrations over the particle coordinates on the intermediate "time-slices" and, as a result, the particle images on each time slice also contribute to the distribution function which significantly improves the convergence of the simulations.

2.2.2   Lindemann parameter

One of the criteria to investigate structural phase transitions (e.g., solid-liquid phase transition) was proposed by Lindemann [28], who used vibration of atoms in the crystal to explain the melting transition. The average amplitude of thermal vibrations increases with temperature of the solid. At some point the amplitude of the vibrations becomes so large that the atoms start to occupy the space of their nearest neighbors and disturb them, and the melting process is initiated. According to Lindemann, the melting might be expected when the root mean vibration amplitude $\sqrt{\langle \delta u^2 \rangle / a^2}$ exceeds a certain threshold value ($\langle \delta u^2 \rangle$ is the particle fluctuation from a lattice site, $a = 1/\sqrt{\pi n}$, n is the density). Namely, when the amplitude reaches at least 10% of the nearest neighbor distance, this quantity exhibits a rapid growth when the temperature becomes close to the melting temperature of the solid phase. While for 3D systems this criterion can be successfully used, in 2D this quantity shows a logarithmic divergence, $\ln(L/a)$, with the increase of the system size L. Instead, to indicate the phase transiton from a liquid to a crystal, in 2D, one should apply the modified Lindemann criterion and use the relative distance fluctuations [29]

$$u_r^{ab} = \frac{1}{N_a N_b} \sum_{i=1}^{N_a} \sum_{j=1}^{N_b} \sqrt{\frac{\langle r_{ij}^2 \rangle}{\langle r_{ij} \rangle^2} - 1}, \tag{4}$$

where r_{ij} is the distance between the particles i and j. To reduce the effect of particle diffusion through the cluster (in a finite system) or through the simulation cell (for a macroscopic system), which leads to very slow convergence with the increase of the system size, in the calculation of (4) we have performed partial averaging over $1\,000$ MC-steps (one block). After the current block has been completed we proceed to a new one and the MC averaging was repeated for the next $1\,000$ MC-steps. The difference in the fluctuations measured from block to block can characterize the ordering in the system and is more effective for large systems.

2.2.3   Nature of the phase transition in 2D systems

Strictly speaking, in classical macroscopic 2D systems at $T \neq 0$ a true crystal state does not exist. The absence of off-diagonal long range order in the system manifests itself in the existance of two disordered phases characterized by different asymptotic behaviours of the pair correlation function $g(r, r')$. The system undergoes a transition at a finite temperature T_{KT} (Kosterlitz-Thouless transition) when the asymptotes $g(r, r')|_{|\mathbf{r}-\mathbf{r}'| \to \infty}$ changes from

$$g(r, r') \approx \frac{\exp(-|\mathbf{r} - \mathbf{r}'|/\xi(T))}{|\mathbf{r} - \mathbf{r}'|^{\alpha(T)}} \quad (T \geq T_{KT}) \quad \text{to} \quad g(r, r') \approx \frac{1}{|\mathbf{r} - \mathbf{r}'|^{\alpha'(T)}} \quad (T < T_{KT}). \tag{5}$$

The important question of the relevence of the standard Kosterlitz-Thouless theory also for 2D *quantum* systems has been disscussed in Ref. [32] for the two-dimensional XY model. A generalization for Coulomb systems is subject of ongoing work [33]. Concerning the interpretation of the results of the present publication we indeed find a abrupt transition in the decay of the maxima and mimima of $g(r, r')$ (see the discussion below) which can be approximated by the asymptotes in Eq. (5).

3   Numerical results: Mesoscopic system

In the following we consider a bilayer system populated with a mesoscopic number of $N_e = N_h = 36$ electrons and holes. The results of our simulations are presented in Figs. 2-3. In our simulations two different densities are analyzed, given by $\lambda = 5$ and $\lambda = 10.5$ which corresponds to the first maxima of the pair distribution function $g_{hh}^{max} = 8.7$ and $g_{hh}^{max} = 19$, respectively. These densities are chosen such that, at the given temperature, hole crystallization is expected to occure, at least for large mass ratios $M = m_h/m_e$. If the density is chosen too low, the Coulomb coupling would to weak for crystallization. On the other hand, if the density is too high, the crystal vanishes due to quantum melting. At the chosen densities the electrons are always in the quantum liquid-like state, while the state of the holes can be changed by varying M.

At the chosen densities the total cluster radius is $R_{\lambda=5} = 70 a_B$ ($R_{\lambda=10.5} = 150 a_B$). That means that the average densities (in a single layer) are for GaAs $n_{\lambda=5} = 9.4 \cdot 10^9 / cm^2$ and $n_{\lambda=10.5} = 2.0 \cdot 10^9 / cm^2$, and for ZnSe $n_{\lambda=5} = 9.9 \cdot 10^{10} / cm^2$ and $n_{\lambda=10.5} = 2.2 \cdot 10^{10} / cm^2$. These values are for the electrons, for the holes the radius slightly decreases when M is increased.
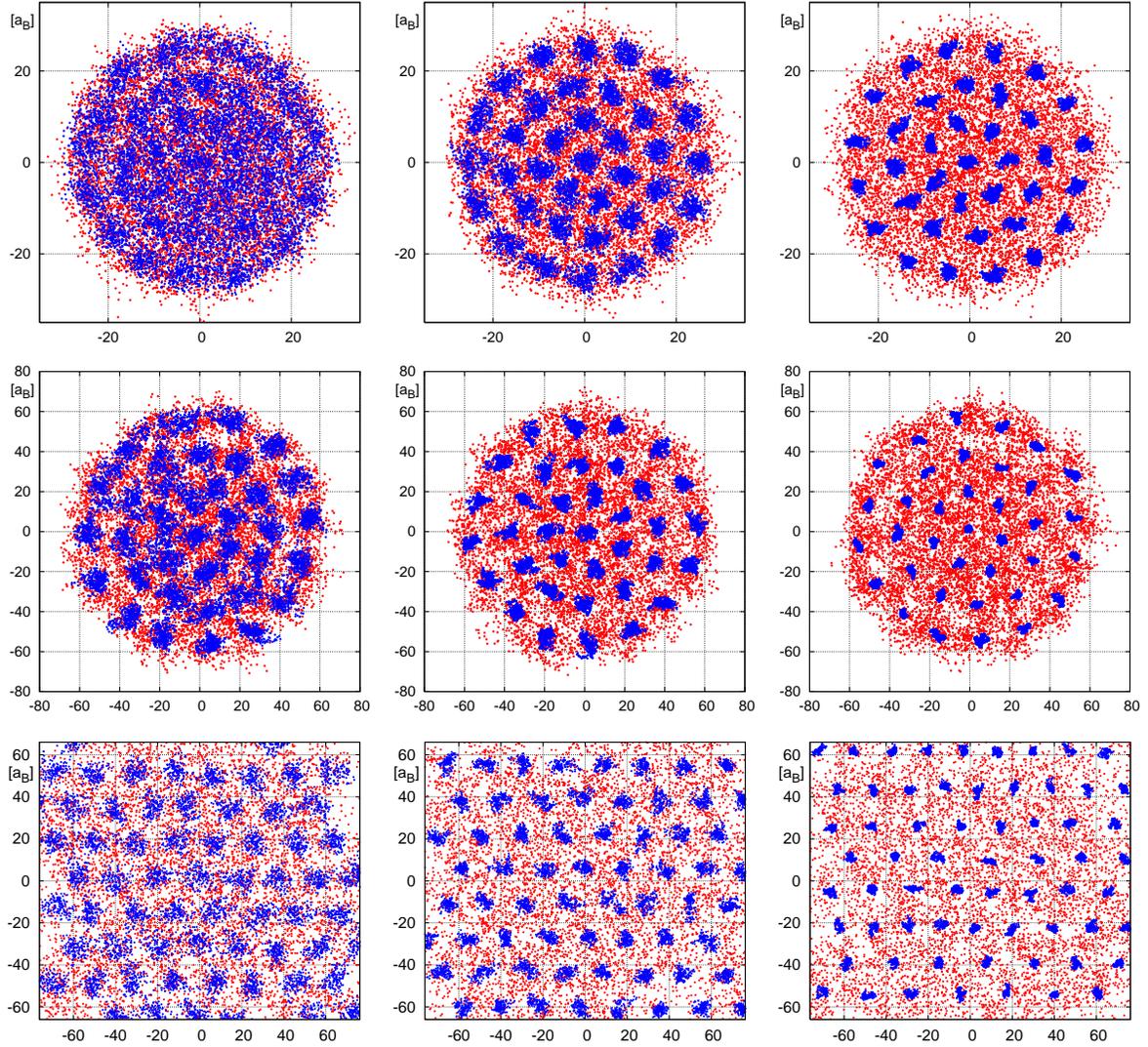
Fig. 1 (Color online) Path integral Monte Carlo configuration of holes (blue points) and electrons (red dots) in a bilayer system with distance $d = 20a_B$, temperature $T = Ha/3000$ and different mass ratios: $M = 5$ (left column), $M = 20$ (center) and $M = 100$ (right). Each particle is represented by 256 dots (path integral) which, for the electrons, are mutually penetrating. *First two rows:* 36 electrons and holes in a harmonic trap with coupling strengths $\lambda = 5$ (upper panel) and $\lambda = 10.5$ (second panel). Shown is a typical snapshot (without statistical averaging). Note the different axis scales in the two panels. *Row 3:* Simulation snapshots of a macroscopic bilayer ($N_e = N_h = 64$ electrons and holes in the simulation cell with periodic boundary conditions, the borders mark the simulation cell. Each particle is shown only once). The density matches the one in the confined system of the second row. There are structural defects as the triangular lettice is not uniform.

Consider first Fig. 1 which gives an overview on the observed behavior for the two densities (first two rows) when the mass ratio is varied in the range from 1 to 100. The first observation is that, in all cases, the electrons are distributed almost continuously, whereas the holes become localized when M exceeds 20 (5) at $\lambda = 5$ (10.5). Due to the rotational symmetry of the trap, the holes are arranged in concentric shells.

The main difference between the mesoscopic system with a parabolic inplane confinement and an infinite system are well-known finite size effects, see e.g. [34] which are related to the rotational symmetry instead of translational symmetry. Further, even when averaged over the modulation caused by the shells the density is not constant over the entire system, cf. left part of Fig. 2. The average density is highest in the center and decreases
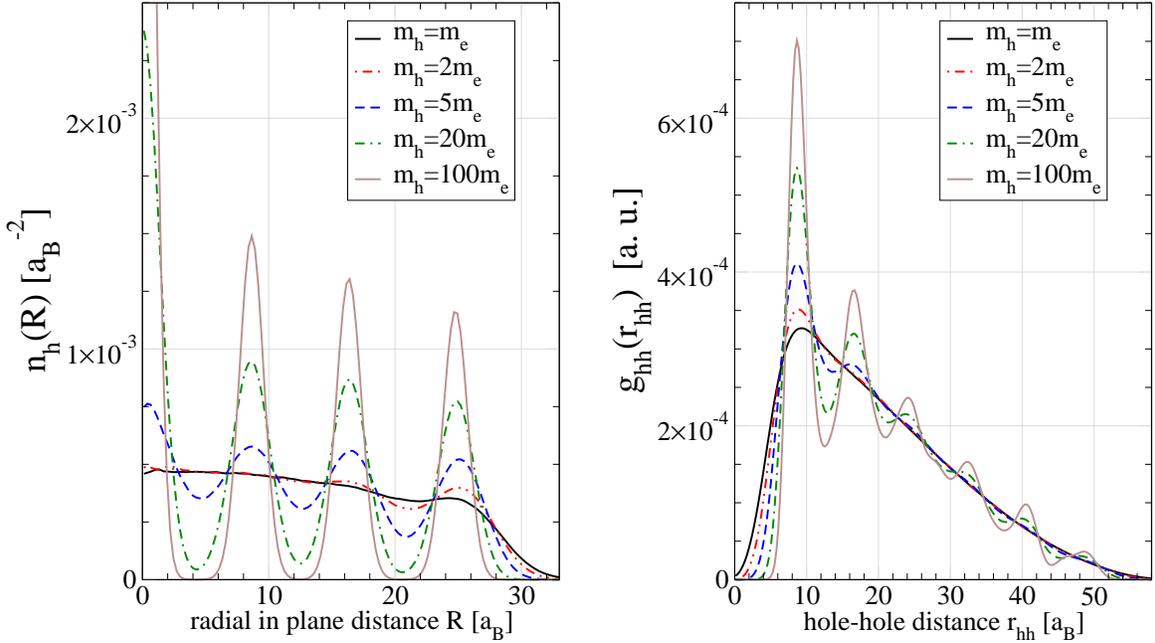
Fig. 2 (Color online) Hole radial distribution (left fig.) and hole-hole pair distribution (right) for $\lambda = 5$ and five mass ratios (see inset) for a mesoscopic confined bilayer with $N_e = N_h = 36$.

towards the cluster surface. Fig. 2 also clearly shows the effect of the mass ratio. With increasing M the hole-hole correlations increase leading to increased hole localiczation [5, 6]. This is accompanied by a pronounced modulation of the radial density $n(R)$ and the pair distribution (PDF) g_{hh}, see Fig. 2. The reduction of the zero point fluctuation with increase of the particle mass M leads to a hole localization and crystal formation. It is found that the shell radii in the radial density profile $n(R)$ in Fig. 2, as well as the peak positons in the hole-hole pair correlation function g_{hh} of the mesoscopic cluster ($\lambda = 5$) are independent from mass ratio M. For $M = 100$ we find that the holes are arranged in 3 shells populated with 16, 12, 7 and a single particle in the center, see Fig. 1.

Fig. 2 shows, that by changing the mass ratio from 1 to 100 the holes exhibit a transiton form a delocalized quantum state with wave function overlap to a highly ordered quasi classical state, while the electrons stay in a quantum fluid state and their correlations change only little with M for the present parameters. We note that the classical Coulomb coupling parameter for $M = 100$ is $\Gamma_{\lambda=5} = \langle U_{corr} \rangle / \langle U_{kin} \rangle = 345$ and $\Gamma_{\lambda=10.5} = 158$, which is beyond the critical value for the macroscopic (OCP) crystallization $\Gamma_{crit} = 137$.

Let us now consider the response of the electrons to the formation of the hole crystal. While the electron density is almost structurelss, some details can be seen in the electron-hole PDF, Fig. 3. This function has a distinct peak at zero (in-plane) distance showing the electrons and hole are pairwise vertically aligned for all values of M. Also, the next peaks of the e-e PDF are aligned with those of g_{hh}. The small shift in the peaks of the two functions is due to the normalization. In order to compare the details of the cluster arrangements with the macroscopic system below, in Fig. 3 we have divided g_{hh} and g_{eh} by the corresponding functions sor $M = 1$ where they are structureless. This allows to largely eliminate the effect of the trap (but slightly shifts the extrema).

4   Numerical results: Macroscopic system

To understand the relevance of our above mesoscopic results for larger systems contaning hundreds or thousands of particles we performed additional simulations for a macroscopic e-h bilayer without confinement potential. We have considered $N_e = N_h = 64$ electrons and holes in a simulation cell of the size $\{L_x \times L_y\} = \{76.185 a_B \times 65.978 a_B\}$ with periodic boundary conditions (PBC). This corresponds to a density parameter $r_s \approx 10$ (average particle distance in units of the electron Bohr radius). This density was chosen to be comparable to the average
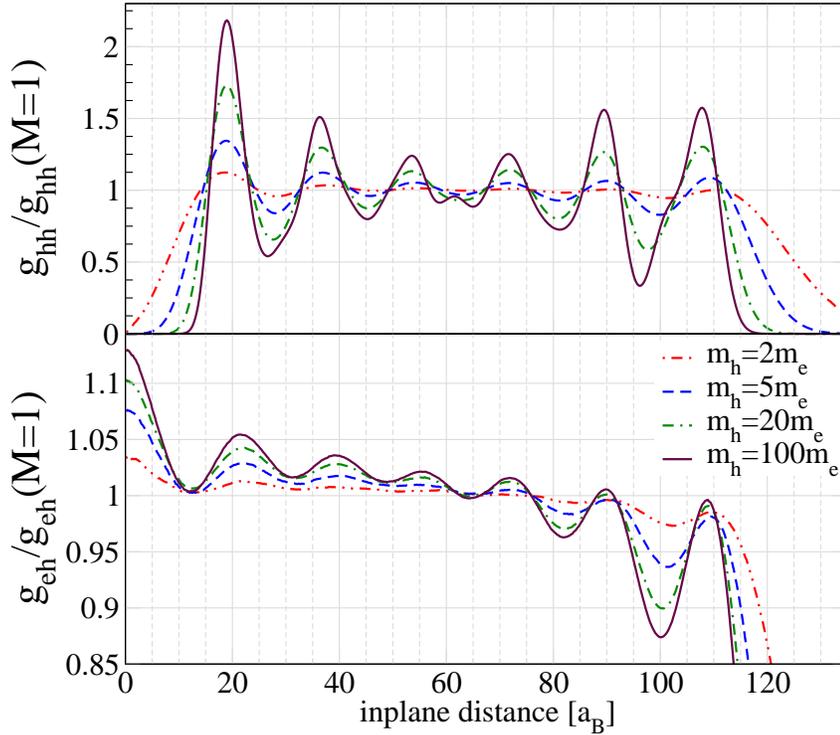
Fig. 3 Hole-hole (upper fig.) and electron-hole (lower fig.) pair distribution functions for the *mesoscopic* bilayer with $N_e = N_h = 36$ and $\lambda = 10.5$ for four values of M (see inset). The curves are normalized to the corresponding PDF for the case $M = 1$ to eliminate the influence of the decay of the average density in the trapped system, cf. Fig. 2. Note that electrons and holes are always pairwise aligned vertically. The plot includes distances up to two times the radius which causes the increase of the PDF for large distances.

density in the finite system (see Sec. 3) for the case of coupling parameter $\lambda = 10.5$. The mass ratio M was varied between 1 and 100, the temperature was fixed to $kT = 1/3000Ha$. The number of particles and the dimensions of the cell, i.e $L_y = \sqrt{3}L_x/2$, were choosen to best fit the symmetry of a triangular lattice. which is expected to be formed by the holes. We note that finite size effects are of the order of few percents, a systematic analysis with larger particle numbers is beyond the scope of this paper.

Let us now consider the results for the macroscopic bilayer. Three typical snapshots for $M = 5, 20, 100$ are shown in the lower row of Fig. 1. As in the mesoscopic system, for all cases the electrons are completely delocalized. In contrast, the hole localization increases from $M = 5$ to $M = 100$. Also, we confirm that the density of the mesoscopic system (second row) is well matched: the average distance between two holes as well as their extension (given by the size of the blue dots) is very close to the trapped case.

Consider now the pair distributions. In Fig. 4 (upper fig.) we show the hole-hole PDF for different mass ratios $1 \leq M \leq 20$. Since the particle number and box size is fixed, the average particle density stays constant and the position of the first peak of the PDF are practically independent of M. However, the general behavior of the PDF changes drastically. For $M \geq 4$ we observe clear oscillations typical for the solid phase. Even the third and fourth peaks are well resolved (the scale exceeds half of our simulation box). These oscillations become rapidly damped by changing M to 3 and below, here the PDF show liquid-like features. The third peak is now strongly suppressed. This transition can be quantified by computing the ratio of the (magnitude of the) first minimum to the first maximum which is $\gamma_1 = 0.48$, for $M = 4$, and $\gamma_1 = 0.65$, for $M = 3$. Similarly, for the third peak this ratio becomes $\gamma_3 = 0.76$ and $\gamma_3 = 0.96$, respectively. The ratio γ_1 is frequently used as an empirical criterion for the solid-liquid transition in classical systems; in a one-component 3D system the critical value is known to be $\gamma_1^* \approx 1/3$. If a universal values exists also in the present two-component 2D quantum system where the transition is expected to be of the Kosterlitz-Thouless type is an interesting question which deserves further analysis.
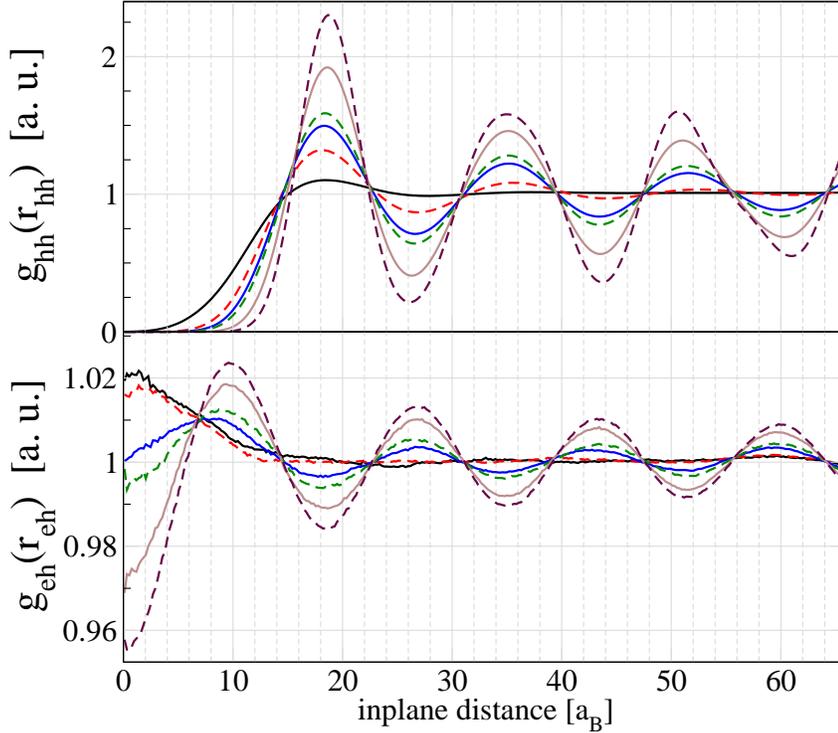
Fig. 4 Hole-hole (upper fig.) and electron-hole (lower fig.) pair distribution functions for the *macroscopic* bilayer with $N_e = N_h = 64$ (with periodic boundary conditions) for the mass ratios $M = 1, 3, 4, 5, 10, 20$ (the maxima increase with increasing M). Note the alternating location of maxima and minima of g_{hh} and g_{eh}.

Let us now compare the pair distributions with those in the mesoscpic system at the same density ($\lambda = 10.5$), Figs. 4 and 3. Interestingly, we find that the first peaks of g_{hh} have approximately the same height, and also the peak positons are very close, see upper parts of the two figures. Further we observe that the minima of g_{hh} are significantly deeper in the macroscopic case. This is explained by intershell rotations which occur in the mesoscopic system [5] and wash out the correlations. The present results are at temperatures above the freezout of these rotations.

Consider now the relative importance of the inter-layer correlations for the stability of the hole crystal. To this end, we have plotted the e-h PDF in Fig. 4 (lower fig.). For the symmetric case, $M = 1$, and also for $M = 3$ we observe similar behavior: the highest probability has the configuration where the electrons reside (in their own layer) just below the holes, as was observed in the mesoscopic system, lower part of Fig. 3. Obviously, the height of this peak is small, the modulation depth is around 2% because of the high electron degeneracy (delocalization). This means that these peaks cannot be associated with bound states (indirect excitons) since the electron density is well above the Mott density n_{Mott} for this system where excitons break up because the repulsion of two excitons exceeds the electron-hole binding. Note that n_{Mott} depends on the layer separation d which governs the binding energy and the typical size a_B^x of an indirect exciton which is of the order of d. Hence, for the present parameters, $d/a_B = 20$ and $r_s \approx 10$, the in-plane exciton size exceeds the separation of two neighboring electrons which causes exciton ionization. On the other hand, reducing d below 10, excitons become stable (for temperatures below the exciton binding energy) which is confirmed by our PIMC simulations.

For larger mass ratios, $M \geq 4$, a completely different behavior of g_{eh} emerges. From our analysis of the hole-hole correlations we know that the holes are now in an "ordered state" (or, in the terms of the Kosterlitz-Thouless theory, in a "less disordered state" with a power-low decay of off-diagonal long-range order). Now, there is no maximum of g_{eh} at zero distance, and the function exhibits oscillations. The explanation is that the electron density is modulated due to the presence of the hole crystal with maxima located in between the holes. While the amplitude of the oscillations is small, (about 1% modulation depth) they are clearly visible
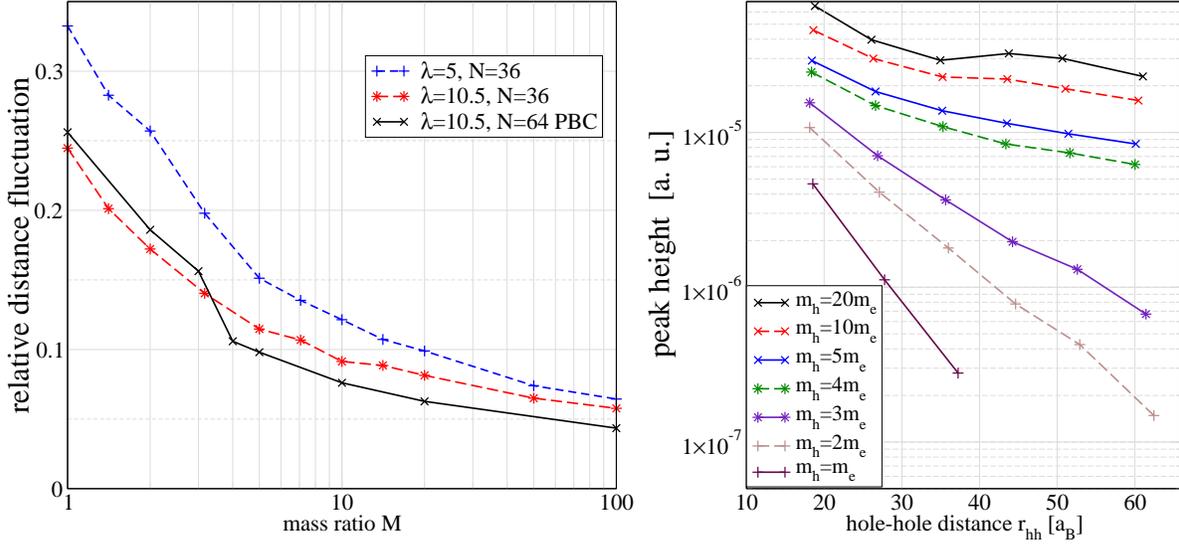
Fig. 5 (Color online) Left Fig.: Relative distance fluctuations of the holes, u_r^{hh}, (Eq. 4), as a function of the mass ratio M for a macroscopic (black solid line) and mesoscopic bilayer system for two densities (see inset). Right Fig.: Decay of the amplitude of the maxima and minima of the hole correlations ($|g_{hh} - 1|$) in the macroscopic system, cf. Fig. 4, for the seven mass ratios – from bottom to top: $M = 1, 2, 3, 4, 5, 10, 20$. Note the change from an exponential (for $M \leq 3$) to a power law decay (for $M \geq 4$) which signals the Kosterlitz-Thouless transition.

and become systematically more pronounced when M increases, see Fig. 4 (lower part). We, therefore, expect that appearance (disappearance) of these oscillations of g_{eh} is an additional indicator of a phase transition in the present asymmetric bilayer system.

Finally, as another quantity sensitive to phase transitions, we consider the relative distance fluctuations u_r^{hh} of the holes, Eq. 4, as a function of M, Fig. 5 (right part). This quantity exhibits a rapid drop between $M = 3$ and $M = 4$ which is related to a localization transition. We can translate from the critical mass ratio (which is expected to be between three and four) to the hole density parameter $r_s^{(h)}$, using $r_s^{(h)} = r_s^{(e)} m_h/m_e$, and the position of the first peak of the hole-hole PDF at $r_s^{(e)} \approx 10$. As a result, we obtain that the phase transition in the hole layer occurs at a critical density in the range $30 < r_s^{*(h)} < 40$. This result is close to the value $r_s^* \approx 37$ known as the critical density of solid-liquid transition in the one-component quantum 2D system at $T = 0$ [24]. Compared to this value, in our bilayer system, we observe indications of stabilization of the "ordered state" of the holes due to presence of the electron layer.

We note that, at smaller values of d (e.g. $d = 5a_B$ and $d = 10a_B$) no hole crystal is found. Instead we observe formation of indirect excitons which form a solid phase of composite particles. At the same time, the interparticle interaction changes from Coulomb to dipole-like which reduces the value of the classical coupling parameter to $\Gamma = \frac{e^2 d^2}{\langle r \rangle^3}/k_B T$. Similar tendencies have also been also in simulations of *symmetric* classical and quantum e-h-bilayers [11, 14].

5 Discussion

Analyzing the peak height (amplitude) of the g_{hh} in the macroscopic system (Fig. 4) in dependence on the peak positon r_{hh} we can deduce to the correlation decay law and compare to the asymptotics (5). In the disordered phase of small mass ratios $M = 1...3$ we find an exponential correlation decay of g_{hh}, see right part of Fig. 5. From mass ratio $M = 1$ to $M = 3$ disordering is lowered and the correlation length increases from $\xi = 6.5$ to $\xi = 13$. Increasing the mass ratio above the critical mass ratio, i.e. $M \geq 4$, we find a topological transition to the Kosterlitz-Thouless phase with power law correlation fall-off.

We may now obtain a critical mass ratio at which quantum melting of the hole crystal takes place. Using as a criterion a critical value of $u_r = 0.15$ of the relative hole-hole distance fluctuations we obtain $M_{crit}(\lambda = 5) \approx 5$

and $M_{crit}(\lambda = 10.5) \approx 2.8$, in the mesoscopic system, and $M_{crit}(r_s = 10) \approx 3.1$, in the macroscopic system (recall that it corresponds to $\lambda \approx 10.5$). Obviously, the absolute numbers are somewhat arbitrary, but the allow for an analysis of the dominant trends. i) M_{crit} depends on density. It decreases when the coupling strength λ increases in agreement with earlier observations for small e-h clusters [23]. ii), there is good agreement between the critical mass ratios of the mesoscopic and the macroscopic system (within 10%). iii) the critical values are much smaller than the value of $M_{crit} \approx 80$ in a 3D bulk system [7] which underlines the remarkable additional control of physical behaviors existing in a bilayer system by a variation of the layer separation d. It is expected that further reduction of d will allow to further reduce M_{crit} and to increase the maximum density of the hole crystal to values below $r_s^{(h)} = 20$ [15].

References

[1] *Strongly Coupled Coulomb Systems*, G. Kalman (ed.), Pergamon Press 1998
[2] D.J. Wineland, J.C. Bergquist, W.M. Itano, J.J. Bollinger, and C.H. Manney, Phys. Rev. Lett. **59**, 2935 (1987)
[3] H. Thomas, G.E. Morfill, V. Demmel, J. Goree, B. Feuerbacher, and D. Möhlmann, Phys. Rev. Lett. **73**, 652 (1994)
[4] M. Bonitz, D. Block, O. Arp, V. Golubnychiy, H. Baumgartner, P. Ludwig, A. Piel, and A. Filinov, Phys. Rev. Lett. **96**, 075001 (2006)
[5] A. Filinov, M. Bonitz and Yu.E. Lozovik, Phys. Rev. Lett. **86**, 3851 (2001); phys. stat. sol. (b) **221**, 231 (2000)
[6] A. Ghosal, A. D. Guclu, C. J. Umrigar, D. Ullmo and H. U. Baranger, Nature Phys. **2** 336 (2006)
[7] M. Bonitz, V.S. Filinov, V.E. Fortov. P.R. Levashov, and H. Fehske, Phys. Rev. Lett. **95**, 235006 (2005) and J. Phys.A: Math. Gen. **39**, 4717 (2006)
[8] B.I. Halperin, and T.M. Rice, Rev. Mod. Phys. **40**, 755 (1968)
[9] A.A. Abrikosov, J. Less-Common Met. **62**, 451 (1978)
[10] L. Segretain, Astron. Astrophys. **310**, 485 (1996)
[11] P. Hartmann, Z. Donko and G. J. Kalman, Europhys. Lett. **72**, 396 (2005)
[12] P. Ludwig, A. Filinov, M. Bonitz, and Yu.E. Lozovik, Contrib. Plasma Phys. **43**, 285 (2003)
[13] P. Ludwig, Diploma thesis: *Mesoscopic exciton clusters in coupled quantum dots*, Rostock University 2003
[14] S. De Palo, F. Rapisarda and G. Senatore, Phys. Rev. Lett. **88**, 206401 (2002); G. Senatore and S. De Palo, Contrib. Plasma Phys. **43**, 363 (2003)
[15] A. V. Filinov, P. Ludwig, V. Golubnychyi, M. Bonitz, and Yu.E. Lozovik, phys. stat. sol. (c) **0**, No. 5 (2003);
A. V. Filinov, M. Bonitz and Yu. E. Lozovik, J. Phys. A: Math. Gen. **36**, 5899-5904 (2003)
[16] E. Anisimovas, and F.M. Peeters, Phys. Rev B **65**, 233302 (2002)
[17] E. Anisimovas, and F.M. Peeters, Phys. Rev B **66**, 075311 (2002)
[18] P. Wachter, B. Bucher, and J. Malar, Phys. Rev. B **69**, 094502 (2004)
[19] P. Ludwig, A. Filinov, M. Bonitz, and H. Stolz, phys. stat. sol. (b) **243**, 2363 (2006)
[20] A. Filinov and M Bonitz, in: *Introduction to Computational Methods for Many Body Systems*, M. Bonitz and D. Semkat (eds.), Rinton Press, Princeton 2006
[21] R.G. Storer, J. Math. Phys. **9**, 964 (1968); A.D. Klemm, and R.G. Storer, Aust. J. Phys. **26**, 43 (1973).
[22] D.M. Ceperley, Rev. Mod. Phys. **67**, 279 (1995).
[23] H. Cords, Diploma thesis: *Crystallization of indirect, mass-asymmetric electron-hole pairs*, Rostock University 2006
[24] B. Tanatar, and D.M. Ceperly, Phys. Rev. B **39**, 5005 (1989).
[25] R. Egger, W. Häusler, C.H. Mak, and H. Grabert, Phys. Rev. Lett. **82**, 3320 (1999); S. Weiss and R. Egger, Phys. Rev. B **72**, 245301 (2005).
[26] F. Rapisarda and G. Senatore, Aust. J. Phys. **49**, 161 (1996); F. Perrot and M.W.C. Dharma-Wardana, Phys. Rev. Lett. 87, 206404 (2001); C. Bulutay, B. Tanatar, Phys. Rev. B **65**, 195116 (2002); M.W.C. Dharma-Wardana and F. Perrot, Phys. Rev. Lett. **90**, 136601 (2003) and references therein.
[27] A.V. Filinov, C. Riva, F.M. Peeters, Yu.E. Lozovik, and M. Bonitz, Phys. Rev. B **70**, 035323 (2004).
[28] F. Lindemann, Z.Phys **11**, 609, (1910).
[29] V.M. Bedanov, G.V. Gadiyak, and Yu.E. Lozovik, Phys. Lett. A, **109** 289 (1985).
[30] V.L. Berezinskii, Zh. Eksp. Theor. Fiz. **61**, 1144 (1971).
[31] J.M. Kosterlitz, D.J. Thouless, J. Phys. C **6**, 1181 (1973).
[32] S.G. Akopov and Yu.E. Lozovik, J. Phys C: Solid State Phys. **15**, 4403 (1982).
[33] A. Filinov, P. Ludwig, Yu.E. Lozovik and M. Bonitz, to be published.
[34] V. Golubnychiy, P. Ludwig, A.V. Filinov, and M. Bonitz, Superlattices and Microstructures **34** No. 3-6, 219 (2004).

5.4 On the Coulomb-Dipole Transition in Mesoscopic Electron-Hole Bilayers

We study the Coulomb-to-dipole transition which occurs when the separation d of an electron-hole bilayer system is varied with respect to the characteristic in-layer distances. An analysis of the classical ground state configurations for harmonically confined clusters with $N \leq 30$ electron-hole pairs reveals that the energetically most favorable state can differ from that of two-dimensional pure dipole or Coulomb systems. Performing a normal mode analysis for the $N = 19$ cluster it is found that the lowest mode frequencies exhibit drastic changes when d is varied. Furthermore, we present quantum-mechanical ground states for $N = 6$, 10 and 12 spin-polarized electrons and holes. We compute the single-particle energies and orbitals in self-consistent Hartree-Fock approximation over a broad range of layer separations and coupling strengths between the limits of the ideal Fermi gas and the Wigner crystal.

The results were published as refereed journal publication:

5.4.1 ***On the Coulomb-Dipole Transition in Mesoscopic Electron-Hole Bilayers,*** P. Ludwig, K. Balzer, A. Filinov, H. Stolz, and M. Bonitz, New Journal of Physics **10**, 083031 (2008)

On the Coulomb–dipole transition in mesoscopic classical and quantum electron–hole bilayers

P Ludwig[1,2,3], **K Balzer**[1], **A Filinov**[1], **H Stolz**[2] **and M Bonitz**[1]

[1] Institut für Theoretische Physik und Astrophysik,
Christian-Albrechts-Universität zu Kiel, D-24098 Kiel, Germany
[2] Institut für Physik, Universität Rostock, D-18051 Rostock, Germany
E-mail: ludwig@theo-physik.uni-kiel.de

Abstract. We study the Coulomb-to-dipole transition which occurs when the separation d of an electron–hole bilayer system is varied with respect to the characteristic in-layer distances. An analysis of the classical ground state configurations for harmonically confined clusters with $N \leqslant 30$ electron–hole pairs reveals that the energetically most favourable state can differ from that of two-dimensional pure dipole or Coulomb systems. Performing a normal mode analysis for the $N = 19$ cluster it is found that the lowest mode frequencies exhibit drastic changes when d is varied. Furthermore, we present quantum-mechanical ground states for $N = 6$, 10 and 12 spin-polarized electrons and holes. We compute the single-particle energies and orbitals in self-consistent Hartree–Fock approximation over a broad range of layer separations and coupling strengths between the limits of the ideal Fermi gas and the Wigner crystal.

[3] Author to whom any correspondence should be addressed.

IOP Institute of Physics Φ DEUTSCHE PHYSIKALISCHE GESELLSCHAFT

Contents

1. Introduction

Self-organized structure formation, in particular Coulomb crystallization [1], is among the most exciting cooperative phenomena in the field of charged many-particle systems. In the case of finite, parabolically confined systems, extensive experimental and theoretical work on various types of two- and three-dimensional (2D and 3D) systems has revealed that in the strong coupling limit charged particles can arrange themselves in a highly ordered crystalline state with a nested shell structure. Examples are ions in Paul and Penning traps [2, 3], dusty plasmas [4]–[11] and electrons in quantum dots and wells [12]–[18]. For these so-called 'artificial atoms', Mendeleev-type periodic tables were found including characteristic occupation numbers, shell closures and unusually stable magic configurations. For a recent overview see [1]. Recently, there has been growing interest in 2D *dipolar* macroscopic systems [19]–[24] as well as finite size dipolar (quantum) clusters in small-scale confinement potentials [25]–[32]. While in particular the ground state and dynamical properties of 2D mesoscopic pure Coulomb and pure dipole interacting particle ensembles in parabolic confinement potentials are well understood, the behaviour of *real* 3D electron–hole double layer systems, where the dipole approximation is not valid, is still poorly investigated. This is despite the fact that the additional degree of freedom, i.e. the layer separation d, is expected to allow for a variety of interesting new effects which are due to the possibility of tuning the effective in-layer interaction potential.

The results presented in this paper are applicable to semiconductor heterostructures and coupled quantum dots as well as to molecular systems, where the dipole moment of the charge carriers and thus the interaction strength is tunable, e.g. [32, 33][4]. For a consistent formulation,

---

[4] Another natural source of confinement arises in low-dimensional semiconductor structures from defects and well width fluctuations. This leads to local potential minima for the charge carriers causing localization of free and bound charges (excitons, biexcitons and trions), e.g. [34]–[36].

we concentrate on the problem of two vertically coupled symmetric layers containing parabolically confined, spin-polarized electrons and holes of identical particle number $N_e = N_h = N$ and effective masses $m_e^* = m_h^* = m^*$, respectively. The underlying Hamiltonian is

$$\hat{H} = \hat{H}_e + \hat{H}_h - \hat{H}_{e-h}, \tag{1}$$

with the intra- and interlayer contributions

$$\hat{H}_{e(h)} = \sum_{i=1}^{N_{e(h)}} \left(-\frac{\hbar^2}{2\, m_{e(h)}^*} \nabla_{\mathbf{r}_i}^2 + \frac{m_{e(h)}^*}{2} \omega_0^2 \mathbf{r}_i^2 + \sum_{j=i+1}^{N_{e(h)}} \frac{e^2}{4\pi\varepsilon\sqrt{(\mathbf{r}_i - \mathbf{r}_j)^2}} \right), \tag{2}$$

$$\hat{H}_{e-h} = \sum_{i=1}^{N_e} \sum_{j=1}^{N_h} \frac{e^2}{4\pi\varepsilon\sqrt{(\mathbf{r}_i - \mathbf{r}_j)^2 + d^2}}, \tag{3}$$

where the electrons (e) and holes (h) are confined to planes of zero thickness which are at a distance d apart. The 2D vectors $\mathbf{r}_{i(j)}$ are the in-plane projections of the particle coordinates, e the elementary charge and ε the static permittivity. The strength of the confinement is controllable by the trap frequency ω_0.

The most fascinating property of this system is that the effective in-layer particle interaction changes with the interlayer separation d: from Coulomb interaction at large d, where both layers are decoupled, to dipole interaction at small $d \to 0$, where the attractive interlayer interaction leads at low temperature to vertical electron–hole coupling and formation of vertically aligned dipoles—excitons. On the other hand, at intermediate values of d, when the repulsive intra- and attractive interlayer interaction energies according to equations (2) and (3) are comparable, the system shows a real 3D behaviour. In [28], it was reported that, as a consequence of the Coulomb–dipole transition, the considered system can exhibit structural changes of its ground state shell configuration when d is varied.

In section 2, we extend these results and present a systematic study of the classical ground states, varying d for mesoscopic clusters with $N \leqslant 30$ particles in each layer. Further, we extract the fundamental dynamical features in the case of weak excitation by solving the dynamical (Hessian) matrix for the ground state configurations found in section 2. Doing this, in section 3, we discuss the d-dependence of the collective N-particle modes for the $N = 19$ cluster. Here, we highlight the close relationship between structural and collective dynamical cluster properties as rotation of shells and vortices. In section 4, we extend the analysis to fermionic e–h quantum bilayers utilizing a self-consistent Hartree–Fock (SCHF) ansatz. In particular, Coulomb-to-dipole transition-induced (critical) quantum phenomena are presented for the clusters with $N = 6$, 10 and 12 electrons and holes. The results include the N-particle densities and the single-particle spectrum and orbitals as functions of coupling strength λ and layer separation d.

2. Classical ground state transitions

The classical ground state corresponding to the equations (1)–(3) is described by the Hamiltonian $H = H_e + H_h - H_{e-h}$ without the kinetic energy, i.e.

$$H_{e(h)} = \sum_{i=1}^N \mathbf{r}_i^2 + \sum_{i<j}^N \frac{1}{\sqrt{(\mathbf{r}_i - \mathbf{r}_j)^2}}, \qquad H_{e-h} = \sum_{i=1}^{N_e} \sum_{j=1}^{N_h} \frac{1}{\sqrt{(\mathbf{r}_i - \mathbf{r}_j)^2 + d^2}}. \tag{4}$$

This dimensionless form is obtained by applying the transformation rules $\{r \to r/r_0, E \to E/E_0, d \to d/r_0\}$ with the characteristic length $r_0 = (e^2/2\pi \varepsilon m\omega_0^2)^{1/3}$ and energy $E_0 = (m\omega_0^2 e^4/32\pi^2\varepsilon^2)^{1/3}$. Note that model (4) contains no explicit dependence on the trap frequency ω_0. The considered classical model system in its ground state is completely defined by only two parameters: the particle number N and the layer separation d, which also influences the in-layer density.

At low temperatures, it is found that the electrons and holes arrange themselves pairwise on nested concentric rings with characteristic occupation numbers $(N_1, N_2, \ldots)$, where N_i denotes the number of electrons (holes) on the ith ring starting from the centre. The ground state configuration is the energetically lowest of all possible *stable* states, whose number rapidly increases with N, and all these have to be found and checked. This task is complicated, since many of the different stable states are energetically close, requiring high-accuracy computations. A systematic search for the global minimum-energy structure in the $4N$-dimensional configuration space was performed by means of an optimized molecular dynamics annealing technique utilizing an adaptive step size control [8, 28]. For each value of N and d, the annealing process was repeated for a large (N- and d-dependent) number of times. This slow (long) annealing process ensures that the lowest-energy state is found with high probability. The critical points of structural transitions d_{cr} were identified as crossing points of the energies of the lowest-energy states as functions of layer separation d.

Extending the analysis of [28], we obtained a periodic table for the particle numbers $N \leqslant 30$ including all structural transitions occurring when d is changed, see table 1. In the limits of pure dipole and Coulomb interaction our results are in full agreement with those of [25] and [12, 16], respectively[5]. Analysing the clusters $N \leqslant 18$, only transitions for $N = 10$ and 12 reported in [28] are found. Due to the much larger configurational space, and thus accordingly higher number of low-energy metastable states, for the clusters $N = 19, \ldots, 30$ in total 6 particle numbers reveal Coulomb–dipole transitions: $N = 19, 21, 23, 26, 29$ and 30. In particular, two transition types are identified:

(A) While for the majority of the investigated clusters the ground state shell configuration of the single layer Coulomb and dipole case are identical, for $N = 10, 21, 23, 26$ and 29 this is not the case. When changing from a long-range Coulomb to a short-range dipole interaction a higher particle number on the inner shell becomes favourable. A similar trend is also known from 2D [5, 6] and 3D [9, 10] Yukawa-clusters when the screening strength is increased[6].

(B) A second type of transition is found for $N = 12, 19$ and 30 that cannot be concluded from different shell occupations in both limits of d: at large values of d again a transition of type (A) takes place, which increases (decreases) the particle number on the inner (outer) shell when d is reduced. But interestingly, at small values of d a second kind of transition to a six-fold-coordinated, commensurate particle configuration is found allowing for an energetically more favourable *closed packing* of the composite dipoles. Such symmetry-induced re-entrant configuration changes are only observed in cases where highly symmetric, 'magic' configurations with a bulk-like triangular structure are involved.

---

[5] In [12], the ground state for $N = 29$ was erroneously given as (5, 10, 14). This was corrected in [16].

[6] The effect is due to the radial balance of total internal F^{int} and external F^{ext} forces on each particle. In contrast to Coulomb, short-range (dipole or Yukawa) forces do contribute to F^{ext} which requires a higher density towards the centre to stabilize the cluster matching $F^{int} = F^{ext}$. For details see [10].

Table 1. Ground state shell structures for 2D Coulomb, bilayer and dipole clusters of N particles in a parabolic confinement. The arrows indicate the direction of the ground state transition from large to small values of d. Magic (commensurate) shell configurations are underlined. For $N \leqslant 5$, only a single shell is populated for all values of d. For all configurational transitions, the critical layer separation d_{cr} as well as the corresponding total energy per composite dipole E_{cr}/N is given. Note that the binding energy $1/d$ which ensures the exact vertical alignment of the electron–hole pairs is excluded from the energy values as it is independent of the cluster configuration.

N	Coulomb	Bilayer	d_{cr}	E_{cr}/N	Dipole
5	5	No transition			5
6	(1,5)	No transition			(1,5)
7	(1,6)	No transition			(1,6)
8	(1,7)	No transition			(1,7)
9	(2,7)	No transition			(2,7)
10	(2,8)	(2,8) → (3,7)	1.0116	3.9167	(3,7)
11	(3,8)	No transition			(3,8)
12	(3,9)	(3,9) → (4,8)	0.9528	4.3463	(3,9)
		(4,8) → (3,9)	0.3253	2.1293	
13	(4,9)	No transition			(4,9)
14	(4,10)	No transition			(4,10)
15	(5,10)	No transition			(5,10)
16	(1,5,10)	No transition			(1,5,10)
17	(1,6,10)	No transition			(1,6,10)
18	(1,6,11)	No transition			(1,6,11)
19	(1,6,12)	(1,6,12) → (1,7,11)	2.182	9.1882	(1,6,12)
		(1,7,11) → (1,6,12)	0.417	3.5697	
20	(1,7,12)	No transition			(1,7,12)
21	(1,7,13)	(1,7,13) → (2,7,12)	3.429	11.6283	(2,7,12)
22	(2,8,12)	No transition			(2,8,12)
23	(2,8,13)	(2,8,13) → (3,8,12)	2.436	10.9959	(3,8,12)
24	(3,8,13)	No transition			(3,8,13)
25	(3,9,13)	No transition			(3,9,13)
26	(3,9,14)	(3,9,14) → (4,9,13)	2.173	11.4266	(4,9,13)
27	(4,9,14)	No transition			(4,9,14)
28	(4,10,14)	No transition			(4,10,14)
29	(4,10,15)	(4,10,15) → (5,10,14)	2.142	12.2357	(5,10,14)
30	(5,10,15)	(5,10,15) → (1,5,10,14)	0.616	6.3934	(5,10,15)
		(1,5,10,14) → (5,10,15)	0.243	3.3410	

These findings coincide with those for single layer statically screened Coulomb systems. Here a change from the long-range Coulomb towards a short-range Yukawa potential by variation of the screening length leads to analogue ground state transitions for the particle numbers $N = 10, 12, 19$ and $N = 21, 23, 26, 29$ as reported in [5] and [6], respectively. Further, a comparison of the ground and metastable states of the single layer Coulomb system (cf table 1 in [16] for $N \leqslant 30$)

shows that if and only if an energetically close metastable configuration with higher centre particle number than in the ground state exists, in fact, a transition of type (A) in the corresponding bilayer system is found. This underlines the Coulomb-to-dipole transition-induced density change effecting configurational transitions of type (A). In contrast, transitions of type (B) are geometry-induced supporting an equally distant, closed packed particle arrangement.

Among all transitions, the most interesting are those of type (B). As an example, we study the $N = 19$ cluster. Here, between $d = 0.417$ and 2.182, the 'magic' configuration $(1,6,12)$ is replaced by the configuration $(1,7,11)$ which possesses a much lower orientational order [37]. Therefore, it is interesting to analyse the normal modes of this cluster and their dependence on d.

3. Collective *N*-particle modes

Starting from the ground state configurations given in section 2, we are interested in the collective excitation behaviour in dependence on d. Here, we will focus on the cluster with $N = 19$ where, upon changing d, finite size effects are expected to play a key role as the ground state structure changes between the hexagonally ordered $(1,6,12)$ configuration and the $(1,7,11)$ circular ring structure as discussed in section 2.

To derive the dynamical properties in the limit of weak excitations, we perform a normal mode analysis [27], [37]–[39]. For small particle displacements $\mathbf{u}(t) = \mathbf{r}(t) - \mathbf{R}$ around their ground state position $\mathbf{R}$, expansion of the potential energy U, equation (1), around $\mathbf{R}$ leads to

$$U(\mathbf{r}) = U_0 + \sum_i^{2N} \underbrace{\left.\frac{\partial U}{\partial r_i}\right|_{\mathbf{R}}}_{=\,0} u_i + \frac{1}{2}\sum_{i,j}^{2N} \underbrace{\left.\frac{\partial^2 U}{\partial r_i \partial r_j}\right|_{\mathbf{R}}}_{=:\,\mathcal{H}_{ij}} u_i u_j + \cdots, \qquad (5)$$
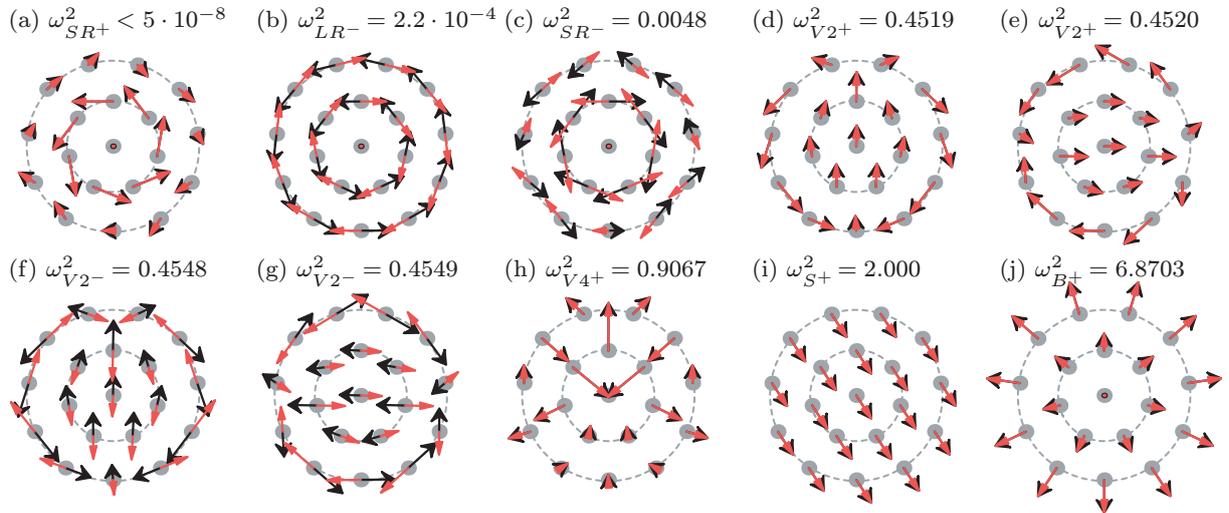
where U_0 is the minimum potential energy and $\mathbf{r} = (x_1, y_1, x_2, y_2, \ldots)$ comprises the in-plane coordinates of all particles. In the stationary states, the linear (force) term vanishes and the second-order partial derivatives provide the elements $\mathcal{H}_{ij}$ of the $2 \times 2N$ Hessian matrix. In the frame of the harmonic approximation, the resulting cluster dynamics is given as a superposition of these collective (normal) modes statistically weighted according to the eigenvalues of $\mathcal{H}$ which are proportional to the squared mode oscillation frequencies ω_i^2. In the following, these eigenfrequencies will be given in units of $\omega_0/\sqrt{2}$.

3.1. Classification of normal modes

As a result of the eigenmode computation, we obtain for each stable configuration of the $N = 19$ cluster a complete set of 76 eigenvalues and eigenvectors. A selection of characteristic and energetically low-lying eigenvectors for $d = d_{cr} = 2.182$, i.e. intermediate between Coulomb and dipole regime, is given in figure 1. As shown in [27], in dipolar bilayer systems the total number of modes can be divided in two types which will be distinguished by the following nomenclature:

$(^+)$ labels modes with *in-phase* collective particle motion in both layers, see figures 1(a), (d), (e), (h)–(o), and

$(^-)$ labels modes with *anti-phase* motion of both layers, see figures 1(b), (c), (f) and (g).

Selected normal modes of the $(1,7,11)$ configuration

(a) $\omega^2_{SR^+} < 5 \cdot 10^{-8}$ (b) $\omega^2_{LR^-} = 2.2 \cdot 10^{-4}$ (c) $\omega^2_{SR^-} = 0.0048$ (d) $\omega^2_{V2^+} = 0.4519$ (e) $\omega^2_{V2^+} = 0.4520$

(f) $\omega^2_{V2^-} = 0.4548$ (g) $\omega^2_{V2^-} = 0.4549$ (h) $\omega^2_{V4^+} = 0.9067$ (i) $\omega^2_{S^+} = 2.000$ (j) $\omega^2_{B^+} = 6.8703$

Selected normal modes of the $(1,6,12)$ configuration

(k) $\omega^2_{V2^+} = 0.5866$ (l) $\omega^2_{SR^+} = 0.6507$ (m) $\omega^2_{V4^+} = 1.3819$ (n) $\omega^2_{SW^+} = 1.9842$ (o) $\omega^2_{B^+} = 6.8704$
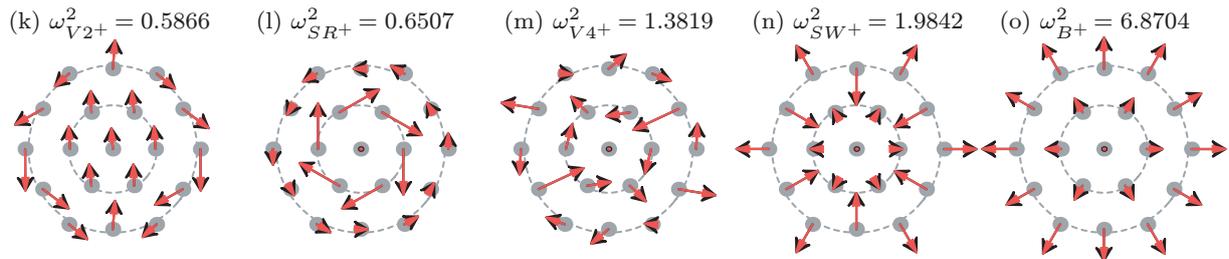
Figure 1. Top view of the eigenvectors of selected characteristic and low-energetic normal modes for the $N = 19$ cluster at $d = d_{cr} = 2.182$ (ordered by frequency, cf numbers above the figures). The points mark the particle positions. The differently shaped (and coloured) arrow heads are assigned to the normal mode eigenvectors in the two different layers and indicate direction and amplitude of particle motion. Modes with in-/anti-phase motion of both layers are labelled with a $^+/^-$ sign, respectively. *Top rows*: eigenvectors of the $(1,7,11)$ configuration: (a) inter-shell rotation (SR$^+$), (b) anti-phase layer rotation (LR$^-$), (c) anti-phase inter-shell rotation (SR$^-$), (d) and (e) in-phase vortex pairs (V2$^+$), (f) and (g) anti-phase vortex pairs (V2$^-$), (h) asymmetric in-phase 4-vortex mode (V4$^+$), (i) sloshing mode (S$^+$), (j) breathing mode (B$^+$). *Bottom row*: eigenvectors of the $(1,6,12)$ configuration: (k) in-phase vortex pair (V2$^+$), (l) in-phase inter-shell rotation (SR$^+$), (m) in-phase 4-vortex mode (V4$^+$), (n) in-phase transverse surface wave (SW$^+$), (o) breathing mode (B$^+$).

Consider first the top rows of figure 1 which show the eigenvectors of the normal modes of the $(1,7,11)$ configuration. The energetically lowest collective particle motion is in all cases the centre of mass cluster rotation mode—the *in-phase* layer rotation LR$^+$. The eigenfrequency of this directed rotation is $\omega = 0$ as for this motion there is no restoring force. Beside this (trivial) mode there are three additional rotational modes: (a) inner versus outer inter-shell rotation SR$^+$, (b) the *anti-phase* rotation of both layers LR$^-$ and (c) anti-phase inter-shell rotation SR$^-$.

Another set of low frequency modes are four vortex pair modes: (d) *in-phase* vortex pair V2$^+$ and (e) (almost) perpendicular oriented vortex pair V2$^+$,[7] (f) and (g) two anti-phase vortex pairs. In the present isotropically confined 2D system, rotationally *asymmetric* modes are typically two-fold degenerate with respect to the spatial alignment of the vectors, cf (d), (e) and (f), (g), respectively. This leads to the fact that, taking into account the two possible phasings of relative particle motion in both layers, the majority of mode types occur as a set of four. Considering this, in the following only one mode per set of four is shown as for the rotational asymmetric, low-energy mode (h) which has the interesting feature that it supports a single-particle exchange between the inner and outer shell, i.e. a transition from the (1,7,11) to the (1,6,12) configuration.

In the case of pure radial eigenvectors, such as the (in-phase) breathing mode (j) as coherent radial motion (compression/expansion) of all particles, there exists one pair of modes only. In addition to (j) there is an anti-phase breathing mode B$^-$ with frequency $\omega_{B^-}^2 = 7.9522$. Another 'universal mode' that is independent of particle number and configuration is the centre of mass sloshing mode S$^+$ (i) with trap frequency ω_0. This mode has a corresponding anti-phase shear or dipole oscillation mode S$^-$. Both modes are two-fold degenerate.

For all these modes a corresponding mode of the (1,6,12) configuration is found. In particular: (k) the V2$^+$-mode, (l) the mode of inter-shell rotation SR$^+$, (m) an energetically low V4$^+$-mode, here supporting a centre directed transition of a particle on the outer shell, and two further examples of radial modes, (n) a transverse surface wave and (o) the breathing mode.

3.2. Change of normal mode spectrum with layer separation

After the classification of the collective modes, we now consider the oscillation frequency dependence on the layer separation d of the $N = 19$ cluster, see figure 2. Of special interest are thereby the two configuration changes of the ground state and their effect on the collective dynamical cluster properties.

Starting at small values of d, an increase of the e–h separation leads to a growing cluster size due to a stronger in-layer particle repulsion resulting from a change of the effective interaction from dipole to Coulomb. This implies a gradual decrease of the mode eigenfrequencies with d since the coupling of all $2N$ particles becomes less rigid and the restoring forces weaken. Only the two-fold degenerate centre of mass oscillations are found to be constant at $\omega_{S^+}^2 = 2$, independent of the interlayer coupling strength or even configuration changes. Confirming [27], the breathing frequency gradually proceeds from $\omega_{B^+}^2 = 10$ in the limit of dipoles ($d \to 0$), to a value of $\omega_{B^+}^2 = 6$ in the limit of decoupled layers ($d \to \infty$). Moreover, modes supporting a transition from the (1,6,12) to the (1,7,11) state and vice versa, i.e. the eigenmodes (h) and (m) in figure 1, are found at low frequencies, i.e. at low excitation energies.

As discussed in section 2, the ground state transitions for the $N = 19$ cluster occur at the critical values of $d_{cr}^{(1)} = 0.417$ and $d_{cr}^{(2)} = 2.182$ and are accompanied by abrupt spectrum transformations. The strongest effect is observed for the in-phase inter-shell rotation SR$^+$ with a remarkable jump of the mode frequency $\omega_{SR^+}^2$ by more than four orders of magnitude. This decrease can be explained by comparing the SR$^+$ mode eigenvectors of the (1,7,11) and (1,6,12)

---

[7] The difference of the two in-phase vortex pair modes (d) and (e) lies, besides rotation of the whole vortex pair by $\sim \pi/2$, in the alignment of the eigenvectors, which is slightly different. This is due to the non-commensurability of the (1,7,11) configuration leading to symmetry breaking. As a result the frequencies differ by about $\Delta\omega_{V2^+}^2 = 10^{-4}$.
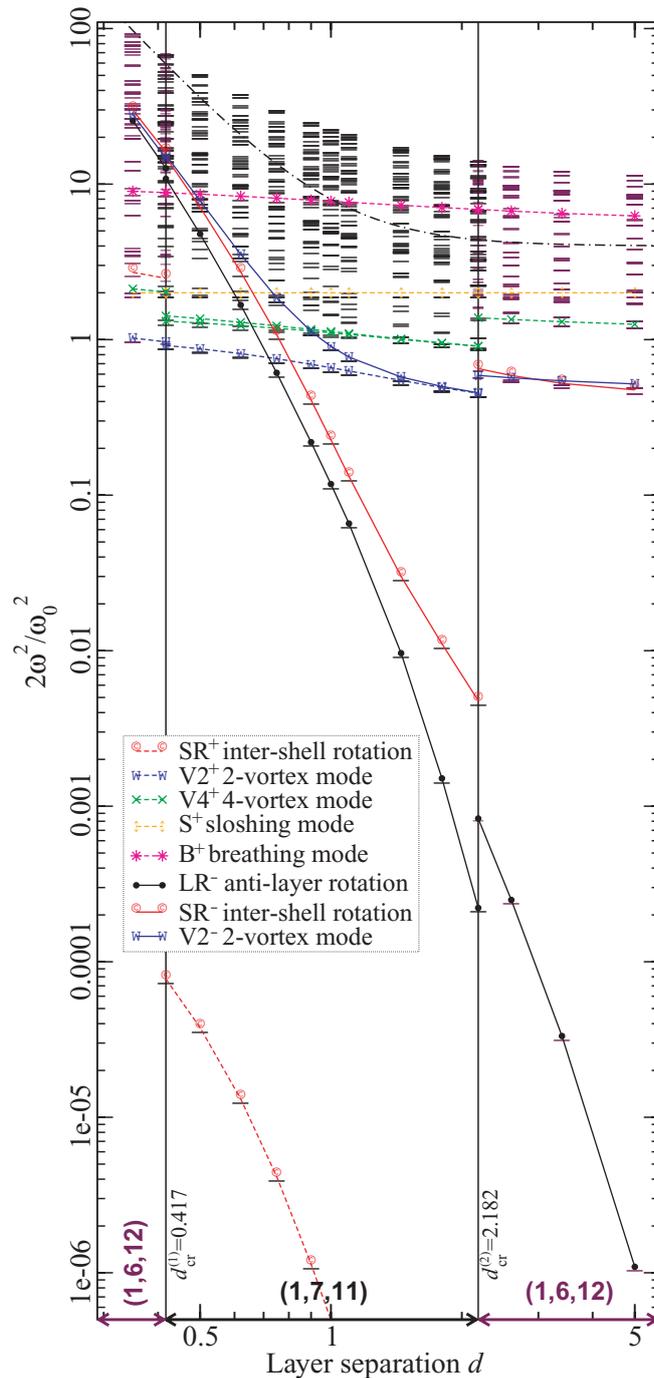
Figure 2. Complete normal mode spectrum for $N = 19$ as function of layer separation d. At $d_{cr}^{(1)} = 0.417$, the ground state configuration changes from (1,6,12) to (1,7,11) and at $d_{cr}^{(2)} = 2.182$ from (1,7,11) to (1,6,12) resulting in a qualitative change of the mode frequencies. The eigenvectors of the selected modes are visualized in figure 1. Modes with in-phase (anti-phase) oscillation of both layers are plotted with dashed (solid) lines. Note that the SR^+ mode continues in the range $1 < d < 2.182$ with a value smaller than 5×10^{-7}. For notation of modes, see figure 1. The black dash-dotted line corresponds to the shear oscillation S^- of a single dipole (see text).

configurations, see figures 1(a) and (l). In the latter case, the oscillation vectors of all particles on the inner shell are directed towards particle positions on the outer shell which strongly increases the restoring forces in the case of the (1,6,12) configuration resulting in a much higher frequency $\omega_{SR^+}^{(1,6,12)}$ than $\omega_{SR^+}^{(1,7,11)}$. The exceptional low frequency $\omega_{SR^+}^{(1,7,11)}$ agrees with results for single layer Coulomb crystals. In [37], the minimal (nonzero) excitation frequency for (1,7,11) and the comparable, non-magic (1,7,12) configuration was reported to be that of the inter-shell rotation with $\omega_{SR}^2 \approx 10^{-8}$. Confirming this, quantum Monte Carlo simulations [14] revealed that the orientational inter-shell melting temperature of the incommensurate (1,7,12) configuration is much lower than for the highly symmetric (1,6,12) structure. In particular, a 9 (!) orders of magnitude difference of the orientational melting temperatures and critical densities of both configurations was found. This shows that the given classical results are of practical relevance also for quantum systems at moderate densities.

Moreover, with respect to the dipole-to-Coulomb transition we found that in the dipole regime at small d the corresponding modes with in-phase and anti-phase oscillation of both layers are energetically clearly separated, cf $SR^{\pm}$ and $V2^{\pm}$ in figure 2. Energetically lowest are the two (degenerate) in-phase vortex pair oscillations $V2^+$. With a gradual transition to the limit of uncoupled layers, the e–h attraction and thus the oscillation frequencies of the anti-phase modes are strongly reduced and converge towards the values of the corresponding in-phase modes. This is found for the $V2^-$ and $V2^+$ modes around $d = 2$ and for the SR^- and SR^+ modes for $d > 2.182$. As a consequence of the layer decoupling, the LR^- anti-phase layer rotation becomes the energetically lowest of the anti-phase modes. This indicates that the primary mechanism of decoupling of the electron and hole layers is the interlayer rotation LR^-.

We note that the (anti-phase) shear mode S^- of a single trapped dipole has the frequency $\omega_{S^-}^2 = 2 + 2/d^3$ (see black dash-dotted line in figure 2). This arises by expanding the electron–hole attraction H_{e-h} of equation (4) for small displacements $\mathbf{u}(t)$ around the ground state position $\mathbf{R}$. Thereby, the first term in ω_{S^-}, being independent of the layer separation d, is due to the harmonic confinement. In a spatially infinite bilayer system [24], its value depends on the local potential energy around $\mathbf{R}$ and is proportional to the Einstein frequency. The second term, which is leading for layer separations $d \ll 1$, corresponds to the shear oscillation of the free (unconfined) dipole.

4. Ground states and single-particle spectrum of quantum bilayers

In this section, we present an extension of the classical results of section 2 to quantum bilayers. Here, in contrast to the classical simulations, the ground state kinetic energy does not vanish even in the limit of temperatures $T \to 0$ resulting in a finite spatial extension of the particle orbitals on the scale of the whole N-particle cluster. Hence, fermionic quantum features such as exchange effects (Pauli exclusion principle) must be included.

In order to treat the e–h bilayer system of equations (1)–(3) quantum mechanically, we introduce the dimensionless coupling parameter λ of a harmonically confined quantum system which relates the characteristic Coulomb energy $E_C = e^2/(4\pi\varepsilon x_0)$ to the characteristic confinement energy $E_0^* = \hbar\omega_0$

$$\lambda = \frac{E_C}{E_0^*} = \frac{e^2}{4\pi\varepsilon x_0\hbar\omega_0} = \frac{x_0}{a_B}, \tag{6}$$

where $x_0 = \sqrt{\hbar/(m\omega_0)}$ denotes the oscillator length and $a_B = 4\pi\varepsilon\hbar^2/(me^2)$ is the effective electron (hole) Bohr radius. Thus, Hamiltonian (4) including the kinetic energy can be rewritten in dimensionless form

$$\hat{H}_{e(h)} = \frac{1}{2}\sum_{i=1}^{N}(-\nabla_i^2 + \mathbf{r}_i^2) + \sum_{i<j}^{N}\frac{\lambda}{\sqrt{(\mathbf{r}_i - \mathbf{r}_j)^2}}, \tag{7}$$

$$\hat{H}_{e-h} = \sum_{i=1}^{N_e}\sum_{j=1}^{N_h}\frac{\lambda}{\sqrt{(\mathbf{r}_i - \mathbf{r}_j)^2 + d^{*2}}}, \tag{8}$$

using the transformation $\{r \rightarrow r/x_0, E \rightarrow E/E_0^*, d^* \rightarrow d/x_0\}$. Note that r and d^* are measured in units of x_0 and thus explicitly depend on the confinement frequency ω_0. The characteristic energies and length scales of the classical (section 2) and quantum system are related by

$$\frac{E_0}{E_0^*} = (\lambda^2/2)^{1/3}, \qquad \frac{r_0}{x_0} = (2\lambda)^{1/3}, \tag{9}$$

so that the layer separations used in the Hamiltonians (3) and (8), respectively, are related by $d^* = (2\lambda)^{1/3} d$.

In the limit $\lambda \rightarrow 0$, both electrons and holes behave as an ideal trapped Fermi gas independent of the layer separation d^*. For $\lambda \rightarrow \infty$, it is $x_0/a_B \gg 1$, and quantum effects vanish. Thus, one recovers classical behaviour and shell configuration changes which coincide with those in table 1. At finite λ, however, intra- and interlayer interactions, together with the parabolic confinement, give rise to a complex quantum many-body problem, which is the subject of the following investigation. In the considered quantum case, ground state properties depend on the two parameters d^* and λ. Therefore, the question of whether the additional degree of freedom will induce additional structural changes arises. To answer this question, we performed self-consistent Hartree–Fock (SCHF) calculations of two coupled electron and hole layers of zero thickness, which are discussed in the next two subsections.

4.1. Second quantization formulation

In order to derive mean-field type equations for the e–h bilayer, we rewrite the exact Hamiltonian (7) and (8) in the second-quantized form $\hat{H} = \hat{H}_e + \hat{H}_h - \hat{H}_{e-h}$, where

$$\hat{H}_{e(h)} = \int d^2r\, \hat{\psi}_{e(h)}^\dagger(\mathbf{r})\, h_0(\mathbf{r})\, \hat{\psi}_{e(h)}(\mathbf{r})$$
$$+ \frac{1}{2}\iint d^2r\, d^2\bar{r}\, \hat{\psi}_{e(h)}^\dagger(\mathbf{r})\, \hat{\psi}_{e(h)}^\dagger(\bar{\mathbf{r}})\frac{\lambda}{\sqrt{(\mathbf{r}-\bar{\mathbf{r}})^2}}\hat{\psi}_{e(h)}(\bar{\mathbf{r}})\, \hat{\psi}_{e(h)}(\mathbf{r}), \tag{10}$$

$$\hat{H}_{e-h} = \iint d^2r\, d^2\bar{r}\, \hat{\psi}_e^\dagger(\mathbf{r})\, \hat{\psi}_h^\dagger(\bar{\mathbf{r}})\frac{\lambda}{\sqrt{(\mathbf{r}-\bar{\mathbf{r}})^2 + d^{*2}}}\hat{\psi}_h(\bar{\mathbf{r}})\, \hat{\psi}_e(\mathbf{r}), \tag{11}$$

with $h_0(\mathbf{r}) = \frac{1}{2}(-\nabla^2 + \mathbf{r}^2)$ denoting the single-particle energy. Further, $\hat{\psi}_{e(h)}^{(\dagger)}(\mathbf{r})$ is the annihilation (creation) operator of spin-polarized electrons and holes at space point $\mathbf{r}$ which satisfy the fermionic anti-commutation relations $[\hat{\psi}_{e(h)}(\mathbf{r}), \hat{\psi}_{e(h)}^\dagger(\bar{\mathbf{r}})]_+ = \delta(\mathbf{r}-\bar{\mathbf{r}})$ and $[\hat{\psi}_{e(h)}^{(\dagger)}(\mathbf{r}), \hat{\psi}_{e(h)}^{(\dagger)}(\bar{\mathbf{r}})]_+ = 0$, where $[\hat{A}, \hat{B}]_+ = \hat{A}\hat{B} + \hat{B}\hat{A}$. In a Hartree–Fock (HF) approach [40],

the four field operator products entering equations (10) and (11) are approximated by sums over double products $\hat{\psi}^\dagger_{e(h)}\hat{\psi}_{e(h)}$ weighted by the generalized electron (hole) density matrix $\rho_{e(h)}(\mathbf{r},\bar{\mathbf{r}}) = \langle \hat{\psi}^\dagger_{e(h)}(\mathbf{r})\hat{\psi}_{e(h)}(\bar{\mathbf{r}})\rangle_{e(h)}$, where the expectation value (ensemble average) is defined as $\langle \hat{A}\rangle_{e(h)} = \mathrm{Tr}\,\hat{\rho}_{e(h)}\hat{A}$. More precisely, with $\eta, \xi \in \{e, h\}$, the 4-operator products are approximated as

$$
\hat{\psi}^\dagger_\eta(\mathbf{r})\,\hat{\psi}^\dagger_\xi(\bar{\mathbf{r}})\,\hat{\psi}_\xi(\bar{\mathbf{r}})\,\hat{\psi}_\eta(\mathbf{r}) \approx + \rho_\eta(\mathbf{r}, \mathbf{r})\,\hat{\psi}^\dagger_\xi(\bar{\mathbf{r}})\,\hat{\psi}_\xi(\bar{\mathbf{r}}) + \rho_\xi(\bar{\mathbf{r}}, \bar{\mathbf{r}})\,\hat{\psi}^\dagger_\eta(\mathbf{r})\,\hat{\psi}_\eta(\mathbf{r})
$$
$$
- \delta_{\eta\xi}\left[\rho_\eta(\mathbf{r}, \bar{\mathbf{r}})\,\hat{\psi}^\dagger_\xi(\bar{\mathbf{r}})\,\hat{\psi}_\xi(\mathbf{r}) + \rho_\xi(\bar{\mathbf{r}}, \mathbf{r})\,\hat{\psi}^\dagger_\eta(\mathbf{r})\,\hat{\psi}_\eta(\bar{\mathbf{r}})\right].
\tag{12}
$$

Here, the first two terms constitute the Hartree term, whereas the last two denote the Fock (exchange) contribution. The Kronecker delta $\delta_{\eta\xi}$ assures that there is no exchange between electrons and holes which is due to the different physical nature of electrons and holes (different energy bands). Inserting the approximate expression (12) into (10) and (11) allows for an effective one-particle description according to

$$
\hat{H}_{e(h)} = \iint \mathrm{d}^2r\,\mathrm{d}^2\bar{r}\,\hat{\psi}^\dagger_{e(h)}(\mathbf{r})\left\{h_0(\mathbf{r})\,\delta(\mathbf{r} - \bar{\mathbf{r}}) + \Sigma^{\mathrm{HF}}_{e(h)}(\mathbf{r}, \bar{\mathbf{r}})\right\}\hat{\psi}_{e(h)}(\bar{\mathbf{r}}),
\tag{13}
$$

$$
\hat{H}_{e\text{-}h} = \iint \mathrm{d}^2r\,\mathrm{d}^2\bar{r}\,\hat{\psi}^\dagger_e(\mathbf{r})\left\{\Sigma^{\mathrm{HF}}_{e\text{-}h}(\mathbf{r}, \bar{\mathbf{r}}) + \Sigma^{\mathrm{HF}}_{h\text{-}e}(\mathbf{r}, \bar{\mathbf{r}})\right\}\hat{\psi}_h(\bar{\mathbf{r}}),
\tag{14}
$$

with the HF self-energies

$$
\Sigma^{\mathrm{HF}}_{e(h)}(\mathbf{r}, \bar{\mathbf{r}}) = \lambda \int \mathrm{d}^2r'\,\frac{\rho_{e(h)}(\mathbf{r}', \mathbf{r}')}{\sqrt{(\mathbf{r}' - \mathbf{r})^2}}\,\delta(\mathbf{r} - \bar{\mathbf{r}}) - \lambda\frac{\rho_{e(h)}(\mathbf{r}, \bar{\mathbf{r}})}{\sqrt{(\mathbf{r} - \bar{\mathbf{r}})^2}},
\tag{15}
$$

$$
\Sigma^{\mathrm{HF}}_{e\text{-}h(h\text{-}e)}(\mathbf{r}, \bar{\mathbf{r}}) = \lambda \int \mathrm{d}^2r'\,\frac{\rho_{h(e)}(\mathbf{r}', \mathbf{r}')}{\sqrt{(\mathbf{r}' - \mathbf{r})^2 + d^{*2}}}\,\delta(\mathbf{r} - \bar{\mathbf{r}}).
\tag{16}
$$

For computational reasons, it is convenient to introduce a basis representation for the electron (hole) field operators,

$$
\hat{\psi}^{(\dagger)}_{e(h)}(\mathbf{r}) = \sum_i \varphi^{(*)}_i(\mathbf{r})\,\hat{a}^{(\dagger)}_{e(h),i}, \quad i \in \{0, 1, 2, \ldots\},
\tag{17}
$$

where the one-particle orbitals or wave functions $\varphi_i(\mathbf{r})$ form an orthonormal complete set and $\hat{a}^{(\dagger)}_{e(h),i}$ is the annihilation (creation) operator of a particle on the level i. Applying the basis expansion (17) to the equations (13) and (14) leads to the matrix representation of the bilayer Hamiltonian (1) which will be given in the following section, cf equations (18)–(20).

4.2. SCHF simulation technique

In matrix representation, the mean-field Hamiltonian for the bilayer system corresponding to the initial equations (1)–(3) reads

$$
h^{e(h)}_{ij} = h^0_{ij} + h^{e\text{-}e(h\text{-}h)}_{ij} - h^{e\text{-}h(h\text{-}e)}_{ij},
\tag{18}
$$

$$
h^{e\text{-}e(h\text{-}h)}_{ij} = \lambda \sum_{kl}\left(w^{e\text{-}e(h\text{-}h)}_{ij,kl} - w^{e\text{-}e(h\text{-}h)}_{il,kj}\right)\rho^{e(h)}_{kl},
\tag{19}
$$

$$h_{ij}^{\text{e-h(h-e)}} = \lambda \sum_{kl} w_{ij,kl}^{\text{e-h(h-e)}} \rho_{kl}^{\text{h(e)}}, \tag{20}$$

with the single-particle (orbital) quantum numbers i and j (k and l), $h_{ij}^{\text{e(h)}}$ being the electron (hole) total energy, h_{ij}^0 the single-particle (kinetic and confinement) energy and $h_{ij}^{\text{e-e(h-h)}}$ ($h_{ij}^{\text{e-h(h-e)}}$) the intra (inter) layer interactions in mean-field approximation. Further, $\rho_{ij}^{\text{e(h)}} = \langle \hat{a}_{\text{e(h)},i}^\dagger \hat{a}_{\text{e(h)},j} \rangle$ denotes the zero-temperature density matrix of electrons and holes with respect to the one-particle basis $\varphi_i(\mathbf{r})$. In equation (19), both the Hartree and the Fock contribution appear, whereas in equation (20) only the Hartree term enters.

The explicit expression for the single-electron (-hole) integral is

$$h_{ij}^0 = \frac{1}{2} \int \mathrm{d}^2 r \, \varphi_i^*(\mathbf{r})(-\nabla^2 + \mathbf{r}^2)\varphi_j(\mathbf{r}), \tag{21}$$

and the two-electron (two-hole) and electron–hole integrals are given by

$$w_{ij,kl}^{\text{e-e(h-h)}} = \iint \mathrm{d}^2 r \, \mathrm{d}^2 \bar{r} \, \frac{\varphi_i^*(\mathbf{r}) \, \varphi_k^*(\bar{\mathbf{r}}) \varphi_j(\mathbf{r}) \varphi_l(\bar{\mathbf{r}})}{\sqrt{(\mathbf{r} - \bar{\mathbf{r}})^2 + \alpha^{*2}}}, \tag{22}$$

$$w_{ij,kl}^{\text{e-h(h-e)}} = \iint \mathrm{d}^2 r \, \mathrm{d}^2 \bar{r} \, \frac{\varphi_i^*(\mathbf{r}) \, \varphi_k^*(\bar{\mathbf{r}}) \, \varphi_j(\mathbf{r}) \, \varphi_l(\bar{\mathbf{r}})}{\sqrt{(\mathbf{r} - \bar{\mathbf{r}})^2 + d^{*2}}}, \tag{23}$$

where $\alpha^* \to 0$ is utilized to avoid the Coulomb singularity for $\mathbf{r} \to \bar{\mathbf{r}}$. A small parameter of $\alpha^* \lesssim 0.01$ has been found to show convergence for all quantities of interest. Details will be given elsewhere [41].

For numerical implementation of the SCHF procedure yielding the eigenfunctions $\phi_i^{\text{e(h)}}(\mathbf{r})$ (HF orbitals) and eigenenergies $\epsilon_i^{\text{e(h)}}$ (HF energies) of Hamiltonian (18), we have chosen the orthonormal Cartesian (2D) harmonic oscillator states

$$\varphi_{m,n}(\mathbf{r}) = \frac{\mathrm{e}^{-(x^2+y^2)/2}}{\sqrt{2^{m+n} \, m! \, n! \, \pi}} \, \mathcal{H}_m(x) \, \mathcal{H}_n(y), \tag{24}$$

with single-particle quantum numbers $i = (m, n)$, $\mathbf{r} = (x, y)$, the Hermite polynomials $\mathcal{H}_m(x)$ and $(m+1)$-fold degenerate energy eigenvalues $\epsilon_{m,n} = m + n + 1$, where $m, n \in \{0, 1, 2, \ldots\}$. The HF orbitals, expanded in the form

$$\phi_i^{\text{e(h)}}(\mathbf{r}) = \sum_{j=0}^{n_{\text{b}}-1} c_{ji}^{\text{e(h)}} \, \varphi_j(\mathbf{r}), \tag{25}$$

with coefficients $c_{ij}^{\text{e(h)}} \in \mathbb{R}$ and respective energies $\epsilon_i^{\text{e(h)}}$, are obtained by iteratively solving the self-consistent Roothaan–Hall equations [42]

$$\sum_{k=0}^{n_{\text{b}}-1} h_{ik}^{\text{e(h)}} \, c_{kj}^{\text{e(h)}} - \epsilon_j^{\text{e(h)}} \, c_{ij}^{\text{e(h)}} = 0, \tag{26}$$

at fixed dimension $n_{\text{b}} \times n_{\text{b}}$ ($i = 0, 1, \ldots, n_{\text{b}} - 1$) according to standard techniques, for details see e.g. [40] and references therein. The resulting electron (hole) density $\rho_{d^*,\lambda}^{\text{e(h)}}(\mathbf{r})$ corresponding

to given values of d^* and λ is defined as

$$\rho_{d^*,\lambda}^{\mathrm{e(h)}}(\mathbf{r}) = \sum_{k=0}^{N-1} \phi_{k,d^*,\lambda}^{\mathrm{e(h)}}(\mathbf{r}) = \sum_{k=0}^{N-1}\sum_{l=0}^{n_{\mathrm{b}}-1} c_{lk,d^*,\lambda}^{\mathrm{e(h)}} \, \varphi_l(\mathbf{r}), \qquad (27)$$

where each HF orbital k is occupied by a single particle only.

For the e–h bilayers with $N \leqslant 10$, we used $n_{\mathrm{b}} = 50$ of the energetically lowest oscillator functions $\varphi_{m,n}(\mathbf{r})$ to expand the HF orbitals, for $N = 12$ we took $n_{\mathrm{b}} = 55$ which was sufficient to obtain convergent results. Due to the electron–hole attraction the cluster size is reduced compared to that of a single layer Coulomb cluster. This favours the use of a moderate number of basis functions to ensure convergence[8].

4.3. Transition from the ideal Fermi gas towards the classical limit

The aim of this part is to investigate the transition from a strongly degenerate quantum system, i.e. $\lambda = 0$, to the classical limit $\lambda \to \infty$. To give a reasonable estimate for the range at which the classical ground state results become valid, we consider a system with $N = 6$ electrons and holes at an intermediate layer separation of $d^* = 1.0$. Of special interest will be the central spot of the (1,5) configuration which can most directly be assigned to a classical particle position.

In contrast to the classical results the HF calculations fully take into account the wave nature of electrons and holes. The quantum many-body effects are evident already at $\lambda = 0$. In the classical case, the total energy in the ground state is zero (all particles sit in the bottom of the trap). In the quantum case, this is prevented by the Pauli principle. Orbital-resolved HF calculations as function of coupling parameter λ are displayed in figure 3. Here, the right panel shows the N-particle density $\rho_{d^*,\lambda}^{\mathrm{e(h)}}(\mathbf{r})$ and the six populated single-particle orbitals $\phi_{i,d^*,\lambda}^{\mathrm{e(h)}}(\mathbf{r})$ for moderate ($\lambda_1 = 5.0$), intermediate ($\lambda_2 = 15.0$) and strong ($\lambda_3 = 35.0$) coupling. The SCHF results reveal that, in particular for small values of λ, obviously several orbitals contribute collectively to the different high-density spots which unambiguously determine the cluster configuration.

Concerning the lowest orbital $i = 0$, with an increase of λ, the overlap with the higher orbitals vanishes and the wave function becomes localized when λ exceeds a value of 35. In contrast, in the investigated range of $\lambda \leqslant 40$ the other particles remain, independently of the observed density modulation, delocalized as can be seen on the orbital pictures. The transition towards the limit of strong correlations can be estimated from the e–h-interaction energy

$$\epsilon_{\mathrm{e-h}}^{(i=0)}(\lambda) = -\iint \mathrm{d}^2 r\, \mathrm{d}^2\bar{r} \, |\phi_{i=0}^{\mathrm{e}}(\mathbf{r})|^2 \frac{\lambda}{\sqrt{(\mathbf{r}-\bar{\mathbf{r}})^2 + d^{*2}}} |\phi_{i=0}^{\mathrm{h}}(\bar{\mathbf{r}})|^2, \qquad (28)$$

of the electron and hole in the lowest orbital. The upper diagram in the left panel of figure 3 displays the λ-dependence for four different approximations. For the ideal system, $\lambda = 0$, electron and hole are not bound and $\epsilon_{\mathrm{e-h}}^{(i=0)}$ vanishes. The black solid line shows the interaction energy (28) obtained from the SCHF simulations which for $\lambda \ll 1$ agrees with perturbation theory (PT), where a linear λ-dependence follows from substituting the ideal wave function $\varphi_{0,0}(\mathbf{r})$, see equation (24), for $\phi_{i=0}^{\mathrm{e(h)}}(\mathbf{r})$ in equation (28).

---

[8] Note that the additional centre particle in the case of $N = 19$ strongly increases the cluster size so that essentially more basis functions ($n_{\mathrm{b}} \gtrsim 90$) are required to ensure convergence. As the problem determining the two-particle integrals, equations (22) and (23), scales with $\mathcal{O}(n_{\mathrm{b}}^4)$ a computation is limited by memory requirements.
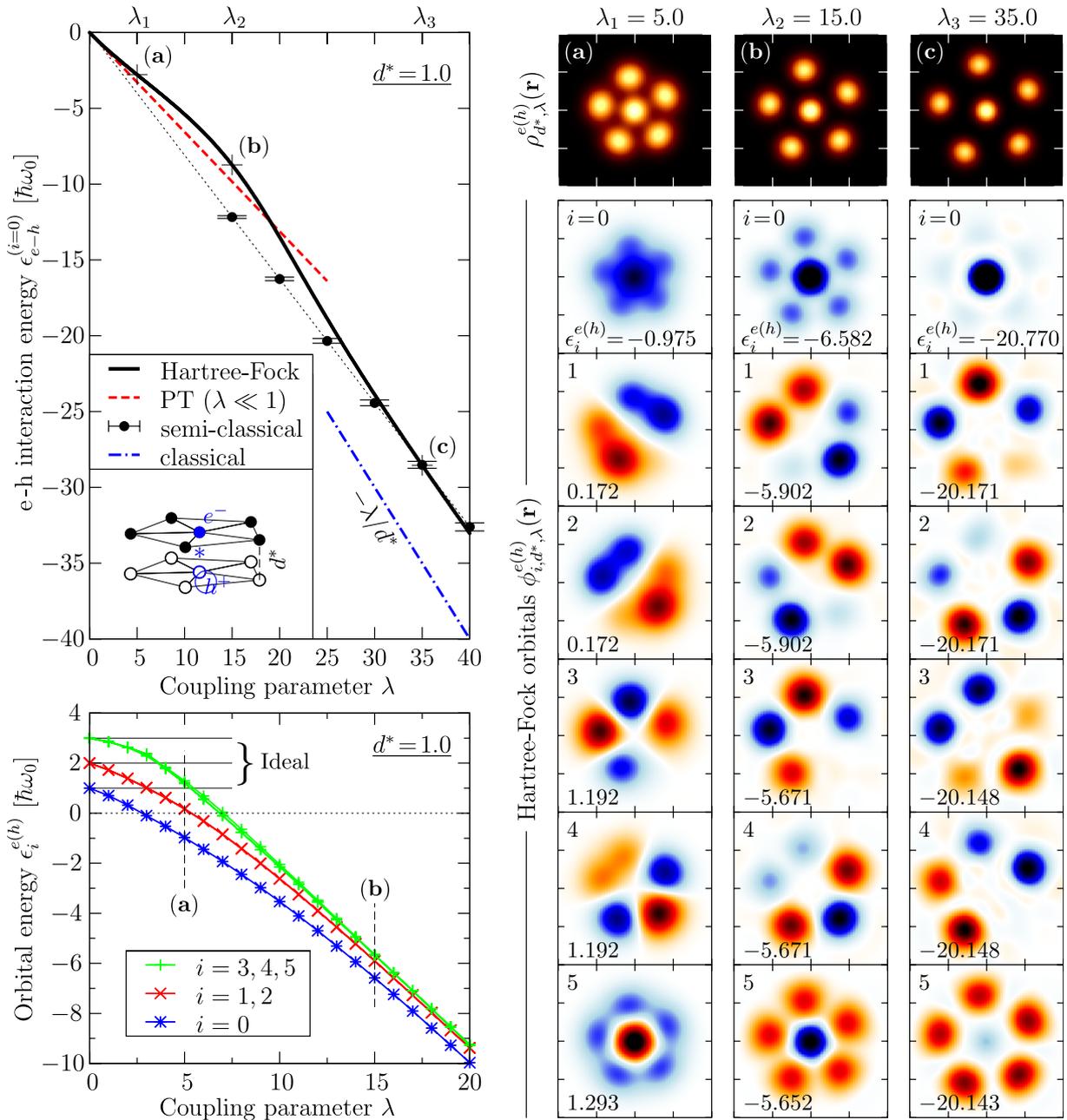
Figure 3. Ground state of the $N = 6$ cluster as function of interaction strength λ for fixed layer separation $d^* = 1.0$. *Right*: accumulated N-particle density $\rho_{d^*,\lambda}^{\mathrm{e(h)}}(\mathbf{r})$, on top, and corresponding single-particle HF orbitals $\phi_{i,d^*,\lambda}^{\mathrm{e(h)}}(\mathbf{r})$ for three different coupling parameters λ. The different signs of the wave function (blue and orange) are separated by white areas of zero amplitude, whereas areas of maximum amplitude are black. Note that the six high-density spots of the N-particle density do not necessarily correspond to the single particles themselves as the configuration appears as a superposition of all orbitals. *Left* (top): electron–hole interaction energy $\epsilon_{\mathrm{e-h}}^{j=0}$, equation (28), of the centre electron and hole states for different approximations and (bottom) HF energy of occupied levels $\epsilon_i^{\mathrm{e(h)}}$ as function of λ.

For $\lambda \gg 1$, a semi-classical result can be derived. Starting from the classical ground state configuration (1,5) the outer particles, together with the confinement, create an effective potential for both centre particles which can be harmonically approximated. The direct quantum mechanical solution of the harmonic problem provides a finite Gaussian electron (hole) extension of width $\sigma = \sigma_e = \sigma_h$. Hence, the e–h-interaction energy (28) of the inner particles can be computed in a semi-classical way using $\phi_{i=0}^{e(h)}(\mathbf{r}) = (\sigma/\pi)^{1/4} e^{-\sigma(x^2+y^2)/2}$. In the strongly correlated regime, starting at $\lambda \geqslant 30$, the semi-classical and SCHF solution coincide very well.

However, in an intermediate coupling range, $\lambda \approx 15$, the e–h interaction energy is reduced compared to the semi-classical solution which reflects the fact that the orbital $i = 0$ substantially deviates from a Gaussian, cf the five side maxima of the orbital $i = 0$ for $\lambda_2 = 15$ in figure 3. With increase of λ this Gaussian becomes more and more peaked describing the transition to the classical limit $|\phi_{i=0}^{e(h)}(r)|^2 \to \delta(r)$[9]. Despite the good agreement with the semi-classical approximation, in the whole investigated range of $\lambda < 40$ the system is found to be essentially non-classical. This becomes evident by comparing with the pure classical result $\epsilon_{e-h}^{(i=0)} = -\lambda/d^*$ which neglects any finite particle extension. Concerning all populated HF orbitals the transition towards the classical limit with increasing λ is shown in the lower left diagram of figure 3 in terms of the orbital energies $\epsilon_{i=(m,n)}^{e(h)}$. As mentioned in section 4.2, the harmonically confined ideal Fermi gas ($\lambda = 0$) is $(m+1)$-fold degenerate with $m, n \in \{0, 1, \ldots\}$. Around $\lambda \geqslant 15$ the energy of the outer particles converges towards a five-fold degenerate energy which is separated from the (lower) energy of the centre particle.

4.4. Quantum ground state configurations and structural transitions for N = 10

Beside the higher numerical effort of a single SCHF computation compared to its classical analogue, a complete study of the ground states requires, in addition to d and N, the exploration of λ as a third degree of freedom. To overcome this problem and to reduce the task, we limit our investigation to the two-shell clusters $N = 10$ and $N = 12$ which were found to exhibit rich ground state properties in the classical limit.

The analysis was done by systematically scanning the phase diagram for fixed values of d^* ranging from 0.1 to 10.0. For each of these d^* values we start from the ideal system at $\lambda = 0$ and increment the coupling parameter stepwise by $\delta\lambda = 0.05$. The convergence of each step is ensured by an adaptive, precision controlled iteration number with up to 2500 iterations of the Roothaan–Hall equations (26) per increment $\delta\lambda$. The described procedure allows for a systematic investigation of the phase diagram by a gradual transition from the ideal Fermi to the strongly coupled system. To verify the results obtained, the ground states with respect to individual points in the phase diagram were recomputed by starting from a random distribution as well as by decreasing the temperature of an initial (high temperature) thermal distribution [41]. All procedures are found to yield the same HF orbitals (energies) and thus the same N-particle densities and shell structures.

The results for the $N = 10$ cluster are presented in figure 4. The ground state phase diagram can be divided into four domains (left panel of figure 4):

(i) At small λ a weakly correlated degenerate Fermi liquid is observed within each layer (blue area in the left figure). The observed electron (hole) density is rotationally symmetric and

---

[9] In the mean-field Hamiltonian (13) and (14) the classical limit is obtained by replacing $\rho_{e(h)}(\mathbf{r}, \mathbf{r}') \to \delta(\mathbf{r} - \mathbf{r}') \sum_{i=1}^{N_{e(h)}} \delta(\mathbf{r} - \mathbf{r}_i)$.
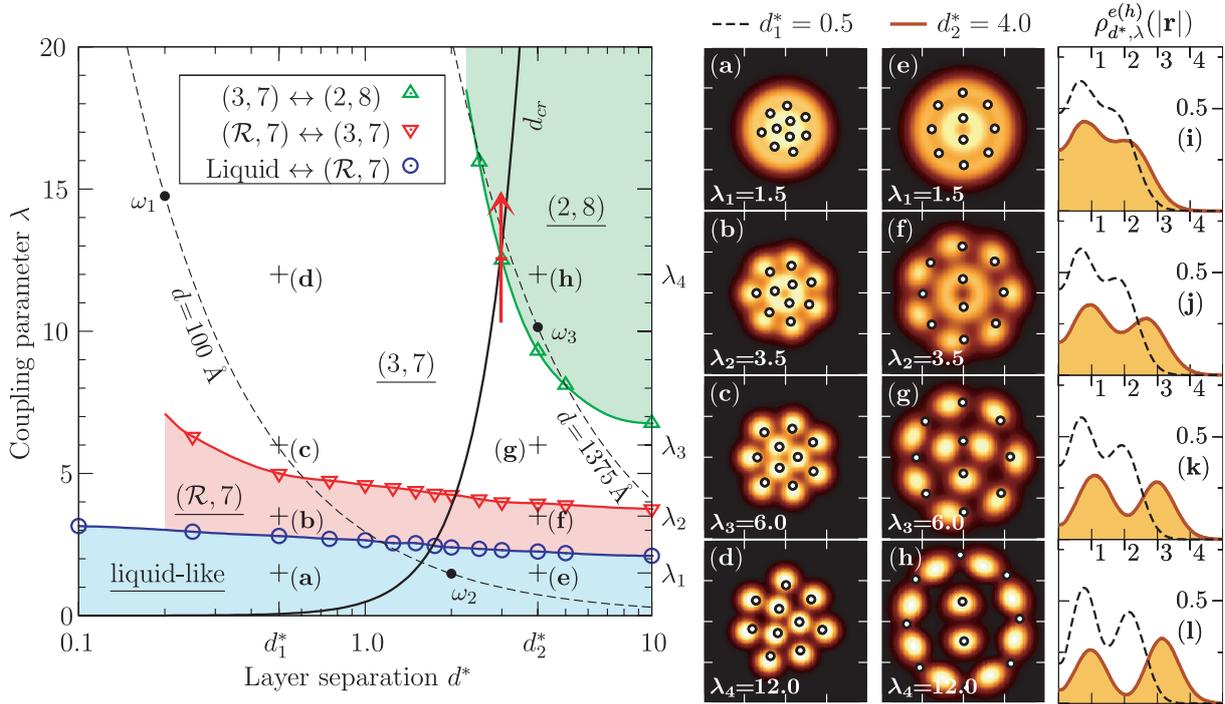
Figure 4. *Left*: (λ, d^*)-phase diagram for the $N = 10$ bilayer in HF approximation. The configuration $(\mathcal{R}, 7)$ means delocalization of charges on the inner ring $\mathcal{R}$. The black solid line indicates the classical ground state transition $(3, 7) \rightarrow (2, 8)$ which occurs at $d_{cr} = 1.0116 r_0$ from left to right. The red arrow points out an inverse transition compared to the classical $(2, 8) \rightarrow (3, 7)$ crossing. The two dashed lines indicate the path when changing ω_0 at fixed layer separation d for a germanium ($\varepsilon = 16\varepsilon_0$, $m^*_{e(h)} = 0.25 m_e$) quantum-well structure, see equation (29); $\omega_1 = 926\,\text{GHz}$, $\omega_2 = 9.26\,\text{THz}$, $\omega_3 = 98\,\text{GHz}$. *Right*: electron (hole) density $\rho^{e(h)}_{d^*,\lambda}(\mathbf{r})$ at characteristic points marked (a) to (h) in the phase diagram. The side length of the contour plots is $9 x_0$. The open circles mark the corresponding classical ground state particle positions. The rightmost column displays the corresponding angle-averaged radial density profiles for $d^* = 0.5$ (4.0), dashed (red) line.

exhibits non-monotonic radial modulations of an (nearly) ideal trapped Fermi gas. The proper density distributions for $d^*_1 = 0.5$ and $d^*_2 = 4.0$ are shown in figures 4(a) and (e), respectively.

(ii) At higher λ two shells separate, see points (b), (f) within the red area in the phase diagram and the corresponding density profile (j). While on the inner ring the electron (hole) density is still isotropic, the density on the outer shell becomes angle-modulated and reveals seven high-density spots. The integrated position probability density on the inner and outer shells is close to 3 and 7, respectively. The configuration will be referred to in the following as $(\mathcal{R}, 7)$ as on the inner ring $\mathcal{R}$ no localized density peaks in $\rho^{e(h)}_{d^*,\lambda}(\mathbf{r})$ are present. *Hence the nomenclature does not indicate the particle numbers, but the number of distinct density peaks*, as the particle orbitals are delocalized over the entire cluster, see discussion in sections 4.3 and 4.6.

(iii) Further increase of the coupling parameter leads to more pronounced (concentric) shells. In particular, the inner radial density decreases which is accompanied by the formation of angular density modulation, see figures 4(c) and (g). The shell configuration is found to be (3,7).

(iv) At a certain value $\lambda_{\text{cr}}(d^*)$, the bilayer system jumps from the (3,7) into the (2,8) shell configuration (green area in the phase diagram), see figures 4(g) and (h).

The general behaviour of (i)–(iii) is independent of the layer separation d^*. The localized (3,7) configuration (iii) emerges in two steps by rotational symmetry breaking from the Fermi liquid (i) maintaining a higher density on the inner than on the outer ring. However, an increase of d^* beyond unity leads, by weakening of the interlayer attraction, to a repulsive intralayer and thus Coulomb-dominated coupling. Consequently, the cluster size increases, compare the density plots of figure 4(a) versus (e), 4(b) versus (f), etc. Moreover, for a fixed $\lambda \gg 1$, the dipole-to-Coulomb transition towards the strongly correlated Coulomb regime induces the (2,8) shell configuration [28] which is observed when d^* is increased from 0.5 to 4.0, see figure 4(d) versus (h). This transition reduces the inner-shell density, see figure 4 right (red versus dashed lines).

Further, at a fixed $d^* > 2.0$ an increase of λ leads to a purely coupling-induced configuration change (3,7) $\rightarrow$ (2,8), see details in section 4.6. For $d^* = 10$, both layers are already weakly coupled and become completely decoupled when d^* is further increased. Consequently, the critical (blue, red and green) curves in the phase diagram converge towards horizontal lines. Note that d^* is measured in units of x_0 and thus depends on the confinement frequency ω_0. This implies for an experimental setup, e.g. a double quantum-well heterostructure with fixed physical layer separation d, that one traces hyperbolas of the form

$$\lambda(d^*) = \frac{d\, e^2\, m_{\text{e(h)}}^*}{4\pi\,\varepsilon\,\hbar^2}\, \frac{1}{d^*(\omega_0)}\,, \tag{29}$$

when changing the trap frequency ω_0, see the dashed lines in the phase diagram of figure 4. The larger the physical layer separation d (or effective particle mass $m_{\text{e(h)}}^*$), the more the hyperbola shifts to larger values of d^*. Interestingly, e.g. for a germanium based quantum well, at fixed layer separation $d = 1375\,\text{Å}$, the ground state structure of the quantum bilayer can be externally controlled by change of ω_0 only.

A comparison of the classical particle positions (open circles in figures 4(a)–(h)), according to equations (9), with the shells and high-density spots of the HF calculations plotted in figure 4 reveals a good agreement. Larger cluster sizes compared to the classical case for small λ are explained by repulsive fermionic exchange interactions. Further, the bold black line in the phase diagram indicates the classical transition from (3,7) to (2,8) which occurs at $d_{\text{cr}} = 1.0116r_0$ when crossing the line from left to right. It is found that the classical line gives a reasonable estimate also for the transition in the quantum bilayer system. Hence the trend, found in section 2 for the classical bilayer system, of centre density reduction with increasing d also holds in the case of a strongly correlated quantum system, where the orbitals extend over several classical particle positions. In the classical limit, i.e. at very large λ (outside of figure 4), the configuration boundary (3,7) $\leftrightarrow$ (2,8) (green curve) and the classical result (black curve) converge. Nevertheless, for intermediate values of λ the red arrow indicates a remarkable point in the phase diagram where the structural transition in the classical and quantum bilayer proceeds in opposite direction. The single-particle orbitals for this transition will be analysed in section 4.6.
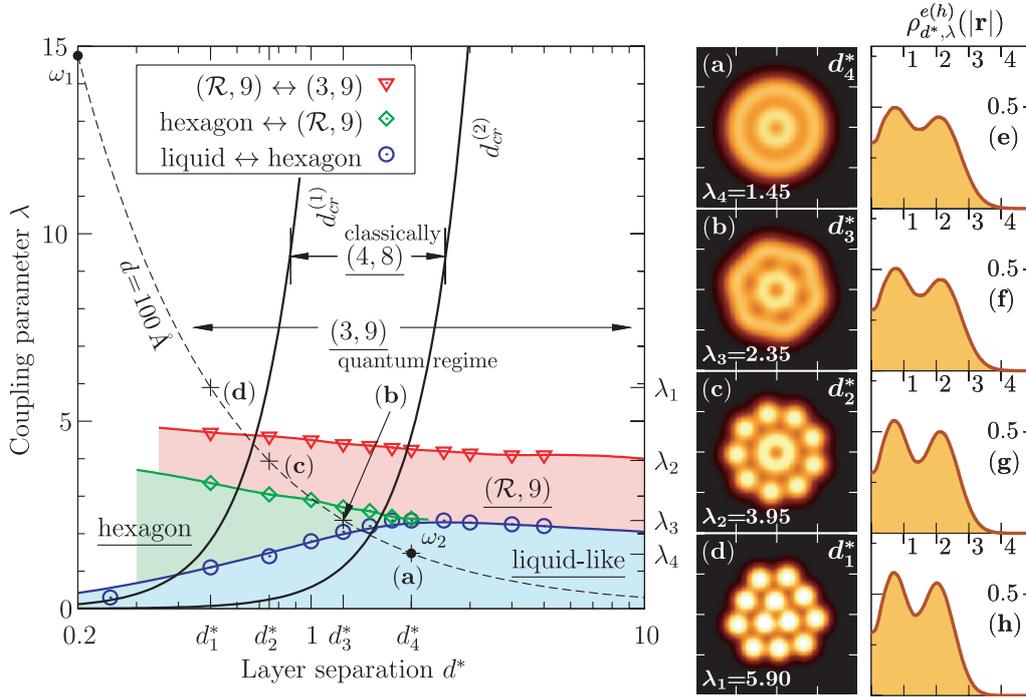
Figure 5. (λ, d^*)-phase diagram showing the quantum shell structures found for the $N = 12$ bilayer in HF approximation. The shown electron (hole) densities $\rho_{d^*,\lambda}^{\mathrm{e(h)}}(\mathbf{r})$ corresponding to tuples (d) $(d_1^*, \lambda_1) = (0.5, 5.9)$, (c) $(d_2^*, \lambda_2) = (0.75, 3.95)$, (b) $(d_3^*, \lambda_3) = (1.25, 2.35)$ and (a) $(d_4^*, \lambda_4) = (2.0, 1.45)$. The frequencies $w_{1,2}$ are as indicated in figure 4. The two black solid lines indicate the classical configuration transitions $(3, 9) \rightarrow (4, 8)$ and $(4, 8) \rightarrow (3, 9)$ at $d_{\mathrm{cr}}^{(1)} = 0.9528 r_0$ and $d_{\mathrm{cr}}^{(2)} = 0.3253 r_0$, respectively, from left to right. In the investigated range $\lambda \leqslant 15$ these transitions were not observed in the quantum bilayer. The right two columns show the (radial) density of the four points (a)–(d) marked in the phase diagram for $d = 100 \,\text{Å}$.

Further, an unusual (2,8) configuration is shown for $\lambda_4 = 12.0$ and $d_2^* = 4.0$ in figure 4(h), where the particle arrangement differs from the classical system. Such a configuration was also found in [28] for a classical single layer system with $1/r^\alpha$ pair interaction and $\alpha \leqslant 0.94$. Thus, the anomalous configuration underlines the effect of the Fermi repulsion in addition to the intralayer Coulomb interaction. However, an increase of λ leads to a reduction of the Fermi effect and wave function overlap and a (2,8) configuration corresponding to the classical one is found.

4.5. Quantum ground state configurations and structural transitions for N = 12

In figure 5, we present the (λ, d^*)-phase diagram for $N = 12$ electrons and holes analogous to figure 4 for $N = 10$. At fixed (physical) layer separation $d = 100 \,\text{Å}$, one passes through four different domains of the phase diagram when the trap frequency is decreased from ω_2 towards ω_1 (see left panel of figure 5):

(i) Analogously to the $N = 10$ cluster at small λ, a weakly correlated circular symmetric Fermi liquid exists within each layer, see point (a) in the blue area of the phase diagram.

(ii) A decrease of the trap frequency to point (b) is accompanied by a structural change to a six-fold rotational cluster symmetry with an outer shape exhibiting hexagonal symmetry. This phase only establishes in the regime of a short-range in-layer potential, i.e. $d^* \leqslant 2$. In the Coulomb case of weakly coupled layers this liquid-like state is not found.

(iii) If the confinement strength is further reduced, see point (c), the cluster passes over to a nine-fold rotational symmetry. While in the cluster core a ring $\mathcal{R}$ of delocalized density is observed, the outer nine high-density spots are situated on a perfectly circular ring, which reproduces the symmetry of the external confinement potential.

(iv) In the limit of small d^* and $\lambda \to \infty$, see figure 5(d), where the in-layer interaction becomes extremely short-range, a commensurate closed packed structure with three-fold rotational symmetry similar to that known from classical dipole systems [28] is found.

Consequently, during the coupling-induced transition from (i) to (iv) the cluster size decreases slightly as the effective in-layer interaction becomes short-ranged. In analogy to $N = 10$, the liquid-like state (i) as well as the $(\mathcal{R}, 9)$ configuration (iii) are found for all values of d^*. The additional configuration (ii), missing in the case of $N = 10$, is limited to a range of strong interlayer attraction.

In contrast to $N = 10$, in total two transitions as function of d were found in the classical $N = 12$ system, cf table 1. However, in the investigated quantum regime, $\lambda \leqslant 15$, we observe *no* configuration changes corresponding to the classical transitions $(3,9) \leftrightarrow (4,8)$, see black lines $d_{cr}^{(1)} = 0.9528 r_0$ and $d_{cr}^{(2)} = 0.3253 r_0$ in figure 5 (left). Hence the two ground state transitions $(3,9) \to (4,8)$ and $(4,8) \to (3,9)$ of type (A) and (B), introduced in section 2, are expected to occur outside of figure 5 in the (semi-)classical region only.

4.6. Single-particle orbitals and single-particle spectrum

In both previous subsections, we discussed the phase diagram based on the N-particle densities. In this part, we pursue the question of how the single-particle spectrum evolves during the transition from (3,7) to (2,8) for the $N = 10$ cluster, see red arrow in figure 4 (left). At fixed $d^* = 3.0$, the configurational transition occurs when changing the coupling parameter from $\lambda_1 = 12$ to $\lambda_2 = 13$. For this transition, the spatially resolved orbitals $\phi_{i,d^*,\lambda}^{e(h)}(\mathbf{r})$ and the N-particle density $\rho_{d^*,\lambda}^{e(h)}(\mathbf{r})$ are collected in figure 6 together with the corresponding one-particle HF spectra $\epsilon_i^{e(h)}$ for both coupling parameters λ_1 and λ_2.

As mentioned in section 4.4, the configuration change $(2,8)_{\lambda_1} \leftrightarrow (3,7)_{\lambda_2}$ is reversed along the red arrow in figure 4 compared with the respective classical transition. Similar to the $N = 6$ cluster discussed in figure 3, the HF orbitals generally extend over several classical particle positions.

In situation (a), i.e. $\lambda_1 = 12$, the energetically highest orbitals $i = 7$, 8 and 9 contribute most to the inner-shell density showing three high-density spots. On the other hand, in (b), i.e. $\lambda_2 = 13$, the orbitals are completely rearranged with the two inner-shell density spots being now formed mainly from the orbitals 3 and 8, leading to embedded orbital energies $\epsilon_3^{e(h)}$ and $\epsilon_8^{e(h)}$ within the spectrum, cf the black circles in the energy term schemes. In addition, all orbital energies of the (2,8) configuration are enclosed in a narrower energy interval compared to (3,7), whereas the energy spectra do not reveal any degeneracy. However, for (2,8) the spectrum separates into two parts of similar energetic substructure with orbital energies $\epsilon_0^{e(h)}$ to $\epsilon_4^{e(h)}$ and $\epsilon_5^{e(h)}$ to $\epsilon_9^{e(h)}$, respectively. Accompanying this fact, one clearly recognizes a change and an
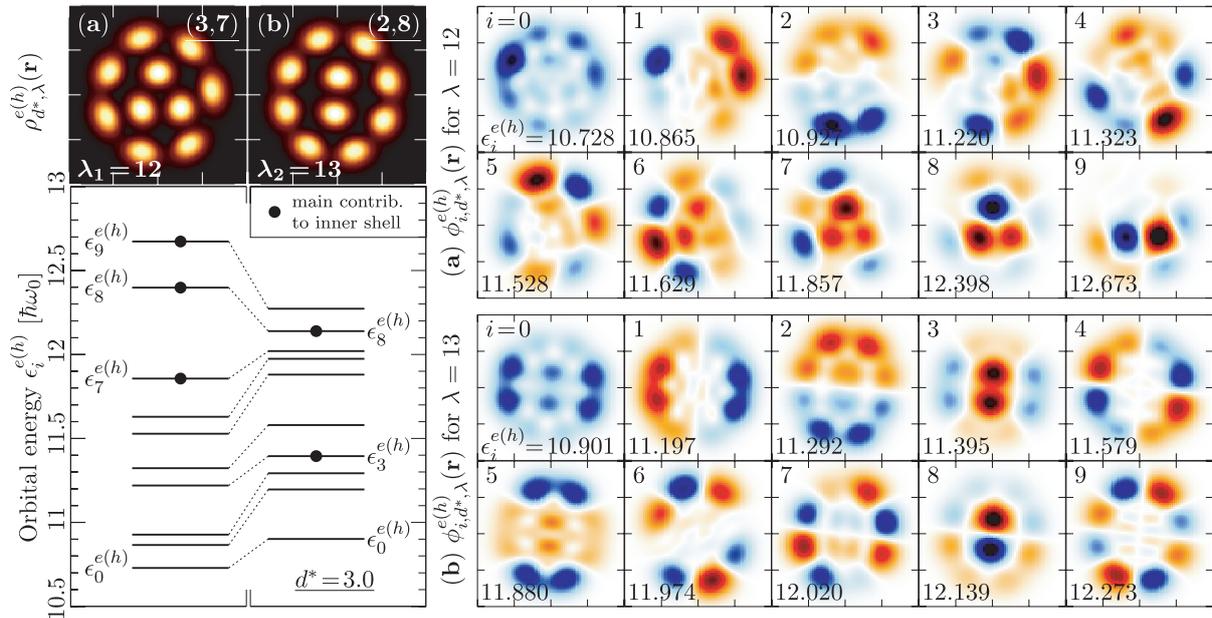
Figure 6. *Left*: HF energy eigenvalues $\epsilon_i^{\mathrm{e(h)}}$ corresponding to the spatial orbitals $\phi_{i,d^*,\lambda}^{\mathrm{e(h)}}(\mathbf{r})$. (a) Bilayer density $\rho_{d^*,\lambda}^{\mathrm{e(h)}}(\mathbf{r})$ and orbitals for $N = 10$ at $d^* = 3.0$ and $\lambda_1 = 12.0$, (b) $\lambda_2 = 13.0$. The black dots denote the orbitals which contribute most to the inner-shell high-density spots. While the inner shell of the (3,7) configuration is essentially built up from the 3 highest orbitals 7, 8 and 9, the inner shell of the (2,8) configuration is mostly formed from the orbitals 3 and 8. *Right*: single-particle orbitals $\phi_{i,d^*,\lambda}^{\mathrm{e(h)}}(\mathbf{r})$ for the cases (a) and (b). The different signs of the wave function (blue and orange) are separated by white areas of zero amplitude, whereas areas of maximum amplitude are black.

increase of the orbital symmetry when crossing over from the (3,7) to the (2,8) configuration. In contrast to (a) the rotational and specular (mirror) symmetry of $\phi_{i,d^*,\lambda}^{\mathrm{e(h)}}(\mathbf{r})$ with respect to perpendicular space axes in (b) is increased. Moreover, the structure of the nodes (white lines with zero amplitude in figure 6 right) of the HF orbitals changes, making the symmetry axes obvious. Particularly, inner and outer shell are clearly more separated by nodes in the (2,8) configuration.

5. Discussion and outlook

In this paper, we have considered ground state and dynamical properties of mesoscopic classical and quantum mass-symmetric electron–hole bilayers. In particular, we focused on the dependence of the properties on the layer separation d. The main effect is the gradual transition from systems with Coulomb interaction in the layers (at large d) to a system with short-range dipole interaction (at small d). Based on extensive classical molecular dynamics calculations we have shown that, with variation of d, several clusters show a sudden change of the ground state shell configuration, including several cases of re-entrant configuration changes which are related to symmetry properties. Furthermore, we have analysed the classical normal modes of

these bilayers and studied the d-dependence of the spectrum for $N = 19$ as a representative example.

A striking result is the energy jump of the inter-shell rotation mode frequency $\omega_{\mathrm{SR}^+}^2$ by more than four orders of magnitude when the 'magic' ground state configuration (1,6,12) is replaced by (1,7,11). This leads us to suggest a new possibility for external control of inter-shell rotation by *exerting strain* on the bilayer system (or alternatively by changing the trap frequency ω_0 by an external electric field [33]), i.e. a scheme which does not require changing particle number [43, 44]. Preparing a sample with d slightly above d_{cr}, rapid compression initiates a ground state transition and thus allows one to 'turn on' the inter-shell rotation of composite dipoles—excitons. Combined with optical excitation this may have interesting applications manipulating coherent emission.

In the second part of this paper, we performed a quantum many-body calculation of the same system within the frame of a SCHF approach. In the low-density limit, where the particles are well localized, classical properties are recovered. On the other hand, upon density increase and growing particle overlap quantum diffraction and exchange effects become important. This has significant consequences for the ground state phase diagram which is much richer than the classical one. There appear new structural phases which are characterized by charge localization on the outer shell coexisting with delocalization on the inner shell. Also, there exist parameter ranges where the classical and quantum systems show opposite shell configuration changes. The main advantage of the quantum many-body calculations is that they yield the complete single-particle energy spectrum and orbital-resolved ground states. We have shown that, even in the Wigner crystal phase where the density shows strong peaks, single peaks do not one-to-one correspond to single particles. On the contrary, in general, several orbitals contribute to a single density peak.

We note that the present quantum results correspond only to the simplest representation of many-body theory—the HF approximation. Thereby all pair interactions have been self-consistently included and direct and exchange terms are treated on the same footing. We have performed several comparisons with first-principle path integral Monte Carlo (PIMC) simulations where, however, the control of statistical fluctuations and the exact treatment of fermions are computationally demanding, especially for temperatures $T \to 0$. Nevertheless, the result has shown that the correct shell configurations are observed and that the HF ground state energies are in essential agreement with the PIMC simulations which fully include correlation effects. This leads us to expect that the quantum results reported in this paper will not change qualitatively when better approximations are considered. Naturally, the first improvement to be made is the inclusion of scattering effects on the level of the second Born approximation of nonequilibrium Green's functions theory, as was done e.g. in [45]–[47]. We are presently developing these calculations which will be reported elsewhere.

References

[1] Bonitz M, Ludwig P, Baumgartner H, Henning C, Filinov A, Block D, Arp O, Piel A, Käding S, Ivanov Y, Melzer A, Fehske H and Filinov V 2008 *Phys. Plasmas* **15** 055704
[2] Wineland D J, Bergquist J C, Itano W M, Bollinger J J and Manney C H 1987 *Phys. Rev. Lett.* **59** 2935
[3] Dubin D H E and Schiffer J P 1996 *Phys. Rev.* E **53** 5249
[4] Astrakharchik G E, Belousov A I and Lozovik Yu E 1999 *Phys. Lett.* A **258** 123
[5] Lai Y J and Lai I L 1999 *Phys. Rev.* E **60** 4743
[6] Kong M, Partoens B and Peeters F M 2003 *New J. Phys.* **5** 23
[7] Arp O, Block D, Piel A and Melzer A 2004 *Phys. Rev. Lett.* **93** 165004
[8] Ludwig P, Kosse S and Bonitz M 2005 *Phys. Rev.* E **71** 046403
[9] Bonitz M, Block D, Arp O, Golubnychiy V, Baumgartner H, Ludwig P, Piel A and Filinov A 2006 *Phys. Rev. Lett.* **96** 075001
[10] Henning C, Baumgartner B, Piel A, Ludwig P, Golubnychiy V, Bonitz M and Block D 2006 *Phys. Rev.* E **74** 056403
Henning C, Ludwig P, Filinov A, Piel A and Bonitz M 2007 *Phys. Rev.* E **76** 036404
[11] Kamimura T, Suga Y and Ishihara O 2007 *Phys. Plasmas* **14** 123706
[12] Bedanov V M and Peeters F M 1993 *Phys. Rev.* B **49** 2667
[13] Ashoori R C 1996 *Nature* **379** 413
[14] Filinov A, Bonitz M and Lozovik Yu E 2001 *Phys. Rev. Lett.* **86** 3851
[15] Reusch B, Häusler W and Grabert H 2001 *Phys. Rev.* B **63** 113313
[16] Kong M, Partoens B and Peeters F M 2002 *Phys. Rev.* E **65** 046602
[17] Ghosal A, Güçlü A D, Umrigar C J, Ullmo D and Baranger H U 2006 *Nat. Phys.* **2** 336
[18] Yannouleas C and Landman U 2007 *Rep. Prog. Phys.* **70** 2067
[19] De Paolo S, Rapisarda F and Senatore G 2002 *Phys. Rev. Lett.* **88** 206401
[20] Hartmann P, Donkó Z and Kalman G J 2005 *Europhys. Lett.* **72** 396
[21] Joglekar Y N, Balatsky A V and Das Sarma S 2006 *Phys. Rev.* B **74** 233302
[22] Mora C, Parcollet O and Waintal X 2007 *Phys. Rev.* B **76** 064511
[23] Astrakharchik G E, Boronat J, Kurbakov I L and Lozovik Yu E 2007 *Phys. Rev. Lett.* **98** 060405
[24] Kalman G J, Hartmann P, DonkóZ and Golden K I 2007 *Phys. Rev. Lett.* **98** 236801
[25] Belousov A I and Lozovik Yu E 2000 *Eur. Phys. J.* D **8** 251
[26] Anisimovas E and Peeters F M 2002 *Phys. Rev.* B **65** 233302
[27] Filinov A, Ludwig P, Golubnychyi V, Bonitz M and Lozovik Yu E 2003 *Phys. Status Solidi* c **0** 1518
[28] Ludwig P, Filinov A, Bonitz M and Lozovik Yu E 2003 *Contrib. Plasma Phys.* **43** 285
[29] Lozovik Yu E, Volkov Yu S and Willander M 2004 *JETP Lett.* **79** 473
[30] Kärkkäinen K, Koskinen M, Manninen M and Reimann S M 2004 *Solid State Commun.* **130** 187
[31] Timofeev V B and Gorbunov A V 2007 *J. Appl. Phys.* **101** 081708
[32] Büchler H P, Demler E, Lukin M, Micheli A, Prokof'ev N, Pupillo G and Zoller P 2007 *Phys. Rev. Lett.* **98** 060404
Micheli A, Pupillo G, Büchler H P and Zoller P 2007 *Phys. Rev.* A **76** 043604
[33] Ludwig P, Filinov A, Bonitz M and Stolz H 2006 *Phys. Status Solidi* b **243** 2363
[34] Filinov A, Peeters F M, Riva C, Lozovik Yu E and Bonitz M 2004 *Few-Body Syst.* **34** 149
[35] Filinov A, Riva C, Peeters F M, Lozovik Yu E and Bonitz M 2004 *Phys. Rev.* B **70** 035323
[36] Bracker A S, Stinaff E A, Gammon D, Ware M E, Tischler J G, Park D, Gershoni D, Filinov A, Bonitz M, Peeters F M and Riva C 2005 *Phys. Rev.* B **72** 035332
[37] Schweigert V A and Peeters F M 1995 *Phys. Rev.* B **51** 7700
[38] Elliott J P and Dawber P G 1979 *Symmetry in Physics I* (London: Macmillan)
[39] Balzer K, Nölle C, Bonitz M and Filinov A 2006 *Phys. Status Solidi* c **3** 2402
[40] Echenique P and Alonso J L 2007 *Preprint* 0705.0337v3 [physics.chem-ph]

[41] Balzer K, van Leeuwen R and Bonitz M 2008 submitted

[42] Roothaan C C J 1951 *Rev. Mod. Phys.* **20** 69
Hall G G 1951 *Proc. R. Soc. Lond.* A **205** 451

[43] Bonitz M, Golubnychiy V, Filinov A V and Lozovik Yu E 2002 *Microelectron. Eng.* **63** 141

[44] Golubnychiy V, Ludwig P, Filinov A V and Bonitz M 2004 *Superlatt. Microstruct.* **34** 219

[45] Bonitz M, Kremp D, Scott D C, Binder R, Kraeft W D and Köhler H S 1996 *J. Phys.: Condens. Matter* **8** 6057

[46] Kwong N H, Bonitz M, Binder R and Köhler S 1998 *Phys. Status Solidi* b **206** 197
Kwong N H and Bonitz M 2000 *Phys. Rev. Lett.* **84** 1768

[47] Dahlen N E and van Leeuwen R 2005 *J. Chem. Phys.* **122** 164102

5.5 Synopsis: Classical and Quantum Coulomb Crystals

Strong correlation effects in classical and quantum plasmas are discussed. In particular, Coulomb (Wigner) crystallization phenomena are reviewed focusing on one-component non-neutral plasmas in traps and on macroscopic two-component neutral plasmas. The conditions for crystal formation in terms of critical values of the coupling parameters and the distance fluctuations and the phase diagram of Coulomb crystals are discussed.

<u>*The review was published as refereed journal publication:*</u>

5.5.1 *Classical and Quantum Coulomb Crystals,*
M. Bonitz, P. Ludwig, H. Baumgartner, C. Henning, A. Filinov, D. Block,
O. Arp, A. Piel, S. Käding, Y. Ivanov, A. Melzer, H. Fehske, and V. Filinov,
Physics of Plasmas **15**, 055704 (2008)

Classical and quantum Coulomb crystals[a)]

M. Bonitz,[1,b)] P. Ludwig,[1] H. Baumgartner,[1] C. Henning,[1] A. Filinov,[1] D. Block,[2] O. Arp,[2]
A. Piel,[2] S. Käding,[3] Y. Ivanov,[3] A. Melzer,[3] H. Fehske,[3] and V. Filinov[4]

[1]*Institut für Theoretische Physik und Astrophysik, Christian-Albrechts-Universität zu Kiel,*
D-24098 Kiel, Germany
[2]*Institut für Experimentelle und Angewandte Physik, Christian-Albrechts-Universität zu Kiel,*
D-24098 Kiel, Germany
[3]*Institut für Physik, Ernst-Moritz-Arndt-Universität, D-17487 Greifswald, Germany*
[4]*Institute for High Energy Density, Russian Academy of Sciences, Izhorskaya 13/19,*
127412 Moscow, Russia

Strong correlation effects in classical and quantum plasmas are discussed. In particular, Coulomb (Wigner) crystallization phenomena are reviewed focusing on one-component non-neutral plasmas in traps and on macroscopic two-component neutral plasmas. The conditions for crystal formation in terms of critical values of the coupling parameters and the distance fluctuations and the phase diagram of Coulomb crystals are discussed. © *2008 American Institute of Physics.*
[DOI: 10.1063/1.2839297]

I. INTRODUCTION

Coulomb crystals (CCs), a periodic arrangement of charged particles, are omnipresent in nature, from astrophysical systems (interior of dwarf stars, Refs. 1 and 2) to laboratory systems (trapped ions, see, e.g., Refs. 3 and 4, plasmas in storage rings, e.g., Refs. 5 and 6, or dusty plasmas, Refs. 7–9, to name a few examples; for an overview, see Ref. 10). CCs add an interesting new species to the large family of crystals in condensed matter, chemistry or biology, for an (incomplete) list, see Table I. We will distinguish CCs from "traditional" crystals (including molecular or ion crystals or metals) by 1. the *governing role of the Coulomb interaction* (in contrast to crystals of neutral particles) and 2. by the *elementary character of the constituents* (in contrast, e.g., to the complex ions forming the lattice of a metal).[11] These two properties bring the CC into the area of plasma physics rather than condensed matter physics, because it is the strength and long range of the Coulomb interaction which dominates the many-particle behavior in these systems, the crystal symmetry, stability, and melting properties.

The research on CC originates in solid state physics. More than seven decades ago Wigner predicted, using the jellium model, that electrons in metals would form, at low density, a bcc lattice, see Ref. 12. A second line of research grew out of the field of classical strongly coupled plasmas. There it was predicted, by computer simulations, that a one-component Coulomb or Yukawa model plasma (OCP) in three and two dimensions would crystallize at sufficiently high density and/or low temperature, e.g., Ref. 10. 3D Coulomb crystals show a bcc symmetry, whereas Yukawa crystals have a bcc and a fcc phase, Ref. 13. In contrast, the ground state of 2D crystals has hexagonal symmetry. However, jellium and OCP are models assuming that the charge species forming the crystal coexists with a second neutraliz-

ing one which forms a static homogeneous background which does not influence the crystal. Such systems do not exist in nature. In real two-component plasmas, crystallization is very different. One important effect is weakening of the Coulomb interaction by dynamic screening. Moreover, the attractive force between different species will favor recombination, i.e., formation of bound states. This will, obviously, strongly reduce the Coulomb coupling and may even prevent crystal formation. Nevertheless, CC formation in a two-component plasma [item AIII. (c) in Table I] is possible and will be discussed below in Sec. VI.

But before we consider the second possibility to achieve Coulomb crystallization: One-component (non-neutral) plasmas which are stabilized by an external "trap," such as an electric potential, cf. item BII in Table I. This principle has been successfully used in experiments with ion crystals, e.g., Refs. 3 and 4 and dusty plasmas, e.g., Refs. 14–18, for an overview, see Refs. 19 and 20, and is expected to function also with electrons in semiconductor quantum dots, Ref. 21. Naturally, the existence of the trap may have a strong influence on the crystal properties. For example, a spherically symmetric trap will favor crystals forming concentric rings (in 2D) or shells (in 3D). This gives rise to interesting symmetry effects, including magic (closed shell) configurations, e.g., Refs. 22–25 familiar from atoms and nuclei and coexistence of shells and bulk behavior in larger systems, Ref. 26.

Coulomb crystals may not only consist of classical "point particles" but also of quantum particles which have a finite extension (electrons in quantum dots, ions in compact stars, etc.) which is of relevance for the properties of CC and is crucial for the phase diagram. Since the issue of quantum plasmas has come into the focus of recent research again in the context of laser plasmas[27] and astrophysics[28] we will consider the influence of quantum effects in some detail. In this paper we study some general properties of Coulomb crystals. Starting from the theoretical description, in Sec. II, we continue with two typical examples of classical and quan-

---

TABLE I. Coulomb crystals (CC) in the world of crystals (incomplete list). CC variants are A.III.b, A.III. (c), B.II. (a), and B.II. (b). 1CS (2CS) denotes one (two) component systems, OCP, the one-component plasma model containing ions plus a homogeneous static neutralizing electron background.

A. Unconfined (macroscopic) crystals	B. Confined crystals (1, 2 or 3D traps)
I. 1CS with attractive interactions Neutral particles (e.g., Lennard-Jones, Morse potentials), "normal" solids, rare gas clusters, etc.	*I. 1CS with attractive interactions* Confinement not necessary, see A I.
II. 1CS with repulsive interactions	*II. 1CS with repulsive interactions*
a. Transient "Coulomb exploding" crystals	a. Classical: Ions, dust particles
b. Charges on surfaces of finite systems (e.g., electrons on helium droplets)	b. Quantum: Electrons in quantum dots
III. 2CS	*III. Periodic confinement*
a. "Normal" crystals: ionic crystals, metals, etc.	e.g., particles in optical lattices,
b. OCP model (ion Coulomb or Yukawa crystal)	electrons in bilayers, superlattices, etc.
c. TCP crystals (electrons, nuclei, holes, positrons)	

tum crystals in traps (Secs. III and IV). This is followed by an analysis of the melting point, Sec. V, after which the special situation of CC in neutral plasmas (Sec. VI) is discussed.

II. MODEL AND PARAMETERS

The Hamiltonian of a system of particles with mass m_i and charge e_i interacting via a statically screened Coulomb (a Yukawa) potential is given by

$$\hat{H} = \sum_{i=1}^{N} \left[-\frac{\hbar^2}{2m_i}\nabla_i^2 + V(\mathbf{r}_i) + \sum_{j<i}^{N} \frac{e_i e_j}{\epsilon} \frac{e^{-\kappa r_{ij}}}{r_{ij}} \right], \quad (1)$$

where $r_{ij} = |\mathbf{r}_i - \mathbf{r}_j|$ and ϵ denotes a static background dielectric constant, which is of the order of 10 in the case of an electron-hole plasma in a semiconductor; in a plasma, $\epsilon=1$. The case of a pure Coulomb system follows in the limit of zero screening, $\kappa \to 0$. In the case of trapped systems a confinement potential $V(r)$ is included which will be assumed isotropic and parabolic, i.e., $V(r)=m\omega^2 r^2/2$. The limit of an unconfined system is achieved by letting $\omega \to 0$. In thermodynamic equilibrium the system properties are determined by the canonical probability distribution P or, in the quantum case, by the density operator $\hat{\rho}$,

$$P(E) = \frac{1}{Z}e^{-\beta E}, \quad \hat{\rho} = \frac{1}{Z}e^{-\beta \hat{H}}, \quad (2)$$

where $\beta=1/k_B T$ is the inverse temperature, and E denotes the total potential energy, i.e., the second plus third term of Eq. (1).

Despite their different form of appearance, all Coulomb (Yukawa) systems exhibit similar fundamental properties governed by the strength of the Coulomb (Yukawa) interaction which is measured by dimensionless control parameters: The coupling parameters Γ_a, r_{sa}, and λ_a of particle species a and the quantum degeneracy parameter χ_a. These parameters are determined by the ratio of characteristic energy and length scales:[29,30]

- *Length scales*: (i) $\bar{r}$, average interparticle distance, $\bar{r} \sim n^{-1/d}$ (n and $d=1,2,3$ denote the density and dimensionality of the system, respectively). (ii) Λ, quantum-mechanical extension of the particles. For free particles we have $\Lambda_a^{\text{free}}=h/\sqrt{2\pi m_a k_B T_a}$ (deBroglie wavelength), for bound particles Λ is given by the extension of the ground state wave function, $\Lambda_a^{\text{bound}}=2\pi a_B$. (iii) a_B, relevant Bohr radius $a_B=\epsilon/e_a e_b \hbar^2/m_{ab}$, where $m_{ab}^{-1}=m_a^{-1}+m_b^{-1}$. (iv) a_{Ba}, effective Bohr radius of an OCP: $a_{Ba}=\epsilon/e_a^2 \hbar^2/m_a$.

- *Energy scales*: (i) $\langle K \rangle$, mean kinetic energy, which in a classical system is given by $\langle K_a \rangle_{\text{cl}}=d/2 k_B T_a$, whereas in a highly degenerate Fermi system $\langle K_a \rangle_{qm}=3/5 E_{Fa}$ holds [$E_F=\hbar^2(3\pi^2 n)^{2/3}/2m$ denotes the Fermi energy]; (ii) $\langle U_c^{ab} \rangle$, mean Coulomb energy, given for free and bound particles by $\langle U_c^{ab} \rangle_f=e_a e_b/4\pi\epsilon \, 1/\bar{r}$ and $\langle U_c^{ab} \rangle_B=e_a e_b/4\pi\epsilon \, 1/2a_B \equiv E_R$ (Rydberg), respectively. Analogously, the mean Yukawa interaction energy is estimated by $\langle U_Y \rangle_f = e^{-\kappa\bar{r}}\langle U_c \rangle_f$.

- *Dimensionless control parameters*: The quantum *degeneracy parameter* $\chi_a \equiv n_a \Lambda_a^d \sim (\Lambda_a/\bar{r}_a)^d$ divides many-body systems into classical ($\chi<1$) and quantum mechanical ones ($\chi \geq 1$). The *Coulomb coupling parameter* is the ratio $|\langle U_c \rangle|/\langle K \rangle$. For classical systems $\Gamma_a \equiv |\langle U_c^{aa} \rangle|/k_B T_a$ results, whereas for quantum systems the role of Γ_a is taken over by the Brueckner parameter, $r_{sa} \equiv \bar{r}_a/a_{Ba} \sim |\langle U_c^{aa} \rangle|/E_{Fa}$. The relation to the parameter, $r_s=\bar{r}/a_B$, familiar from atomic units is $r_s=r_{sa}[1-m_a/m_a+m_b]$. Similarly one can introduce coupling parameters for Yukawa systems and of different species.

In a *two-component plasma* different masses and charges of the species may give rise to unequal coupling and quantum degeneracy of the species. In particular, in a dense electron-ion plasma classical ions and quantum electrons may coexist. Analogously ions may be strongly coupled while the electrons are only weakly coupled, see Sec. VI. The ratio of the degeneracy parameters scales as $\chi_a/\chi_b = (m_b/m_a)^{1/2}$, whereas the ratios of the coupling parameters
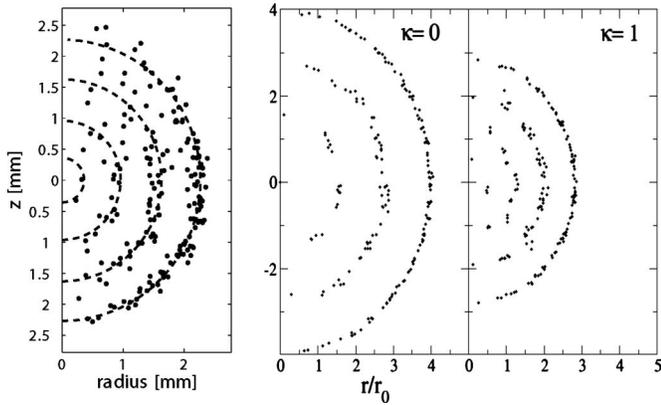
FIG. 1. Radial particle distribution for $N=190$ particles given in cylindrical coordinates. Left: Experiment. Right two figures: Simulation results with Coulomb ($\kappa=0$), and Yukawa ($\kappa=1$) potential. The length unit in the right two figures is r_{oc}, given by Eq. (4), from Ref. 24.

are given by $\Gamma_a/\Gamma_b=(e_a/e_b)^{2-1/d}$ and $r_{sa}/r_{sb}=(m_a/m_b) \times(e_a/e_b)^{2+1/d}$, where local charge neutrality, $n_a e_a=n_b e_b$, has been assumed.

III. CLASSICAL COULOMB AND YUKAWA CRYSTALS IN TRAPS

Coulomb crystallization in a spherical 3D geometry was first observed for ultracold ions in Penning or Paul traps.[3] A second candidate are ions created by ionization of cooled trapped atoms. Recent simulations[31] also show that untrapped ions, expanding due to Coulomb repulsion, might crystallize if they are properly laser cooled during the expansion. Finally, so-called "Yukawa balls" have been observed in dusty plasmas,[17,32] see Fig. 1. Their theoretical description is again based on the Hamiltonian (1) (for an overview on earlier theoretical results and simulations, see Ref. 10). This model has, in fact been shown to correctly describe the dusty plasma measurements[24,33]; 3D concentric shells where the populations N_s are sensitive to the screening strength κ. With increasing κ the reduced repulsion leads to an increased population of the inner shells. The quality of the experiments is so high that the shell populations can be measured accurately, allowing for comparisons with the simulations. In fact, very good agreement is found for $\kappa r_0 \approx 0.6$, cf. Fig. 2, which shows the relevance of screening effects in these confined dusty plasma crystals. Furthermore, screening has an important effect on the average radial density profile of these crystals. In contrast to Coulomb crystals, where the density is approximately constant, with increasing κ there is an increasingly rapid decay of the density towards the surface.[34,35]

As in the 2D case closed shell configurations and a "Mendeleyev table" exist (see, e.g., Refs. 23, 24, and 36). The dependence of the crystal stability on the number of particles can be seen from their melting temperatures. For example, the closure of the first spherical shell occurs at $N=12$, which gives rise to a particularly high crystal stability (high melting temperature), cf. Fig. 4 below.
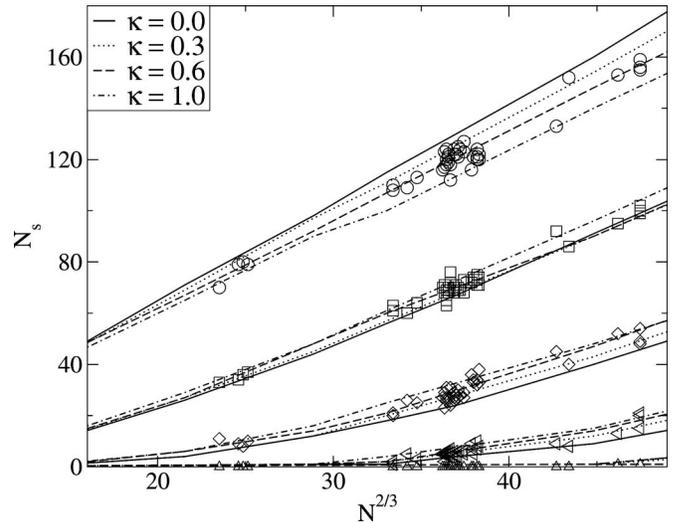

FIG. 2. Number of particles N_s on the shells of Yukawa balls with different N and κ. Table I contains experimental (last line) and theoretical shell configurations for $N=190$. $N_1 \ldots N_4$ denote the particle numbers on the ith shell beginning in the center. The figure shows the shell populations for 40 experimentally observed Yukawa balls (symbols) and molecular dynamics simulation results for several κ values (Ref. 24). κ is given in units of r_0^{-1} defined by $m\omega^2 r_0^2=e^2/r_0$, temperature is in units of $E_0=e^2/r_0$.

IV. QUANTUM COULOMB CRYSTALS IN TRAPS

When the trapped CC is cooled, eventually the deBroglie wavelength Λ will exceed the interparticle distance and quantum effects will become relevant. While for ion crystals this may require sub-micro-Kelvin temperatures this regime is easily accessible with (the much lighter) electrons in nanostructures. At the same time, there quantum crystal formation and detection is hampered by impurities and defects. Therefore, the results shown below are obtained by means of computer simulations. The density operator (2) with the 2D Hamiltonian (1) is evaluated by performing first-principle path integral Monte Carlo (PIMC) simulations; for details, see Refs. 37 and 38. Results for the probability density of 19 electrons in a 2D harmonic trap are shown in Fig. 3. We observe a shell structure similar as in the classical case. However, the particles are now not pointlike but have a finite extension and an elliptic shape which minimizes the total energy. When the system is compressed by increasing ω, the wave functions of the electrons start to overlap—first within each shell, cf. central part of Fig. 3, and finally also particles on different shells overlap giving rise to a quantum liquid
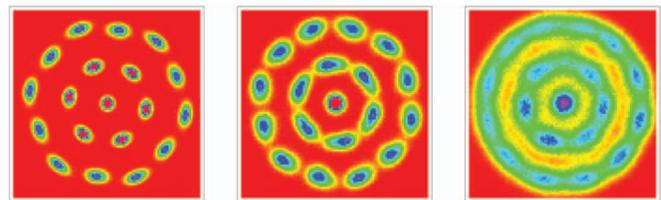

FIG. 3. (Color) 19-electron quantum Wigner "crystal" (left), radially ordered crystal (center), and mesoscopic fermionic liquid (right). From left to right quantum melting at constant temperature occurs. Dots correspond to the probability density ρ of the electrons in the 2D plane which varies between ρ_{max} (pink) and zero (red).

state. This process of *quantum melting* occurs even at zero temperature, giving rise to an interesting phase diagram of quantum CC,[21] see also Sec. V.

V. CONDITIONS FOR CRYSTAL FORMATION

Phase coexistence is determined by the equality of the thermodynamic potentials (such as the free energy) in the two phases which often requires very accurate and expensive calculations. In macroscopic plasmas there exist many alternative criteria for crystallization: Peaks of the specific heat, sufficiently strong modulations of the pair distribution or the static structure factor, and so on. These quantities yield practically the same melting point, for an analysis see, e.g., Ref. 39. In contrast, in trapped systems, in particular, when the particle number is reduced, the results for the phase boundaries may strongly depend upon the chosen quantity and the way it is computed. It turns out that, for the class of systems described by Eq. (1), two quantities are particularly useful to localize the melting point: Critical values of the coupling parameter and of the distance fluctuations of the particles around their equilibrium positions. We mention that, for very small systems, recently a more appropriate quantity has been proposed: the variance of the block-averaged interparticle distance fluctuations, see Ref. 40.

A. Critical values of the coupling parameter

Let us start with the simplest case of Eq. (1): A *macroscopic classical plasma* ($\omega=0$) containing a single charge component. We can rewrite the ratio of energy and temperature which determines the thermodynamic properties, cf. Eq. (2), as

$$\beta E = f(\Gamma,\kappa) = \Gamma \sum_{1\leq j<i}^{N} \frac{e^{-\bar{\kappa}\bar{r}_{ij}}}{\bar{r}_{ij}} \quad \text{with} \quad \bar{r}_{ij} = \frac{r_{ij}}{\bar{r}}, \quad \bar{\kappa}=\kappa\bar{r}. \tag{3}$$

For Coulomb systems ($\kappa=0$) βE is characterized by a single parameter, the coupling parameter Γ, i.e., different Coulomb systems (containing different types of particles, having different temperature or density) are expected to show the same behavior if they have the same values of Γ. In particular, as was revealed by simulations, CC occurs at $\Gamma_{cr}\simeq175$ in 3D and $\Gamma_{cr}\simeq137$ in 2D. In a Yukawa OCP ($\kappa>0$) the effect of screening suggests introducing $\Gamma_Y(\kappa)\rightarrow\Gamma e^{-\bar{\kappa}\bar{r}}$, however, this does not correctly reproduce the κ-dependence of the melting curve. The reason is that melting is not determined by the absolute value of the energy but by the energy contribution of particle fluctuations around their ground state positions r_{i0}. Expanding Eq. (3) around r_{i0}, defining $\xi_{ij}=\bar{r}_{ij}-\bar{r}_{ij0}$, and taking into account that the first derivatives vanish we obtain $\beta\Delta E=\beta(E-E_0-E_{com})=\Gamma\sum_{j<i}^{N}\xi_{ij}^2/\bar{r}_{ij0}^3(1+\bar{\kappa}\bar{r}_{ij0}+\bar{\kappa}^2\bar{r}_{ij0}^2/2)e^{-\bar{\kappa}\bar{r}_{ij0}}+\cdots$. The dots denote terms with mixed derivatives and higher order terms, and E_0 and E_{com} are the energy in the ground state and of center of mass excitations (which are not relevant for the melting), respectively.

For the case of two particles, this expression can be written in a Coulomb-type form, $\beta\bar{r}_0^3\Delta E=\Gamma_Y(\kappa)\xi^2$, with the Yukawa coupling parameter $\Gamma_Y(\kappa)=\Gamma e^{-\bar{\kappa}\bar{r}}[1+\kappa\bar{r}+(\kappa\bar{r})^2/2]$.

Assuming that, at the melting point, the critical coupling parameter is universal (3D case), $\Gamma_{Ycr}=175$, the phase boundary of the (bcc) crystal in the Γ-κ plane is approximated by $\Gamma_{cr}(\kappa)=175\cdot e^{\kappa\bar{r}}[1+\kappa\bar{r}+(\kappa\bar{r})^2/2]^{-1}$. Interestingly, simulations have shown that this result holds reasonably well not just for small particle numbers but also in a macroscopic system.[41]

Consider now a *classical crystal in a trap*. Here the density is externally controlled by the trap frequency ω which determines the mean interparticle distance. The basic properties are best illustrated for two particles. The ground state is obtained from the minimum of the relative potential energy Eq. (1) with the result

$$\frac{e^{\kappa r_0}r_0^3}{1+\kappa r_0} = \frac{e^2}{\frac{m}{2}\omega^2} \equiv r_{0c}^3. \tag{4}$$

Equation (4) yields the two-particle distance, $r_0(\kappa)$, as a function of the distance in an unscreened system, r_{0c}.[24] In analogy to the macroscopic case we introduce a Coulomb coupling parameter, $\Gamma_2\equiv e^2/(k_BTr_0)$. The corresponding coupling parameter for Yukawa interaction, Γ_{2Y}, again follows from expansion of the energy around the ground state, $\beta r_0^3\Delta E=\Gamma_{2Y}(\kappa)\xi^2$ with the result[24] $\Gamma_{2Y}=\Gamma_2 e^{-\kappa r_0}(1+\kappa r_0+\kappa^2 r_0^2/3)$ slightly differing from the above expression. In a similar way, the ground state and effective coupling parameter can be defined for any particle number, but this has to be done numerically.[23,42] The results are strongly N-dependent due to the importance of shell filling and finite size effects. This leads to strong variations of the crystal stability with N as can be seen in the melting temperatures, left part of Fig. 4; see, e.g., Refs. 43 and 44.

Consider now a *macroscopic quantum OCP*. We rewrite the Hamiltonian (1) in dimensionless units

$$\beta\frac{\hat{H}}{2E_R} = g(r_s,T,\kappa) = -\frac{\beta}{r_s^2}\sum_i \nabla_{\bar{r}_i}^2 + \frac{\beta}{r_s}\sum_{1\leq j<i}^{N}\frac{e^{-\bar{\kappa}\bar{r}_{ij}}}{\bar{r}_{ij}}, \tag{5}$$

which depends on the quantum coupling parameter r_s and temperature separately, leading to a more complex behavior than in a classical OCP where only one parameter Γ exists. The existence of three energy scales, quantum kinetic energy (first term), interaction energy (second), and thermal energy has a direct consequence for the phase boundary $T_{cr}(n)$ of Coulomb crystals, cf. Fig. 4. While for a classical crystal, the slope of the boundary is always positive, $dT_{cr}(n)/dn>0$, given by a constant value of Γ, for quantum crystals, there exists a maximum value of the temperature, T_{cr}^{max}, where the slope changes sign. For densities to the left of the maximum the phase boundary is dominated by "normal," i.e., thermal melting, whereas for densities exceeding the value of the maximum, by a competition of quantum kinetic and interaction energy. For sufficiently large densities (with decreasing r_s) quantum melting is observed, even at zero temperature, cf. Fig. 4. The corresponding critical values of the Brueckner parameter of a Coulomb OCP at $T=0$ are $r_s^{cr}\approx100(160)$ in 3D and $r_s^{cr}\approx37$ in 2D for fermions (bosons),[21,45] and references therein. These values are still under investigation. Also, generalization of the results to a quantum Yukawa OCP
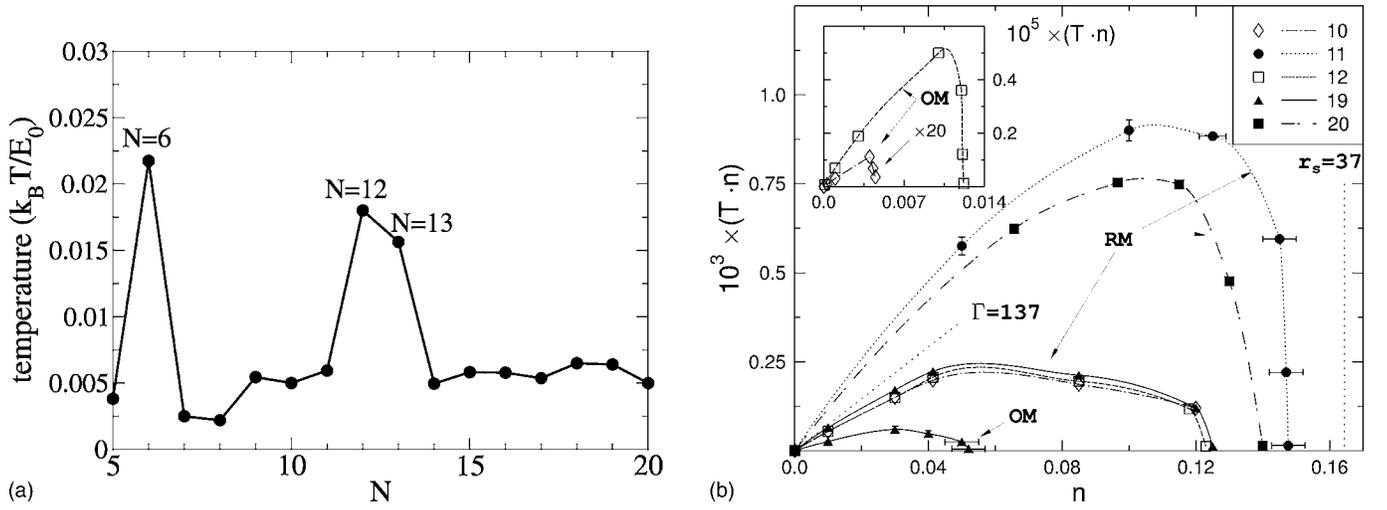
FIG. 4. Left: Melting temperature of small 3D spherical Yukawa crystals vs particle number. Right: Phase diagram of the mesoscopic 2D Wigner crystal for different particle numbers N. OM (RM) denotes the boundary of orientational (radial) melting. Here the dimensionless density n and temperature T are defined as $n = \sqrt{2}l_0^2/r_0^2 = (a_B/r_0)^{1/2} \approx r_s^{-1/2}$ and $T = k_B T/E_0$, where $l_0^2 = \hbar/(m\omega_0)$, $E_0 = e^2/\epsilon_b r_0$ with r_0 given by $e^2/\epsilon_b r_0 = m\omega^2 r_0^2/2$, from Refs. 21 and 43.

has only recently been attempted; see Ref. 46, and references therein.

Finite trapped quantum plasmas show the same general behavior as a macroscopic quantum OCP and, in addition, finite size effects as in case of the classical crystals in traps. As a consequence, the crystal phase boundary is strongly *N*-dependent, as can be seen for the 2D case in Fig. 4. Further, in 2D the competition of hexagonal (bulk) symmetry and spherical symmetry induced by the trap leads to possible additional phases, both in classical and quantum trapped plasmas. The most prominent one is a partially ordered phase where particle ordering occurs within each shell, but no order of different shells with respect to each other exists. Only at significantly larger values of the coupling parameter the orientational fluctuations freeze out [orientational freezing or melting (OM)] and the crystal enters the fully ordered phase, cf. Fig. 4. The location of this phase boundary is strongly dependent on the crystal symmetry and may vary with *N* by many orders of magnitude.[21,22] In 3D trapped plasmas no radially melted phase is observed because there is generally a much larger energy barrier for intershell rotations.

B. Critical values of the distance fluctuations

The appearance of different coupling parameters in the case of classical and quantum plasmas makes it very difficult to construct a joint phase diagram of Coulomb crystals. An alternative approach to the crystal phase boundary uses, as the starting point, the magnitude of the relative interparticle distance fluctuations of the particles around their lattice positions. Expanding, as in Sec. V A, the total energy fluctuations ΔE in a Taylor series up to second order and diagonalizing the result allows us to express ΔE as a superposition of $d \cdot (N-2)$ relative normal modes. For this system of independent 1D quantum harmonic oscillators with the phonon modes $\omega_\lambda(q)$ of polarization λ all thermodynamic properties

at a given temperature T are known. For example, the thermodynamic average of the distance fluctuations $\langle \delta x^2 \rangle = \langle x^2 \rangle - \langle x \rangle^2$ is given by[2]

$$\langle \delta x^2 \rangle = \frac{1}{2} \sum_q \sum_{\lambda=1}^{d} \frac{\hbar}{m\omega_\lambda(q)} f_\lambda(q,T),$$

(6)

with $f_\lambda(q,T) = \coth \dfrac{\hbar \omega_\lambda(q)}{2k_B T}$.

For a macroscopic classical OCP, $f_\lambda(q,T) \to 2k_B T/\hbar \omega_\lambda(q)$, and the average over the phonon spectrum yields, in case of a bcc crystal, $\langle \delta x^2 \rangle = 12.973 \bar{r}^2/\Gamma$. The result for the relative distance fluctuations $u_{\mathrm{rel}} \equiv \sqrt{\langle \delta x^2 \rangle/r_0^2}$ normalized to the nearest neighbor distance, $r_0 = (3\pi^2)^{1/6}\bar{r}$, is

$$u_{\mathrm{rel}}^{cl} = \sqrt{\frac{12.973}{(3\pi^2)^{1/6}} \frac{1}{\Gamma}} \to 0.155,$$

(7)

where the last number is the critical value obtained by using $\Gamma = 175$.

Analogously, we obtain for a quantum OCP bcc crystal at zero temperature, where $f_\lambda(q,T) \to 1$,

$$\langle \delta x^2 \rangle = \frac{3^{1/2}}{2} u_{-1} r_{sa}^{3/2} a_{Ba}^2,$$

(8)

with $u_{-1} \equiv \langle \omega_{pa}/\omega_\lambda \rangle$ denoting the moment of order minus one of the phonon spectrum which equals 2.7986 for a bcc crystal.[47] This yields for the relative distance fluctuations

$$u_{\mathrm{rel}}^{q} = \sqrt{\frac{0.783}{r_s^{1/2}}} \to 0.28(0.249),$$

(9)

where the last number is the critical value for fermions (bosons), using $r_s^{\mathrm{cr}} = 100\ (160)$. Note that these fluctuations are mainly due to quantum diffraction effects, i.e., the finite extension of the particle wave functions. Spin effects (quantum exchange) play a minor role for the location of the crys-

tal phase boundary which is clear since, in the crystal state, the wave function overlap has to be small. Nevertheless, the physical properties of crystals of bosons may be essentially different from those of fermions. The reason is that interacting bosons may show superfluid behavior which may even persist in the crystal phase. This state is called a *supersolid* and was predicted 30 years ago[48–50] and was recently observed in PIMC simulations of trapped bosonic plasma crystals.[51]

Equations (7) and (9) are very useful as they establish the relation between relative distance fluctuations and the relevant coupling parameter in the two limiting cases of classical and quantum plasmas. To connect the two limits along the whole phase boundary, cf. Fig. 4, one has to use the full phonon spectrum, Eq. (6), without expansion of the function f_λ. The temperature and density dependence of u_{rel} remains an open question although some interpolations have been attempted, see e.g., Ref. 2. Further improvements, in particular, in the quantum regime, may require to include anharmonic corrections, e.g., Ref. 52, since their finite extension lets the particles explore ranges of the potential energy which cannot be approximated by a parabola, e.g., Ref. 46.

VI. UNCONFINED TWO-COMPONENT COULOMB CRYSTALS

As discussed in the Introduction, crystal formation in two-component plasmas (TCP) competes with bound state formation. One may, therefore, ask whether there exist parameters where CC exist and, at the same time, Coulomb bound states are ionized. In comparison to an OCP, in a TCP, we have at our disposal two additional parameters to realize these two conditions: The mass ratio $M = m_h/m_e$ and charge ratio $Z = e_h/e_e$ (in a nonequilibrium mass-asymmetric plasma there is further the possibility of different temperatures of the components[53]). The first requirement is obvious: The heavy component (ions or holes) has to be sufficiently strongly correlated such that it can form an OCP Wigner crystal. The second condition is that electrons have sufficiently high kinetic energy to escape the ionic binding potential. For classical electrons this requires a sufficiently high temperature whereas in a quantum plasma ionization is possible when electron wave functions of neighboring atoms start to overlap; this leads to tunnel ionization (Mott effect) which occurs at a sufficiently high density. In summary, we find two alternative sets of conditions,

$$\Gamma_i \geq \Gamma^{\text{cr}} \quad \text{and} \quad \frac{d}{2} k_B T_e > E_R, \quad \text{classical case}, \quad (10)$$

$$r_{si} \geq r_s^{\text{cr}} \quad \text{and} \quad r_{se} < r_{se}^{\text{Mott}}, \quad \text{quantum case}, \quad (11)$$

where in 3D $r_{se}^{\text{Mott}} \approx 1.2$. The phase boundary of the Coulomb crystal of the heavy particles can be obtained using the harmonic lattice theory results of Sec. V B. For the quantum case, we may use, for $\langle \delta x_h^2 \rangle$, Eq. (8) and express the nearest-neighbor distance of the heavy particles, r_{0h}, by that of the electrons,
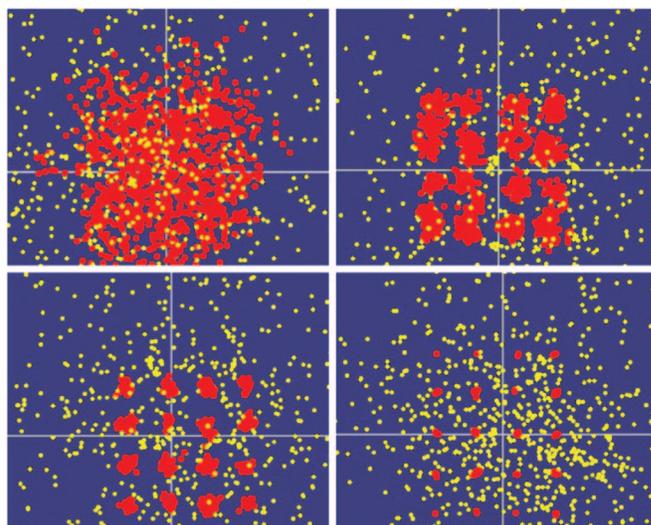

FIG. 5. (Color) Snapshots of a Coulomb crystal of heavy particles (red clouds) embedded into a Fermi gas of electrons (yellow) in a macroscopic two-component (neutral) plasma (spin averaged results) for mass ratio $M = 12$ (top left), $M = 50$ (top right), $M = 100$ (bottom left), and $M = 400$ (bottom right). The density corresponds to $r_{se} = 0.64$; the temperature is $T_e = T_h = 0.06 E_R$. First-principle two-component PIMC simulations.

$$u_{\text{rel},h}^2 = \frac{\langle \delta x_h^2 \rangle}{r_{0h}^2} = \frac{3^{1/2} u_{-1}}{2\alpha^2} \frac{r_{sh}^{3/2}}{Z^{2/3} r_{se}^2} \frac{a_{Bh}^2}{a_B^2}, \quad (12)$$

where $\alpha_{\text{bcc}} = (3\pi^2)^{1/3}$. Assuming that, at the phase boundary, the critical value of the fluctuations is given by the OCP result, Eq. (9), and $r_{se} = r_{se}^{\text{Mott}}$ we readily obtain the existence conditions of a CC of fermionic (bosonic) ions in a two-component plasma, $M^{\text{cr}} Z^{4/3} = 83.3$ (132.8). This agrees with the result of Ref. 53 where it was obtained from a different derivation. Thus crystallization requires a minimum mass ratio M between heavy and light particles. This condition is fulfilled for compact dwarf stars where a crystal of carbon and oxygen nuclei (fully ionized atoms) is expected to exist.[1,2] Further candidates are crystals of protons which was recently confirmed by PIMC simulations, cf. Refs. 46 and 54, or α-particles, see Ref. 53. Both systems might be accessible in laboratory experiments in the near future. Another area where such two-component CC should be observable are electron-hole plasmas in intermediate valence semiconductors, see Refs. 53 and 55 where one could also verify the critical value of M experimentally, although values of M as large 80 exists only in some special materials. Another promising candidate are charge asymmetric bilayers where hole crystallization is expected to occur already for $M \lesssim 10$,[56] which is due to the 2D confinement of the particles.

The analytical predictions of heavy particle crystallization in a TCP have been verified by PIMC simulations where both electrons and heavy particles have been treated fully quantum mechanically.[53,55,57] As can be seen in Fig. 5, with increasing M, indeed hole localization becomes more pronounced and, between $M = 50$ and $M = 100$, a transition to crystal-like behavior is observed. A quantitative analysis based on the relative distance fluctuations of the heavy particles, left part of Fig. 6, confirms that the liquid-solid transition takes place around $M \sim 80$. This is a novel kind of
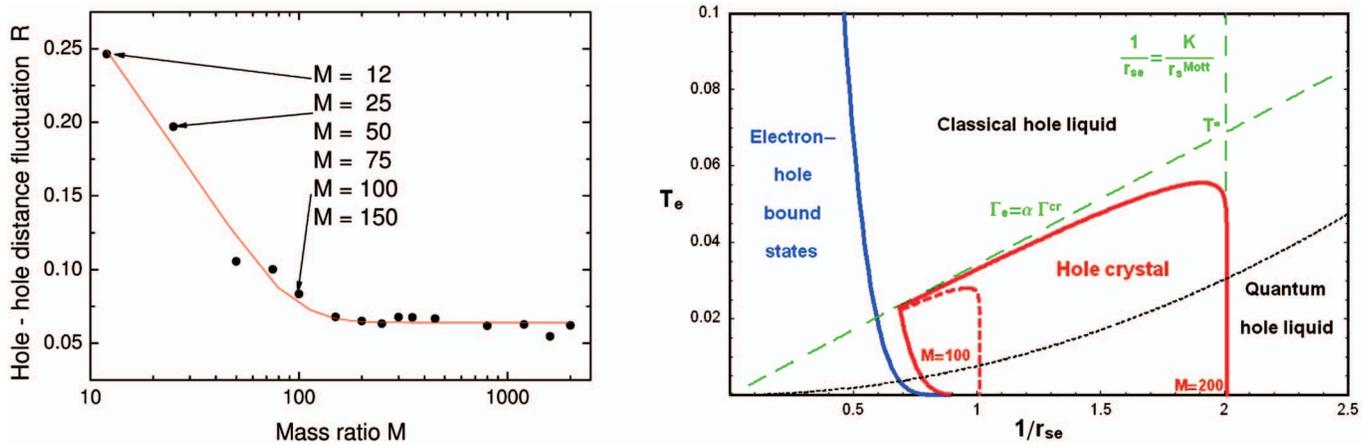
FIG. 6. (Color) Left: Mean-square relative heavy particle distance fluctuations vs mass ratio M for $T_e = 0.096$ and $r_{se} = 0.63$. Symbols are simulation results; the line is the best fit (Ref. 55). [Reprinted with permission from Bonitz et al., J. Phys. A **39**, 4717 (2006). Copyright (2006) by IOP Publishing Ltd.] Right: Qualitative phase diagram of a Coulomb crystal of heavy particles ("holes") in a macroscopic two-component (neutral) plasma. $T_e = [(3/2)k_B T]/E_R$ and $K = (M+1)/(M^{cr}+1)$. [Reprinted with permission from Bonitz et al., Phys. Rev. Lett. **95**, 235006 (2005). Copyright (2005) by the American Physical Society.]

quantum phase transition, where melting occurs at constant temperature and density, by "changing" the heavy particle mass. The phase diagram of the two-component CC is sketched in Fig. 6 for the two values $M = 100$ and $M = 200$. The larger M the more extended is the crystal phase in the density-temperature plane. The crystal phase is bounded from above by the (green dashed) line $\Gamma_h = \Gamma_{cr}$ and from the right (high densities) by the (vertical green dashed) line $r_{sh} = r_s^{cr}$. This is the simplest approximation where the influence of the electrons on the heavy particle interaction has been neglected. Improvements require the inclusion of screening effects,[46] as discussed above, this leads to a destabilization of the crystal. At the same time, the heavy particle crystal also influences the spatial distribution of the electrons which stabilizes the crystal compared to the OCP case. Thus, there exists two competing effects for the crystal stability. A detailed comparison of the crystal phase diagram in an OCP and a TCP, therefore, still remains an interesting open question. Finally, it has been predicted by Abrikosov[58] that, in the presence of a hole crystal, the electrons should tend to form Cooper pairs, i.e., exhibit superconductivity which yet remains to be verified experimentally.

VII. CONCLUSIONS

In this paper we have given an overview on strong correlation effects in classical and quantum plasmas, in particular on Coulomb (Wigner) crystallization. We have discussed the possible occurrences of Coulomb crystals, first, in trapped one-component plasmas and, second, in two-component neutral plasmas. The conditions for crystal formation have been summarized in terms of known critical values for the coupling parameters as well as in terms of critical values of the relative interparticle distance fluctuations. Using the data for the critical parameters it is possible to construct the phase diagram of strongly coupled Coulomb matter which was discussed for two cases: Mesoscopic classical and quantum plasmas in a parabolic 2D trap and two-component mass-asymmetric plasmas.

[1]For details, see, e.g., L. Segretain, Astron. Astrophys. **310**, 485 (1996).
[2]G. Chabrier, Astrophys. J. **414**, 695 (1993).
[3]D. J. Wineland, J. C. Bergquist, W. M. Itano, J. J. Bollinger, and C. H. Manney, Phys. Rev. Lett. **59**, 2935 (1987).
[4]M. Drewsen, C. Brodersen, L. Hornekær, J. S. Hangst, and J. P. Schiffer, Phys. Rev. Lett. **81**, 2878 (1998).
[5]T. Schätz, U. Schramm, and D. Habs, Nature (London) **412**, 717 (2001).
[6]U. Schramm, T. Schätz, and D. Habs, Phys. Rev. Lett. **87**, 184801 (2001).
[7]J. H. Chu and I. Lin, Phys. Rev. Lett. **72**, 4009 (1994).
[8]H. Thomas, G. E. Morfill, V. Demmel, J. Goree, B. Feuerbacher, and D. Möhlmann, Phys. Rev. Lett. **73**, 652 (1994).
[9]Y. Hayashi and K. Tachibana, Jpn. J. Appl. Phys., Part 1 **33**, L804 (1994).
[10]D. H. E. Dubin and T. M. O'Neill, Rev. Mod. Phys. **71**, 87 (1999).
[11]In trapped one-component CC such as ion or dust crystals the second restriction does not apply, but these systems are clearly separated from the traditional crystals by the external confinement.
[12]E. Wigner, Phys. Rev. **46**, 1002 (1934).
[13]S. Hamaguchi, R. T. Farouki, and D. H. E. Dubin, Phys. Rev. E **56**, 4671 (1997).
[14]A. Melzer, T. Trottenberg, and A. Piel, Phys. Lett. A **191**, 301 (1994).
[15]J. B. Pieper, J. Goree, and R. A. Quinn, Phys. Rev. E **54**, 5636 (1996).
[16]Y. Hayashi, Phys. Rev. Lett. **83**, 4764 (1999).
[17]O. Arp, D. Block, A. Piel, and A. Melzer, Phys. Rev. Lett. **93**, 165004 (2004).
[18]T. Antonova, B. M. Annaratone, D. D. Goldbeck, V. Yaroshenko, H. M. Thomas, and G. E. Morfill, Phys. Rev. Lett. **96**, 115001 (2006).
[19]A. Piel and A. Melzer, Plasma Phys. Controlled Fusion **44**, R1 (2002).
[20]V. E. Fortov, A. V. Ivlev, S. A. Khrapak, A. G. Khrapak, and G. E. Morfill, Phys. Rep. **421**, 1 (2005).
[21]A. V. Filinov, M. Bonitz, and Yu. E. Lozovik, Phys. Rev. Lett. **86**, 3851 (2001).
[22]V. M. Bedanov and F. M. Peeters, Phys. Rev. B **49**, 2667 (1994).
[23]P. Ludwig, S. Kosse, and M. Bonitz, Phys. Rev. E **71**, 046403 (2005).
[24]M. Bonitz, D. Block, O. Arp, V. Golubnychiy, H. Baumgartner, P. Ludwig, A. Piel, and A. Filinov, Phys. Rev. Lett. **96**, 075001 (2006).
[25]H. Totsuji, C. Totsuji, T. Ogawa, and K. Tsuruta, Phys. Rev. E **71**, 045401 (2005).
[26]J. P. Schiffer, Phys. Rev. Lett. **88**, 205003 (2002).
[27]D. Kremp, Th. Bornath, M. Bonitz, and M. Schlanges, Phys. Rev. E **60**, 4725 (1999).

[28] For a recent overview, see M. Marklund and P. K. Shukla, Rev. Mod. Phys. **78**, 591 (2006).

[29] M. Bonitz, *Quantum Kinetic Theory* (Teubner, Stuttgart/Leipzig, 1998).

[30] M. Bonitz, D. Semkat, A. Filinov, V. Golubnychyi, D. Kremp, D. O. Gericke, M. S. Murillo, V. Filinov, V. E. Fortov, W. Hoyer, and S. W. Koch, J. Phys. A **36**, 5921 (2003).

[31] T. Pohl, T. Pattard, and J. M. Rost, Phys. Rev. Lett. **92**, 155003 (2004).

[32] For a recent overview, see D. Block, M. Kroll, O. Arp, A. Piel S. Käding, Y. Ivanov, A. Melzer, C. Henning, H. Baumgartner, P. Ludwig, and M. Bonitz, Plasma Phys. Controlled Fusion **49**, B109 (2007).

[33] H. Baumgartner, H. Kählert, V. Golubnychiy, C. Henning, S. Käding, A. Melzer, and M. Bonitz, Contrib. Plasma Phys. **47**, 281 (2007).

[34] C. Henning, H. Baumgartner, A. Piel, P. Ludwig, V. Golubnychiy, M. Bonitz, and D. Block, Phys. Rev. E **74**, 056403 (2006).

[35] C. Henning, P. Ludwig, A. Filinov, A. Piel, and M. Bonitz, Phys. Rev. E **76**, 036404 (2007).

[36] K. Tsuruta and S. Ichimaru, Phys. Rev. A **48**, 1339 (1993).

[37] A. Filinov and M. Bonitz, in *Introduction to Computational Methods for Many-Body Physics*, edited by M. Bonitz and D. Semkat (Rinton, Princeton, 2006).

[38] V. S. Filinov, M. Bonitz, W. Ebeling, and V. E. Fortov, Plasma Phys. Controlled Fusion **43**, 743 (2001).

[39] P. Hartmann, Z. Donko, P. M. Bakshi, G. Kalman, and S. Kyrokos, IEEE Trans. Plasma Sci. **35**, 332 (2007).

[40] J. Böning, H. Baumgartner, P. Ludwig, A. Filinov, M. Bonitz, and Yu. E. Lozovik, "Melting of trapped few particle systems," Phys. Rev. Lett. (to be published).

[41] V. E. Fortov, O. S. Vaulina, O. F. Petrov, V. I. Molotkov, A. M. Lipaev, V. M. Torchinsky, H. M. Thomas, G. E. Morfill, S. A. Khrapak, Yu. P. Se-menov, A. I. Ivanov, S. K. Krikalev, A. Yu. Kalery, S. V. Zaletin, and Yu. P. Gidzenko, Phys. Rev. Lett. **90**, 245005 (2003).

[42] O. Arp, D. Block, M. Bonitz, H. Fehske, V. Golubnychiy, S. Kosse, P. Ludwig, A. Melzer, and A. Piel, J. Phys.: Conf. Ser. **11**, 234 (2005).

[43] V. Golubnychiy, H. Baumgartner, M. Bonitz, A. Filinov, and H. Fehske, J. Phys. A **39**, 4527 (2006).

[44] S. W. S. Apolinario and F. M. Peeters, Phys. Rev. E **76**, 031107 (2007).

[45] D. M. Ceperley and B. J. Alder, Phys. Rev. Lett. **45**, 566 (1980).

[46] B. Militzer and R. L. Graham, J. Phys. Chem. Solids **67**, 2136 (2006).

[47] D. A. Baiko, D. G. Yakovlev, H. E. De Witt, and W. L. Slattery, Phys. Rev. E **61**, 1912 (2000).

[48] G. V. Chester and L. Reatto, Phys. Rev. **155**, 88 (1967).

[49] A. F. Andreev and I. M. Lifshitz, Sov. Phys. JETP **29**, 1107 (1969).

[50] A. J. Leggett, Phys. Rev. Lett. **25**, 1543 (1970).

[51] A. Filinov, J. Böning, M. Bonitz, and Yu. E. Lozovik, "Supersolid artificial atoms," Phys. Rev. Lett. (submitted).

[52] D. H. E. Dubin, Phys. Rev. A **42**, 4972 (1990).

[53] M. Bonitz, V. S. Filinov, V. E. Fortov, P. R. Levashov, and H. Fehske, Phys. Rev. Lett. **95**, 235006 (2005).

[54] V. S. Filinov, M. Bonitz, and V. E. Fortov, JETP Lett. **72**, 245 (2000) [Pis'ma Zh. Eksp. Teor. Fiz. **72**, 361 (2000)].

[55] M. Bonitz, V. S. Filinov, V. E. Fortov, P. R. Levashov, and H. Fehske, J. Phys. A **39**, 4717 (2006).

[56] P. Ludwig, A. Filinov, Yu. Lozovik, H. Stolz, and M. Bonitz, Contrib. Plasma Phys. **47**, 335 (2007).

[57] V. Filinov, H. Fehske, M. Bonitz, V. E. Fortov, and P. R. Levashov, Phys. Rev. E **75**, 036401 (2007).

[58] A. A. Abrikosov, J. Less-Common Met. **62**, 451 (1978).

6 Summary and Discussion

The main focus of the present thesis has been devoted to the understanding of self-organized structure formation of charged particles in traps as one of the most exciting cooperative phenomena in many-body systems. In particular, the collective behavior of confined few-particle systems is strongly governed by symmetry and surface effects as well as the precise number of particles involved. A small ensemble of charged particles in an isotropic trapping potential tends to form concentric shells. These "artificial atoms" have unique features absent in real atoms: by controlling the confinement strength they can be transformed from a weakly coupled state to a strongly coupled, crystal-like phase. The aim of this thesis was to study the conditions and the principles of structure formation in confined few-particles systems, namely three-dimensional spherical dusty plasma crystals and low-temperature electron-hole systems in quasi two-dimensional semiconductor structures. In order to achieve a deeper understanding of structural transitions under the influence of strong Coulomb interaction and, particularly, quantum statistical and finite temperature effects, the author performed detailed numerical simulations by means of molecular dynamics, classical and quantum Monte Carlo methods. The main results of the thesis at hand can be summarized into the following five subtopics.

Ground states of Coulomb crystals. The first part of chapter 3 deals with the theoretical exploration of the structural ground state properties of spherically confined Coulomb systems in the strong coupling regime. The classical periodic table of harmonically confined *2D Coulomb systems* is well-known by the work of [25, 26, 34, 36, 45, 46, 47] and others and has been proven to be a valuable reference for experiments, e.g. [1, 6, 8]. On the contrary, the ground states of spherical *3D Coulomb systems* have not been systematically studied yet or the data have been erroneous. Within the present thesis a detailed study of the classical ground states of 3D spherical Coulomb clusters in the range $N \leq 160$ was performed by extensive MD simulations with high accuracy. By means of a topological 3D Voronoi analysis of the relative particle arrangement on the

shell surfaces, "fine structure" states in the energy spectrum could be identified. This topological feature is restricted to 3D clusters and not present in 2D systems.

The presented results are currently of strong interest, as 3D Coulomb crystals have been recently generated in different physical systems, namely one-component ion plasmas [9, 27], and dusty plasmas [15, 90]. The ground state data are also expected to be important for quantum 3D Coulomb clusters which may exist, e.g., in semiconductor quantum dots in the strong coupling limit. It can be noted that recent work of other theoretical research groups confirms the correctness of the presented data [42, 107, 108, 109].

Coulomb screening effects.   In the second part of chapter 3 the author addresses the question regarding the effect of Debye screening in view of the structural properties of spherical plasma crystals ("Yukawa balls" [162]). Within the model of an isotropic, statically-screened Coulomb interaction between the dust grains and a spherical external parabolic confinement (which is independent of screening), excellent agreement with dusty plasma experiments [15] was achieved without any free parameters in the simulations. The most remarkable finding of the MD simulations is the high sensitivity of the shell occupation numbers to the precise value of the inverse Debye screening length κ.

The validity of the theoretical model, and in particular, the effect of the Coulomb screening on the cluster configuration was demonstrated on the representative example of the $N = 190$ cluster (which was measured first [15]). While the number of shell stays constantly four, the inner (outer) shells become gradually higher (lower) populated when the screening parameter κ is increased. Therefore, the MD simulations allowed to determine the Coulomb screening parameter $\kappa_{exp} \approx 0.6$ from the experimentally measured shell configurations. The value agrees well with independent estimations based on experimental parameters [111]. Thus the structural behavior gives rise to a novel non-invasive diagnostic to determine the Debye screening length on the basis of the observed shell occupation numbers measured in experiments. It should be noted that an alternative theoretical model by H. Totsuju et al. [113] suggests approximately screening-independent shell populations (which do not coincide with the experimental findings [15, 32]).

The high sensitivity of the shell occupation numbers to the range of the interaction potential raised the question of the generic ground state particle distribution of a confined Yukawa plasma. The author investigates this issue in the first part of chapter 4 by considering the limit of large particle numbers within the model of discrete charges. While the radial density profile of a harmonically confined (unscreened) Coulomb system

is known to be constant, the numerical results reveal that a screened pair interaction changes the charge distribution drastically. Approaching large clusters of $N = 10^3 \ldots 10^4$ charged particles, a finite screening parameter κ (i.e. a transition from a pure Coulomb to a Yukawa system) is found to induce a strong inhomogeneity in the shell-averaged radial density profile with a strictly monotonic density increase towards the trap center to establish a (local) force equilibrium. This essential Coulomb screening effect has been neglected in previous investigations of trapped Yukawa systems [114]. Moreover, the screening-induced radial density gradient explains the configurational rearrangement of Yukawa crystals when κ is changed by the plasma environment. The results are also found to be of direct importance for the understanding of systematic structural transitions in electron-hole bilayer systems. Here, a transition from a long-range Coulomb to a short-range dipole interaction is induced by a decrease of the layer separation d.

Melting of classical and quantum few-particle systems. A key issue concerning few-particle systems is the reliable and consistent quantification of melting transitions, which emerge as a gradual process in finite clusters [2, 20, 21]. Due to the lack of a general theory of melting and freezing in finite-size systems, empirical rules are frequently employed [19, 117]. A well-established criterion (often referred to as "Lindemann criterion") for defining phase transitions in finite systems is based on changes of the *relative Interparticle Distance Fluctuations* (IDF) u_{rel}. In analogy to macroscopic systems, this criterion rests upon the abrupt loss of spatial pair correlations, which is quantified by a rapid increase of u_{rel} in the solid-liquid transition region. However, a careful inspection of u_{rel} revealed that the "Lindemann criterion" will suggest different melting temperatures and densities depending on how the associated IDF value is computed. In particular, the IDF was found to yield divergent and ambiguous results since it is dominated by a few rare (particle exchange) events. To overcome these convergence problems, the *block-averaged IDF* was introduced (first in section 5.3). This quantity allows for a statistical suppression of exponentially rare events and a consistent quantitative analysis of crystal phase boundaries. Further systematic studies aiming at the investigation of the precise details of the solid-liquid phase transition gave rise to the introduction of the *Variance of the block averaged IDF* (VIDF) as a robust, convergent and highly sensitive indicator. The VIDF is unambiguously peaked in the center of the finite melting interval and allows to reliably detect the melting point and the critical fluctuations u_{rel}^{crit}. Advantages of the VIDF as a fluctuation based quantity that constitutes a melting criterion are, (i) the universality of being rigorously applicable to

both classical and quantum systems, and (ii) its direct relation to the physical processes taking place during a phase transition.

Strongly correlated indirect excitons in quantum wells.   The central topic of chapter 5 was the investigation of strongly correlated electrons and holes in a single quantum well heterostructure. The investigation started with a detailed theoretical discussion of requirements of an electrostatic confinement for *spatially indirect excitons* in view of experimental realization. To this end the author quantitatively analysed different electrostatic setups confining neutral excitons within the quantum well plane by means of the quantum-confined Stark effect. In the proposed trap geometry, the parabolic lateral confinement on the micrometer scale is produced by the strong inhomogeneous field of a single tip electrode on top of the semiconductor sample. Using PIMC simulations, electron and holes are shown to form stable permanent dipoles aligned perpendicular to the quantum well plane in the presence of the electric field. The dipole moment causes various favorable (collective) properties of the indirect excitons which were discussed. In particular, the strong repulsive interaction between the indirect excitons prevents droplet formation and stabilizes the excitons up to high densities. On the basis of the considered trap, the author discussed the influence of electric field strength, tip-to-sample distance, excitation intensity (related to the exciton population of the trap) and temperature on the confined N-exciton system. The broad range of accessible exciton and trap parameters allowed to predict the parameter ranges, in which interesting many-particle phenomena, including Wigner crystallization of (composite bosonic) excitons, are expected to occur in GaAs and ZnSe based quantum wells.

Electron-hole bilayer systems.   A second concern in chapter 5 was the investigation of a remarkable feature of quasi-two-dimensional electron-hole bilayer systems: the gradual transition from pure (long-range) Coulomb to (short-range) dipole intralayer interaction, which occurs when the separation between electron and hole layer d is reduced with respect to the average intralayer interparticle distance. The detailed analysis of the classical ground state configurations for harmonically confined clusters with $N \leq 30$ electrons and hole pairs revealed that at intermediate values of d the energetically most favorable state frequently differs from that found in limits of pure dipole [44] and Coulomb [26, 36] single layer systems. The classical ground state structures were found to be in essential agreement with corresponding quantum systems in the intermediate and strongly coupling regime. Furthermore, the analysis of the normal mode excitation spectrum for the exceptional $N = 19$ cluster pointed out that the lowest mode frequencies exhibit drastic

jumps (of several orders of magnitude) when d is varied. This abrupt change of the collective N-particle behavior highlights the close relationship between structural and collective dynamical cluster properties and suggests – in combination with optical excitation – the implementation of an optoelectronic nano switch which can be controlled by exerting strain on the bilayer system.

Further attention was directed to the effect of mass-asymmetry in electron-hole bilayer systems. By varying the hole to electron mass ratio $M = m_h/m_e$ between 1 and 100 at low temperature, fixed layer separation and high density, it could be demonstrated that the hole behavior can be tuned from delocalized (quantum liquid-like) to localized (crystal-like), while the electrons remain delocalized. The complicated interplay between Coulomb correlations (such as electron-hole pairing) and quantum effects of both, electrons and holes, was fully taken into account by performing first-principle path integral Monte Carlo simulations. While in bulk semiconductors holes are found to undergo a phase transition to a crystalline state if the mass ratio exceeds a critical value of $M_{cr} \approx 80$ [5], in the present thesis it was shown that in bilayer systems M_{cr} can be drastically reduced by properly choosing the layer separation and the in-layer particle density. As a striking result, hole crystallization was found already for $M_{cr} \leq 10$. The theoretical finding is in the range of experimental accessibility with standard semiconductor materials and underlines the exciting physical phenomena available in (quantum) bilayer systems.

Bibliography

[1] R.C. Ashoori, *Electrons in artificial atoms*, Nature **379**, 413 (1996)

[2] A. Filinov, M. Bonitz, and Yu.E. Lozovik, *Wigner crystallization in mesoscopic 2D electron systems*, Phys. Rev. Lett. **86**, 3851 (2001)

[3] C.C. Grimes and G. Adams, *Evidence for a Liquid-to-Crystal Phase Transition in a Classical, Two-Dimensional Sheet of Electrons*, Phys. Rev. Lett. **42**, 795 (1979)

[4] P. Leiderer, W. Ebner and V.B. Shikin, *Macroscopic electron dimples on the surface of liquid helium*, Surface Science **113**, 405 (1982)

[5] M. Bonitz, V.S. Filinov, V.E. Fortov. P.R. Levashov, and H. Fehske, *Crystallization in Two-Component Coulomb Systems*, Phys. Rev. Lett. **95**, 235006 (2005)

[6] D.J. Wineland, J.C. Bergquist, W.M. Itano, J.J. Bollinger, and C.H. Manney, *Atomic-Ion Coulomb Clusters in an Ion Trap*, Phys. Rev. Lett. **59**, 2935 (1987)

[7] W.M. Itano, J.J. Bollinger, J.N. Tan, B. Jelenkovic, X.-P. Huang, and D.J. Wineland, *Bragg diffraction from crystallized ion plasmas*, Science **279**, 686 (1998)

[8] M. Block, A. Drakoudis, H. Leuthner, P. Seibert and G. Werth, *Crystalline ion structures in a Paul trap*, J. Phys. B: At. Mol. Opt. Phys. **33**, 375 (2000)

[9] A. Mortensen, E. Nielsen, T. Matthey, and M. Drewsen, *Observation of Three-Dimensional Long-Range Order in Small Ion Coulomb Crystals in an rf Trap*, Phys. Rev. Lett. **96**, 103001 (2006)

[10] Wen-Tau Juan, Zen-Hong Huang, Ju-Wang Hsu, Yin-Ju Lai, and Lin I, *Observation of dust Coulomb clusters in a plasma trap*, Phys. Rev. E **58**, R6947 (1998)

[11] Wen-Tau Juan, Ju-Wang Hsu, Zen-Hong Huang, Yin-Ju Lai, and Lin I, *Structures and Motions of Strongly Coupled Quasi-2D Dust Coulomb Clusters in Plasmas: From Small N to Large N*, Chinese Journal of Physics **73**, 184 (1999)

[12] M. Klindworth, A. Melzer, A. Piel, V.A. Schweigert, *Laser-excited intershell rotation of finite Coulomb clusters in a dusty plasma*, Phys. Rev. B **61**, 8404 (2000)

[13] A. Melzer, M. Klindworth, and A. Piel, *Normal Modes of 2D Finite Clusters in Complex Plasmas*, Phys. Rev. Lett. **87**, 115002 (2001)

[14] A. Melzer, *Mode spectra of thermally excited two-dimensional dust Coulomb clusters*, Phys. Rev. E **67**, 016411 (2003)

[15] O. Arp, D. Block, A. Piel and A. Melzer, *Dust Coulomb Balls: Three-Dimensional Plasma Crystals*, Phys. Rev. Lett. **93**, 165004 (2004)

[16] A.V. Gorbunov and V.B. Timofeev, *Collective state in a Bose gas of interacting interwell excitons*, JETP Lett. **83**, 146 (2006)

[17] V.B. Timofeev, A.V. Gorbunov *Collective state of the Bose gas of interacting dipolar excitons*, Journal of Applied Physics **101**, 081708 (2007)

[18] V.B Timofeev, A.V. Gorbunov and A.V. Larionov, *Long-range coherence of interacting Bose gas of dipolar excitons*, J. Phys.: Condens. Matter **19**, 295209 (2007)

[19] Y. Zhou, M. Karplus, K. D. Ball, and R. S. Berry, *The distance fluctuation criterion for melting: Comparison of square-well and Morse potential models for clusters and homopolymers*, J. Chem. Phys. **116**, 2323 (2002)

[20] D.D. Frantz, *Magic number behavior for heat capacities of medium-sized classical Lennard-Jones clusters*, J. Chem. Phys. **115**, 6136 (2001)

[21] A. Proykova and R.S. Berry, *Insights into phase transitions from phase changes of clusters*, J. Phys. B: At. Mol. Opt. Phys. **39**, R 167 (2006)

[22] H.P. Büchler, E. Demler, M. Lukin, A. Micheli, N. Prokof'ev, G. Pupillo, and P. Zoller, *Strongly Correlated 2D Quantum Phases with Cold Polar Molecules: Controlling the Shape of the Interaction Potential*, Phys. Rev. Lett. **98**, 060404 (2007)

[23] A. Lomakin, N. Asherie, and G.B. Benedek, *Liquid-solid transition in nuclei of protein crystals*, Proc. Natl. Acad. Sci. USA. **100**, 10254 (2003)

[24] S. Hamaguchi, R.T. Farouki and D.H.E. Dubin, *Triple point of Yukawa systems*, Phys. Rev. E **56**, 4671 (1997)

[25] Y.E. Lozovik, V. Mandelshtam, *Coulomb clusters in a trap*, Phys. Lett. A **145**, 269 (1990)

[26] V.M. Bedanov and F.M. Peeters *Ordering and phase transitions of charged particles in a classical finite two-dimensional system*, Phys. Rev. B **49**, 2667 (1994)

[27] A. Mortensen, *Aspects of Ion Coulomb Crystal based Quantum Memory for Light*, Ph.D. thesis, University of Aarhus (2005)

[28] A. Melzer, S. Käding, D. Block and A. Piel, Stereoskopie in staubigen Plasmen, Photonik **6**, 56 (2007)

[29] O. Vaulina, S. Khrapak and G. Morfill, *Universal scaling in complex (dusty) plasmas*, Phys. Rev. E **66**, 016404 (2002)

[30] L.P. Kouwenhoven and C.M. Marcus, *Quantum Dots*, Physics World **11**, 35 (1998)

[31] O. Arp, D. Block, M. Bonitz, H. Fehske, V. Golubnychiy, S. Kosse, P. Ludwig, A. Melzer, and A. Piel, *3D Coulomb Balls: Experiment and Simulation,* Journal of Physics: Conference Series **11**, 234-247 (2005)

[32] M. Bonitz, D. Block, O. Arp, V. Golubnychiy, H. Baumgartner, P. Ludwig, A. Piel, and A. Filinov, *Structural properties of screened Coulomb balls,* Phys. Rev. Lett. **96**, 075001 (2006)

[33] R.W. Hasse and V.V. Avilov *Structure and Madelung energy of spherical Coulomb crystals*, Phys. Rev. A **44**, 4506 (1991)

[34] V.A. Schweigert and F.M. Peeters, *Spectral properties of classical two-dimensional clusters*, Phys. Rev. B **51**, 7700 (1995)

[35] B. Reusch, W. Häusler, and H. Grabert, *Wigner molecules in quantum dots*, Phys. Rev. B **63**, 113313 (2001)

[36] M. Kong, B. Partoens, and F.M. Peeters, *Transition between ground state and metastable states in classical two-dimensional atoms*, Phys. Rev. E **65**, 046602 (2002)

[37] P. Ludwig, S. Kosse, and M. Bonitz, *Structure of spherical three-dimensional Coulomb crystals*, Phys. Rev. E **71**, 046403 (2005)

[38] P. Ludwig, K. Balzer, H. Stolz and M. Bonitz, *On the Coulomb-dipole transition in mesoscopic electron-hole bilayers*, New Journal of Physics **10**, 083031 (2008)

[39] M. Bonitz, V. Golubnychiy, A.V. Filinov and Yu.E. Lozovik, *Single-Electron control of Wigner crystallization*, Microelectronic Engineering **63**, 141 (2002)

[40] V. Golubnychiy, P. Ludwig, A. Filinov, and M. Bonitz, *Controlling intershell rotations in mesoscopic electron clusters,* Superlattices and Microstructures **34**, 219 (2004)

[41] P. Ludwig, A. Filinov, M. Bonitz, and H. Stolz, *Quantum Stark confined strongly correlated indirect excitons in quantum wells,* phys. stat. sol. (b) **243**, No. 10 2363-2366 (2006)

[42] S.W.S. Apolinário, *Structural and dynamical properties of finite size two- and three-dimensional Wigner crystals*, Ph.D. thesis, Universiteit Antwerpen (2008)

[43] G.E. Astrakharchik, J. Boronat, I.L. Kurbakov, and Yu. E. Lozovik, *Quantum Phase Transition in a Two-Dimensional System of Dipoles*, Phys. Rev. Lett. **98**, 060405 (2007)

[44] A.I. Belousov, Yu.E. Lozovik, *Mesoscopic and macroscopic dipole clusters: structure and phase transitions*, Eur. Phys. J. D **8**, 251 (2000)

[45] Ying-Ju Lai and Lin I, *Packings and defects of strongly coupled two-dimensional Coulomb clusters: Numerical simulation*, Phys. Rev. E **60**, 4743 (1999)

[46] G.E. Astrakharchik, A.I. Belousov and Yu.E. Lozovik, Properties of two-dimensional dusty plasma clusters, *Physics Letters A* **258**, 123 (1999)

[47] M. Kong M, B. Partoens, and F.M. Peeters, *Structural, dynamical and melting properties of two-dimensional clusters of complex plasmas*, New J. Phys. **5**, 23 (2003)

[48] B.J. Alder and T.E. Wainwright, *Phase Transition for a Hard Sphere System*, Journal of Chem. Phys. **27**, 1208 (1957)

[49] B.J. Alder and T.E. Wainwright, *Studies in Molecular Dynamics. I. General Method*, Journal of Chem. Phys. **31**, 459 (1959)

[50] B.J. Alder and T.E. Wainwright, *Studies in Molecular Dynamics. II. Behavior of a small number of elastic spheres*, Journal of Chem. Phys. **33**, 1439 (1960)

[51] J.R. Cash and A.H. Karp, *A variable order Runge-Kutta method for initial value problems with rapidly varying right-hand sides*, ACM Transactions on Mathematical Software **16**, 201 (1990)

[52] W.H. Press, S.A. Teukolsky, W.T. Vetterling, B.P. Flannery, *Numerical Recipes in C*, Cambridge University Press (1992)

[53] P. Ludwig, *Mesoskopische Exzitonencluster in gekoppelten Quantenpunkten*, Diplomarbeit, Universität Rostock (2003)

[54] N. Metropolis, A.W. Rosenbluth, M.N. Rosenbluth, A.H. Teller, and E. Teller, *Equation of state calculation by fast computing machines*, Journal of Chemical Physics **21**, 1087 (1953)

[55] J. Dongarra and F. Sullivan, *Guest Editors Introduction to the top 10 algorithms*, Computing in Science & Engineering **2**, 22 (2000)

[56] D.W. Heermann, Computer Simulation Methods in Theoretical Physics, 2nd edition Springer-Verlag New York, Berlin, Heidelberg (1990)

[57] K. Binder, *Computersimulationen*, Physik Journal **5**, 25 (2004)

[58] A. Filinov, J. Böning, and M. Bonitz, *Path Integral Monte Carlo Simulations of Charged Particles in Traps*, Chapter in: Springer Lecture Notes in Physics **739**, 397 (2008)

[59] M. Bonitz and D. Semkat (eds.), *Introduction to Computational Methods for Many-Body Physics*, Rinton Press, Princeton (2006)

[60] W. Janke, *Monte Carlo Methods in Classical Statistical Physics*, Chapter in: Springer Lecture Notes in Physics **739**, 79 (2008)

[61] R.P. Feynman and A.R. Hibbs, *Quantum Physics and Path Integrals*, McGraw-Hill, New York (1965)

[62] H.F. Trotter, *Approximation of semi-groups of operators*, Pacific J. Math. **8**, 887 (1958)

[63] H. De Raedt and B. De Raedt, *Applications of the generalized Trotter formula*, Physical Review A **28**, 3575 (1983)

[64] M. Boninsegni, N. Prokof'ev, and B. Svistunov, *Worm Algorithm for Continuous-Space Path Integral Monte Carlo Simulations*, Phys. Rev. Lett. **96**, 070601 (2006)

[65] R.G. Storer, *Path-Integral Calculation of the Quantum-Statistical Density Matrix for Attractive Coulomb Forces*, J. Math. Phys. **9**, 964 (1968)

[66] A.D. Klemm and R.G. Storer, *The structure of quantum fluids: helium and neon*, Australian Journal of Physics **26**, 43 (1973)

[67] D.M. Ceperley, *Path integrals in the theory of condensed helium*, Reviews of Modern Physics **67**, 279 (1995)

[68] B. Militzer, *Path Integral Monte Carlo Simulations of Hot Dense Hydrogen*, Ph.D. thesis, University of Illinois at Urbana-Champaign (2000)

[69] L.B. i Barberà, *Path Integral Monte Carlo. Algorithms and applications to quantum fluids*, Ph.D. thesis, Universitat Politècnica de Catalunya (2002)

[70] V. Golubnychiy, *Molecular Dynamics simulations of strongly correlated mesoscopic and macroscopic Coulomb systems*, Ph.D. thesis, Christian-Albrechts-Universität zu Kiel (2004)

[71] D.M. Ceperley, *Fermion Nodes*, J. Stat. Phys. *63*, 1237 (1991)

[72] V.S. Filinov, M. Bonitz, W. Ebeling, and V.E. Fortov, *Thermodynamics of hot dense H-plasmas: Path integral Monte Carlo simulations and analytical approximations*, Plasma Physics and Controlled Fusion **43**, 743 (2001)

[73] V. Filinov, H. Fehske, M. Bonitz, V.E. Fortov, and P.R. Levashov, *Correlation effects in partially ionized mass asymmetric electron-hole plasmas*, Phys. Rev. E **75**, 036401 (2007)

[74] C.H. Mak, R. Egger, and H. Weber-Gottschick, *Multilevel Blocking Approach to the Fermion Sign Problem in Path-Integral Monte Carlo Simulations*, Phys. Rev. Lett. **81**, 4533 (1998)

[75] M.V. Dikovsky and C.H. Mak, *Analysis of the multilevel blocking approach to the fermion sign problem: Accuracy, errors, and practice*, Phys. Rev. B **63**, 235105 (2001)

[76] A. Filinov, M. Bonitz, and W. Ebeling, *Improved Kelbg potential for correlated Coulomb systems*, J. Phys. A: Math. Gen. **36**, 5957 (2003)

[77] B. Jakob, P.-G. Reinhard, C. Toepffer, and G. Zwicknagel, *Wave packet simulation of dense hydrogen*, Phys. Rev. E **76**, 036406 (2007)

[78] Robert E. Wyatt, *Quantum Dynamics with Trajectories*, Series: Interdisciplinary Applied Mathematics (2005)

[79] V. Filinov, M. Bonitz, A. Filinov, and V. Golubnychiy, *Wigner Function Quantum Molecular Dynamics*, Chapter in: Springer Lecture Notes in Physics **739**, 41 (2008)

[80] P.N. Roy, S. Jang, and G.A. Voth, *Feynman path centroid dynamics for Fermi–Dirac statistics*, J. Chem. Phys. **111**, 5303 (1999)

[81] W.D. Kraeft, D. Kremp, W. Ebeling, and G. Röpke, *Quantum Statistics of Charged Particle Systems*, Akademie-Verlag, Berlin (1986)

[82] M. Bonitz, *Quantum Kinetic Theory*, Teubner-Verlag, Stuttgart/Leipzig (1998)

[83] M. Bonitz, D. Semkat, A. Filinov, V. Golubnychiy, D. Kremp, D.O. Gericke, M.S. Murillo, V. Filinov, V.E. Fortov, W. Hoyer, and S.W. Koch, *Theory and Simulation of Strong Correlations in Quantum Coulomb Systems*, J. Phys. A: Math. Gen. **36**, 5921 (2003)

[84] H. Kählert, P. Ludwig, H. Baumgartner, M. Bonitz, D. Block, S. Käding, A. Melzer, and A. Piel, *Probability of metastable configurations in spherical three-dimensional Yukawa crystals*, submitted to Phys. Rev. E, ArXiv:0805.3016

[85] Y. Ivanov, P. Ludwig, A. Melzer, A. Filinov, and M. Bonitz, *Normal modes of spherical dust clusters*, Poster at DPG Spring meeting, Düsseldorf, March 19-23 2007, Verhandlungen der Deutschen Physikalischen Gesellschaft, P7.42

[86] A. Filinov, P. Ludwig, V. Golubnychiy, M. Bonitz, and Yu.E. Lozovik, *Equilibrium and dynamical properties of few particle systems in quantum dots and bilayers*, phys. stat. sol. (c) **0**, 1518 (2003)

[87] C. Henning, K. Fujioka, P. Ludwig, A. Piel, A. Melzer, and M. Bonitz, *Existence and Vanishing of the Breathing Mode in Strongly Correlated Finite Systems*, Phys. Rev. Lett. **101**, 045002 (2008)

[88] M. D. Jones and D. M. Ceperley, *Crystallization of the One-Component Plasma at Finite Temperature*, Phys. Rev. Lett. **76**, 4572 (1996)

[89] S.L. Gilbert, J.J. Bollinger, and D.J. Wineland, *Shell-Structure Phase of Magnetically Confined Strongly Coupled Plasmas*, Phys. Rev. Lett. **60**, 2022 (1988)

[90] O. Arp, D. Block, M. Klindworth, and A. Piel, *Confinement of Coulomb balls*, Phys. Plasmas **12**, 122102 (2005)

[91] J.H. Chu and Lin I, *Direct observation of Coulomb crystals and liquids in strongly coupled rf dusty plasmas*, Phys. Rev. Lett. **72**, 4009 (1994)

[92] H. Thomas, G.E. Morfill, V. Demmel, J. Goree, B. Feuerbacher and D. Möhlmann,

Plasma Crystal: Coulomb Crystallization in a Dusty Plasma, Phys. Rev. Lett. **73**, 652 (1994)

[93] Y. Hayashi and K. Tachibana, *Observation of coulomb-crystal formation from carbon particles grown in a methane plasma*, Japan. J. Appl. Phys. **33**, L804 (1994)

[94] A. Melzer, T. Trottenberg and A. Piel, *Experimental determination of the charge on dust particles forming Coulomb lattices*, Phys. Lett. A **191**, 301 (1994)

[95] V.E. Fortov, A.V. Ivlev, S.A. Khrapak, A.G. Khrapak, G.E. Morfill, *Complex (dusty) plasmas: Current status, open issues, perspectives*, Physics Reports **421**, 1-103.(2005)

[96] A. Bouchoule, *Dusty Plasmas: Physics, Chemistry and Technological Impacts in Plasma Processing*, John Wiley & Sons Ltd., New York (1999)

[97] G.S. Selwyn, J. Singh and R. S. Bennett, *In situ laser diagnostic studies of plasma-generated particulate contamination*, J. of Vacuum Science & Technology A **7**, 2758 (1988)

[98] P. Roca i Cabarrocas, *Plasma enhanced chemical vapor deposition of amorphous, polymorphous and microcrystalline silicon films*, J.of Non Cryst. Solids **31**, 266 (2000)

[99] F. Verheest (ed.), *Waves in Dusty Space Plasmas*, Kluwer Academic Publishers, Dordrecht (2002)

[100] K. Qiao, and T.W. Hyde, *Numerical simulation and analysis of thermally excited waves in plasma crystals*, Advances in Space Research **34**, 2390 (2004)

[101] F. Diedrich, E. Peik, J.M. Chen, W. Quint, and H. Walther, *Observation of a Phase Transition of Stored Laser-Cooled Ions*, Phys. Rev. Lett. **59**, 2931 (1987)

[102] J.I. Cirac and P. Zoller, *Quantum Computations with Cold Trapped Ions*, Phys. Rev. Lett. **74**, 4091 (1995)

[103] H. Ikezi, *Coulomb solid of small particles in plasmas*, Phys. Fluids **29**, 1764 (1986)

[104] D.H.E. Dubin and T.M. O'Neill, *Trapped nonneutral plasmas, liquids, and crystals (the thermal equilibrium states)*, Rev. Mod. Phys. **71**, 87 (1999)

[105] G. Morfill and H. Kersten, *Focus on Complex (Dusty) Plasmas*, New J. Phys. **5** (2003)

[106] S. Ichimaru, *Strongly coupled plasmas: high-density classical plasmas and degenerate electron liquids*, Rev. Mod. Phys. **54**, 1017 (1982)

[107] S. W. S. Apolinário, B. Partoens and F. M. Peeters, *Structural and dynamical aspects of small three-dimensional spherical Coulomb clusters*, New Journal of Physics **9**, 283 (2007)

[108] T. Kamimura, Y. Suga and O. Ishihara, *Configurations of Coulomb clusters in plasma*, Phys. Plasmas **14**, 123706 (2007)

[109] K. Qiao, M. Benesh, and T. Hyde, Structural Phases of Bounded Three-Dimensional Screened Coulomb Clusters (Finite Yukawa System) IEEE transactions on plasma science **35**, 346 (2007)

[110] H. Baumgartner, D. Asmus, V. Golubnychiy, P. Ludwig, H. Kählert, and M. Bonitz, *Structural transitions of finite spherical Yukawa crystals*, accepted for publication in New J. Phys. (2008), ArXiv:0805.4617

[111] D. Block, *Experiments on structural formation in plasmas*, habilitation thesis, Christian-Albrechts-Universität zu Kiel (2008)

[112] H. Baumgartner, H. Kählert, V. Golubnychiy, C. Henning, S. Käding, A. Melzer, and M. Bonitz, *Shell structure of Yukawa balls*, Contrib. Plasma Phys. **47**, 281 (2007)

[113] Hiroo Totsuji, Takafumi Ogawa, Chieko Totsuji, and Kenji Tsuruta, *Structure of spherical Yukawa clusters: A model for dust particles in dusty plasmas in an isotropic environment*, Phys. Rev. E **72**, 036406 (2005)

[114] T.E. Sheridan, *Continuum model for the breathing oscillation of a spherical complex plasma*, Phys. Plasmas **13**, 022106 (2006)

[115] M. Drewsen, C. Brodersen, L. Hornekær, J. S. Hangst, and J. P. Schiffer, *Large Ion Crystals in a Linear Paul Trap*, Phys. Rev. Lett. **81**, 2878 (1998)

[116] K. Tsuruta and S. Ichimaru, *Binding energy, microstructure, and shell model of Coulomb clusters*, Phys. Rev. A **48**, 1339 (1993)

[117] H. Löwen, *Melting, freezing and colloidal suspensions*, Physics Reports **237**, 249 (1994)

[118] F.A. Lindemann, *Über die Berechnung molekularer Eigenfrequenzen*, Phys. Zeitschrift **11**, 909 (1910)

[119] J.J. Gilvarry, *The Lindemann and Grüneisen Laws*, Physical Review **102**, 308 (1956)

[120] J.P. Hansen and L. Verlet, *Phase Transitions of the Lennard-Jones System*, Phys. Rev. **184**, 151 (1969)

[121] H. Löwen, T. Palberg, and R. Simon, *Dynamical criterion for freezing of colloidal liquids*, Phys. Rev. Lett. **70**, 1557 (1993)

[122] P. Ludwig, J. Böning, D. Bühr, T. Ott, and M. Bonitz, to be published

[123] T. Meier, P. Thomas, S.W. Koch, *Coherent Semiconductor Optics: From Basic Concepts to Nanostructure Applications*, Springer-Verlag, (2007)

[124] C.F. Klingshirn, *Semiconductor Optics*, Third Edition, Springer-Verlag (2007)

[125] L.V. Keldysh and A.N. Kozlov, *Collective properties of excitons in semiconductors*, Zh. Eksp. Teor. Fiz. **54**, 978 (1968); Sov. Phys. JETP **27**, 521 (1968)

[126] A. Griffin, D.W. Snoke, and S. Stringari (eds.), *Bose-Einstein Condensation*, Cambridge, New York (1995)

[127] S. De Palo, F. Rapisarda, and G. Senatore, *Excitonic Condensation in a Symmetric Electron-Hole Bilayer*, Phys. Rev. Lett. **88**, 206401 (2002)

[128] J. Shumway, and D.M. Ceperley, *Quantum Monte Carlo simulations of exciton condensates*, Solid State Communications **134**, 19 (2005)

[129] A. Posazhennikova, *Colloquium: Weakly interacting, dilute Bose gases in 2D*, Rev. Mod. Phys. **78**, 1111 (2006)

[130] L.V. Butov, A.L. Ivanov, A. Imamoglu, P.B. Littlewood, A.A. Shashkin, V.T. Dolgopolov, K.L. Campman, and A.C. Gossard, *Stimulated Scattering of Indirect Excitons in Coupled Quantum Wells: Signature of a Degenerate Bose-Gas of Excitons*, Phys. Rev. Lett. **86**, 5608 (2001)

[131] D. Snoke, *Spontaneous Bose Coherence of Excitons and Polaritons*, Science **298**, 1368 (2002)

[132] L.V. Butov, *Condensation and pattern formation in cold exciton gases in coupled quantum wells*, J. Phys.: Condens. Matter **16**, R1577 (2004)

[133] C.W. Lai, J. Zoch, A.C. Gossard, and D.S. Chemla, *Phase Diagram of Degenerate Exciton Systems*, Science **303**, 503 (2004)

[134] D. Snoke, *Coherent questions*, Nature **443**, 403 (2006)

[135] P. Wachter, *Exciton condensation in an intermediate valence compound: TmSe0.45Te0.55*, Solid State Communications **118**, 645 (2001)

[136] P. Wachter, B. Bucher, and J. Malar, *Possibility of a superfluid phase in a Bose condensed excitonic state*, Phys. Rev. B **69**, 094502 (2004)

[137] D. Fröhlich, G. Dasbach, G. Baldassarri Höger von Högersthal, M. Bayer, R. Klieber, D. Suter, and H. Stolz, *High resolution spectroscopy of yellow 1S excitons in Cu2O*, Solid State Communications **134**, 139 (2005)

[138] H. Stolz, M. Kira, and S.W. Koch, *Quantenoptik in Halbleitern*, Physik Journal **7**, 37 (2008)

[139] Yu.E. Lozovik and O.L. Berman, *Quantum crystallization of two-dimensional dipole systems*, Physics of the solid state **40**, 1228 (1998)

[140] A. Filinov, M. Bonitz, and Yu.E. Lozovik, *Excitonic clusters in coupled quantum dots*, J. Phys. A: Math. Gen. **36**, 5899 (2003)

[141] Yu.E. Lozovik, S.Yu. Volkov, and M. Willander, *Structural Properties of the Condensate in Two-Dimensional Mesoscopic Systems of Strongly Correlated Excitons*, JETP Letters **79**, No. 10, 473 (2004)

[142] P. Hartmann, Z. Donkó, and G.J. Kalman, *Structure and phase diagram of strongly-coupled bipolar charged-particle bilayers*, Europhys. Lett. **72**, 396 (2005)

[143] C. Mora, O. Parcollet, and X. Waintal, *Quantum melting of a crystal of dipolar bosons*, Phys. Rev. B **76**, 064511 (2007)

[144] M.J. Kellogg, *Evidence for Excitonic Superfluidity in a Bilayer Two-Dimensional Electron System*, Ph.D. thesis, California Institute of Technology (2005)

[145] O.L. Berman, Y.E. Lozovik, D.W. Snoke, and R.D. Coalson, *Superfluidity of dirty indirect excitons and magnetoexcitons in a two-dimensional trap*, Phys. Rev. B 73, 235352 (2006)

[146] E. Kim, and M.H.W. Chan, *Probable observation of a supersolid helium phase* Nature **427**, 225 (2004)

[147] Y.N. Joglekar, A.V. Balatsky, and S. Das Sarma, *Wigner supersolid of excitons in electron-hole bilayers*, Phys. Rev. B **74**, 233302 (2006)

[148] V.V. Solov'ev, I.V. Kukushkin, J.H. Smet, K. von Klitzing, and W. Dietsche, *Indirect Excitons and Double Electron-Hole Layers in a Wide Single GaAs/AlGaAs Quantum Well in a Strong Electric Field*, JETP Letters **83**, 553 (2006)

[149] V.V. Solov'ev, I.V. Kukushkin, J.H. Smet, K. von Klitzing, and W. Dietsche, *Kinetics of Indirect Electron-Hole Recombination in a Wide Single Quantum Well in a Strong Electric Field*, JETP Letters **84**, 256 (2006)

[150] Z. Vörös, D.W. Snoke, L. Pfeiffer, and K. West, *Trapping Excitons in a Two-Dimensional In-Plane Harmonic Potential: Experimental Evidence for Equilibration of Indirect Excitons*, Phys. Rev. Lett. **97**, 016803 (2006)

[151] A.L. Ivanov, P.B. Littlewood, and H. Haug, *Bose-Einstein statistics in thermalization and photoluminescence of quantum-well excitons*, Phys. Rev. B **59**, 5032 (1999)

[152] D. Snoke, S. Denev, Y. Liu, L. Pfeiffer, and K. West, *Long-range transport in excitonic dark states in coupled quantum wells* Nature **418**, 754 (2002)

[153] L.V. Butov, A.C. Gossard, and D.S. Chemla, *Macroscopically ordered state in an exciton system*, Nature **418**, 751 (2002)

[154] Z. Vörös, D.W. Snoke, L. Pfeiffer, and K. West, *Equilibration of two-dimensional excitons in an in-plane harmonic potential*, phys. stat. sol. (c) **3**, No. 7, 2461 (2006)

[155] S. Ben-Tabou de-Leon and B. Laikhtman, *Phase diagram of quasi two-dimensional electron-hole gas in single and coupled quantum wells*, phys. stat. sol. (a) **190**, 689 (2002)

[156] K. Sperlich, P. Ludwig, A. Filinov, K. Balzer, M. Bonitz, and H. Stolz, to be published

[157] E. Wigner, *On the Interaction of Electrons in Metals*, Phys. Rev. **46**, 1002 (1934)

[158] R. Egger, W. Häusler, C.H. Mak, and H. Grabert, *Crossover from Fermi Liquid to Wigner Molecule Behavior in Quantum Dots*, Phys. Rev. Lett. **82**, 3320 (1999)

[159] A. Ghosal, A.D. Güçlü, C.J. Umrigar, D. Ullmo, and H.U. Baranger, *Correlation Induced Inhomogeneity in Circular Quantum Dots*, Nature Physics **2**, 336 (2006)

[160] A.V. Gorbunov and V.B. Timofeev, *Large-scale coherence of the Bose condensate of spatially indirect excitons* JETP Lett. **84**, 329 (2006)

[161] Foundations of Crystallography, *IUCr: Report of the Executive Committee for 1991*, Acta Crystallogr. A**48** 922–946, 928 (1992)

[162] D. Block, M. Kroll, O. Arp, A. Piel S. Käding, Y. Ivanov, A. Melzer, C. Henning, H. Baumgartner, P. Ludwig, and M. Bonitz, *Structural and dynamical properties of Yukawa balls,* Plasma Physics and Controlled Fusion **49**, B109-B116 (2007)

[163] P. Ludwig, A. Filinov, M. Bonitz, and Yu.E. Lozovik, *Ground state and structural transitions in mesoscopic electron-hole bilayers*, Contrib. Plasma Phys. **43**, 285 (2003)

[164] H. Totsuji, C. Totsuji, T. Ogawa, and K. Tsuruta, *Ordering of dust particles in dusty plasmas under microgravity*, Phys. Rev. E **71**, 045401(R) (2005)

[165] M. Lampe, G. Joyce, G. Ganguli, and V. Gavrishchaka, *Interactions between dust grains in a dusty plasma*, Phys. Plasmas **7**, 3851 (2000)

[166] M. Lampe, V. Gavrishchaka, G. Ganguli, and G. Joyce, *Effect of Trapped Ions on Shielding of a Charged Spherical Object in a Plasma*, Phys. Rev. Lett. **86**, 5278 (2001)

[167] G. Joyce, M. Lampe, and G. Ganguli, *Instability-Triggered Phase Transition to a Dusty-Plasma Condensate*, Phys. Rev. Lett. **88**, 095006 (2002)

[168] M. Lampe, G. Joyce, and G. Ganguli, *Structure and dynamics of dust in streaming plasma: Dust molecules, strings, and crystals*, IEEE transactions on plasma science **33**, 57 (2005)

[169] C. J. Pethick, and H. Smith, *Bose-Einstein Condensation in Dilute Gases*, Cambridge, New York, 2002

[170] F. Baletto and R. Ferrando, *Structural properties of nanoclusters: Energetic, thermodynamic, and kinetic effects*, Rev. Mod. Phys. **77**, 371 (2005)

[171] A.L. Mackay, *A dense non-crystallographic packing of equal spheres*, Acta Cryst. **15**, 916 (1962)

[172] M. Drewsen, I. Jensen, J. Lindballe, N. Nissen, R. Martinussen, A. Mortensen, P. Staanum and D. Voigt, *Ion Coulomb crystals: a tool for studying ion processes*, International Journal of Mass Spectrometry **229**, 83 (2003)

[173] V. Negoita and D. W. Snoke, and K. Eberl, *Harmonic-potential traps for indirect excitons in coupled quantum wells*, Phys. Rev. B **60**, 2661 (1999)

[174] C.-W. Lai, *Spatially Indirect Excitons in Coupled Quantum Wells*, Ph.D. thesis, University of California, Berkley (2004)

[175] J.B. Shumway, *Quantum Monte Carlo simulations of electrons and holes*, Ph.D. thesis, University of Illinois at Urbana-Champaign (1999)

[176] C. Yannouleas and U. Landman, *Symmetry breaking and quantum correlations in finite systems: studies of quantum dots and ultracold Bose gases and related nuclear and chemical methods*, Rep. Prog. Phys. **70**, 2067 (2007)

[177] G. J. Kalman , P. Hartmann, Z. Donkó, and K. I. Golden, *Collective Excitations in Electron-Hole Bilayers*, Phys. Rev. Lett. **98**, 236801 (2007)

[178] E. Anisimovas and F.M. Peeters, *Correlated few-particle states in artificial bipolar molecule*, Phys. Rev. B **65**, 233302 (2002)

[179] J. D. Feldmann, G. J. Kalman, P. Hartmann, and M. Rosenberg, *Ground State of Magnetic Dipoles on a Two-Dimensional Lattice: Structural Phases in Complex Plasmas*, Phys. Rev. Lett. **100**, 085001 (2008)

List of Publications

Complete List of the Author's Peer-Reviewed Journal Publications

(1) A.V. Filinov, P. Ludwig, V. Golubnychiy, M. Bonitz, and Yu.E. Lozovik,
    Equilibrium and dynamical properties of few particle systems in quantum dots and bilayers,
    phys. stat. sol. (c) **0**, No. 5, 1518 (2003)

(2) P. Ludwig, A. Filinov, M. Bonitz, and Yu.E. Lozovik,
    Ground state and structural transitions in mesoscopic electron-hole bilayers,
    Contrib. Plasma Phys. **43**, No. 5-6, 285 (2003)

(3) V. Golubnychiy, P. Ludwig, A.V. Filinov, and M. Bonitz,
    Controlling intershell rotations in mesoscopic electron clusters,
    Superlattices and Microstructures **34**, No. 3-6, 219-224 (2004)

(4) P. Ludwig, S. Kosse, and M. Bonitz,
    Structure of spherical three-dimensional Coulomb crystals,
    Phys. Rev. E **71**, 046403 (2005)

(5) O. Arp, D. Block, M. Bonitz, H. Fehske, V. Golubnychiy, S. Kosse, P. Ludwig, A. Melzer, and A. Piel,
    3D Coulomb Balls: Experiment and Simulation,
    Journal of Physics: Conference Series **11**, 234-247 (2005)

(6) M. Bonitz, D. Block, O. Arp, V. Golubnychiy, H. Baumgartner, P. Ludwig, A. Piel, and A. Filinov,
    Structural properties of screened Coulomb balls,
    Physical Review Letters **96**, 075001 (2006)

(7) A. Filinov, P. Ludwig, Yu.E. Lozovik, M. Bonitz, and H. Stolz,
Strongly correlated indirect excitons in quantum wells in high electric fields,
J. Phys: Conf. Series **35**, 197 (2006)

(8) P. Ludwig, A. Filinov, M. Bonitz, and H. Stolz,
Quantum Stark confined strongly correlated indirect excitons in quantum wells,
phys. stat. sol. (b) **243**, No. 10, 2363-2366 (2006)

(9) A. Filinov, M. Bonitz, P. Ludwig, and Yu.E. Lozovik,
Path integral Monte Carlo results for Bose condensation of mesoscopic indirect excitons,
phys. stat. sol. (c) **3**, No. 7, 2457-2460 (2006)

(10) C. Henning, H. Baumgartner, A. Piel, P. Ludwig, V. Golubnychiy, M. Bonitz, and D. Block,
Ground state of a confined Yukawa plasma,
Phys. Rev. E **74**, 056403 (2006)

(11) P. Ludwig, A. Filinov, Yu. Lozovik, H. Stolz, and M. Bonitz,
Crystallization in mass-asymmetric electron-hole bilayers,
Contrib. Plasma Phys. **47**, 335-344 (2007)

(12) C. Henning, P. Ludwig, A. Filinov, A. Piel, and M. Bonitz,
Ground state of a confined Yukawa plasma including correlation effects,
Physical Review E **76**, 036404 (2007)

(13) D. Block, M. Kroll, O. Arp, A. Piel S. Käding, Y. Ivanov, A. Melzer, C. Henning, H. Baumgartner, P. Ludwig, and M. Bonitz,
Structural and dynamical properties of Yukawa balls,
Plasma Physics and Controlled Fusion **49**, B109-B116 (2007)

(14) M. Bonitz, P. Ludwig, H. Baumgartner, C. Henning, A. Filinov, D. Block, O. Arp, A. Piel, S. Käding, Y. Ivanov, A. Melzer, H. Fehske, and V. Filinov,
Classical and quantum Coulomb crystals,
Physics of Plasmas **15**, 055704 (2008)

(15) J. Böning, A. Filinov, P. Ludwig, H. Baumgartner, M. Bonitz, and Yu.E. Lozovik,
Melting of trapped few particle systems,
Physical Review Letters **100**, 113401 (2008)

(16) P. Ludwig, K. Balzer, H. Stolz and M. Bonitz,
On the Coulomb-dipole transition in mesoscopic electron-hole bilayers,
New Journal of Physics **10**, 083031 (2008)

(17) C. Henning, K. Fujioka, P. Ludwig, A. Piel, A. Melzer, and M. Bonitz,
Existence and Vanishing of the Breathing Mode in Strongly Correlated Finite Systems,
Physical Review Letters **101**, 045002 (2008)

(18) H. Kählert, P. Ludwig, H. Baumgartner, M. Bonitz, D. Block, S. Käding,
A. Melzer, and A. Piel,
Probability of metastable configurations in spherical three-dimensional Yukawa crystals,
submitted to Phys. Rev. E, arXiv:0805.3016

(19) H. Baumgartner, D. Asmus, V. Golubnychiy, P. Ludwig, H. Kählert, and
M. Bonitz,
Structural transitions of finite spherical Yukawa crystals,
accepted for publication in New Journal of Physics (2008), arXiv:0805.4617

(20) S. Käding, D. Block, A. Melzer, A. Piel, H. Kählert, P. Ludwig, and M. Bonitz,
Shell transitions between metastable states of Yukawa balls,
Phys. Plasmas **15**, 073710 (2008)

Contributions to books and the arXiv.org e-Print archive

(1) P. Ludwig, S. Kosse, V. Golubnychiy, M. Bonitz, and H. Fehske,
Tables of mesoscopic 3D Coulomb balls,
Preprint at arXiv: physics/0409100

(2) M. Bonitz, V.S. Filinov, A. Filinov, V. Golubnychiy, P. Ludwig, H. Baumgartner,
P. Levashov, V.E. Fortov, and H. Fehske,
Structure Formation in Strongly Correlated Coulomb Systems,
In: Irreversible Prozesse und Selbstorganisation, Eds. T. Pöschel, H. Malchow, L.
Schimansky-Geier, Logos-Verlag, Berlin, 143-158 (2006)

Selected Contributions to International Conferences

(1) P. Ludwig, A. Filinov, M. Bonitz, H. Stolz, and Yu.E. Lozovik,
Quantum Stark confined strongly correlated indirect excitons in quantum wells,
Poster at APS March meeting, Denver, Colorado, March 5-9 2007,
Bulletin of the American Physical Society, Series II, Volume 52, No.1, March 2007

(2) P. Ludwig, A. Filinov, M. Bonitz, H. Stolz, and Yu.E. Lozovik,
Crystallization in mass-asymmetric electron-hole bilayers,
Poster at APS March meeting, Denver, Colorado, March 5-9 2007,
Bulletin of the American Physical Society, Series II, Volume 52, No.1, March 2007

(3) Y. Ivanov, P. Ludwig, A. Melzer, A. Filinov, and M. Bonitz,
Normal modes of spherical dust clusters,
Poster at DPG Spring meeting, Düsseldorf, March 19-23 2007,
Verhandlungen der Deutschen Physikalischen Gesellschaft, P7.42, 2007

(4) M. Bonitz, D. Asmus, V. Golubnichiy, H. Baumgartner, and P. Ludwig,
Structural transitions in spherical 3D screened Coulomb crystals,
Poster at 49th Annual Meeting of the Division of Plasma Physics, Orlando, Florida, November 12-16 2007,
Bulletin of the American Physical Society, Volume 52, No.16, YP8 22, Nov. 2007

(5) P. Ludwig, A. Filinov, H. Stolz, and M. Bonitz,
Crystallization of strongly correlated indirect excitons,
Poster at DPG spring meeting, Berlin, February 25-29 2008,
Verhandl. DPG (VI) 43, 1/HL 17.16, 2008

(6) P. Ludwig, A. Filinov, K. Balzer, M. Bonitz, K. Sperlich, and H. Stolz,
Strongly correlated spatially indirect electron-hole states in quantum wells,
Poster at the 9th International Workshop on Nonlinear Optics and Excitation Kinetics in Semiconductors, Klink/Müritz, May 26-29 2008,
Contribution P-68

(7) P. Ludwig, C. Henning, H. Kählert, H. Baumgartner, A. Filinov, and M. Bonitz,
Theory and simulation of spherical Yukawa crystals,
Talk at International Conference "Strongly Coupled Coulomb Systems", Camerino (Italy), July 2008

Danksagung

Wechselwirkung und Austausch machen das Forscherleben erst interessant, deshalb möchte ich an dieser Stelle all denen danken, die durch ihr Wirken mittel- oder unmittelbaren Einfluß auf die Entstehung dieser Arbeit genommen haben, bzw. diese erst möglich gemacht haben.

☺ An erster Stelle möchte ich Prof. Dr. Michael Bonitz danken, den ich im WS 2001 in seinem Seminar „Computational Physics" kennengelernt habe, und der mich von Anfang an für seine Forschung im Feld der Vielteilchenphysik begeistern konnte. Mit seinem unermüdlichen Engagement hat er in den letzten Jahren mein Arbeiten und Denken, auch über die Physik hinaus, entscheidend geprägt.

☺ Darüber hinaus möchte ich Prof. Dr. Heinrich Stolz danken, der mich in seine sympathische Arbeitsgruppe aufgenommen hat und es mir ermöglicht hat, im Rahmen des Rostocker Graduiertenkollegs „Stark korrelierte Vielteilchensysteme" tätig zu werden.

☺ Danken möchte ich insbesondere auch Dr. Alexei Filinov für die freundschaftliche Betreuung dieser Arbeit. Ohne ihn wäre eine so schnelle und direkte Einarbeitung und Nutzung von PIMC nicht möglich gewesen.

☺ Danken möchte ich an dieser Stelle auch meinen Schreibtisch- und Flurkollegen Vova Golubnychiy, Sylvio Kosse, Hilko Cords, Karsten Balzer, Andrea Fromm, Sebastian Bauch, Henning Baumgartner, Jens Böning, Daniel Asmus, Hanno Kählert, Torben Ott und ganz besonders auch Christian Henning für die vielen fruchtbaren wissenschaftlichen Diskussionen.

☺ Danken möchte ich meiner Familie: meiner lieben Mama, Oma, Opa, Ulla, Peter (euch auch Dank für die schönen Aufenthalte in Rostock und Greifswald), Udo, Doris, Sebastian, Steffi und Kati, die mich auf meinem Weg begleitet und unterstützt haben, sowie meiner Fanny, die so viel Sonne in mein Leben bringt.

Selbständigkeitserklärung

Erklärung:

Hiermit versichere ich, dass ich die vorliegende Arbeit selbständig angefertigt und ohne fremde Hilfe verfasst habe, keine außer den von mir angegebenen Hilfsmitteln und Quellen dazu verwendet habe und die den benutzten Werken inhaltlich und wörtlich entnommenen Stellen als solche kenntlich gemacht habe.

Bei den Arbeiten, in denen ich als erster Autor genannt bin, war ich dementsprechend auch federführend. Zu allen Veröffentlichungen wurden substantielle Beiträge in Form von eigenen Rechnungen (Elektrodynamik, Normalmodenanalyse, u.a.) und selbst-ständig durchgeführten Simulationen (MD, MC, PIMC) beigetragen. Die Zielsetzung und konzeptionelle Planung der einzelnen Arbeiten sowie die Interpretation der Resultate wurden gemeinschaftlich mit den Betreuern dieser Arbeit (Prof. Dr. M. Bonitz, Dr. A. Filinov und Prof. Dr. H. Stolz) erarbeitet. Methodenentwicklung erfolgte in Kooperation mit den Mitautoren. Die Hartree-Fock Rechnungen wurden von Karsten Balzer durchgeführt. Die analytische Theorie zum Dichteprofil der Yukawaplasmen wurde von Christian Henning entwickelt. Die Experimente zu den Staubigen Plasmen wurden von den jeweils genannten Mitautoren experimenteller Seite durchgeführt bzw. betreut.

Ich versichere, dass die vorliegende Dissertation weder ganz noch zum Teil bei einer anderen Stelle im Rahmen eines Prüfungsverfahrens vorgelegt worden ist. Ich habe keine früheren Promotionsversuche unternommen.

Rostock, 29. August 2008

—Patrick Ludwig—